ATOMISTIC MODELING OF THE AL AND FE_2O_3 MATERIAL SYSTEM USING CLASSICAL MOLECULAR DYNAMICS

A Dissertation
Presented to
The Academic Faculty

By

Vikas Tomar

In Partial Fulfillment
of the Requirements for the Degree
Doctor of Philosophy in Mechanical Engineering

Georgia Institute of Technology

December, 2005

ATOMISTIC MODELING OF THE AL AND FE_2O_3 MATERIAL SYSTEM USING CLASSICAL MOLCECULAR DYNAMICS

Approved by:

Dr. Min Zhou, Advisor
The George W. Woodruff School of Mechanical Engineering
Georgia Institute of Technology

Dr. David McDowell
The George W. Woodruff School of Mechanical Engineering
Georgia Institute of Technology

Dr. Jianmin Qu
The George W. Woodruff School of Mechanical Engineering
Georgia Institute of Technology

Dr. Sathya Hanagud
School of Aerospace Engineering
Georgia Institute of Technology

Dr. Naresh Thadhani
School of Materials Science and Engineering
Georgia Institute of Technology

Dr. Karl Jacob
School of Polymer, Textile and Fiber Engineering
Georgia Institute of Technology

Date Approved:
October 17, 2005

To My Mom, Dad, Sister, Brother, and Jinhyun

ACKNOLEDGEMENTS

I wish to thank my advisor, Dr. Min Zhou, for his unending support as well as for a series of '*frank discussions*' that have helped me in achieving my professional targets as well as in my professional development for an academic career. I am especially thankful to Dr. David McDowell, Dr. Jianmin Qu, Dr. Farrokh Mistree, Dr. Karl Jacob, Dr. Naresh Thadhani, Dr. Mo Li, and Dr. Sathya Hanagud for extending their support to my career as well as to my research. This research work was supported by an AFOSR-MURI grant to Georgia Tech and computations were carried out at NAVO, ERDC, ARL, AHPCRC, and JPL major shared resources centers. Timely progress in this work would not have been possible without regular discussions at MURI meetings. I earnestly appreciate prompt administrative support of Ms. Cecelia Jones at innumerable occasions during my stay at Georgia Tech. My life during the span of last four and a half years at Georgia Tech would have been very difficult without wonderful colleagues and friends. I wish to thank Karel Minnaar, Greg Ingram, John Clayton, Doug Spearot, Wuwei Liang, Jim Shepherd, Mahesh Shenoy, Ambarish Kulkarni, Vivek Sharma, Nitin Patel, Abhijit Gogulapati, Xia Lu, Jitesh Panchal, Haejin Choi, Abhinav Saxena, Karthik Krishnan, Nishanth Gurnani, Jie Yang, Kai Liu, Jason Mayeur, and many other friends who were always ready to celebrate and share trivialities of research and life with me. I cannot thank enough my fiancée Jinhyun Lee for her patience, understanding, and support that made the coupling between my work and my life an interesting experience.

TABLE OF CONTENTS

LIST OF TABLES

LIST OF FIGURES

SUMMARY

One of the recent advances in materials science has focused on developing materials that have two or more crystalline systems mixed at the nanoscale. Until now, the development and the analyses of such materials have primarily been experimental. Computational analyses required to support experimental advances are in the nascent stage. In the current research, a framework based on classical molecular dynamics (MD) is developed for analyzing deformation mechanisms in nanostructural materials consisting of more than one crystalline system. The material system of focus is a combination of *fcc*-Al and α-Fe_2O_3. The framework includes the development of an interatomic potential, a scalable parallel MD code, nanocrystalline composite structures, and methodologies for the quasistatic and dynamic strength analyses. The interatomic potential includes an embedded atom method (EAM) cluster functional, a Morse type pair function, and a second order electrostatic interaction function. The framework is applied to analyze the nanoscale mechanical behavior of the Al+Fe_2O_3 material system in two different settings. First, quasistatic strength analyses of nanocrystalline composites with average grain sizes varying from 3.9 nm to 7.2 nm are carried out. Second, shock wave propagation analyses in single crystalline Al, Fe_2O_3, and one of their interfaces are carried out.

The quasistatic strength analyses reveal that the deformation mechanisms in the analyzed nanocrystalline structures are affected by a combination of factors including high fraction of grain boundary atoms and electrostatic forces. Effect of each factor on the deformation mechanism in a nanocrystalline structure is dependent on the volume fractions of the Al

and Fe_2O_3 phases in the structure. Consequently, the constitutive responses of the nanocrystalline composites lie in between those of nanocrystalline Al and nanocrystalline Fe_2O_3. A direct Hall-Petch (H-P) relationship is observed in compression for the composites and nanocrystalline Fe_2O_3 where compressive electrostatic forces dominate the deformation mechanism. A reverse H-P relationship is observed in tension as well as in compression for nanocrystalline Al and in tension for nanocrystalline Fe_2O_3 due to the dominance of grain boundary sliding in the tensile deformation mechanism. Commonly observed tension-compression strength asymmetry in macroscale polycrystalline materials is fount to accentuate to an order of two to three times asymmetry in the single phase nanocrystalline structures owing to the differences in the movement of grain boundary atoms during compressive and tensile deformations. Analyses of the shock wave propagation in single crystalline systems reveal that the shock wave velocity (U_S) and the particle velocity (U_P) relationships as well as the type and the extent of deformation in single crystals are strongly correlated with the choice of crystallographic orientation for the shock wave propagation which in turn determines the mechanism of shock-induced deformation. Analyses of the shock wave propagation through an interface between Al and Fe_2O_3 reveal a threshold U_P value above which the crystalline structural order of a region surrounding the interface makes a transition to amorphous structural order. Further analyses indicate a possibility that such transformation may be a shock-induced reactive structural transformation. Overall, the framework and the analyses establish an important computational approach for investigating the mechanical behavior of complex nanostructures at the atomic length- and time-scales.

CHAPTER 1

INTRODUCTION

Recent advances in technology have strengthened focus on the development of synthetic materials with improved functionality, see for example Tjong and Chen (2004). A systematic integration of material synthesis, experimental characterization, computational modeling, and analytical modeling with materials design is required for this purpose. Research activities in each of these areas must incorporate analyses at a range of length- and time-scales. A broad classification of the range involves nanoscopic (1 Å to 10 nm/ 1 fs to 10 ps), microscopic (10 nm to 1 μm/ 10 ps to 1 ns), mesoscopic (1 μm to 1 mm/ 1 ns to 1 μs), and macroscopic (beyond 1 mm/beyond 10 μs) length- and time-scales. As a part of the classification, atomic level modeling and characterization at the nanoscopic length- and time-scales provides important insights regarding the effect of nanostructural morphology on desired operating behavior (mechanical or electrical or thermal or a combination of all three). Nanoscale analyses are being used for modifying existing constitutive models in order to have improved accuracy to describe the mechanical deformation in materials with nanoscale architecture, see for example Warner et al. (2004). However, currently such analyses can only focus on a limited set of materials, see for example Buehler et al. (2004). Evolution in the nanoscale materials research is required to analyze a much wider set of materials that includes materials with complex nanoscale morphologies. With this motivation the current research focuses on analyzing the constitutive behavior of complex nanostructured materials. The focus is also on

analyzing the effect of nanostructural morphology on the mechanisms of deformation. The approach of analyses is based on classical molecular dynamics (MD).

MD is an important technique for analyzing nanoscopic behavior of materials and has been widely used for analyzing the deformation mechanisms in single-phase materials, see for example Kadau et al. (2002), Abraham (2003), Van Swygenhoven et al. (2004), and Buehler et al. (2004). Consequently, MD simulations of single-phase materials are well set for integration in the overall material design objectives. However, significant improvements are required for MD to be applicable to the modeling of complex materials consisting of more than one phase or crystal system. One of the primary focuses of recent developments in materials research is synthesis of multiphase materials with multi-functional characteristics. Energetic Fe_2O_3+Al nanocomposites synthesized through a sol-gel process by Tillotson et al. (2001) are one example that offers the promise of combined chemical reactivity and mechanical strength when mixed with an appropriate nanoscopic reinforcement such as epoxy, cf. Granier and Pantoya (2004). A comprehensive nanoscale analysis of such a system must include details of the chemical reactivity as well as its relation with the mechanical and energetic characteristics. A methodology based on time variant quantum mechanics is the most appropriate approach for such task. However, quantum mechanics can only be used for very small lengthscales (~10 Å) and timescales (~1 ps). The effect of nanoscale morphology of complex materials on their constitutive behavior cannot be analyzed at such small scales. MD based on phenomenological interatomic potentials can be used at length- and time-scales of the order of 100 nm and 1 ns, respectively. Therefore, it is more appropriate to use MD

for analyzing the correlation between deformation mechanisms and nanostructural morphology that affects the constitutive behavior of complex materials. With this philosophy the current research focuses on developing a MD framework for analyzing nanoscopic mechanical behavior of the *fcc*-Al+α-Fe_2O_3 material system.

The fundamental information required for a reliable MD simulation is an interatomic potential to describe physical properties of the crystalline systems under study. The interatomic potential is used to calculate forces on atoms. The forces are used in the equations of motion for atoms. By integration of the equations of motion, the time evolution of the dynamics in a MD material system is obtained. The statistical mechanical analyses and the structural analyses of atomic trajectories are then used to characterize the nanoscopic behavior of the material system. MD replaces a comprehensive quantum mechanical treatment of interatomic forces with a phenomenological description in the form of an interatomic potential. Consequently, an MD simulation is appropriate only in the domain of properties to which the parameters of the interatomic potential are fitted. In addition, the following limitations are important to understand the applicability of MD simulations for analyzing the nanomechanical deformation,

1. MD simulations can only be carried out at timescales of the order of ps and lengthscales of the order of nanometers (nm). Consequently, the physical phenomena with long range spatial order or with large perturbation time periods are out of the reach of the MD simulations,

2. MD simulations of the nanomechanical deformation have inherently high rates of deformation owing to the limitations on the length- and time-scales that can be analyzed,
3. MD simulations use phenomenological interatomic potentials. Consequently, the accuracy of material behavior prediction using MD is limited. However, MD simulations have proven to provide accurate qualitative trends on the nanomechanical deformation mechanisms and the nanomechanical strength in agreement with experiments, see for example Kadau et al. (2002), Abraham (2003), Van Swygenhoven et al. (2004), and Buehler et al. (2004).

Considering the above limitations, it is possible to use MD for analyzing the mechanical behavior of a material during shock wave propagation with the shock-front widths of the order of nm and to obtain the mechanical behavior of a polycrystalline material with grain sizes of the order of a few nm. MD analyses of shock-wave propagation need to be carried out at high particle velocity (U_P) values. At low U_P values, the shock-front width is of the order of micrometers, a lengthscale that is inaccessible to MD simulations.

Within the scope of the above limitations, the current research focuses on analyzing mechanical deformation in the Al+Fe_2O_3 material system. The MD framework includes the development of an interatomic potential for the Al+Fe_2O_3 material system, implementation of the potential within a high performance scalable parallel MD code, and generation of single-phase as well as composite nanocrystalline material samples using Voronoi tessellation. Overall framework is used in the following settings;

1. Characterization of the quasistatic strengths of nanocrystalline Al and nanocrystalline Fe_2O_3 under tension as well as under compression and of the Al+ Fe_2O_3 composites with different volume fractions and different average grain sizes under compression, and
2. Characterization of the shock wave propagation in single crystalline Al, single crystalline Fe_2O_3, and their interfaces in order to calculate the dynamic strengths as well as in order to analyze structural order at the Al and Fe_2O_3 interfaces as a function of shock loading velocity for investigating a possibility of shock-induced reactive structural transformation.

The potential includes an embedded atom method (EAM) cluster functional, a Morse type pair function, and a second order electrostatic interaction function. The potential is intended for analyzing quasistatic mechanical deformation of nanocrystalline structures and for analyzing shock wave propagation in single crystalline structures. For this it is required that the potential accurately accounts for lattice cohesive energy at a range of lattice compression and expansion states (lattice EOS), lattice bulk modulus, lattice elastic constants, and generalized stacking fault and surface energies. While the lattice EOS is accounted for in the potential functional form, the rest of the properties are considered during the fitting procedure. The potential is fitted to the lattice constants, elastic constants, and cohesive energies of *fcc*-Al, *bcc*-Fe, α-Fe_2O_3, α-Al_2O_3, and B2 Fe-Al, accounting for the fact that mixtures of Al and Fe_2O_3 are chemically reactive and mechanical deformations may cause the formation of these phases as thermite reaction products or intermediates. To obtain close approximations of the behavior of mixtures

with any combination of the atomic elements, the potential is formulated and fitted such that the Al-Al, Fe-Fe, O-O, Fe-O, and Al-O interactions are accounted for in an explicit and interdependent manner. In addition to being fitted to the lattice constants, elastic constants, and cohesive energies, this potential also gives predictions of the surface and stacking fault energies for the crystalline components that compare well with the predictions of established potentials for the individual components in the literature. This research is the first contribution in the field of the development of multicomponent interatomic potentials.

The quasistatic strength characterizations are carried out at 300 K. Nanocrystalline structures are obtained by filling randomly oriented crystallites in nanograins generated using Voronoi tessellation. The structures have three different average grain sizes, viz., 3.9 nm, 4.7 nm, and 7.2 nm. In the nanocrystalline composites the crystallites to fill the nanograins are chosen based on the specified value of the volume fraction. Using this strategy, for a specified grain size the orientations of the individual grains in nanocrystalline Al, in nanocrystalline Fe_2O_3, and in Al+Fe_2O_3 composites is kept the same. The focus of the quasistatic MD simulations is on analyzing how the relationship among the grain size, the volume fraction, and the loading directionality affects the strength of a nanocrystalline material system. The outcome of this research is important for understanding the mechanical behavior of materials with nanoscopic phase morphology and phase mixing. This research is the first to report the analyses of mechanical deformation in nanocrystalline composite structures.

The shock wave propagation analyses are carried out in <100>, <110>, and <111> oriented single crystalline Al, in <0001> oriented single crystalline Fe_2O_3 and through an interface between the {100} surface of single crystalline Al and the {0001} surface of single crystalline Fe_2O_3. The focus of analyses in single crystals with various orientations is on obtaining relationships between the shock wave velocity (U_S) and U_P and on analyzing the effect of single crystalline orientation on the U_S-U_P relationships. In addition, the structural deformation mechanisms during shock wave propagation are analyzed. Shock wave propagation analyses through the interface aim at describing the changes in structural order, temperature, pressure, and energy in a region surrounding the interface as a function of U_P. The primary aim here is to obtain an account of the conditions responsible for changes in the structural order at the Al-Fe_2O_3 interface as a function of shock loading velocity with a view to understand the shock-induced reactivity in this material system.

Building on the above research tasks, this thesis is divided into main four chapters (2-5) followed by conclusive chapters 6 and 7. Chapter 2 describes the interatomic potential. The MD framework used for the quasistatic and shock wave propagation simulations is described in chapter 3. Chapter 4 presents results of the quasistatic deformation analyses. Chapter 5 presents results of the shock wave propagation analyses. Chapter 6 offers an overall summary and conclusion to the current research with a discussion on the significance of the current research. Finally, Chapter 7 delves into future research directions.

CHAPTER 2

THE INTERATOMIC POTENTIAL FOR *fcc*-Al+α-Fe_2O_3 MATERIAL SYSTEM

MD simulations of an atomic ensemble require a phenomenological description of interactions among atoms. This description is obtained by fitting the parameters of an interatomic potential functional to a specific set of the physical properties of crystalline systems under study. Such a phenomenological description may not be suitable for use in MD simulations at all temperatures and loading rates. However, it is useful within the domain of the specific physical properties to which the potential parameters are fitted, see for example Kadau et al. (2002) and Buehler et al. (2004). MD simulations of the Al+Fe_2O_3 material system require an interatomic potential that describes the physical properties of Al, Fe_2O_3, and the products of their reaction. However, no such interatomic potential is available. Therefore, in the current research, first an interatomic potential to describe interactions among atoms in the *fcc*-Al+α-Fe_2O_3 material system is developed. This research is the first to report an interatomic potential for a multicomponent material system.

The potential includes an EAM cluster functional, a Morse type pair function, and a second order electrostatic interaction function for describing a combination of metallic, covalent, and ionic interactions in the *fcc*-Al+α-Fe_2O_3 material system. The potential is intended for analyzing mechanical deformation of nanocrystalline materials and for analyzing shock wave propagation in single crystalline systems. For this it is required that the potential accurately accounts for lattice cohesive energy at a range of lattice

compression and expansion states (lattice EOS), lattice bulk modulus, lattice elastic constants, and generalized stacking fault and surface energies. While the lattice EOS is accounted for in the potential functional form, the rest of the properties are considered during the fitting procedure. The potential is fitted to the lattice constants, elastic constants, and cohesive energies of *fcc*-Al, bcc-Fe, α-Fe_2O_3, α-Al_2O_3, and B2 Fe-Al, accounting for the fact that mixtures of Fe_2O_3 and Al are chemically reactive and deformations may cause the formation of these phases as thermite reaction products or intermediates. To obtain close approximations of the behavior of mixtures with any combination of the atomic elements, the potential is formulated and fitted such that the Al-Al, Fe-Fe, O-O, Fe-O, and Al-O interactions are accounted for in an explicit and interdependent manner. In addition to being fitted to the lattice constants, elastic constants, and cohesive energies, this potential also gives predictions of the surface and stacking fault energies for the crystalline components that compare well with the predictions of established potentials for the individual components in the literature. Next, an overview on the research related to the development of interatomic potentials is described. This is followed by a description of the interatomic potential.

2.1 Introduction

Interatomic potentials for MD simulations are based on various physical and symmetry criteria and are constructed by fitting parameters of the functional form to the experimental values of the bulk properties and, if appropriate, to the properties of the

defects. For particles with no net charge, the potentials are based on the idea that interatomic force is repulsive if atoms are very close and attractive while vanishing smoothly to zero when distance between atoms increases. Range of the potential-interaction distance varies according to the kind of interaction. When an empirical fitting is used to determine parameters of an interatomic potential, there is no uniqueness in the result: in most cases a number of quite different models can yield satisfactory agreement.

The general conditions that an interatomic potential should satisfy are accuracy, (the most demanding test of accuracy involves quantitative comparison of predictions from the potential being tested with a wide range of unambiguous experimental data), and stability with respect to the desired lattice structure (otherwise they can derive unphysical geometries and energies in some circumstances). Earlier developments for interatomic potentials include purely collisional "hard-sphere" potentials, cf. Alder and Wainwright (1957), and smooth potential models such as those for monoatomic fluids, cf. Rahman (1964) and Verlet (1967). In a very general approximation, the energy E of interactions among N atoms can be decomposed into terms for pairs, triplets, quadruplets etc. of atoms as

$$E = \sum_{i<j} V_2(r_{ij}) + \sum_{i,j,k} V_3(r_{ij}, r_{jk}, r_{ik}) + \sum_{i,j,k,l} V_4(r_{ij}, r_{ik}, r_{il}, r_{jk}, r_{jl}, \cdots) + \ldots\ldots \qquad (2.1)$$

Pair potentials, like the Lennard-Jones (LJ) potential, describe interaction between two atoms in a system assuming that it is not explicitly dependent upon the exact positions of other atoms. On the other hand, many-body potentials take explicitly into account the

surroundings of interacting atoms. Among many body potentials, one can distinguish two groups of potentials: (1) the potentials where three-body and higher order terms are considered explicitly, cf. Stillinger and Weber (1985), Moriarty (1988), and Tersoff (1990); (2) the potentials where effectively many-body interactions are considered such as EAM, cf. Foiles et al. (1986), and Finnis-Sinclair, cf. Finnis and Sinclair (1984), potentials. The former consider the angular dependency in the potential functional explicitly and apply to materials in which the electronic configuration is not negligible and bonds are primarily covalent (this is the case, for instance, of metals with the d-band not fulfilled or semiconductors with tetragonal symmetry). The latter are spherically symmetric and describe simple metals (their extension, viz., embedded defect (ED) and modified embedded atom method (MEAM), cf. Baskes (1992), Baskes and Johnson (1994), and some semi-empirical potentials have also proven good for the transition metals and the semiconductors). These potentials are derived as an approximation to the local density functional theory. One of the great advantages of the EAM potentials over simple pair potentials is their ability to model properties such as the elastic constants and the stacking fault energy in the regions of low symmetry with a degree of computational difficulty which is approximately twice that involved in models that use pair potentials of the same cut-off radius. Descriptions of the interatomic interactions in organic systems are based on significantly different criteria, cf. Barth (2001) and Gavezzotti (2002). In the current research, potentials are based on a combination of a second order description of the electrostatic interactions and the EAM.

α-Fe_2O_3+*fcc*-Al nanocomposites are chemically active thermite mixtures, cf. Arnaiz et al. (1998) and Nayak and Dahotre (2002). Obviously, the possibility of the formation of Al_2O_3, Fe and other intermediate states needs to be considered. Therefore, the potential is required to simultaneously describe the behavior of the α-Fe_2O_3, *fcc*-Al, α-Al_2O_3, and *bcc*-Fe. To state it differently, Al-Al, Fe-Fe, Al-Fe, Al-O, Fe-O, and O-O interactions and the coupling between these interactions must be accounted for. This task necessitates a functional form that allows multi-body, pairwise, and electrostatic interactions among the different species to be described. Our approach here is to first fit the potential parameters for the Al-Al, Fe-Fe, Al-O, Fe-O and O-O interactions to the lattice constants, elastic modulus, and cohesive energies of *fcc*-Al, *bcc*-Fe, α-Fe_2O_3, and α-Al_2O_3. To determine the Fe-Al parameters, the potential is then fitted to the lattice constants, elastic modulus, and cohesive energies of B2 Fe-Al. Consequently, the potential is capable of simultaneously describing the crystalline properties of *fcc*-Al, *bcc*-Fe, B2 Fe-Al, α-Fe_2O_3, and α-Al_2O_3. With this relatively general applicability, we surmise that the potential provides reasonable approximations of the Al-Al, Fe-Fe, Al-Fe, Al-O, Fe-O, and O-O interactions and their couplings in the presence of each other as may exist in a general system with a combination of these atomic components.

Both α-Fe_2O_3 and α-Al_2O_3 belong to a family of scalenohedral hexagonal (trigonal) crystals, cf. Wyckoff (1963), Catti et al. (1995), Levin and Brandson (1998) and Rollman et al. (2004). These oxides can be characterized as having mixed ionic and covalent bonds. Interatomic potentials for these oxides have been developed following fully ionic descriptions, cf. Mackrodt and Stewart (1979), Lewis and Catlow (1985), Gale et al.

(1992), Alvarez et al. (1992), Grimes (1994), Rustad et al. (1995), Wilson et al. (1996), Belashchenko (1997), Minervini and Grimes (1999), Minervini et al. (1999) and Gao et al. (2003); EAM based approaches, cf. Baskes (1992), Strietz and Mintmire (1994), and Ohira and Inoue (1998); density functional based approaches, cf. Kenny et al. (1998); and mixed covalent-ionic descriptions, cf. Belashchenko et al. (1998) and Belashchenko and Ostraovski (2001). *fcc*-Al, *bcc*-Fe, and B2-Fe-Al are part of the cubic family of crystals. Potentials for *fcc*-Al have been described by Foiles et al. (1986), Voter and Chen (1987), Baskes (1992), Ercolessi and Adams (1993), Robertson et al. (1994), Mishin et al. (1999) and Kan Hachiya (2002). Among these, the MEAM based formulation of Baskes (1992) has the smallest cut-off range, i.e. only nearest neighbors are considered. This potential has been recently modified by Baskes et al. (2001) based on *ab initio* results to more accurately predict the stacking fault energy and surface energy of *fcc*-Al. Interatomic potentials for *bcc*-Fe have been developed by Pasianot et al. (1991), Baskes (1992), Simonelli et al. (1993) and Farkas et al. (2001). Among these potentials, the model of Farkas et al. (2001) seems most promising since both *ab initio* and experimental data are taken into account. Potential models for Fe-Al intermetallic systems have been developed by Besson and Morillo (1997) and Vailhe and Farkas (1997). The model of Besson and Morillo (1997) is more promising than the model of Vailhe and Farkas (1997) since it is fitted to a wider range of properties. In our research here, the functional form is a combination of the EAM functional by Foiles et al. (1986), the pair function by Besson and Morillo (1997), and the electrostatic function by Strietz and Mintmire (1994).

Another requirement for such a multicomponent interatomic potential is that it prescribes a smooth transition of structure at the interface of two different crystal regions. For example, *fcc*-Al close to α-Fe_2O_3 can be oxidized to form an Al_pO_q structure or it can bond with Fe to form Al_xFe_y structure. Commonly used approaches to achieve this transition include the Tersoff bond order potential, cf. Tersoff (1988), and the ES+EAM model of Strietz and Mintmire (1994). The Tersoff bond-order potential was initially used to model phases of silicon and was later extended to describe carbon and hydrocarbon systems by Brenner (1990) in the form of Brenner reactive bond order potential (REBO). The latest variation in this regard is the generalized extended empirical bond-order dependent (GEEBOD) potential with a functional representation of the van der Waals interactions and the electrostatic interactions, cf. Che et al. (1999). On the other hand, the ES+EAM model has been used by Kalia et al. (2000) for pressure-induced reactions between aluminum and oxygen under quasi-static conditions. This model uses the principle of electronegativity equalization, cf. Mortier et al. (1985) and Rappe and Goddard III (1991), to determine the local-environment-dependent charge of an atom. It is ideally suited for the description of systems which have primarily mixed ionic-covalent bonding with a strong ionic character. Similar approaches are taken by Rick et al. (1994) for polar systems, by Liu et al. (1997) for a new *ab initio* water potential, and by Goddard III et al. (2002) for pressure-induced phase transformation in ferroelectrics. In the current work, a modified ES+EAM term is included in the potential in order to describe the transition from one crystal system to the other at the interfaces between a metallic system such as *fcc*-Al and an ionic system such as α-Fe_2O_3.

2.2 Functional Form of the Interatomic Potential

The functional form for the potential is a combination of the existing potentials in the literature for the individual crystalline components, i.e.,

$$\mathrm{E}^{total}\left(r,q\right)=E_{es}^{Al}\left(r,q\right)+E_{es}^{Fe}\left(r,q\right)+E_{es}^{\mathrm{O}}\left(r,q\right)+ \left\{\sum_{Al,Fe,O}F_i\left(\sum_{Al,Fe,O}\left[\rho_j\left(r_j\right)\right]\right)+\frac{1}{2}\sum_{Al,Fe,O}\sum_{Al,Fe,O}\sum_{i(\neq j)}\phi_{ij}\left(r_{ij}\right)\right\}_{E_{glue}} \tag{2.2}$$

Each part of this potential model consists of a term (E_{glue}) similar to the EAM potential with a generalized cluster functional, cf. Carlsson (1990), and a term (E_{es}) for second-order electrostatic interactions between environment-dependent charges. The electrostatic interactions are considered for point charges located at atomic core centers as well as for diffused charges around the atomic cores. Specifically, for one particular atomic species (Al, Fe, or O) the total energy is a function of interatomic distance **r** and charges ***q*** in the form

$$E\left(\mathbf{r},\boldsymbol{q}\right)=E_{glue}\left(\mathbf{r}\right)+E_{es}\left(\mathbf{r},\boldsymbol{q}\right)\cdot \tag{2.3}$$

Here,

$$E_{glue}\left(\mathbf{r}\right)=\sum_i F_i\left(\rho_i\right)+\frac{1}{2}\sum_{i(\neq j)}\phi_{ij}\cdot \tag{2.4}$$

is the glue potential with a generalized cluster functional $F(\rho)$ and pair interaction potential ϕ_{ij}. The form of $F(\rho)$ is chosen as

$$F(\rho) = E_0 A\left(\rho \ln(\rho)\right)^B \cdot \tag{2.5}$$

In the above expression, E_0, A and B are parameters and ρ is the embedding electron density, cf. Baskes (1992), whose functional form is taken to be the same as that used by Foiles et al. (1986). This functional form is derived such that it accounts for the lattice EOS, cf. Foiles et al. (1986). The pair interaction function $\phi_{ij}(r)$ is based on that used by Besson and Morillo (1997) for Fe-Al alloys, i.e.,

$$\phi_{ij}(r) = \psi\ (r) - \psi\left(D_p\right) + \frac{D_p}{20}\left[1 - \left(\frac{r}{D_p}\right)^{20}\right]\psi'\left(D_p\right), \quad \text{for } r < D_p. \tag{2.6}$$

Note that the interaction goes to zero smoothly at the cutoff distance D_p. $\psi(r)$ in the above expression is taken as

$$\psi(r) = \psi_0\left[\exp\left(-2\gamma(r-t)\right) - 2\exp\left(-\gamma(r-t)\right)\right]\cdot \tag{2.7}$$

Here, γ, ψ_0 and t are parameters to be determined through fitting.

The electrostatic term in Eq. (2.3) is

$$E_{es}(\mathbf{r},\boldsymbol{q}) = \sum_i q_i \chi_i + \frac{1}{2}\sum_{i(\neq j)} q_i q_j V_{ij}. \tag{2.8}$$

Here, χ is the instantaneous electronegativity and V is the electrostatic pair interaction potential. $E_{es}(\mathbf{r},\boldsymbol{q})$ includes point charge interactions as well as interactions among charges distributed around the centers of atomic cores. For simplicity, the charge distributions are taken to be spherical. This expression for $E_{es}(\mathbf{r},\boldsymbol{q})$ is obtained by describing the energy of a neutral atom i as a Taylor series in valence charges q_i as, cf. Rappe and Goddard III (1991),

$$E_i(q_i) = E_i(0) + \chi_i^0 q_i + \frac{1}{2} J_i^0 q_i^2 \cdot \tag{2.9}$$

The first derivative χ_i^0 on the right hand side is denoted as the electronegativity, cf. Iczkowski and Margrave (1961) and Mortier et al. (1985). The second derivative J_i^0 has been associated with atomic hardness, cf. Parr and Pearson (1983), or with self-Coulomb repulsion, cf. Rappe and Goddard III (1991). The electrostatic energy $E_{es}(\mathbf{r},\boldsymbol{q})$ of a set of interacting atoms with atomic charges q_i is the sum of the atomic energies E_i and the electrostatic interaction energies between all pairs of atoms, i.e.,

$$\begin{aligned} E_{es} &= \sum_i E_i(q_i) + \frac{1}{2}\sum_{i\neq j} V_{ij}(\boldsymbol{r}_{ij}; q_i, q_j) \\ &= \sum_i \left(E_i(0) + \chi_i^0 q_i + \frac{1}{2} J_i^0 q_i^2 \right) + \frac{1}{2}\sum_{i\neq j} \left(\int d^3 r_1 \int d^3 r_2 \rho_i(\mathbf{r}_1; q_i)\, \rho_j(\mathbf{r}_2; q_j) / r_{12} \right) \cdot \end{aligned} \tag{2.10}$$

Here, the second term on the right hand side describes electrostatic interactions, with $\rho_i(\mathbf{r}_1; q_i)$ being the charge distribution around atom *i* (including the nuclear point charge) with a total charge of q_i. The form used for $\rho_i(\mathbf{r}_1; q_i)$ is given by Strietz and Mintmire (1994), i.e.

$$\rho_i(\mathbf{r}; q_i) = Z_i \delta(\mathbf{r} - \mathbf{r}_i) + (q_i - Z_i) f_i(\mathbf{r} - \mathbf{r}_i) \cdot \tag{2.11}$$

Here, Z_i is the *effective* nuclear point charge which must satisfy the condition $0 < Z_i < Z_i$, with Z_a being the total nuclear charge of the species to which atom *i* belongs (Al, Fe or O). Function f_i describes the radial distribution of the valence charges in space. It is chosen to be in the Gaussian form to correspond to Slater 1s orbital, i.e.,

$$f_i(r) = \frac{\xi_i^3}{\pi} \exp(-2\xi_i r) \cdot \tag{2.12}$$

Replacing $\rho_i(\mathbf{r}_1; q_i)$ from Eq. (2.11) in Eq. (2.10) leads to

$$\begin{aligned} \sum_{i \neq j} V_{ij}(\boldsymbol{r}_{ij}; q_i, q_j) = \sum_i \sum_{j(\neq i)} \Big\{ & q_i q_j [f_i \mid f_j] + q_i Z_j \big([j \mid f_i] - [f_i \mid f_j]\big) + q_j Z_i \big([i \mid f_j] - [f_i \mid f_j]\big) \\ & + Z_i Z_j \big([f_i \mid f_j] - [i \mid f_j] - [j \mid f_i] + 1/r_{ij}\big) \Big\} \cdot \end{aligned} \tag{2.13}$$

Here,

$$\left[f_i \mid f_j \right] = \int d^3\boldsymbol{r}_1 \int d^3\boldsymbol{r}_2 \frac{f_i(\boldsymbol{r}_1) f_j(\boldsymbol{r}_2)}{\boldsymbol{r}_{12}} \tag{2.14}$$

is the two-center Coulomb interaction integral between f_i and f_j and

$$\left[j \mid f_i \right] = \int d^3\boldsymbol{r} \frac{f_i(\boldsymbol{r})}{\left| \boldsymbol{r} - \boldsymbol{r}_j \right|} \tag{2.15}$$

is the nuclear attraction integral. The integration in the above equations can be easily calculated using prolatorial spheroidal coordinates, cf. Roothan (1951). The expressions for these integrals are

$$\left[j \mid f_i \right] = \frac{1}{R_{ij}} \left\{ 1 - \left[\left(1 + \xi_i^s R_{ij} \right) \exp\left(-2\xi_i^s R_{ij} \right) \right] \right\}, \tag{2.16}$$

and

$$\left[f_i \mid f_j \right] = \begin{cases} \dfrac{1}{r_{ij}} \left\{ \begin{array}{l} 1 - \left(1 - \dfrac{\xi_i^2 + \xi_j^2}{\xi_i^2 - \xi_j^2} \right) \left\{ \dfrac{1}{4} \left[2 + \dfrac{\xi_i^2 + \xi_j^2}{\xi_i^2 - \xi_j^2} \right] + \dfrac{1}{4} \xi_i r_{ij} \right\} \exp\left(-2\xi_i r_{ij} \right) - \\ \left(1 + \dfrac{\xi_i^2 + \xi_j^2}{\xi_i^2 - \xi_j^2} \right) \left\{ \dfrac{1}{4} \left[2 - \dfrac{\xi_i^2 + \xi_j^2}{\xi_i^2 - \xi_j^2} \right] + \dfrac{1}{4} \xi_j r_{ij} \right\} \exp\left(-2\xi_j r_{ij} \right) \end{array} \right\} & \text{if } \xi_i \neq \xi_j, \\ \dfrac{1}{r_{ij}} \left\{ 1 - \left[1 + \dfrac{11}{8} \left(\xi_i r_{ij} \right) + \dfrac{3}{4} \left(\xi_i r_{ij} \right)^2 + \dfrac{1}{6} \left(\xi_i r_{ij} \right)^3 \right] \exp\left(-2\xi_i r_{ij} \right) \right\} & \text{otherwise}. \end{cases} \tag{2.17}$$

Equations (2.10) and (2.13) can be combined to yield

$$E_{es} = \sum_i \left(E_i(0) + q_i \chi_i \right) + \frac{1}{2} \sum_{i,j \neq i} \left\{ q_i Z_j \left([j \mid f_i] - [f_i \mid f_j] \right) + q_j Z_i \left([i \mid f_j] - [f_j \mid f_i] \right) \right\} + \frac{1}{2} \sum_i q_i^2 J_i^0 + \frac{1}{2} \sum_{i,j \neq i} \left\{ q_i q_j [f_i \mid f_j] + Z_i Z_j \left([f_i \mid f_j] - [i \mid f_j] - [j \mid f_i] + 1/r_{ij} \right) \right\}. \quad (2.18)$$

The above expression can be simplified and expressed as

$$E_{es} = E_0 + \sum_i q_i \chi_i + \frac{1}{2} \sum_{i,j} q_i q_j E_{ij}, \quad (2.19)$$

such that

$$E_0 = \sum_i E_i(0) + \frac{1}{2} \sum_{i \neq j} Z_i Z_j \left([f_i \mid f_j] - [i \mid f_j] - [j \mid f_i] + 1/r_{ij} \right) \quad (2.20)$$

defines the ground state energy,

$$\chi_i = \chi_i^0 + \sum_{j \neq i} Z_j \left([j \mid f_i] - [f_i \mid f_j] \right) = \chi_i^0 + \sum_{j \neq i} Z_j \left(\int d^3 r \frac{f_j(r)}{|r - r_i|} - \int d^3 r_1 \int d^3 r_2 \frac{f_i(r_1) f_j(r_2)}{r_{12}} \right) \quad (2.21)$$

defines the instantaneous electronegativity, and

$$E_{ij} = \begin{cases} J_i^0 & i = j, \\ \int d^3 r_1 \int d^3 r_2 \dfrac{f_i(r_1) f_j(r_2)}{r_{12}} & i \neq j; \end{cases} \quad (2.22)$$

defines the electrostatic interactions in the system. The exponential form of f leads the integrals in the above equations to decompose into a leading $1/r_{ij}$ term and additional terms to exponentially decay as a function of r_{ij}. All lattice sums, therefore, can be decomposed into terms involving $1/r_{ij}$ and terms which are exponentially damped. The long range terms cancel each other out in Eq. (2.21), leaving only $1/r_{ij}$ terms in the expression for E_{ij} in Eq. (2.22). The reduced expression is

$$\chi_i = \chi_i^0 + \sum_{j\neq i}\frac{Z_j}{r_{ij}}\begin{cases}\left\{\begin{array}{l} -\left[\left(1+\xi_i^s r_{ij}\right)\exp\left(-2\xi_i^s r_{ij}\right)\right]+ \\ \left(1-\dfrac{\xi_i^2+\xi_j^2}{\xi_i^2-\xi_j^2}\right)\left\{\dfrac{1}{4}\left[2+\dfrac{\xi_i^2+\xi_j^2}{\xi_i^2-\xi_j^2}\right]+\dfrac{1}{4}\xi_i r_{ij}\right\}\exp\left(-2\xi_i r_{ij}\right)+ \\ \left(1+\dfrac{\xi_i^2+\xi_j^2}{\xi_i^2-\xi_j^2}\right)\left\{\dfrac{1}{4}\left[2-\dfrac{\xi_i^2+\xi_j^2}{\xi_i^2-\xi_j^2}\right]+\dfrac{1}{4}\xi_j r_{ij}\right\}\exp\left(-2\xi_j r_{ij}\right) \end{array}\right\} & \text{if } \xi_i \neq \xi_j \\ \left\{\begin{array}{l} -\left[\left(1+\xi_i^s r_{ij}\right)\exp\left(-2\xi_i^s r_{ij}\right)\right]+ \\ \left[1+\dfrac{11}{8}\left(\xi_i r_{ij}\right)+\dfrac{3}{4}\left(\xi_i r_{ij}\right)^2+\dfrac{1}{6}\left(\xi_i r_{ij}\right)^3\right]\exp\left(-2\xi_i r_{ij}\right) \end{array}\right\} & \text{otherwise} \end{cases} \tag{2.23}$$

for χ_i and

$$E_{ij} = \begin{cases}\dfrac{1}{r_{ij}}\left\{\begin{array}{l} 1-\left(1-\dfrac{\xi_i^2+\xi_j^2}{\xi_i^2-\xi_j^2}\right)\left\{\dfrac{1}{4}\left[2+\dfrac{\xi_i^2+\xi_j^2}{\xi_i^2-\xi_j^2}\right]+\dfrac{1}{4}\xi_i r_{ij}\right\}\exp\left(-2\xi_i r_{ij}\right)- \\ \left(1+\dfrac{\xi_i^2+\xi_j^2}{\xi_i^2-\xi_j^2}\right)\left\{\dfrac{1}{4}\left[2-\dfrac{\xi_i^2+\xi_j^2}{\xi_i^2-\xi_j^2}\right]+\dfrac{1}{4}\xi_j r_{ij}\right\}\exp\left(-2\xi_j r_{ij}\right) \end{array}\right\} & \text{if } \xi_i \neq \xi_j, \\ \dfrac{1}{r_{ij}}\left\{1-\left[1+\dfrac{11}{8}\left(\xi_i r_{ij}\right)+\dfrac{3}{4}\left(\xi_i r_{ij}\right)^2+\dfrac{1}{6}\left(\xi_i r_{ij}\right)^3\right]\exp\left(-2\xi_i r_{ij}\right)\right\} & \text{otherwise,} \end{cases} \tag{2.24}$$

for E_{ij} (if $i \neq j$). In Eq. (2.20), E_0 depends only on the nuclear charges and does not depend on charges q_i . Correspondingly, E_0 is not accounted for separately during energy calculations. This term is considered to be included as part of the glue part of the interatomic potential E_{glue} which consists of a volume-dependent many-body term accounting for the ground state zero charge energy and a term accounting for the effective pair interactions. Overall, the parameters needed to completely specify the potential are

1. A, B, r_0 , β , t , and cutoff distance D_p for describing the density functional and cluster function for each of Al, Fe and O (a subtotal of 3×6=18 parameters);
2. D_p , ψ_0 , γ, and t_k for describing each of the Al-Al, Al-Fe, Fe-Fe, O-O, Al-O, and Fe-O effective pair interactions (a subtotal of 6×4=24 parameters); and
3. ξ (Gaussian charge distribution parameter), Z (core charge), χ_0 , J_0 , and the short range electrostatic cutoff radius for exponentially decaying terms of the interatomic potential for specifying the electrostatic energy of Al, O, and Fe atoms (a subtotal of 3×5=15 parameters).

The total number of parameters is 57. In addition, note that charges q_{Al}, q_{o} and q_{Fe} are fixed. Based on the above description, for an Al and Fe_2O_3 nanocomposite structure the interatomic potential has

$$\mathrm{E}_{ES}^{Al} = q_{Al}\left\{\chi_{Al}^{0} + \sum_{j(\neq i)} Z_j\left[\int d^3r \frac{f_{Al}(r)}{|r-r_j|} - \int d^3r_1 \int d^3r_2 \frac{f_{Al}(r_1) f_j(r_2)}{r_{12}}\right]\right\} + \frac{1}{2}\left\{\sum_i q_{Al}^2 J_{Al}^0 + \sum_{i,j(\neq i)} q_{Al} q_j \int d^3r_1 \int d^3r_2 \frac{f_{Al}(r_1) f_j(r_2)}{r_{12}}\right\} \quad j = Al, Fe \text{ or } O \qquad (2.25)$$

and

$$\mathrm{E}_{ES}^{Fe} = q_{Fe}\left\{\chi_{Fe}^{0} + \sum_{j(\neq i)} Z_j\left[\int d^3r \frac{f_{Fe}(r)}{|r-r_j|} - \int d^3r_1 \int d^3r_2 \frac{f_{Fe}(r_1) f_j(r_2)}{r_{12}}\right]\right\} + \frac{1}{2}\left\{\sum_i q_{Fe}^2 J_{Fe}^0 + \sum_{i,j(\neq i)} q_{Fe} q_j \int d^3r_1 \int d^3r_2 \frac{f_{Fe}(r_1) f_j(r_2)}{r_{12}}\right\} \quad j = Al, Fe \text{ or } O \qquad (2.26)$$

and

$$\mathrm{E}_{ES}^{O} = q_{O}\left\{\chi_{O}^{0} + \sum_{j(\neq i)} Z_j\left[\int d^3r \frac{f_{Al}(r)}{|r-r_j|} - \int d^3r_1 \int d^3r_2 \frac{f_{O}(r_1) f_j(r_2)}{r_{12}}\right]\right\} + \frac{1}{2}\left\{\sum_i q_{O}^2 J_{O}^0 + \sum_{i,j(\neq i)} q_{O} q_j \int d^3r_1 \int d^3r_2 \frac{f_{O}(r_1) f_j(r_2)}{r_{12}}\right\} \quad j = Al, Fe \text{ or } O \qquad (2.27)$$

electrostatic terms and

$$F^{Al} = \mathrm{E}_0^{Al}\mathrm{A}^{Al}\left[\left(\sum \rho^{Al} + \sum \rho^{Fe} + \sum \rho^{O}\right)\ln\left(\sum \rho^{Al} + \sum \rho^{Fe} + \sum \rho^{O}\right)\right]^{\mathrm{B}^{Al}}, \qquad (2.28)$$

and

$$F^{Fe} = \mathrm{E}_0^{Fe}\mathrm{A}^{Fe}\left[\left(\sum \rho^{Al} + \sum \rho^{Fe} + \sum \rho^{O}\right)\ln\left(\sum \rho^{Al} + \sum \rho^{Fe} + \sum \rho^{O}\right)\right]^{\mathrm{B}^{Fe}}, \qquad (2.29)$$

and

$$F^{O} = \mathrm{E}_0^{O}\mathrm{A}^{O}\left[\left(\sum \rho^{O} + \sum \rho^{Al} + \sum \rho^{Fe}\right)\ln\left(\sum \rho^{O} + \sum \rho^{Al} + \sum \rho^{Fe}\right)\right]^{\mathrm{B}^{O}}, \qquad (2.30)$$

cluster functional terms and

$$\phi_{pair}^{Al} = \frac{1}{2}\sum_{j(\neq i)} \left\{ \begin{array}{l} \sum_{\alpha,\beta} \psi_0^{\alpha-\beta} \left[\exp\left(-2\gamma^{\alpha-\beta}\left(r - t^{\alpha-\beta}\right)\right) - 2\exp\left(-\gamma^{\alpha-\beta}\left(r - t^{\alpha-\beta}\right)\right)\right] - \\ \sum_{\alpha,\beta} \psi_0^{\alpha-\beta} \left[\exp\left(-2\gamma^{\alpha-\beta}\left(\mathrm{D}^{\alpha-\beta} - t^{\alpha-\beta}\right)\right) - 2\exp\left(-\gamma^{\alpha-\beta}\left(\mathrm{D}^{\alpha-\beta} - t^{\alpha-\beta}\right)\right)\right] - \\ \sum_{\alpha,\beta} \frac{\mathrm{D}^{\alpha-\beta}}{20}\left[1 - \left(\frac{r}{\mathrm{D}^{\alpha-\beta}}\right)^{20}\right]\left[\begin{array}{l} -2\gamma^{\alpha-\beta}\exp\left(-2\gamma^{\alpha-\beta}\left(\mathrm{D}^{\alpha-\beta} - t^{\alpha-\beta}\right)\right) + \\ 2\gamma^{\alpha-\beta}\exp\left(-\gamma^{\alpha-\beta}\left(\mathrm{D}^{\alpha-\beta} - t^{\alpha-\beta}\right)\right) \end{array}\right] \end{array} \right\}, \quad (2.31)$$

(α, β)={Al-Al, Al-Fe, Al-O}

and

$$\phi_{pair}^{Fe} = \frac{1}{2}\sum_{j(\neq i)} \left\{ \begin{array}{l} \sum_{\alpha,\beta} \psi_0^{\alpha-\beta} \left[\exp\left(-2\gamma^{\alpha-\beta}\left(r - t^{\alpha-\beta}\right)\right) - 2\exp\left(-\gamma^{\alpha-\beta}\left(r - t^{\alpha-\beta}\right)\right)\right] - \\ \sum_{\alpha,\beta} \psi_0^{\alpha-\beta} \left[\exp\left(-2\gamma^{\alpha-\beta}\left(\mathrm{D}^{\alpha-\beta} - t^{\alpha-\beta}\right)\right) - 2\exp\left(-\gamma^{\alpha-\beta}\left(\mathrm{D}^{\alpha-\beta} - t^{\alpha-\beta}\right)\right)\right] - \\ \sum_{\alpha,\beta} \frac{\mathrm{D}^{\alpha-\beta}}{20}\left[1 - \left(\frac{r}{\mathrm{D}^{\alpha-\beta}}\right)^{20}\right]\left[\begin{array}{l} -2\gamma^{\alpha-\beta}\exp\left(-2\gamma^{\alpha-\beta}\left(\mathrm{D}^{\alpha-\beta} - t^{\alpha-\beta}\right)\right) + \\ 2\gamma^{\alpha-\beta}\exp\left(-\gamma^{\alpha-\beta}\left(\mathrm{D}^{\alpha-\beta} - t^{\alpha-\beta}\right)\right) \end{array}\right] \end{array} \right\}, \quad (2.32)$$

(α, β)={Fe-Fe, Al-Fe, Fe-O}

and

$$\phi_{pair}^{O} = \frac{1}{2}\sum_{j(\neq i)} \left\{ \begin{array}{l} \sum_{\alpha,\beta} \psi_0^{\alpha-\beta} \left[\exp\left(-2\gamma^{\alpha-\beta}\left(r - t^{\alpha-\beta}\right)\right) - 2\exp\left(-\gamma^{\alpha-\beta}\left(r - t^{\alpha-\beta}\right)\right)\right] - \\ \sum_{\alpha,\beta} \psi_0^{\alpha-\beta} \left[\exp\left(-2\gamma^{\alpha-\beta}\left(\mathrm{D}^{\alpha-\beta} - t^{\alpha-\beta}\right)\right) - 2\exp\left(-\gamma^{\alpha-\beta}\left(\mathrm{D}^{\alpha-\beta} - t^{\alpha-\beta}\right)\right)\right] - \\ \sum_{\alpha,\beta} \frac{\mathrm{D}^{\alpha-\beta}}{20}\left[1 - \left(\frac{r}{\mathrm{D}^{\alpha-\beta}}\right)^{20}\right]\left[\begin{array}{l} -2\gamma^{\alpha-\beta}\exp\left(-2\gamma^{\alpha-\beta}\left(\mathrm{D}^{\alpha-\beta} - t^{\alpha-\beta}\right)\right) + \\ 2\gamma^{\alpha-\beta}\exp\left(-\gamma^{\alpha-\beta}\left(\mathrm{D}^{\alpha-\beta} - t^{\alpha-\beta}\right)\right) \end{array}\right] \end{array} \right\}, \quad (2.33)$$

(α, β)={Al-O, Fe-O, O-O}

pair interaction terms. In the Al phase of the composite only F^{Al} and ϕ_{pair}^{Al} terms are used. In these terms Al-O and Al-Fe interactions are not considered. The parameters in these terms are obtained by fitting to the properties of *fcc*-Al. In the Fe_2O_3 phase of the composite E_{ES}^{Fe}, E_{ES}^{O}, F^{Fe}, F^{O}, ϕ_{pair}^{Fe}, and ϕ_{pair}^{O} terms are used. In these terms Fe-Al and O-Al interactions are not considered. The parameters in these terms are obtained by fitting to the properties of α-Fe_2O_3.

At the interfaces of Al and Fe_2O_3 all the above terms with the inclusion of an additional term E_{ES}^{Al} are considered. E_{ES}^{Al} is considered to include the possibility that Al atoms at the interface may be oxidized under the effect of charged Fe and O atoms. The electronegativity equalization, cf. Strietz and Mintmire (1994), is carried out to determine atomic charges of the Al, Fe, and O atoms in an interfacial region covered by the short range electrostatic cutoff (10 Å). The choice of cutoff is explained in chapter 3. The methodology of the electronegativity equalization is based on a description of the total electrostatic energy of an array of atoms as a function of the atomic charges (valences) and the position, see Eqs. (2.10) and (2.20). For well behaved parameters J_i^0 and functions $f_i(r)$, the electrostatic energy has a well-defined minimum. The values of charges, q_i, are chosen such that the electrostatic energy, E_{es}, is minimized subjected to the constraint that the sum of charges is constant, cf. Strietz and Mintmire (1994). This condition is algebraically equivalent to the electronegativity equalization condition which requires that the chemical potentials $\mu = \mu_i = \partial E_{\mathrm{es}} / \partial q_i$ be equal. With the consideration of all E_{ES}^{Al}, E_{ES}^{Fe}, E_{ES}^{O}, F^{Al}, F^{Fe}, F^{O}, ϕ_{pair}^{Al}, ϕ_{pair}^{Fe}, and ϕ_{pair}^{O} terms the behavior of Al, Fe, and

O atoms at the Al-Fe_2O_3 interfaces can be accounted for. This procedure for calculating interatomic interactions in a composite represents an approximation and is one of the underlying assumptions of the MD framework in the current research. We surmise that by providing reasonable approximations of the Al-Al, Fe-Fe, Al-Fe, Al-O, Fe-O, and O-O interactions through fitting to the individual phase properties and by providing the coupling of these interactions in the presence of each other using electronegativity equalization, it is possible to describe interatomic interactions in a general system that consists of a combination of the individual phases. This postulate is verified later by applying the potential to analyze the structure of an interface between {100} Al and {0001} Fe_2O_3. As will be shown later the structural order at the interface is in accordance with the experimental and theoretical observations.

2.3 Fitting and Testing of the Potential Parameters

The potential parameters are determined by fitting the functional form to the lattice constants, cohesive energies, and elastic constants of *fcc*-Al, bcc-Fe, α-Al_2O_3 and α-Fe_2O_3. The parameters related to the Fe-Al pair interactions are determined by fitting to the formula unit energy of B2 Fe-Al. The fitting process involves the minimization of the weighted sum of the squared differences between target property values (experimental or *ab initio*) and values calculated from a trial parameter set. Specifically, the minimization follows the least-squares approach of Gale and Rohl (2003) and is carried out for residual

$$F = \sum_k \omega_k \left[f_k - f_k \left(trial \right) \right]^2 \tag{2.34}$$

with respect to all possible choices of parameters. Here, ω_k are weights and are taken as unity and f_k represent the physical properties being fitted to. In this procedure, a functional parameter set corresponding to a global minimum of *F* is first obtained using a genetic algorithm, cf. Woodley et al. (1999) and Cappello and Mancuso (2003). This parameter set is then subjected to refined local minimization using the Newton-Raphson (NR) approach. The use of the genetic algorithm before the NR scheme is one general approach for the least square minimization of residual *F*, cf. Gale and Rohl (2003). An alternative is to use quantum mechanical treatments followed by an empirical fitting based on the physics of the problem, cf. Gale and Rohl (2003). Differences between the crystalline components and the lack of information regarding their interactions in the current work dictate the use of the genetic algorithm approach.

Since the potential is a combination of existing potentials for individual crystalline components in the literature, the initial trial parameter sets are taken to be those in the literature for the individual components. The NR fit starts with a numerical Hessian (second order derivative matrix) and changes to BFGS updating of the exact Hessian, cf. Press et al. (1992), based on the magnitude of the gradient norm of residual *F* as the gradient norm reduces in magnitude. The last step in this process is rational function optimization (RFO), cf. Banerjee et al. (1985), which removes imaginary modes from the Hessian, thus forcing it to be positive-definite and ensuring that the parameters obtained correspond to a stable lattice structure. This structure in general is associated with non-zero internal forces at the atomic positions. Therefore, a relaxation fitting is carried out

following the RFO step in order to zero out the internal forces. In this scheme, the displacements of the force-field optimized structure relative to the target structure also form part of the fitting function, as opposed to the use of only the forces on the atoms at the target structure as in a conventional fit, cf. Gale and Rohl (2003). This treatment is found to be superior to conventional fitting schemes since it probes the forces as well as the Hessian matrix, rather than just the former. Table 2.1 shows the gradient norms and average errors in the fitting of elastic constants, lattice constants, and cohesive energies for all the components. The order of fitting is such that the density and functional parameters are obtained first, followed by the pair parameters and then the electrostatic parameters.

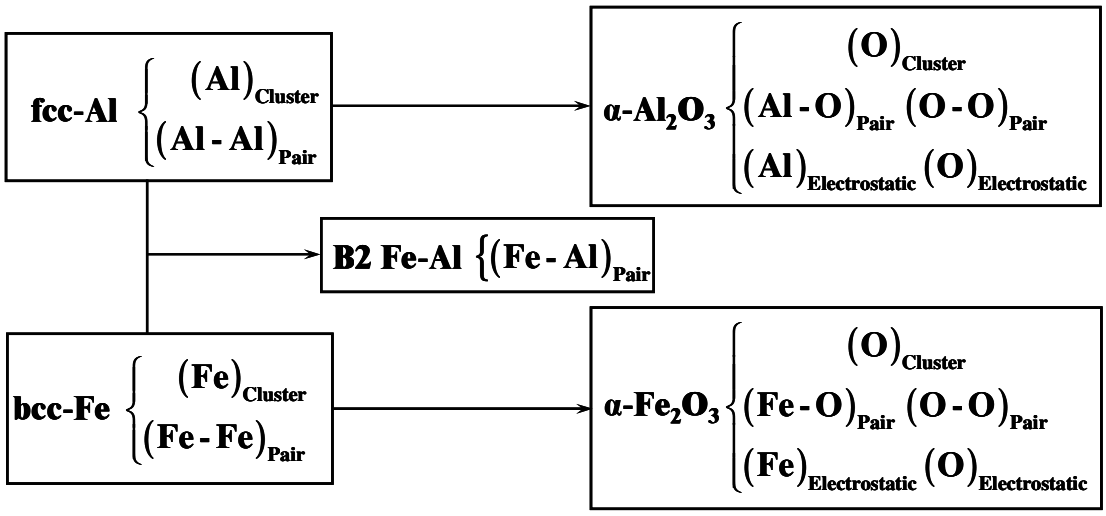

Figure 2.1 An illustration of the fitting procedure

Figure 2.1 provides a schematic illustration of the fitting sequence. The Al and Fe cluster functional parameters and the Al-Al, Fe-Fe, and Al-Fe pair parameters are first determined by fitting to the properties of *fcc*-Al, bcc-Fe and B2 Fe-Al. In the subsequent fitting, the O cluster functional parameters, the O-O, Al-O, and Fe-O pair parameters, and

the Al, Fe, and O electrostatic parameters are determined solely by fitting to the properties of α-Al_2O_3 and α-Fe_2O_3. During this procedure, the Al and Fe cluster functional parameters and the Al-Al and Fe-Fe pair parameters are kept constant. The Al electrostatic parameters and the Al-O pair parameters are solely determined by fitting to the properties of α-Al_2O_3. The Fe electrostatic parameters and the Fe-O pair parameters are solely determined by fitting to the properties of α-Fe_2O_3. However, the O cluster functional parameters, the O electrostatic parameters, and the O-O pair parameters are determined to obtain the best fit to the α-Al_2O_3 and α-Fe_2O_3 properties with the overall potential parameter set. For this purpose, after determining the Al and Fe electrostatic parameters and the Al-O and Fe-O pair parameters by fitting to the properties of α-Al_2O_3 and α-Fe_2O_3, the fitting procedure focuses on varying the O cluster functional parameters, the O electrostatic parameters, and the O-O pair parameters while keeping all other parameters fixed for the best possible fit to the α-Al_2O_3 and α-Fe_2O_3 properties. The fitting is carried out in the molecular statics code general utility lattice statics (GULP) 1.3, cf. Gale and Rohl (2003). This program is authored by Prof. Julian D Gale (Department of Chemistry, Imperial College, London, UK). Originally intended as a code for interatomic potential fitting, GULP evolved to include energy minimization and many other useful features. Although similar in some ways to other molecular statics codes, for example CASCADE, GULP is different in that it maximizes the use of crystal symmetry to make structure generation easier and to speed up calculations. For the purpose of interatomic potential fitting, this code required implementation of the potential functional form. The specific information required to be implemented into the code is the functional form of the energy and its derivative upto the third order. GULP has the inherent ability

to develop crystal structures from the specification of space group numbers (167 for Al_2O_3 and α-Fe_2O_3, 224 for bcc-Fe, and 229 for *fcc*-Al). Once functional form of the energy and its derivatives upto third order are implemented within GULP, the fitting procedure is straightforwardly carried out using the instructions manual.

In GULP, calculations of the elastic constants are based on the work of Catlow and Mackrodt (1982). In this work the calculation of elastic constants based on Born and Huang (1954) theory of crystal lattice is described. The main contribution of this work is the inclusion of crystal symmetry to speed up calculations of the lattice constants. The temperature in this formulation is not explicitly considered. Instead, the fitting is assumed to be carried out at the temperature at which the properties are specified. This research uses properties specified at room temperature (300 K). Table 2.2 to Table 2.6 show the properties of *fcc*-Al, bcc-Fe, α-Al_2O_3 and α-Fe_2O_3 used during fitting. The tables also show values of the lattice constants, elastic constants, and cohesive energies predicted by the potential. Reasonable agreement is seen between the predicted values and the experimental/*ab initio* values. In *fcc*-Al the fitting fares better than was the case for the potential of Voter and Chen (1987). In the case of *bcc*-Fe the fitting is comparable to the predictions made by the potential of Farkas et al. (2001). In the case of α-Al_2O_3 the fitted properties compare well with the values provided by Strietz and Mintmire (1994). In the case of α-Fe_2O_3 no comparable interatomic potential is available. Accordingly, the properties are compared to the experimental values provided by Huntington (1958). Overall, the predictions compare well with the established potentials for the individual crystalline components that are found in the literature.

Table 2.1 Sum of squares and corresponding average errors during initial fitting for each crystal component

	fcc-Al		bcc-Fe		B2 Fe-Al		α-Al_2O_3		α-Fe_2O_3	
	Sum of Squares	**%Error**	**Sum of Squares**	**%Error**	**Sum of Squares**	**%Error**	**Sum of Squares**	**%Error**	**Sum of Squares**	**%Error**
Genetic	0.01190	2	12.095741	15	35.692603	15	836.55	50	70.99636	12
Derivative	0.522408	4	0.058	0.5	0	0	18.53	7	2.68	2

Table 2.2 Fitted and predicted properties of *fcc*-Al using parameter set

(* properties used for testing the fitted potential parameter set;
‡ comparable polycrystalline values since single-crystalline values are unavailable)

		Mishin et al. (1999)	Voter and Chen (1987)	Experimental/*ab initio*	Prediction
Lattice Properties	a_0(Å)	4.05	4.05	4.05 *CRC Hanbbook (1983)*	4.05
	E_0(eV/atom)	-3.36	-3.36	-3.36 *CRC Hanbbook (1983)*	-3.51
	C_{11}(GPa)	114	107	114.3 *Simons and Wang (1977)*	116.56
	C_{12}(GPa)	61.6	65.2	61.9 *Simons and Wang (1977)*	60.13
	C_{44}(GPa)	31.6	32.2	31.6 *Simons and Wang (1977)*	25.13
	B(GPa)	79	79	79 *Simons and Wang (1977)*	78.9
***Surface Energy**	γ_s (110) (mJ/m^2)	1006	959	980‡ *LE Murr (1975)*	1102.4*
	γ_s (111) (mJ/m^2)	870	823	980 ‡ *LE Murr (1975)*	913.7*
	γ_s (100) (mJ/m^2)	943	855	980 ‡ *LE Murr (1975)*	1001.5*
***Stacking Fault Energy**	γ_{sF} (mJ/m^2) $\frac{a}{6}\langle 112\rangle\{111\}$	168/146	93/76	213(unstable), 166 (stable) *LE Murr (1975), Rautioaho (1982), Westmacott(1971), Jen Hartford (1998)*	265/175*

Table 2.3 Fitted and predicted properties of *bcc*-Fe using parameter set

(* properties used for testing the fitted potential parameter set;
‡ comparable polycrystalline values since single-crystalline values are unavailable)

		Farkas et al. (2001)	**Experimental/*ab initio***	**Prediction**
Lattice Properties	a_0(Å)	2.87	2.87 *Kittel (1971)*	2.87
	E_0(eV/atom)	-4.28	-4.28 *Kittel (1971)*	-4.28
	C_{11}(GPa)	256	252 *Hirth and Lothe (1982)*	251.4
	C_{12}(GPa)	136	138 *Hirth and Lothe (1982)*	136.7
	C_{44}(GPa)	113	122 *Hirth and Lothe (1982)*	122
	B(GPa)	173	173 *Hirth and Lothe (1982)*	174.93
***Surfaces Energy**	γ_s (110) (mJ/m²)	1530	2100‡ *(Mendelev, 2003)*	1760
	γ_s (111) (mJ/m²)	2027	2100 ‡ *(Mendelev, 2003)*	2035.7
	γ_s (100) (mJ/m²)	1890	2100 ‡ *(Mendelev, 2003)*	1936.6
***Stacking Fault Energy**	γ_{sF} (mJ/m²) $\frac{a}{2}\langle 111\rangle\{110\}$	1100	----	1600/575

Table 2.4 Fitted and predicted properties of B2 Fe-Al using parameter set

		Experimental/ *ab initio*	**Prediction**	
Lattice Properties B2 FeAl	a_0(Å)	2.90 ***(Besson and Morillo, 1997)***	2.90	2.90
	E_0(eV/FeAl pair)	-8.15 ***(Besson and Morillo, 1997)***	-8.15	-8.15

Table 2.5 Fitted and predicted properties of α-Al_2O_3 using parameter set

(* properties used for testing the fitted potential parameter set)

		Strietz and Mintmire, (1994)	**Experimental/ *ab initio***	**Prediction**
Lattice Properties	Lattice Energy (eV)	-31.8	-31.8 (I unit) ***CRC Hanbbook (1983)***	-31.8
	q_{Al}(e)	2.9	1.3 ***(Lewis et al.1982)***	3.0
	C_{11}(GPa)	537	497 ***Wachtman et al. (1960, 1969)***	505.9
	C_{12}(GPa)	180	164 ***Wachtman et al. (1960, 1969)***	188.2
	C_{13}(GPa)	106	111 ***Wachtman et al. (1960, 1969)***	97.77
	C_{33}(GPa)	509	498 ***Wachtman et al. (1960, 1969)***	469.23
	C_{14}(GPa)	-30	-24 ***Wachtman et al. (1960, 1969)***	-64.98
	C_{44}(GPa)	130	147 ***Wachtman et al. (1960, 1969)***	165.97
	a_0(Å)	4.7602	4.7602 ***Wachtman et al. (1960, 1969)***	4.7602
	C_0(Å)	12.9912	12.9912 ***Wachtman et al. (1960, 1969)***	12.9912
***Surface Energy (mJ/m^2)**	(0001) (unrelaxed)	3670	3770 ***Manassidis et al. (1993, 1994)***	3550
	(0001) (relaxed)	2670	1760 ***Manassidis et al. (1993, 1994)***	2500

Table 2.6 Fitted and predicted properties of α-Fe_2O_3 using parameter set

(* properties used for testing the fitted potential parameter set)

		Experimental/ *ab initio*	**Prediction**
Lattice Properties	Lattice Energy (eV)	-101.178 (I unit) *Catti et al. (1995)*	-101.185
	q_{Al}(e)	2.602 *Catti et al. (1995)*	3.0
	C11(GPa)	242 *Huntington (1958)*	238.2
	C12(GPa)	55 *Huntington (1958)*	50.72
	C13(GPa)	16 *Huntington (1958)*	28.75
	C33(GPa)	228 *Huntington (1958)*	223.08
	C14(GPa)	-13 *Huntington (1958)*	-13.12
	C44(GPa)	85 *Huntington (1958)*	78.05
	a0(Å)	5.035 *Catti et al. (1995)*	5.035
	C0(Å)	13.747 *Catti et al. (1995)*	13.747
***Surface Energy (mJ/m²)**	(0001) (unrelaxed)	5260 *Mackrodt(1987)*	5540
	(0001) (relaxed)	1530 *Mackrodt(1987)*	2050

Table 2.7 Pair parameters of the potential

	Ψ (eV)	**t (Å)**	**γ (Å^{-1})**	**Cutoff (Å)**
Al-Al	237.008963	4.003143	0.006436	7.0
Al-O	39.770657	1.021318	1.160757	7.0
Al-Fe	79.232208	2.098726	0.946525	7.0
Fe-Fe	1.073706	2.58029	0.969895	7.0
O-O	10.180285	1.0000	0.763738	7.0
Fe-O	2.653694	0.999972	2.110824	7.0

Table 2.8 Cluster and electrostatic parameters of the potential

	A	**B**	**E_0 (eV)**	**r_0 (Å)**	**β_0 (Å^{-1})**	**t_0**	**χ (eV)**	**J (eV)**	**ξ(Å^{-1})**	**Z**
Al	0.9739	1.000	4.769	-3.024332	0.938493	86.15	-55.333	1.94422	0.77344	3.5245
Fe	0.041333	1.000	7.659	1.743248	1.01471	2.128185	1.5834	2.59674	0.595758	6.2
O	1.000	1.000	2.558	1.412648	1.806365	0.895404	5.48	14.03	2.14	0.0

Nanomechanical modeling of a single crystalline or a polycrystalline system using MD involves interactions along dissimilar interfaces. In addition, it is possible during deformation that planar defects such as stacking faults are formed in the bulk of the crystals, see for example Kadau et al. (2002) , Abraham (2003), Van Swygenhoven et al. (2004), and Buehler et al. (2004).

Since the purpose of the potential is to carry out MD simulations under the quasistatic and shock loadings, the potential accurately accounts for lattice cohesive energy at a range of lattice compression and expansion (lattice EOS), lattice bulk modulus, lattice elastic constants, and generalized stacking fault and surface energies. The lattice EOS is accounted in the EAM functional form. The potential parameters are fitted to the lattice elastic constants and lattice bulk modulus. Since the lattice bulk modulus is obtained as a slope of pressure versus lattice volume curves, the correct lattice mechanical behavior is ensured during shock-induced compressive mechanical deformation. In addition, we require the potential to be able to predict the values of stacking fault and surface energy of the modeled crystal systems that compare well with those predicted by the available potentials in literature for the individual crystal systems. This requirement is important for obtaining correct description of the atomic interactions at interfaces between different components or between separately oriented crystals in a polycrystalline setting. Using MD simulations of quasistatic deformations, see for example Schiøtz and Jacobsen (2003) and Van Swygenhoven et al. (2004), as well as of shock loadings, see for example Kum (2003) and Bringa et al. (2004), it has been shown that the a potential with the fitted and tested property database such as the one in the current research is sufficient for

modeling nanoscale mechanical deformation. Taken together with the fitted properties, the potential with the tested properties offers a realistic description of the material system.

Table 2.2 to Table 2.6 show a comparison of the surface and generalized stacking fault energies of the crystalline components calculated using the potential with the experimental/*ab initio* values reported in the literature. The generalized stacking fault energies for *fcc*-Al and *bcc*-Fe are calculated using the approach of Zimmerman et al. (2000). In this approach, a shear displacement is given to one half of a block of a single crystal relative to the other part. After the shear displacement, the energy per unit area of the crystalline block is calculated. The difference between this energy and the bulk energy per unit area is then plotted as a function of the shear displacement. As expected, with increase in the shear displacement the difference between the two energy values reaches a peak and then starts to dip. Later, it reaches a minima corresponding to the shear displacement for formation of a stable stacking fault. The peak of the curve is referred to as the unstable stacking fault energy. The minimum of the curve is referred to as the stable stacking fault energy. In *fcc*-Al, $a/2\langle\bar{1}10\rangle$ unit dislocation dissociates into $a/6\langle\bar{1}\,\bar{1}2\rangle$ and $a/6\langle\bar{1}2\bar{1}\rangle$ partial dislocations. Correspondingly, $a/6\langle\bar{1}\,\bar{1}2\rangle\{111\}$ partial dislocation energy is of importance. In *bcc*-Fe $a/2\langle111\rangle\{110\}$ dislocation energy is of importance, cf. Farkas et al. (2001). To calculate the $a/6\langle\bar{1}\,\bar{1}2\rangle\{111\}$ generalized stacking fault energy of *fcc*-Al, displacement increments of 0.25 Å are introduced on the $(11\bar{1})$ plane in the $\langle\bar{1}\,\bar{1}2\rangle$ direction. The X, Y, and Z axes of the crystalline block are therefore

aligned in the $\langle 11\bar{1}\rangle$, $\langle \bar{1}\,\bar{1}2\rangle$ and $\langle \bar{1}10\rangle$ crystallographic orientations, respectively. In *bcc*-Fe, the $a/2\langle 111\rangle(110)$ generalized stacking fault energy is calculated with displacement increments of 0.4 Å in $\langle 111\rangle$ direction on (110) plane. The X, Y, and Z axes of the crystalline block are aligned in the $\langle 110\rangle$, $\langle \bar{1}12\rangle$ and $\langle 1\,\bar{1}1\rangle$ crystallographic orientations, respectively. The energy vs. shear displacement curves for the above calculations are shown in Figure 2.2.

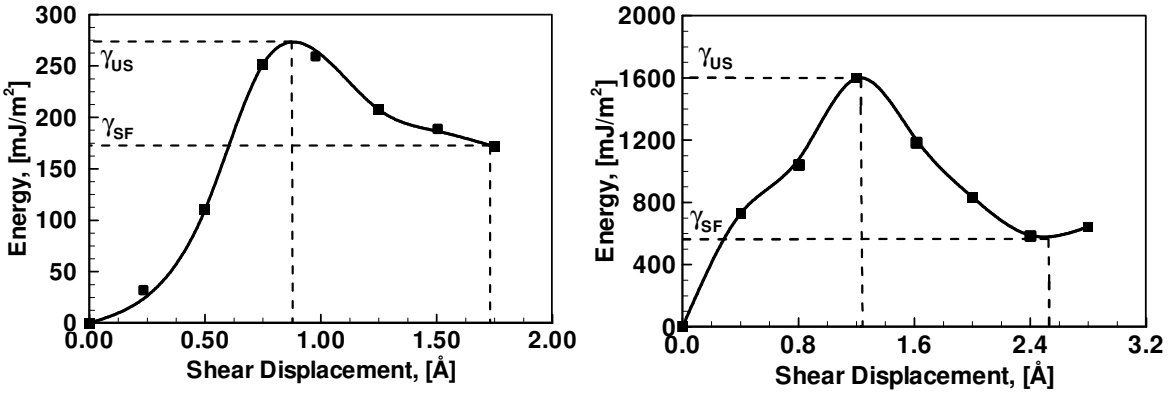

(a) (b)

Figure 2.2 (a) Generalized $a/6\langle \bar{1}\,\bar{1}2\rangle\{111\}$ stacking fault energy of *fcc*-Al, (b) Generalized $a/2\langle 111\rangle\{110\}$ stacking fault energy of *bcc*-Fe

It is clear that the potential overpredicts the stable and unstable stacking fault energies for both *fcc*-Al and *bcc*-Fe. In *fcc*-Al, the extent of over-prediction is the same as that of the well-established Mishin and Farkas potential, cf. Mishin et al. (1999), which has been extremely useful in modeling surface defect formation in Al single crystals and polycrystals. In *bcc*-Fe, experimental or quantum mechanical values of the stacking fault energy are not available in the literature. Therefore, we choose to compare the results of our calculations with a well established Farkas et al. (2001) potential. The predicted value

here is of the same order of magnitude as that given by the Farkas et al. (2001) potential. Overall, testing of the stacking fault energies suggests that the potential is appropriate for analyzing defects in *fcc*-Al and *bcc*-Fe crystalline systems in a manner similar to the other established potentials.

The thermodynamic penalty for cleaving a surface from a bulk material is measured according to the surface energy. Given a bulk energy of E_{bulk} and an energy E_{surf} for the same system with a surface created, then the surface energy, γ_s, is defined as $\gamma_s = \left(E_{bulk} - E_{surf}\right)/A$. Here, A is the surface area of newly created surface, cf. Gale and Rohl (2003). In this research we follow the approach of Strietz and Mintmire (1994) to calculate γ_s by creating a free surface along the desired cleavage direction using 3D periodic boundary conditions (PBCs), cf. Gale and Rohl (2003). Unrelaxed surface energy is calculated by subtracting the energy of bulk crystal from the energy of an unrelaxed cleaved crystal. Relaxed surface energy is calculated by subtracting the energy of bulk crystal from the energy of a relaxed cleaved crystal (equilibrating MD at near 0 K). Surface energy values reported in literature for *fcc*-Al and *bcc*-Fe are not highly reliable. Therefore, it is desired that the surface energies of low-index planes such as that of {100}, {110}, and {111} planes be close to the surface energy of an average orientation. This value is 980 mJ/m^2 for *fcc*-Al (Mishin et al. (1999)) and 2452 mJ/m^2 for bcc-Fe (Murr (1975)). In addition, we require that $\gamma_s\{110\} > \gamma_s\{100\} > \gamma_s\{111\}$ in *fcc*-Al and $\gamma_s\{111\} > \gamma_s\{100\} > \gamma_s\{110\}$ in bcc-Fe. Both of these requirements are met, as shown in Table 2.2 and Table 2.3. For α-Fe_2O_3 and α-Al_2O_3, the surface energy values for {0001} surface

are calculated. Both the relaxed and unrelaxed values are quite close to what is reported in the literature, cf. Mackrodt et al. (1987) and Manassidis and Gillan (1994).

Overall, the potential along with the chosen parameter set, listed in Table 2.7 and Table 2.8, offers a useful tool for analyzing the nanomechanical deformation in the *fcc*-Al+α-Fe_2O_3 system using MD. The potential is the single most important tool for desired MD framework in the current research. It is implemented in a scalable parallel MD code to carry out the nanomechanical simulations. The next chapter describes the framework developed for carrying out MD simulations.

2.4 Chapter Summary and Insights

An interatomic potential for carrying out MD simulations of the nanomechanical deformation in the *fcc*-Al+α-Fe_2O_3 material system is developed. The materials system has a combination of the metallic, covalent, and ionic bonds. Accordingly, the potential model includes an EAM functional, a Morse type pair function, and a second order electrostatic interaction functional. This potential is the first reported multicomponent interatomic potential. The potential is intended for use in MD simulations of *fcc*-Al, *bcc*-Fe, α-Fe_2O_3, and α-Al_2O_3 as well for a system made up of a combination of these crystal systems. Therefore, it is fitted to the cohesive energy, the lattice constants, and the elastic constants of all the crystal systems. The potential predicts the surface and stacking fault energies of the crystal systems in excellent agreement with the corresponding experimental measurements. The predictions also compare well with the predictions of

other established potentials in the literature. The potential is intended for the quasistatic mechanical deformation and shock wave propagation simulations. The closeness of the values of predicted properties with the corresponding experimental values indicates that the potential is ready for integration into an overall MD framework for carrying out these tasks.

CHAPTER 3

THE FRAMEWORK FOR MOLECULAR DYNAMICS MODELING

The framework for MD simulations requires integration of the interatomic potential within a scalable parallel MD code for simulating large atomic ensembles. The framework also requires a careful layout of steps such as the selections of atomic ensembles (for e.g. nanocrystalline structures), visualization schemes for identifying the deformation mechanisms, integration algorithms with appropriate parameters, and initial or boundary values for carrying out MD simulations. The framework is intended for the quasistatic and dynamic strength calculations. The quasistatic strength calculations are carried out for three different grain sizes (7.2 nm, 4.7 nm, and 3.9 nm) of nanocrystalline Al and nanocrystalline Fe_2O_3 as well as of their composites with two different volume fractions: 1. 60% *fcc*-Al + 40% α-Fe_2O_3, 2. 60% *fcc*-Al + 40% α-Fe_2O_3. Recently, an asymmetry in the strength and deformation levels during tensile and compressive loadings of some nanocrystalline materials such as *fcc*-Ni was observed to be more pronounced than that in the strength and deformation levels of the corresponding single crystals, cf. Lund et al. (2004). In order to investigate similar asymmetry in the current material system, the quasistatic strength analyses are carried out under tensile as well as compressive loading. Dynamic strength analyses are carried out using shock wave propagation simulations in <100>, <110>, and <111> oriented single crystalline Al and in <0001> oriented single crystalline Fe_2O_3. Eight different plate impact velocities (0.5 km/sec to 4 km/sec with an interval of 0.5 km/sec) are applied during analyses. The shock wave propagation analyses also focus on calculating the U_S-U_P relationships and

on analyzing the shock-induced structural deformation in the single crystalline systems. The shock wave propagation analyses are also carried out through an interface of Al and Fe_2O_3 for analyzing a reactive structural transformation in a region surrounding the interface as a function of shock loading. The MD framework developed to carry out the above analyses consists of the following components:

1. A parallel high-level programming language MD code in which the force and energy calculations using the interatomic potential are implemented;
2. A tool for visualizing the trajectory of an atomic ensemble as it evolves under specified initial and boundary conditions;
3. A visualization scheme for implementation in the visualization tool for required graphical rendering of the atomic trajectories;
4. An algorithm for generating 3-D polycrystalline structures with a specified grain size distribution and implementation of the algorithm using a high level programming language;
5. An algorithm for carrying out the quasistatic strength calculations for nanocrystalline structures under tension and compression and implementation of the algorithm into the parallel high-level programming language MD code; and
6. An algorithm for carrying out shock wave propagation analyses at the specified particle velocity values.

This chapter describes layout of the above components. The next section describes the parallel high-level programming language MD code with associated algorithms. The next section also describes the visualization approaches used during structural analyses. In the following section, the method used for developing nanocrystalline structures with a specified average grain size is described. This is followed by a characterization of the developed nanocrystalline structures. The algorithm used for quasistatic strength calculations is described next followed by a description of the shock wave propagation methodology used in the current research. The structure of the Al and Fe_2O_3 interface after MD equilibration is characterized following that. The chapter ends with a summary of the framework as a prelude to the analyses presented in the following chapters.

3.1 High-Level Parallel MD Code and MD Visualization Tools

MD simulations are carried out using a modified version of a scalable parallel code, DL_POLY 2.14, see Smith et al. (2002), which uses the atom-decomposition paradigm, see Vincent and Merz (1995), for high performance computing. High level programming language used in this code is FORTRAN-90. The modifications to the code include implementations of the interatomic potential, the quasistatic strength calculations algorithms, the algorithm for planar shock wave generation, the procedures for reading I/P parameters specific to the applied initial and boundary conditions, procedure for electronegativity equalization, and the O/P schemes for generating atomic trajectory and corresponding statistical mechanical quantities such as the virial stress. The electronegativity equalization, cf. Strietz and Mintmire (1994), is carried out to determine

atomic charges at the Al and Fe_2O_3 interfaces in a region covered by the short range electrostatic cutoff (10 Å) on either sides. The methodology of the electronegativity equalization is based on a description of the total electrostatic energy of an array of atoms as a function of the atomic charges (valences) and the position, see Eqs. (2.10) and (2.20). For well behaved parameters J_i^0 and functions $f_i(r)$, the electrostatic energy has a well-defined minimum. The values of charges, q_i, are chosen such that the electrostatic energy, E_{es}, is minimized subjected to the constraint that the sum of charges is constant, cf. Strietz and Mintmire (1994). This condition is algebraically equivalent to the electronegativity equalization condition which requires that the chemical potentials $\mu = \mu_i = \partial E_{\text{es}} / \partial q_i$ be equal. Once the charges are determined, the electrostatic part of the total energy is calculated using Ewald summation techniques, cf. Ewald (1921), Parry (1975), Rhee et al. (1989), Greengard and Rokhlin (1987), Ding et al. (1992), and Darden et al. (1993). The short range electrostatic cutoff value of 10 Å used during calculations is obtained by matching the values of the Coulomb energy and the Coulomb virial as a function of the short range electrostatic cutoff. In addition, a convergence analysis for the variation in the electrostatic energy as a function of the short range cutoff was carried out. The cutoff value of 10 Å satisfied both criteria.

The code with all the implementations needed synchronization with GULP 1.3 in terms of the energy and force calculations for the Al+ Fe_2O_3 material system. For this purpose, the energy and atomic trajectory calculations in trial atomic ensembles consisting of various combinations of the Al, Fe, Al_2O_3, and Fe_2O_3 crystalline systems were matched from the runs of both DL_POLY 2.14 and GULP 1.3. GULP is a serial program and

therefore cannot be used for atomic ensembles with more than 2000 atoms. Modified DL_POLY 2.14, on the other hand, gave satisfactory performance for atomic ensembles with upto 100000 atoms. Systems with more than 100000 atoms could not be analyzed because of the limitations imposed by memory requirements of CPUs in the distributed memory supercomputers used to carry out the simulations. Once DL_POLY 2.14 was calibrated with GULP 1.3 in terms of the energy and force calculations, standardization of visualization schemes for the structural analyses was carried out.

The visualization tool used to analyze the trajectory of atomic ensembles during MD simulations is VISUAL MOLECULAR DYNAMICS (VMD), cf. Humphrey et al. (1996), developed at the university of Illinois, Urbana Champaign. This tool is based on *tcl* programming script for developing user specific programs of visualization. Specific scripts were developed to obtain the movies and the snapshots of atomic configurations for required visualization. APPENDIX A1 shows one such script. The script specifies colors for atoms in various atomic configurations based on a visualization scaling parameter obtained by applying physics based models. The physics associated with differently colored atoms in the atomic configurations is then used for identifying defect formation and propagation.

Three different physics based parameters can be used to assign colors to atoms in a deforming *fcc*-Al atomic ensemble: 1. centrosymmetry parameter by Kelchner et al. (1998), 2. common neighbor analyses (CNA) parameter by Honeycutt and Anderson (1987), and 3. slip-vector magnitude parameter by Zimmerman et al. (2001). The

centrosymmetry parameter is not useful in a nanocrystalline setting for identifying grain boundaries, cf. Rodríguez de la Fuente et al. (2002). The CNA has been used in past to identify the motion of dislocations through grain boundaries by Van Swygenhoven and Caro (1997). However, CNA is not appropriate for identifying the magnitude of dislocation burger vectors. The slip-vector approach has been used in past by Zimmerman et al. (2001) and Rodríguez de la Fuente et al. (2002) to identify dislocations and to analyze the magnitude of Burger's vector during nanoindentation. In the current research, the visualization is primarily used for identifying the extent of dislocation emission at the low-angle and high-angle grain boundaries that result in stacking fault formation. The focus is also on differentiating between the motions of grain boundary atoms during tensile and compressive deformations. For this purpose the slip-vector approach is the most appropriate.

Figure 3.1 (a) shows grain boundaries in a model polycrystalline Al sample identified using the slip-vector approach. The figure also shows the corresponding slip-vector scale. In *fcc*-Al unit glissile dislocation is $a/2[110]$ dislocation with Burgers vector magnitude of 2.87 Å which is close to the upper limit of the slip-vector scale shown in Figure 3.1 (a). It is clear from the figure that by using the shown slip-vector scale, the motion of atoms in grain boundaries can be easily differentiated from the motion of atoms inside the grains. Accordingly, throughout the current research, the slip-vector approach is used for identifying defects in *fcc*-Al atomic ensembles with the scale shown in Figure 3.1 (a).

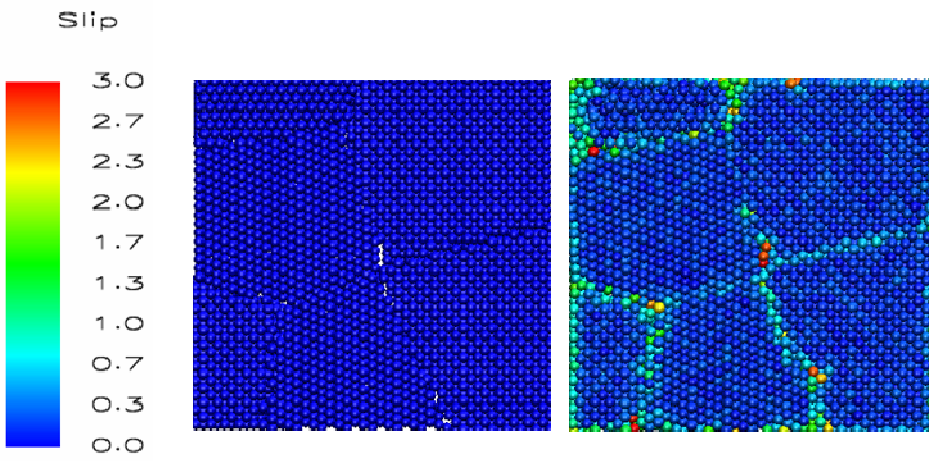

(a)

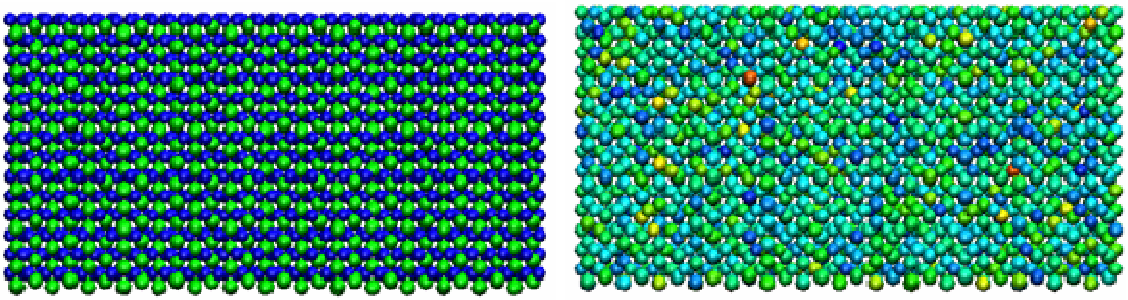

(b)

Figure 3.1 An illustration of the application of the slip-vector approach in (a) identifying grain boundaries in polycrystalline Al and (b) identifying structural order in single crystalline Fe_2O_3

In the case of Fe_2O_3 all three visualization approaches failed to recognize any structural pattern. The primary reason is the difference between the cubic unit cell structure for Al and the rhombohedral primitive unit cell structure for Fe_2O_3. For example, in Figure 3.1 (b), a hexagonal Fe_2O_3 supercell after MD equilibration for 10 ps is compared with its visualization using the slip-vector approach. No clear structural pattern is visible. It is clear that the visualization approach fails even in the case of single crystalline Fe_2O_3. Accordingly, for ensembles in which Fe_2O_3 is present, the partial and the total radial

distribution functions (RDF) and bond angle distribution function (BDF) are extensively used to identify the structural order.

The partial RDF for an atomic pair α-β, $g_{\alpha\beta}$, is determined from, cf. Gutie´rrez and Johansson (2002),

$$g_{\alpha,\beta} = \frac{\left\langle n_{\alpha,\beta}(r, r+\Delta r)\right\rangle}{4\pi r^2 \Delta r}\frac{V}{N_\beta}, \quad (\alpha, \beta = atom\,1, atom\,2)\cdot \tag{3.1}$$

Here, $\left\langle n_{\alpha,\beta}(r, r+\Delta r)\right\rangle$ denotes the average number of particles of species β surrounding a particle of species α in a spherical shell between r and $r+\Delta r$, and N_β is the total number of particles of species β, and V is the volume of system. For calculating the total Fe_2O_3 RDF, the partial Fe-Fe, Fe-O and O-O RDFs are summed up together. RDF is important to identify the average bond length between α and β in a particular region. The BDF for an atomic pair α-β, $g_{\alpha\beta\alpha}(\theta)$, is defined for angles between the nearest neighbor atoms. For example, in a diamond crystal, it is a delta function centered at θ =109.47°. For an amorphous crystal, large angled distortions occur resulting in significant width of the BDF. The angles between particles $\theta_{\alpha\beta\alpha}$ are defined for particles of type α that located inside of the first coordination sphere of a particle of type β. The cosine law is applied to calculate angles on the known coordinates of particles. The BDF is calculated using the expression

$$g_{\alpha\beta\alpha}(\theta) = \frac{\sum_{\beta} n_{\alpha\beta\alpha}(\theta, \theta + \Delta\theta)}{\sum_{\beta} N_{\alpha\beta\alpha}}. \quad (3.2)$$

Here, $n_{\alpha\beta\alpha}(\theta, \theta + \Delta\theta)$ is the number of angles between particles $\alpha - \beta - \alpha$ in limits from θ to $\theta + \Delta\theta$ for particles of type α, located in the first coordination sphere of a particle of type β, $N_{\alpha\beta\alpha}$ is number of all $\theta_{\alpha\beta\alpha}$ angles. Both functions, the RDF and the BDF, do not provide long-range structural information. However, their computations give an opportunity to obtain features of the short-range order that can be compared with experimental data.

3.2 Generation of Nanocrystalline Structures for MD Simulations

The nanocrystalline structures used in the current research are:

1. Nanocrystalline *fcc*-Al with three different average grain sizes (PAl1 with average grain size 7.2 nm, PAl2 with average grain size 4.7 nm, and PAl3 with average grain size 3.9 nm);
2. Nanocrystalline α-Fe_2O_3 with three different average grain sizes, (PHt1 with average grain size 7.2 nm, PHt2 with average grain size 4.7 nm, and PHt3 with average grain size 3.9 nm); and
3. Nanocrystalline *fcc*-Al+α-Fe_2O_3 composites with two different volume fractions: a. 60% *fcc*-Al+40%α-Fe_2O_3 (NCP641 with average grain size 7.2 nm, NCP642 with average grain size 4.7 nm, and NCP643 with average grain

size 3.9 nm), b. 40%*fcc*-Al+60%α-Fe_2O_3 (NCP461 with average grain size 7.2 nm, NCP462 with average grain size 4.7 nm, and NCP463 with average grain size 3.9 nm).

Nanocrystalline Al, nanocrystalline Fe, and their composites with the same average grain size have the same orientation and grain size distributions. The nanocrystalline structures are generated by growing grains inside a cubic box. In order to duplicate a bulk nanocrystalline material, the box is repeated in all 3 dimensions by imposing periodic boundary conditions (PBCs). The size of nanostructures used during MD simulations is guided by computational limitations such as the memory and the computational time required. Under the limitations, the size of the cubic box to generate nanocrystalline structures is kept at 10 nm × 10 nm × 10 nm. The size is chosen such that in any structure the maximum number of atoms does not exceed 100000. With limitation on the size of the cubic box, the maximum grain size in MD simulations is limited to approximately 10 nm. However, the upper limit on grain size is further reduced depending upon the requirements regarding the number of grains in the cubic box. As will be shown later, the largest grain size obtained by the bi-division of the cubic box in all three-dimensions is approximately 8.2 nm with the average grain size being 7.2 nm. Size of the structures analyzed using MD simulations of the shock wave propagation is kept at 15 nm × 6 nm × 6 nm. This combination of cross-section (6 nm × 6 nm) and length (15 nm) is found to be the best fit to obtain a planar steady shock wave while keeping in tune with the computational limitations.

3.2.1 Schemes for Generating Nanocrystalline Materials

In past few years, nanocrystalline materials have been formed as atom clusters of a variety of materials with average grains sizes in the range of 5-50 nm. They are synthesized through evaporation and condensation of high-purity gases followed by consolidation in-situ under ultrahigh vacuum conditions. Desirable sizes of the grains are generally below 100 nm, since it is in this size range (often below 10 nm) at which various properties begin to change significantly as a result of various confinement effects. Transmission electron microscopy (TEM) has shown that the grains in nanocrystalline materials are essentially equiaxed, similar to the atom clusters form which they are formed, although departures from spherical structures are expected simply from efficient packing of the clusters during consolidation. The grains also appear to retain narrow log-normal grain size distributions typical of the clusters formed in the gas-condensation methods. Measurements of these distributions before and after cluster consolidation by dark-field electron microscopy yield similar results. Grain-size distributions in deformation-produced nanostructures can be somewhat broader. Observations using both electron and x-ray scattering indicate that there is no preferred crystallographic orientation or texture of grains and that the grains in the nanoscopic contact are essentially randomly oriented with respect to each other, cf. Siegel (1994a) and Siegel (1994b).

The morphology of nanoscopic materials on a variety of lengthscales has an important bearing on their properties. The morphology includes a series of geometric and structural

properties such as grain size, grain shape, grain boundary structure and thickness, triple junction and grain boundary area, grain misorientation and texture, etc. For an average grain size range between 5 nm and 10 nm, the percentage of gain boundary atoms ranges between approximately 5% and 50%, cf. Siegel (1994a) and Siegel (1994b). Several early investigations of nanocrystalline metals, including x-ray diffraction, Mössbauer spectroscopy, positron lifetime studies, and extended x-ray absorption fine-structure (EXAFS) measurements, have been interpreted in terms of the grain boundary atomic structures that may be random, rather than possessing either the short-range or long-range order normally found in grain boundaries of conventional coarser-grained polycrystalline materials.

Observations involving Mössbauer spectroscopy, conventional and atomic-resolution TEM, and x-ray diffraction suggest the presence of nonequilibrium grain boundaries in nanocrystalline materials with structures and properties that differ significantly from those of coarse-grained materials, cf. Phillpot et al. (1995). However, direct observations by high resolution electron microscopy (HREM) have indicated that their structures are similar to those of conventional high-angle grain boundaries, cf. Siegel and Thomas (1991). Evidence for the porosity in nanocrystalline materials has been obtained by positron annihilation spectroscopy (PAS), precise densitometry, porosimetry measurements, and small angle neutron scattering (SANS). A variety of such measurements have shown that the total porosity is smaller than or equal to the grain size of the materials (although some larger porous flaws have been observed by optical and scanning electron microscopy). The porosity ranges from about 15-25% for ceramics to

less than 5% for metals, cf. for example Kumar et al. (2003a) who analyzed virtually pore free nanocrystalline Ni. Presently available experimental evidences suggest that dislocations are seldom present in nanocrystalline materials. When they are observed, it is primarily either in materials at the upper end of the grain size range or in limited instances in immobile or locked configurations, Siegel (1994a) and Siegel (1994b). In spite of much experimental work on the structure and the properties of nanocrystalline materials, a structural model consistent with the experimental observations and one that permits some of the anomalous properties of these materials to be predicted has not evolved.

Microscopic lengthscale simulations for material failure modeling regularly use digitally generated micrographs of experimental specimens, see for example Zhai et al. (2004). However the same cannot be extended to the nanoscopic MD simulations of mechanical deformation. Current experimental techniques are limited in their ability to digitally photograph the morphology of a nanostructured material for use in the MD simulations, cf. Siegel (1994a) and Siegel (1994b). Therefore, instead of using digital nano-graphs, the polycrystalline materials in this research are computationally generated using the state of the art Voronoi tessellation technique. Careful analyses of grain boundaries in computer generated pure metallic nano-samples using Voronoi tessellation have been reported earlier. The disorder in grain boundaries has been interpreted as an amorphous structural characteristic of the grain boundaries. Controversial results on the structure of grain boundaries in nanocrystalline materials have been reported, cf. Stern et al. (1995), Loffler and Weissmuller (1995), Lu and Sun (1997), Sanders et al. (1998), and Zhao et al.

(2002). Two extreme pictures have been proposed: the earliest, supported by some experiments and computer simulations, cf. Herr et al. (1990), Keblinski et al. (1997), and Keblinski et al. (1999), suggests a non-equilibrium, highly disordered ‘‘frozen-gas like’’ grain-boundary structure that is substantially different from the grain boundary structure in coarse-grained polycrystalline materials. More recent experiments, see for example Siegel (1991) and Stern et al. (1995), suggest that grain boundaries in nanocrystalline materials are similar to those found in coarse-grained polycrystalline materials.

The studies in the literature use different measuring techniques, which are often not directly comparable. Another problem is that different synthesis techniques and different aging and annealing histories have been used in various experimental studies. A considerable effort both in refining experimental techniques such as x-ray diffraction and absorption measurements and high-resolution electron microscopy and in comparing different synthesis techniques is required to clarify this controversy. In addition, it must not be forgotten that the computer representation of nanocrystalline materials is not fully acceptable because some experiments have shown that the degree of disorder in grain boundaries depends on the age of a sample and its thermal history. Only as prepared samples show short-range uncorrelated atomic displacements. In aged and annealed samples it has been shown that the disorder is characterized by displacements correlated over several lattice parameters. Due to computational limitations, simulations usually describe the equivalent to ‘‘as-prepared’’ samples, i.e., samples with very short annealing times. This point may be a limitation in the predictive capabilities of simulations and is

carefully considered when drawing conclusions from computer simulations in the present research.

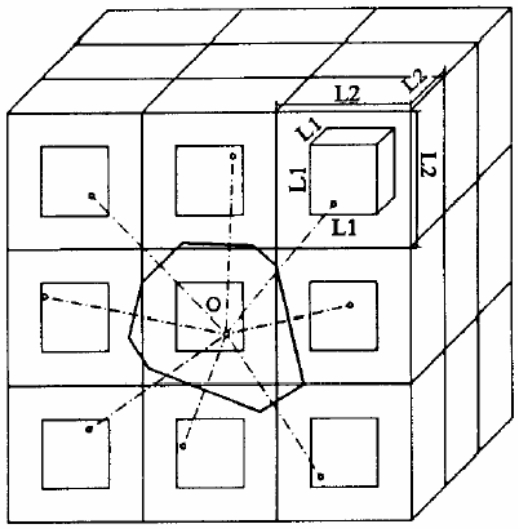

Figure 3.2 Schematics for 3-D Voronoi tessellation cf. Chen (1995)

Computationally generated nanocrystalline materials have been used by Schiøtz et al. (1998) for studying the reverse Hall-Petch (H-P) relation, by Zheng et al. (2003) for modeling ferromagnets, and by Lund et al. (2004) for analyzing the tension-compression strength asymmetry and associated grain size variation and grain misorientation effect on the mechanical response. The most successful approaches for computational generation of nanocrystalline structures are required to be statistical in nature in order to acquire the experimentally observed log-normal grain size distribution, cf. Gross and Li (2002). The primarily used approaches are the monodispersive grain growth method, cf. Gleiter (2000), the melt growth method, cf. Phillpot et al. (1995), Keblinski et al. (1997), and Keblinski et al. (1998), and the Voronoi tessellation method, cf. Voronoi (1908), Chen (1995), Van Swygenhoven et al. (1999a), and Schiøtz et al. (1999). While, the monodispersive grain growth technique is non-statistical in nature, the latter follow a

fixed Voronoi-Poisson grain-size distribution which is rarely observed in experiments, cf. Gross and Li (2002). However, from mesoscale simulations it is known that a Voronoi starting structure evolves very quickly towards (but never reaches) a log-normal distribution, cf. Haslam et al. (2001). Gross and Li (2002) have combined the Monte-Carlo method with the Voronoi tessellation method for grain-growth for generating nanocrystalline structures with specified probability distribution of the grain sizes. Using this technique, the distribution of grain sizes can be aligned according to any experimentally observed grain size distribution. In next subsections, these approaches are discussed, followed by a description of the algorithm used for the generation of nanocrystalline composites in the current research.

3.2.1.1 Voronoi Tessellation

In this method, three-dimensional grains are generated inside a cubic box with specified dimensions. The average grain size is determined by the number of subdivisions specified for the box, cf. Chen (1995). Based on the number of specified subdivisions the box is divided into small cubic blocks, see Figure 3.2. At the center of each small cubic block, an even smaller cubic block is formed, which is used as the nucleus distribution area of the crystallite corresponding to the small block. For this purpose a random point (grain growth nucleus) is selected within each smaller block as the site of grain nucleation. The polyhedra around each point are then created to simulate the nanocrystalline grains. Random distribution of the grain growth nuclei inside smaller cubic blocks results in random size distribution of the polyhedral grains. By controlling the size of smaller cubic block, a potential problem of having grains with very sharp ends can be avoided. The

polycrystalline structure obtained using this method is then subjected to the MD equilibration in order to relax atoms along geometric polyhedra grain boundaries. Three-dimensional PBCs are imposed during MD runs on the box for simulating a bulk polycrystalline material. Van Swygenhoven and Caro (1997) and Schiøtz et al. (1999) have used this technique to create systems that mimic the grain structure of nanocrystalline metals generated by inert gas condensation. The shapes of grains seem to be almost equiaxed. The grains are essentially dislocation free. Due to low number of grains in the nanocrystalline setting it is not possible to distinguish between a log-normal or a normal grain size distribution. At the room temperature (300 K) the length of MD equilibration did not affect the mechanical properties of the nanocrystalline material samples. Haslam et al. (2001) chose a columnar and textured microstructure generated using Voronoi tessellation in their study. An initial microstructure containing 25 periodically repeated grains with an average grain diameter of d=15 nm was chosen during analyses. Their mechanical deformation analyses on nanocrystalline structures were in close agreement with actual experimental features of the mechanical behavior.

3.2.1.2 Melt Growth Method

Phillpot et al. (1995) developed this MD based method to grow space-filling, fully dense three-dimensional polycrystals. This approach focuses on a description of the structure and the properties of a relaxed and fully dense nanocrystalline sample irrespective of the kinetic processes required for its synthesis. At the beginning of the MD simulations for generating nanocrystalline structures, small pre-oriented single crystal seeds are

randomly embedded in the melt in a cubic box similar to the one used during Voronoi tessellation. The melt consists of atoms of the same material in disordered liquid state. The sample is subsequently cooled below the melting point to enable the crystal growth under an applied external pressure. Finally, a material that has been annealed and is free of pores such that the grain boundaries are in a relaxed ground state is obtained. To ensure a fully relaxed structure, the samples are annealed by heating to approximately half the melting temperature and then cooling back to zero temperature under zero external stress. In spite of rather small number of grains in the simulation cell, thermal expansion of the material is practically isotropic and almost identical to that of a perfect crystal. The final fully relaxed material sample contains large perfect-crystal regions separated by well-defined grain boundaries, most of which have approximately the same width and energy. The melt-growth method is found to induce a large number of defects (mainly stacking faults) in the grains because of rapid solidification. The stacking faults are clearly visible in the nanocrystalline metal generated using the melt growth method in Figure 7 of Phillpot et al. (1995). In the current research, we focus on using specimens that are initially defect free. Accordingly, an approach based on the Voronoi tessellation method is an appropriate choice.

3.2.1.3 Inverse Monte-Carlo Method with Voronoi Tessellation

Gross and Li (2002) and Zheng et al. (2003) used this approach to develop structures with a given orientation distribution function as well as a given grain size distribution function. A key step in the approach is to use the available distributions of the

microstructural attributes as inputs, some of which may be from experiments and some may be hypothetical ones. Since usually only the grain size distribution, $P(d)$, where d is the grain size, is known, $P(d)$ is taken as the primary input. Other microstructural quantities and their distributions can also be produced using the same algorithm if their distribution functions are known. The algorithm consists of the following steps:

(a) Take N points or grains and distribute them randomly in a space of volume V;

(b) Construct Voronoi polyhedral cells around each of the points and compute the grain size or volume, d, of the polyhedral cells;

(c) Compute $P(d)$ from the Voronoi cells and calculate a penalty function, $\chi^2 = \left(1/N\right)\sum_i^N \left[P_{input}(d_i) - P(d_i)\right]^2$, where the input distribution function $P_{input}(d_i)$ can be taken from experiments, or theory;

(d) Move the center of each grain randomly; then go to steps (b) and (c); and

(e) If χ is smaller than that in the previous configuration, keep the move; if χ is larger, but exp $(-\chi/\alpha) \leq \rho$, where ρ is a random number and α is a small number ($\alpha \rightarrow 0$), keep the move; Otherwise do not move the grain center.

The entire process repeats many times until χ approaches a preset number, for e.g. $\chi_{final}=10^{-3}$. The algorithm is similar to the inverse Monte Carlo method in which the selection rule for approximating the targeting function (step e) is a probability process. Table 3.1 lists the average grain sizes of the nanocrystalline materials used by various researchers along with the methods used to generate the nanocrystalline structures. In the current research, nanocrystalline structures are generated such that a cubic box of size 10

nm has 8, 27, and 64 grains. As will be shown later, these numbers of grains correspond to the average grain sizes of 7.2 nm, 4.7 nm, and 3.9 nm, respectively. It has been observed that for small number of grains there is no difference between a Voronoi-Poisson grain size distribution or a log normal grain size distribution, cf. Haslam et al. (2001). Since the maximum number of grains in the cubic box is limited to 64, we use Voronoi tessellation for generating nanocrystalline structures without probability based evolution approach of Gross and Li (2002) and Zheng et al. (2003). The target grain size distribution is the log-normal distribution with 10% standard deviation.

Table 3.1 A survey of the average grain sizes of the nanocrystalline materials used by various researchers

Researcher	Grain Size (nm)	Method
Chen (1995)	1.62	Voronoi
Phillpot et al. (1995)	3.8,4.3,5.4,7.3	Melt Growth
Van Swygenhoven and Caro (1997)	3.4,5.2,8.0,10.0,12.0	Melt Growth
Gross and Li (2002)	6nm	Voronoi
Schiøtz et al. (1998)	3.3-6.6 nm	Voronoi
Yamakov et al. (2002a)	45 nm (2D)	Voronoi
Haslam et al. (2001)	15 nm (2D)	Voronoi

3.2.2 Algorithm

Input:

1. Volume fractions of Al and Fe_2O_3;
2. Size of the cubic block (nm) as lengths in the x, y, and z directions; and
3. Number of subdivisions of the box in each direction (number of grains).

The algorithm for nanocrystalline structures generation uses the following three stages, (**S1** to **S3**):

S1: *For the given cubic block size and the number of subdivisions, the distribution of the nuclei for grain growth is obtained.*

As pointed out earlier, block size is taken to be 10 nm. Three subdivisions viz. 8, 27, and 64 are specified during simulations. The following steps are followed during random generation of the nuclei for grain growth:

1. Divide the cubic block with the given size into a smaller number of cubes with the given number of subdivisions;
2. Inside each smaller cube form another cube of half the dimensions of the small cube (this is done in order to have smallest possible deviation in grain sizes from the mean grain size and to exclude the possibility of forming grains with sharp ends or pear shaped facets) and generate a random point in this cube;
3. Locate the coordinates of the random points in the nearest neighbor boxes of each random point.

S2: *Statistical characterization of the grain size distribution in all structures is carried out.*

1. For a given distribution of the nuclei for the grain growth, obtain the grain size distribution histogram for structures with 8, 27, and 64 grains (grain size is calculated by averaging the intercept lengths of the polyhedral grains along

all facets, cf. Meijering (1953), Kumar et al. (1992), and Han and Kim (1998)),

2. Compare each histogram with the target log-normal and normal distributions having 10% standard deviation, and
3. Choose the distribution of nuclei for given number of grains that has the least deviation from the target grain size distributions.

Two to three iterations were required to achieve an acceptable fit of the grain size distribution to the the target distributions for all subdivisions of the cubic box. A standard deviation of approximately 10% was targeted in all distributions.

S3: *For acceptable distributions of nuclei, nanocrystalline structures are obtained.*

In this step, specific crystalline systems are allocated to the grain growth nuclei based on the specified volume fraction values for the nanocrystalline structure. The constituent volume fraction is incorporated using a random number generator. A crystal system is allocated to a grain growth nucleus based on the value of a random number generated based on the position of the nucleus in the cubic box. In addition, it is made sure that the orientations of neighboring grains are different from each other and that the composites have Al most possibly surrounding Fe_2O_3 and vice-versa. For grain growth in each grain, one of the three different orientations, viz., [001], [010], and [001] is selected randomly using another random number generator. Once crystalline systems with different orientations are allocated to all grain growth nuclei, the nanocrystalline structure is obtained by growing grains. This step is carried out by growing specifically oriented crystallites at each grain growth nucleus. An atom belongs to a particular grain only if the

atom's distance from its grain growth nuclei is smaller than its distance from all the neighboring nuclei. In the grain boundaries of the nanocrystalline structures, it is possible that two atoms from two different grains get too close to each other to cause unphysically large energy. In such cases one of the atoms is randomly removed.

Using the algorithm, 12 nanocrystalline structures are generated with grain sizes ranging from 3.9 nm to 7.2 nm (PAl1, PHt1, NCP461, NCP641 with grain size 7.2 nm; PA21, PHt2, NCP462, NCP642 with grain size 4.7 nm, and PAl3, PHt3, NCP463, NCP643 with grain size 3.9 nm). Figure 3.3 shows these structures in order of increasing grain size in rows and in order of increasing Al volume fraction in columns. As pointed out earlier, in all nanocrystalline structures with the same average grain size, the grain size distribution and the distribution of grain orientations is the same regardless of composition. Figure 3.4 shows histograms of the grain size distribution in the nanocrystalline structures and compares them to the prescribed log-normal and normal distributions. The agreement of the grain size distributions with the log normal and the normal distributions with approximately 10% standard deviation is evident. Once geometric nanocrystalline samples have been obtained, they need to be subjected to MD equilibration in order to relax atoms along grain boundaries. This procedure is important to allow unfavorable local atomic configurations in the grain boundaries to relax. Schiøtz et al. (1999) found that the duration of annealing, if of the order of ps, is not important nor is the temperature, however annealing as such is necessary as well as important. Accordingly, all samples are annealed for 10 ps at 300 K similar to the procedure by Schiøtz et al.

(1999). This procedure is also similar to that of Chen (1995) and Van Swygenhoven and Caro (1998).

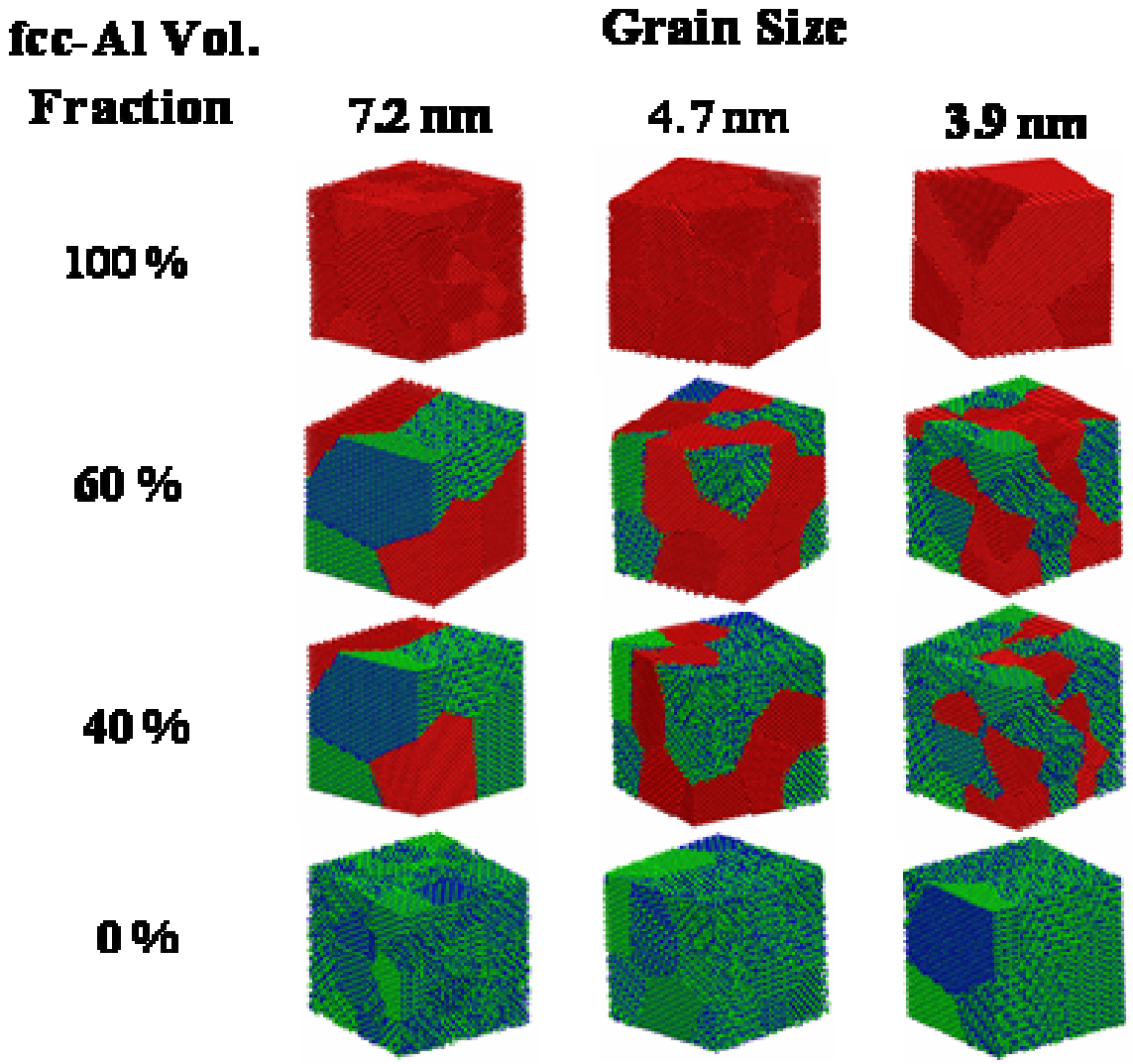

Figure 3.3 Set of nanocrystalline structures before MD equilibration

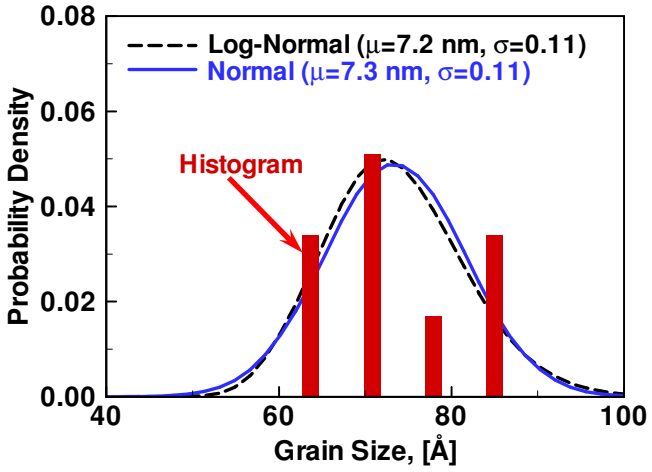

(a)

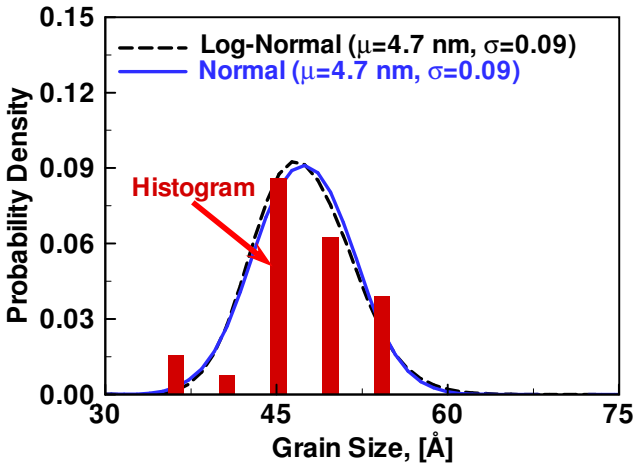

(b)

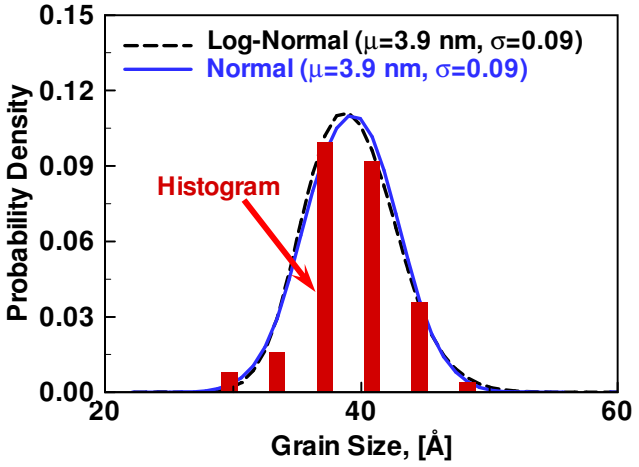

(c)

Figure 3.4 A comparison of the histograms of grain size distribution in the nanocrystalline structures with the target log-normal and normal grain size distributions

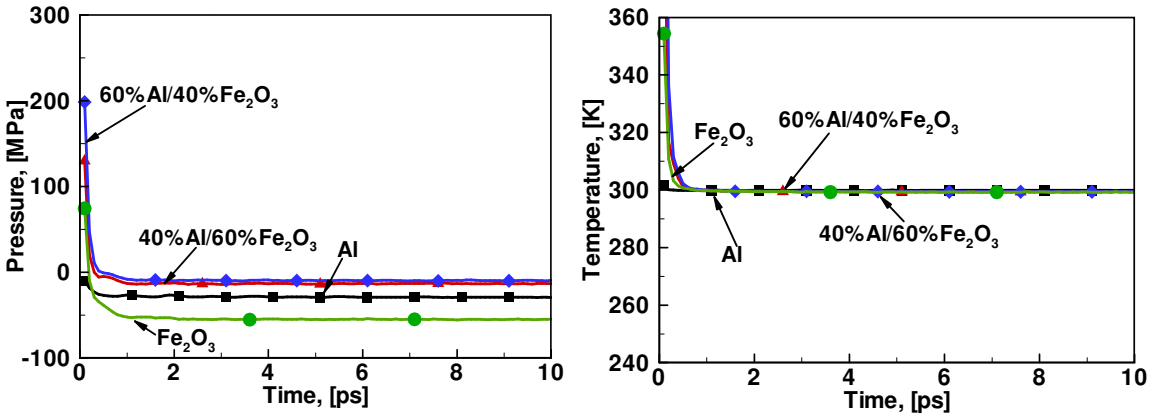

(a) (b)

Figure 3.5 Time history of (a) the pressure and (b) the temperature in nanocrystalline structures during MD equilibration

Figure 3.5 shows time history of the pressure and the temperature during MD equilibration of PAl1, PHt1, NCP461, and NCP641. As shown the pressure and the temperature were stabilized in a period of 2 ps in all structures. Equilibration during this initial time period in PHt1, NCP461, and NCP641 involves a large shuffling of atoms to relieve internal stresses arising out of purely geometrical nanocrystalline arrangement of atoms. On the other hand in PAl1, the shuffling is minimal. After equilibration, we were able to observe grain boundary clearly in nanocrystalline Al samples using the slip-vector approach. The visualization in case of PHt, NCP46, and NCP64 samples gave altogether different results. The next sections discuss these results.

3.3 Nanocrystalline Al after Equilibration

Samples of nanocrystalline Al, viz., PAl1, PAl2, and PAl3, before and after the MD equilibration are shown in Figure 3.6. In order to compare the movement of atoms in the

grains and along grain boundaries only the cross-sections at the middle of the samples are shown. For visual comparison, orientation of each grain at the cross-section is also shown in Figure 3.6 (a). Recently, Liao et al. (2004) observed that experimental samples of nanocrystalline Al had grains with random mix of the low-angle and high-angle mismatches at the grain boundaries. The similar experimental observations on nanocrystalline Ni have been reported by Kumar et al. (2003a). In Figure 3.6 each sample contains randomly oriented grains in such a way that the grain boundaries have a mix of the low-angle and high-angle mismatches. For convenience, the low-angle and high-angle mismatches are clearly identified in non-equilibrated samples, see Figure 3.6 (a). Figure 3.6 (b) shows the samples after equilibration.

Since the grains are cut randomly, it is not possible to identify a coincident site lattice structure in grain boundaries. Van Swygenhoven et al. (2000), Van Swygenhoven et al. (2001) report that the grain boundary region of nanocrystalline Cu and Ni with grain sizes in the range of 5-12 nm constructed from a Voronoi model has a degree of structural coherence and misfit accommodation occurring in a regular pattern. Actual positions of the atoms in the regions with disorder are random or liquid like. During MD equilibration, the majority of atomic movement in all samples is restricted along the grain boundaries. The current research focuses on analyzing the constitutive behavior of polycrystalline structures as a function of the grain size, the volume fraction, and the loading directionality.

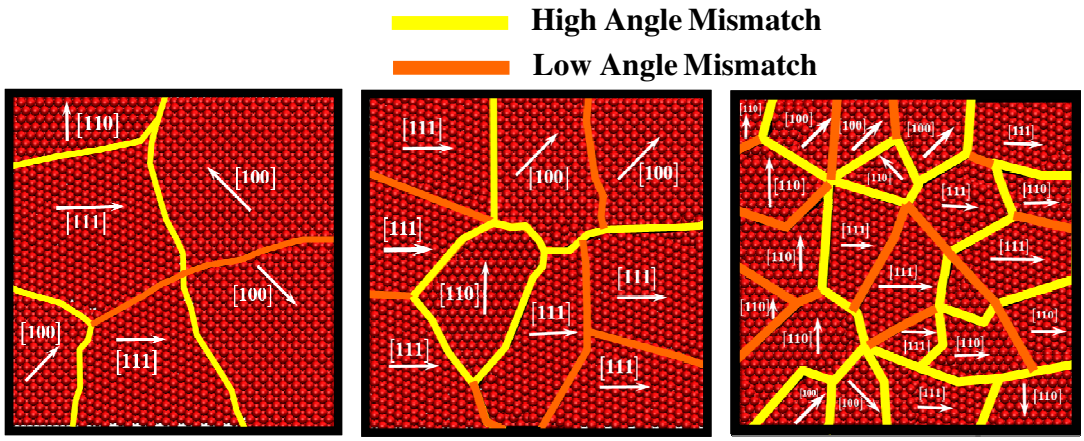

(a)

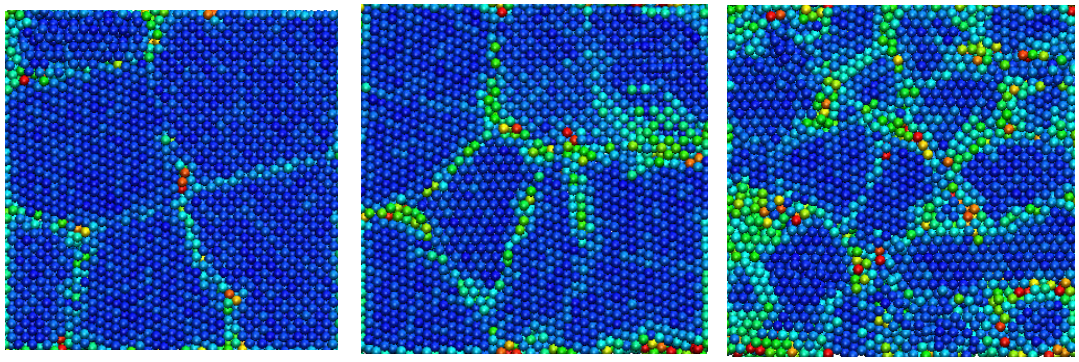

(b)

Figure 3.6 (a) Illustration of the low-angle and high-angle grain boundary mismatches before MD equilibration in all samples of nanocrystalline Al and (b) the slip-vector based viewgraphs of the same samples after MD equilibration for identifying the thickness of grain boundaries, (for ease of comparison, only the middle section is analyzed)

The contribution of grain boundary atoms to the overall deformation is, therefore, characterized with a broad classification of grain boundaries into the low-angle and high-angle grain boundaries. Thicknesses of the high-angle grain boundaries is higher than that of the low-angle grain boundaries. In PAl1 and PAl2, {100}-{111} high-angle mismatch grain boundary is the one with the highest thickness. However, in PAl3 {110}-{111} and {110}-{100} high-angle mismatches have the highest thickness. The thickness of the

high-angle grain boundaries varies from 1 nm in PAl1 to approximately 2 nm in PAl3. Higher thickness of the high-angle grain boundaries indicates higher atomic movement along high-angle mismatches. This is expected since the degrees of freedom for atoms in a boundary with higher mismatch between adjacent grains are higher. Consequently, the probability of dislocation emission from the high angle grain boundaries is higher.

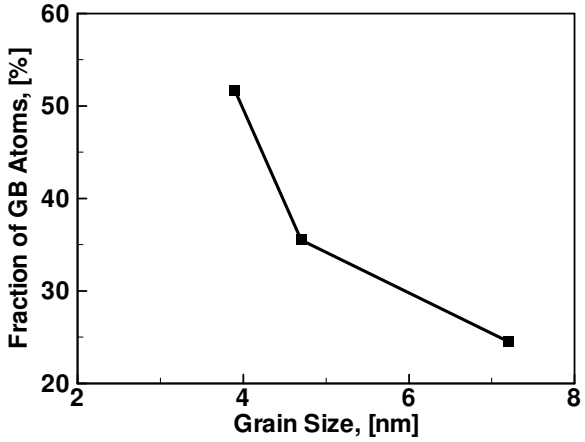

Figure 3.7 A comparison of the fraction of grain boundary atoms as a function of the average grain size in nanocrystalline Al after MD equilibration

Figure 3.7 shows the fraction of the total number of atoms in grain boundaries in all three samples. As shown there is a non-linear increase in the number of atoms along grain boundaries as the grain size is reduced. PAl1 has 25% atoms along grain boundaries, whereas in PAl3 the fraction is approximately 52%. Tjong and Chen (2004) have also observed that a nanocrystalline material with an average grain diameter of 5 nm possesses approximately 49% grain boundary atoms. In Figure 3.7, there is a sharp increase in the fraction of atoms as a function of grain size. The increase in the fraction of grain boundary atoms with reduction in the grain size is attributed to the increase in surface area of grains available for interfacing with the neighboring grains and to the increase in the number of neighboring grains which in turn affects the factors such as the

presence of disclinations and triple junctions. There is no experimental or theoretical evidence in favor or against the sharp increase. We speculate that this sharp increase is associated with the way the Voronoi tessellated structures are generated and admit it as a feature of the nanocrystalline structure generation procedure. It is clear that the deformation mechanism in nanocrystalline Al will become increasingly dependent on the average grain size with reduction in the average grain size. In Figure 3.8 the partial Al-Al RDFs for all three grain sizes before and after the MD equilibration are shown. The RDFs differ from that of a perfect *fcc*-Al crystal before and after equilibration in two ways. First, the peaks are not sharp delta functions, but are somewhat broadened even before equilibration, denoting a degree of mismatch along the grain boundaries. In addition, in all the structures the RDFs do not go to zero after the first two peaks. The broadening of the RDF peaks after equilibration is in part due to the strain fields inside the grains (originating from the grain boundaries) and in part due to atoms in or near the grain boundaries sitting close to (but not at) the lattice positions. The RDF not going to zero between the peaks denotes a disorder which in this case comes from the grain boundaries. The average depth of the RDF valleys reduces with decrease in the average grain size. Clearly, this signifies a higher fraction of atoms in the grain boundaries and a higher amount of mismatch along grain boundaries in PAl2 and PAl3 in comparison to that in PAl1. PAl1 has a higher fraction of atoms in bulk *fcc*-Al crystalline order and therefore has sharper RDF peaks than PAl2 and PAl3. There is a gradual reduction in the fraction of bulk atoms (reduction in the height of the RDF peaks) and a gradual increase in the fraction of grain boundary atoms (shallowing of the RDF valleys) with reduction in the average grain size.

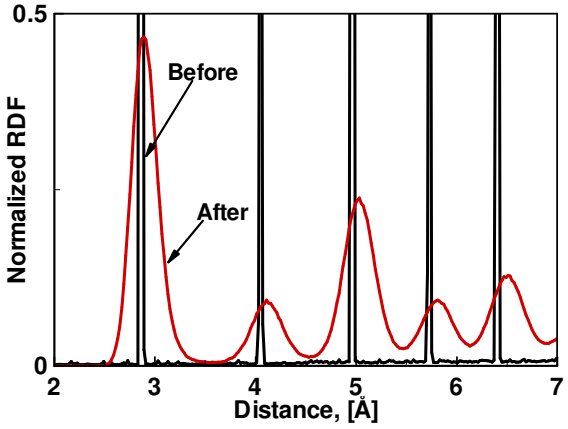

(a)

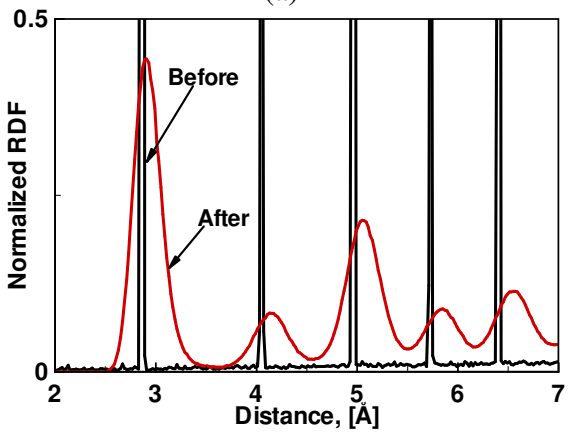

(b)

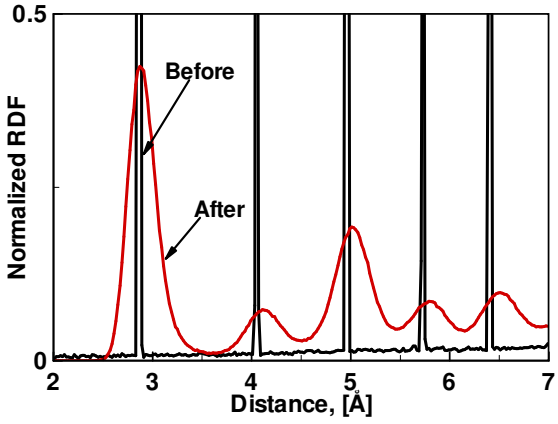

(c)

Figure 3.8 A comparison of the partial Al-Al RDFs for nanocrystalline Al with grain size (a) 7.2 nm, (b) 4.7 nm, and (c) 3.9 nm, before and after MD equilibration

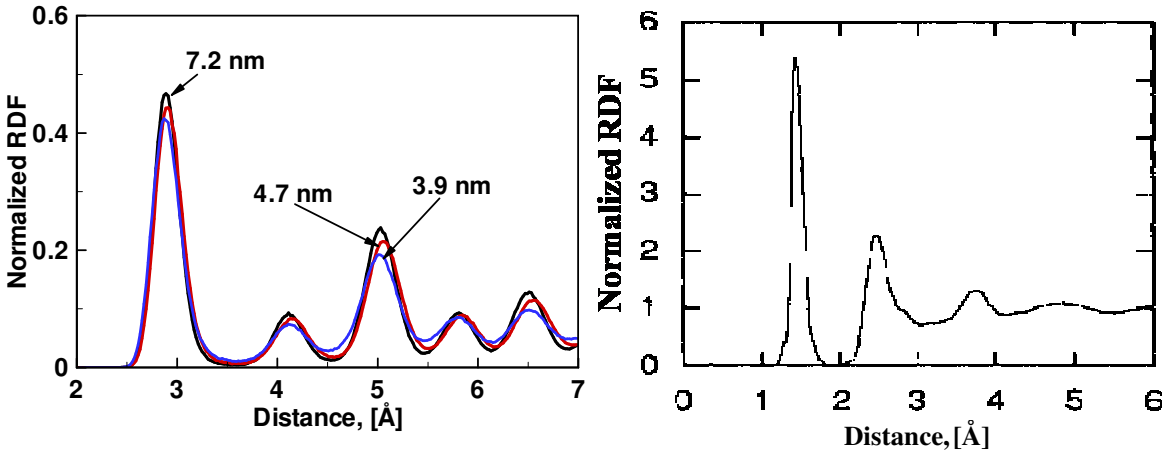

Figure 3.9 (a) Partial Al-Al RDFs for polycrystalline Al at all grain sizes after MD equilibration and (b) RDF for amorphous carbon

In order to understand the broadening of peaks of the RDFs in Figure 3.8, the RDFs for nanocrystalline Al after equilibration and of amorphous Carbon are compared in Figure 3.9. In the case of amorphous Carbon, the short-range order is expressed by two distinct and broad peaks, following by a quite flat tail, which is a characteristic of the RDF of an amorphous structure. The first peak is centered near the graphite bond length (1.42 Å) and is broad enough to include the diamond bond length (1.54 Å), so that many bonds, in the graphite-like structure, can be specified as diamond-like bonds. The liquid phase exhibits a very similar form for the RDF, except that the peaks are broader and shallower than in the amorphous one. The RDFs for PAl1, PAl2, and PAl3 after equilibration have a difference in the peaks as well as in the valleys with variation of the average grain size. PAl1 exhibits stronger crystalline order. Consequently, it has the maximum fraction of atoms in the *fcc*-Al crystalline setting and the minimum fraction of atoms in the grain boundaries and other structural disorders denoted by the valleys of the RDF. PAl3

exhibits strongest disorder with the minimum fraction of atoms in the *fcc*-Al crystalline setting and the maximum fraction of atoms along grain boundaries and other defects.

3.4 Nanocrystalline Fe_2O_3 and Al+Fe_2O_3 Composites after Equilibration

Figure 3.10 shows the middle section of polycrystalline Fe_2O_3 (PHt1, PHt2, PHt3) before and after the MD equilibration. In all structures a significant degree of crystalline structural order is lost after the equilibration. The slip-vector approach cannot be used to analyze the structural order in Fe_2O_3 because of the reasons described in earlier section. Attempts to use other established approaches were also not successful. A question that arises from observing the figure is whether the structure is still crystalline and we are not able to observe its actual structural order because of its complex primitive unit cell setting or whether it has altogether lost its crystallinity and has become amorphous. Another question is whether this structure formation arises because of the malfunctioning potential or is it actual structural attribute at the lengthscale of analyses?

In order to answer these questions, first the potential is used to equilibrate a single crystal of Fe_2O_3 with and without PBCs for 5 ps. Figure 3.11 shows the single crystalline Fe_2O_3 before equilibration (Figure 3.11 (a)), after equilibration with PBCs imposed (Figure 3.11 (b)), and after equilibration with no PBCs imposed and cluster conditions enforced (Figure 3.11 (c)).

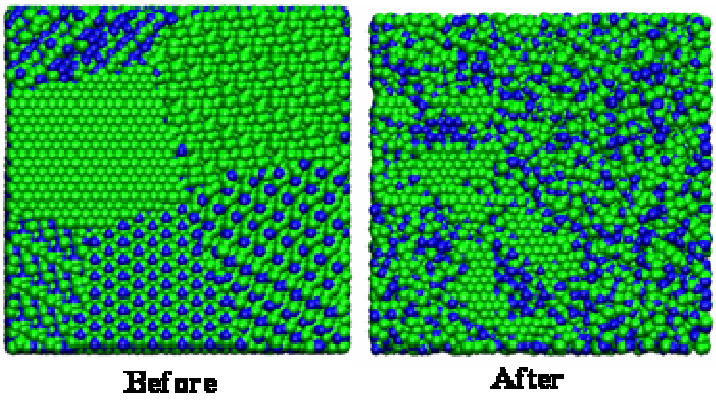

(a)

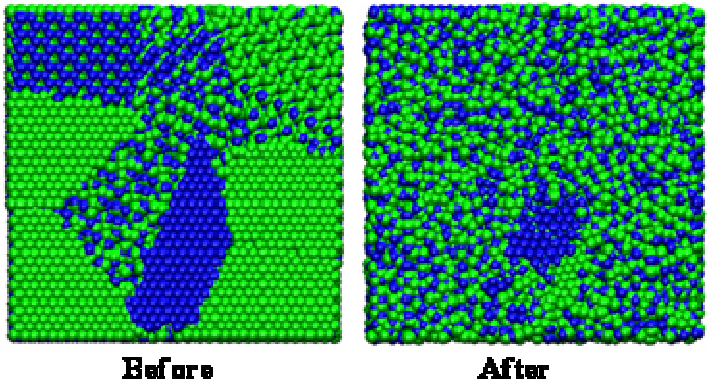

(b)

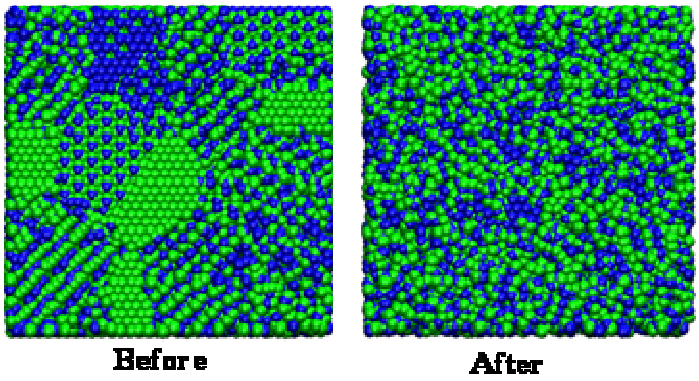

(c)

Figure 3.10 A section of polycrystalline Fe_2O_3 with grain size (a) 7.2 nm, (b) 4.7 nm, and (c) 3.9 nm before and after MD equilibration

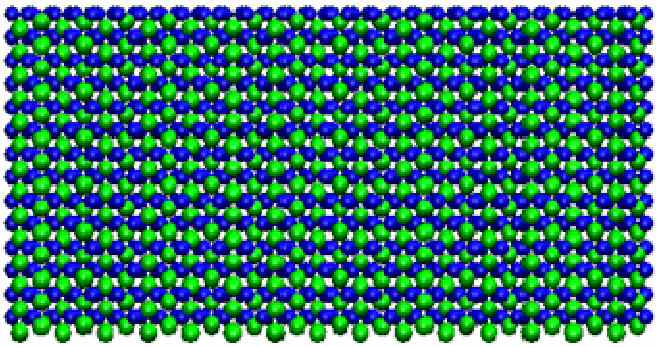

(a)

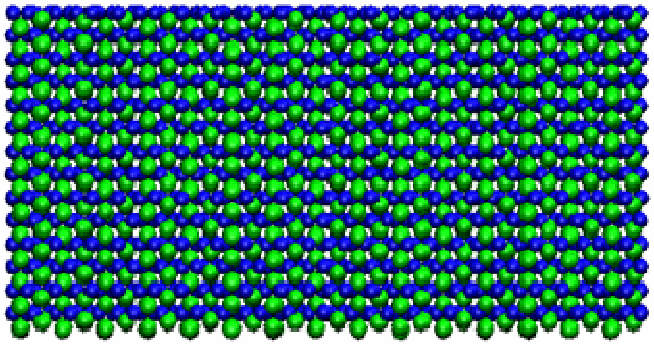

(b)

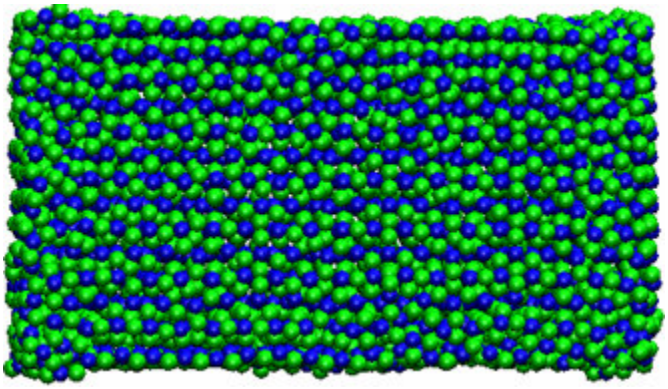

(c)

Figure 3.11 Single Crystal Fe_2O_3, (a) before equilibration, (b) after equilibration with periodic boundary conditions imposed, and (c) after equilibration as a cluster

As shown, in the single crystalline setting with or without the PBCs imposed (barring surface reconstruction in the cluster in Figure 3.11 (c)), the structural order is the same as in the non-equilibrated single crystal. This observation verifies that the potential works for Fe_2O_3 single crystal as a bulk with PBCs imposed or as a cluster without PBCs imposed. Another important question is whether there is a large pressure in polycrystalline Fe_2O_3 due to unphysical position of atoms in grain boundaries that causes the nanocrystalline structure to convert to an amorphous one? In order to answer this question, the pressure during equilibration of PHt1, PHt2, and PHt3 is compared with the pressure during equilibration of single crystalline Fe_2O_3 in the bulk and cluster settings, see Figure 3.12 (a). The pressure during equilibration of PHt1, PHt2, and PHt3 is comparable to that observed during equilibration of the single crystalline Fe_2O_3 in the periodic and cluster settings indicating that the potential is indeed working correctly. In order to investigate that whether unphysical energy of the atoms lying very close together along grain boundaries is causing such structural disorder, the time-history of the pressures during MD equilibration of nanocrystalline Fe_2O_3 (PHt1) when the number of atoms along the grain boundaries is higher (150393) or lower (84723) from the current value (93390) are compared in Figure 3.12 (b). The decrease in the number of atoms along grain boundaries doesn't affect the pressure during equilibration. However, an increase causes pressure to rise by the two orders of magnitude. This verifies that the current nanocrystalline Fe_2O_3 structures have an optimum number of atoms along the grain boundaries. Another important conclusion is that the grain boundary atoms play a very strong role in the overall virial pressure of the structure. This can be attributed to strong electrostatic forces among atoms along grain boundaries.

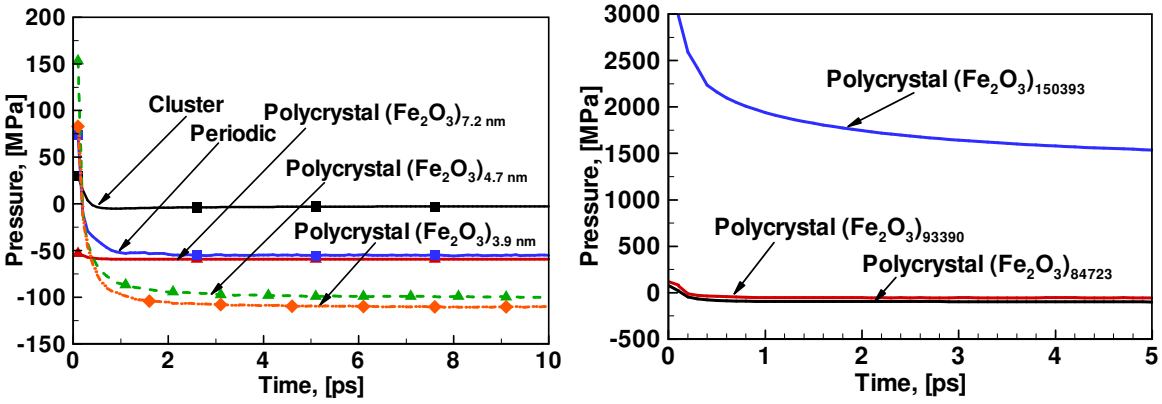

(a) (b)

Figure 3.12 (a) Time history of the pressure during equilibration of Fe_2O_3 in various crystalline settings and (b) time history of pressure during MD equilibration of 7.2 nm grain size Fe_2O_3 nanocrystalline structure with different number of atoms along grain boundaries

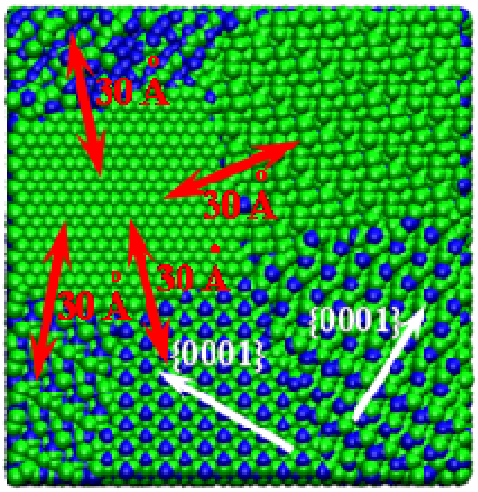

Figure 3.13 an illustration of the effective range of electrostatic interaction along grain interfaces in nanocrystalline Fe_2O_3 with the average grain size 7.2 nm (red arrows signify the effective range of electrostatic interaction along grain boundaries; white arrows signify crystalline orientation)

Electrostatic forces in a bulk ionic material do not converge as a function of the interatomic distance. However, research has shown that beyond a certain cutoff radius it

is possible to neglect interatomic interactions, Wolf (1992). The effective value of the corresponding cutoff distance is approximately 30 Å. For smaller distances between charged atoms the electrostatic forces are very strong. However, as the distance between charged atoms increases, the force between them dies out as r^{-5}, cf. Wolf (1992). Figure 3.13 compares the effective cutoff distance along grain boundaries of PHt1. As shown, the effective electrostatic force along the grain boundary covers entire grain at the length scale of the order of 7.2 nm. This results in strong inter-granular forces in grains which are oriented in different directions. The change in structural order, therefore, is not limited to the grain boundary atoms. An amorphous structural order emerges from strong intermixing that follows strong inter-granular forces.

In order to analyze the structural order in nanocrystalline Fe_2O_3 in more detail, the Fe-Fe, Fe-O, and O-O partial RDFs for PHt1 before and after the equilibration are plotted in Figure 3.14 (a), (b), and (c), respectively. The peaks denoting the crystalline order in PHt1 disappear after equilibration, resulting in partial RDFs with amorphous characteristics. Figure 3.14 (d) shows the total Fe_2O_3 RDF for PHt1 obtained by summing up the partial Fe-Fe, Fe-O, and O-O RDFs. The total Fe_2O_3 RDF also shows the change in the structural order of PHt1 from crystalline to amorphous. An important conclusion that can be drawn form Figure 3.14 is that the total Fe_2O_3 RDF is a good indicator of the structural order in PHt1 before as well as after the equilibration. In the following and in the next chapters the total Fe_2O_3 RDF is used to identify the structural order instead of the partial Fe-Fe, Fe-O, and O-O RDFs. In Figure 3.15, the total Fe_2O_3 RDFs for PHt1, PHt2, and PHt3 after the equilibration are compared with the total RDFs for Fe_2O_3 with grain

size 3-9 nm in a Fe_2O_3-SiO_2 sol-gel nanocomposite developed by Casula et al. (2001) and Cannas et al. (2004) in 3 different types of structural settings, (A and B are variations of sol-gel composites and C is obtained after mechanical mixing). The lengthscales in both plots are similar. Both plots show amorphous characteristics for Fe_2O_3 at the similar lengthscales. It can be safely concluded that at the lengthscale of this study, Fe_2O_3 in polycrystalline setting has amorphous structural order.

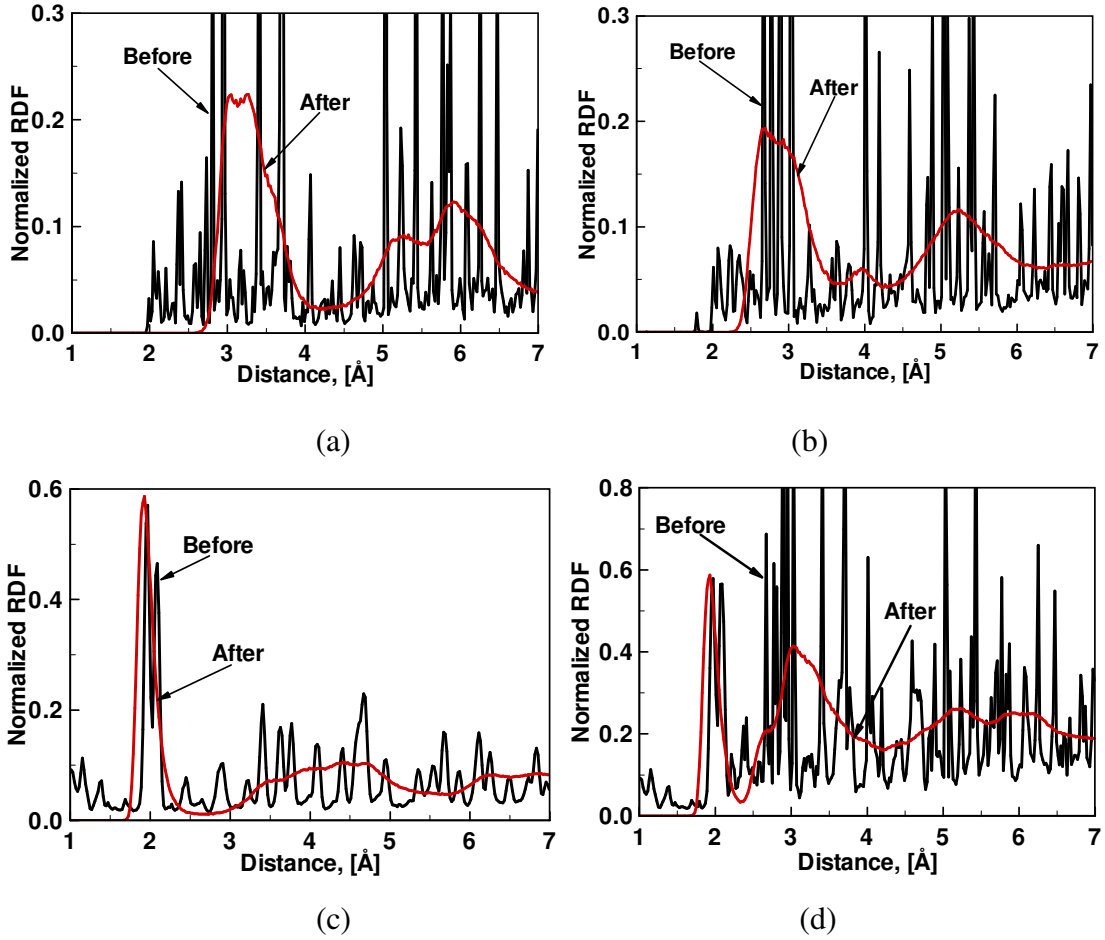

Figure 3.14 (a) The Fe-Fe, (b) the O-O, (c) the Fe-O, and (d) the total Fe_2O_3 RDF for nanocrystalline Fe_2O_3 with grain size 7.2 nm before and after the MD equilibration

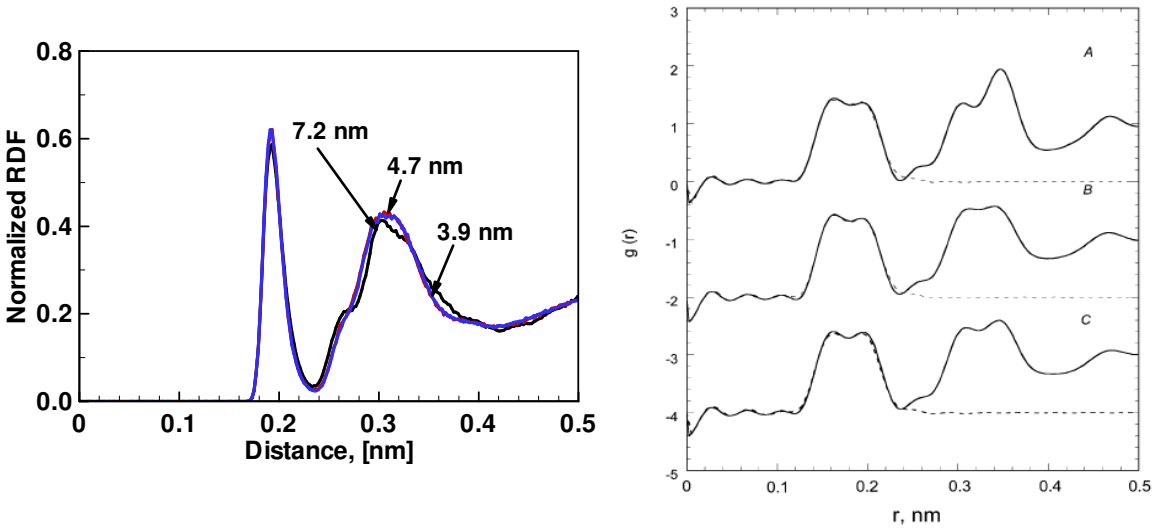

(a) (b)

Figure 3.15 (a) Total Fe_2O_3 RDFs for nanocrystalline Fe_2O_3 with all grain sizes and (b) Total Fe_2O_3 RDFs for nanocrystalline Fe_2O_3 in the work of Cannas et al. (2004) for 3 different types (A, B, C) of samples

Figure 3.16 and Figure 3.17 show the partial Al-Al RDFs (Figure 3.16 (a) and Figure 3.17 (a)) and the total Fe_2O_3 RDFs (Figure 3.16 (b) and Figure 3.17 (b)) for NCP641, NCP642, NCP643, NCP461, NCP462, and NCP463. As shown, the partial Al-Al RDFs in both figures have crystalline characteristics similar to that observed in the case of PAl1, PAl2, and PAl3. The total Fe_2O_3 RDFs in both the figures have amorphous characteristics similar to that observed in the case of PHt1, PHt2, and PHt3. The peaks of partial Al-Al RDFs in NCP64 for a particular grain size are higher than that of partial Al-Al RDFs in NCP46 for the same grain size. This indicates that the fraction of Al atoms in defects and grain boundaries increases with increase in the Fe_2O_3 volume fraction. The interfacial activity along Al and Fe_2O_3 interfaces is the primary reason. Increased interfacial activity at the Al and Fe_2O_3 interfaces is expected to contribute significantly to the deformation mechanisms in the composites.

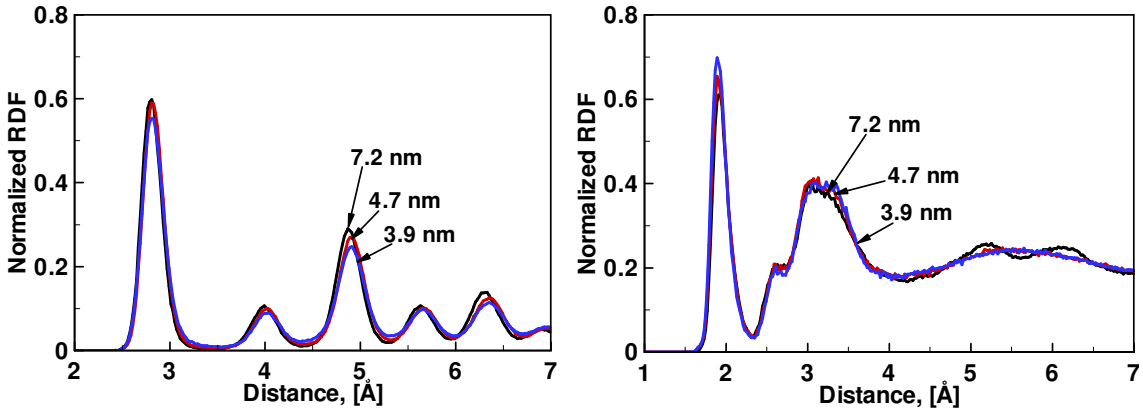

Figure 3.16 (a) The partial Al-Al RDFs and (b) the total Fe_2O_3 RDFs for 60%Al+40%Fe_2O_3 with different grain sizes

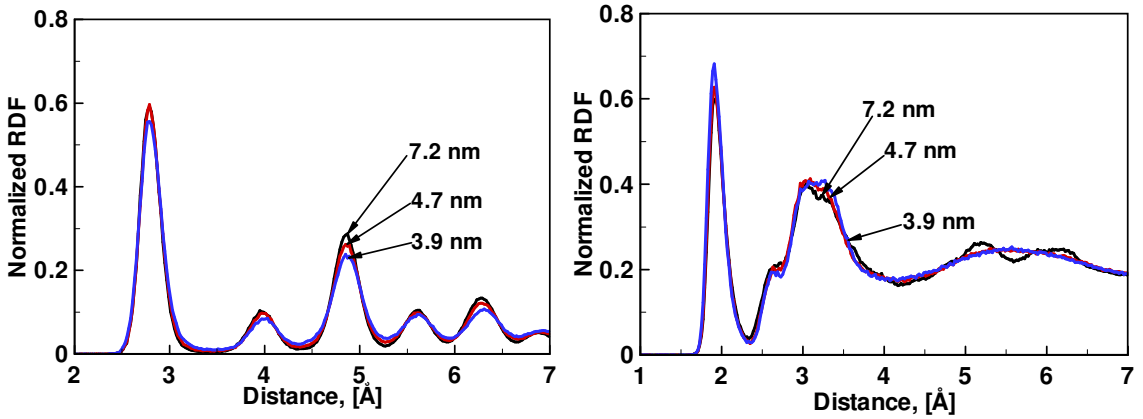

Figure 3.17 (a) The partial Al-Al RDFs and (b) the total Fe_2O_3 RDFs for 40%Al+60%Fe_2O_3 with different grain sizes

Figure 3.18 shows the nanocrystalline structure set after equilibration. Chapter 4 presents the analyses of quasistatic mechanical deformation of these samples. The next section describes the algorithm used to carry out the calculations.

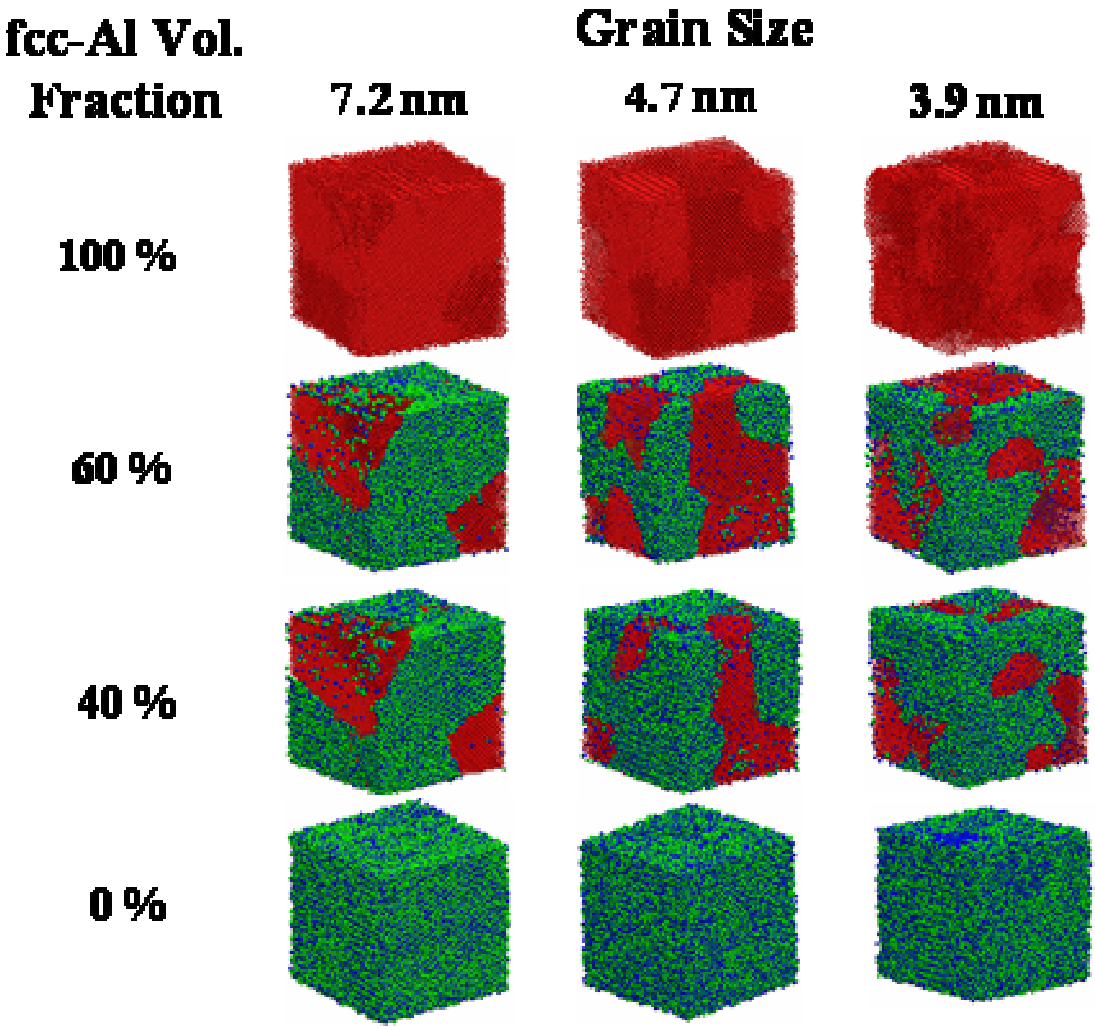

Figure 3.18 Set of nanocrystalline structures used during simulations after the MD equilibration

3.5 Algorithm for the Calculation of Quasi-static Strength

MD simulations are commonly performed in uniaxial tension. Schiøtz et al. (1998) and Schiøtz et al. (1999) carried out MD simulations of the quasistatic mechanical deformation by stretching nanocrystalline samples in one direction. The deformation strain was calculated by recording the position of individual atoms. The average stress in

a sample as a function of the amount of deformation was calculated in order to obtain the stress-strain relations. We apply a modification to this method during simulations. Another alternative is to use the method of Van Swygenhoven and Caro (1997) who recorded strain-time curves at several values of applied uniaxial stress in the range 1–3 Giga Pascal (GPa), and at different temperatures between 300 K and 500 K. Spearot et al. (2005) have used both methods and found that the modified Schiøtz et al. (1999) method explained in the following works better by controlling the strains and thereby simulating a controlled displacement test. In the method an algorithm based on a combination of the algorithms for NPT and NVT ensembles is used. In this algorithm stretching at a specified rate is carried out on the specified MD structural supercell using a modification of Melchionna et al. (1993) NPT equations of motion, cf. Spearot et al. (2005). The Melchionna et al. (1993) algorithm for isotropic fluctuations of an MD supercell is specified as;

$$\frac{d\boldsymbol{r}(t)}{dt} = \boldsymbol{v}(t) + \eta\left(\boldsymbol{r}(t) - \boldsymbol{R_0}\right), \tag{3.3}$$

$$\frac{d\boldsymbol{v}(t)}{dt} = \frac{\boldsymbol{f}(t)}{m} - \left[\chi(t) + \eta(t)\right]\boldsymbol{v}(t), \tag{3.4}$$

$$\frac{d\chi(t)}{dt} = \frac{1}{\tau_T^2}\left(\frac{T}{T_{ext}} - 1\right), \tag{3.5}$$

$$\frac{d\eta(t)}{dt} = \frac{1}{Nk_B T_{ext}\tau_P^2} V(t)\left(P - P_{ext}\right), \tag{3.6}$$

and,

$$\frac{dV(t)}{dt} = 3\eta(t)V(t). \tag{3.7}$$

Here, η is the barostat friction coefficient, $\boldsymbol{R_0}$ is the system center of mass, τ_P is a specified time constant for pressure fluctuations, P is the instantaneous pressure and V is the system volume. In Spearot et al. (2005), the Eq. (3.6) is modified as:

$$\frac{d\eta(t)}{dt} = \frac{1}{Nk_B T_{ext}\tau_P^2} V(t)(P - P_{ext}) - \gamma\eta \cdot \tag{3.8}$$

γ acts here as a damping coefficient to reduce the fluctuations in pressure during application of the NPT algorithm. The algorithm is based on alternative steps of equilibration and stretching in order to simulate a quasistatic deformation. The system is initially equilibrated at a specified temperature for a given period of time. After equilibration, the computational cell is stretched in the specified direction using the values of η=0.1 and -0.1 ps^{-1} for tension and compression, respectively.

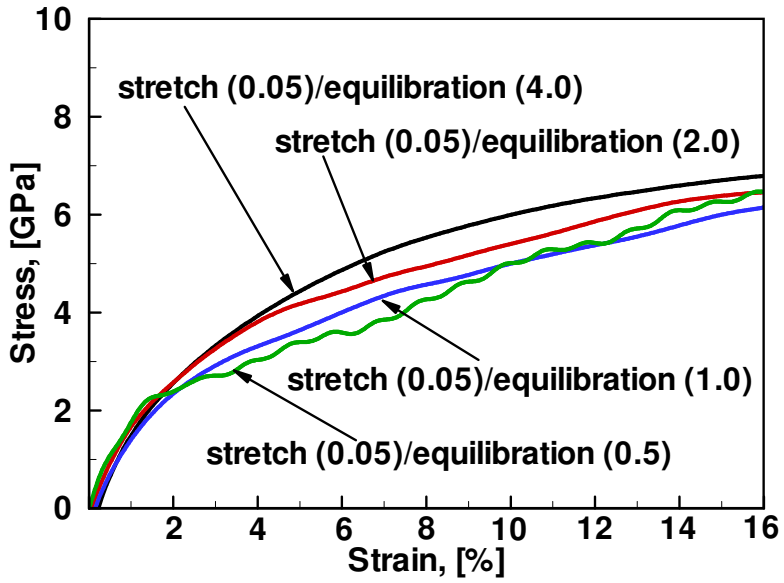

Figure 3.19 A comparison of the stress-strain relations with fixed stretching time period and different equilibration time periods

The values of γ=0.5 and P_{ext}=1 atmosphere (atm) are used during simulations. T_{ext} is set at 300 K during simulations. It is possible that the period of equilibration in between the steps of stretching may affect the stress-strain responses. In order to choose the right time period for equilibration, quasistatic stress-strain curves for a sample polycrystalline material were recorded for four different equilibration periods viz. 0.5 ps, 1.0 ps, 2.0 ps and 4.0 ps with the same stretching period of 0.05 ps. Fluctuations in the recorded stress values were found to be within ±5% of the mean stress values at all the strains, see Figure 3.19. Considering the computational costs involved, the equilibration time period of 2.0 ps was chosen for carrying out the MD simulations. During MD simulations PBCs are applied in all directions. It is assumed that by applying PBCs it is possible to simulate a 3-D polycrystalline material with grain sizes following the specified grain-size distribution. Smaller number of grains compared with the real samples may induce anisotropy in the measured properties. Van Swygenhoven and Caro (1998) measured elastic and plastic properties along three cubic axes of trial Voronoi tessellated nanocrystalline material samples. They concluded that fluctuations in the stress-strain responses exist but are not significant. Therefore, anisotropy in directionality of loading is not considered during simulations. By this it is presumed that the simulation results are reflective of the actual physics of the deformation in nanocrystalline materials. Thereby, the conclusions drawn should be applicable to actual laboratory test specimens. It is also appropriate to point out that the scope of this research is limited to the initial loading of the nanocrystalline structures. Unloading, though interesting, is not considered during simulations. Zimmerman et al. (2004) have shown that virial stress formulation of Zhou (2003) can be considered as a limiting case of fully dynamic case of Hardy (1981)

formalism of atomic stress. Therefore, for stress calculations we use virial stress methodology of Zhou (2003) and Zhou and McDowell (2002) during quasistatic deformation simulations and Hardy's formalism, see Zimmerman et al. (2004), during dynamic shock simulations. Stress calculations are carried out on the current volume and therefore correspond to *true stress*. The strains, accordingly, are calculated to correspond to the current volume and are therefore *true strains*. The important framework steps for the quasistatic strength analyses are:

1. Equilibrate the nanocrystalline structures at 300 K for 10 ps,
2. Stretch/Compress the nanocrystalline structures using the NPT-NVT algorithm by ±20 % and obtain average stress-strain relations, and
3. Use VMD based structural defect visualization scheme with the RDFs and the stress-strain relations to analyze the mechanical behavior of nanocrystalline structures.

The next section presents the approach used for analyzing the shock wave propagation.

3.6 Shock Wave Propagation Algorithm for MD Shock Simulations

An approximate but desirably complete description of the response of a material to shock loading can be obtained by combining the available continuum theories, the experimental tools, and the meso-scale analysis capability, see for example Baer (2000), Do and Benson (2001), Baer and Trott (2002), and Baer (2002). However, MD shock simulations on single crystalline supercells are important to understand the effect of shock on defect propagation and its relation with the plate impact velocity and shock-front velocity

relationships. MD simulations of shock wave propagation must follow certain limitations. In order to minimize edge effects and thereby model an infinite plate of material, MD shock wave simulations have to use PBCs transverse to the shock wave propagation direction. Therefore, in a finite MD system with a small cross-section, stacking faults appear as a series of 'bands' at an angle to the shock wave propagation direction, cf. Straub et al. (1979) and Wagner et al. (1992). The spacing of the stacking fault bands doubles when the cross-sectional dimension doubles.

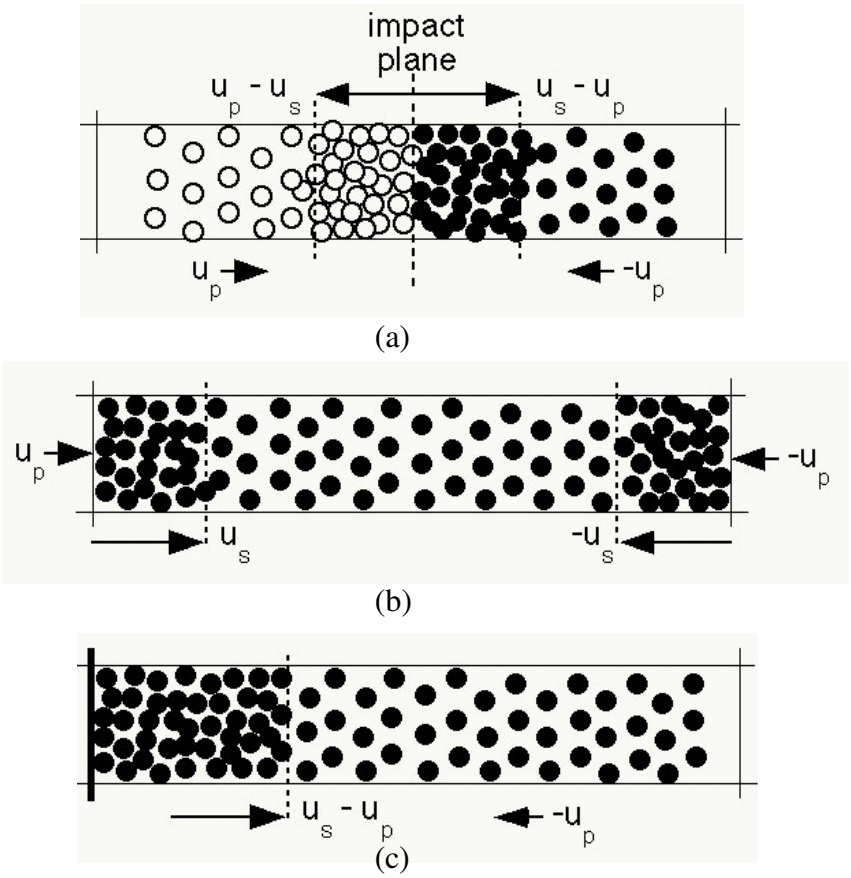

Figure 3.20 Illustration of three primary methods for generating shock waves: (a) symmetric impact, (b) shrinking periodic boundaries, and (c) momentum mirror (piston velocity u_p, shock velocity u_s), cf. Holian et al. (1999).

There are three primary schemes to generate shock waves in MD simulations, cf. Tsai and Trevino (1981), Rice et al. (1996), Holian and Lomdahl (1998), Holian et al. (1999), and Zhakhovskii et al. (1999): 1. symmetric impact, 2. shrinking *PBC*, and 3. momentum mirror, see Figure 3.20. Out of these schemes, the momentum mirror method is the simplest, and for solids, it's foolproof, particularly when phase transformations or plasticity give rise to splitting in the shock wave structure, cf. Holian and Lomdahl (1998) and Zybin et al. (2002). Accordingly, the momentum mirror method is chosen to generate shock waves in the current research. Choice of the momentum mirror method is also motivated by nonstationary character of shock waves at moderate shock loading, which arises because of a split two-wave (elastic-plastic) structure of the shock waves. In the momentum mirror method, an atomistic shock wave in a direction can be generated by imposing a combination of the initial and boundary conditions. The boundary conditions are: a specularly reflecting "momentum mirror", or a stationary piston at the origin (a particle's collision with the mirror is detected when its X-position at the end of a time step is found to be negative, whereupon the X-velocity is reversed, and the X-coordinate is replaced by its absolute value); and transverse (Y and Z) PBCs (image particles enter with the same velocity as the exiting particle, but at the opposite "wall"). Initial conditions are: particle positions and initial Maxwell–Boltzmann distribution velocities corresponding to temperature T_0 and augmented by a drift velocity $-U_P$ toward the mirror. The corresponding atomic ensemble has constant energy. However, the volume is not constant and therefore it cannot be classified as a canonical ensemble.

As soon as the "target" material collides with the stationary, infinitely smooth piston, a shock wave begins moving to the right (positive X direction) at the velocity U_S-U_P. By Galilean invariance, this is equivalent to a piston moving at the velocity U_P into a stationary material, with the shock wave moving out in front of the piston at the shock-front velocity U_S. For the purposes of visualization, the former frame of reference has advantage that the shocked material is now stagnated against the immobile piston with the average velocity equal to zero. However, a possibility exists that material near the mirror can heat up in a way that is distinct from the symmetric impact method and the shrinking PBCs method. For this reason, in computing averages over the shocked state, material near the mirror is disregarded in the current research.

Figure 3.21 shows {100} Al single crystal before and after the shock wave generation at U_P=1.5km/s. Al (111) stacking faults after the generation of shock wave are apparent from the figure. Apart from the initial and boundary conditions, only other input to the MD simulations of a shock wave is the interaction potential between atoms. In the case of the EAM potentials for metals, besides elastic constants, an additional defect or surface property such as the stacking fault energy must be incorporated into the fitting procedure, cf. Holian et al. (1991) and Mishin et al. (2001). The potential developed in the current research includes these characteristics. Accordingly, it is assumed that reliable results are obtained after shock wave propagation analyses with the potential. The shock wave propagation simulations are carried out in <100>, <110>, and <111> oriented single crystalline Al, in <0001> oriented single crystalline α-Fe_2O_3, and through an interface between {100} surface of *fcc*-Al and {0001} surface of Fe-terminated α-Fe_2O_3. The

single crystals are generated as supercells by cutting the bulk crystals along specified orientations. Size of the single crystals as well as of the interface structure for the shock wave propagation analyses is kept at 15 nm × 6 nm × 6 nm because of the computational limitations. As pointed out earlier, this cross-section (6 nm × 6 nm) and length (15 nm) combination is found to be the best fit to obtain a planar steady shock wave while keeping in tune with the computational requirements.

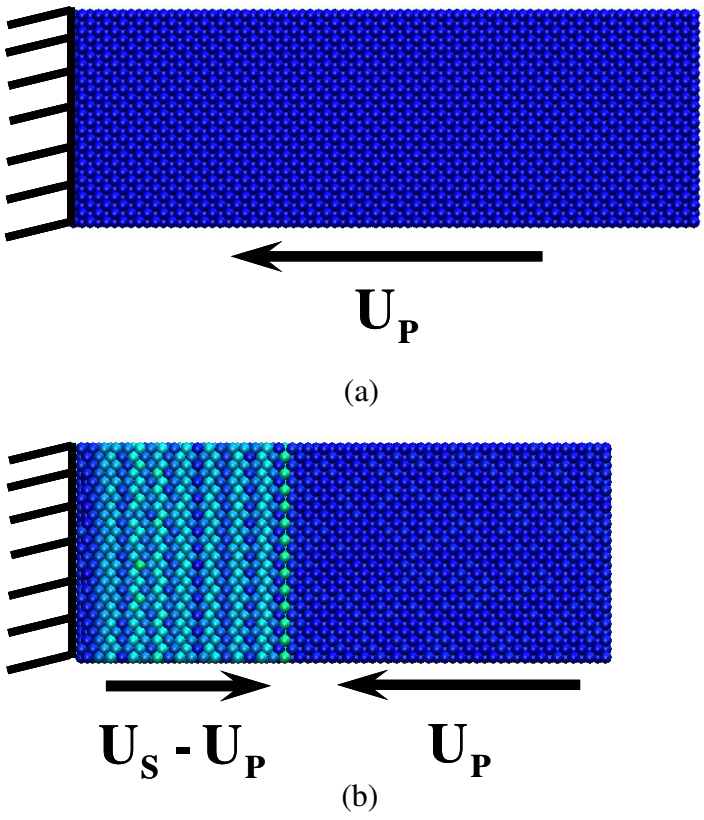

Figure 3.21 Schematic for shock-wave front identification using the slip-vector approach (a) undisturbed crystal and (b) crystal with shock wave propagating at the shock-front velocity U_S

At the sizescales of MD simulations, only the shock wave propagation with shock-front widths of the order of nanometers can be analyzed. Correspondingly, MD shock wave

propagation analyses have to carried out at U_P values of the order of km/sec. In the current research, eight different U_P values ranging from 0.5 km/sec to 4 km/sec are chosen for analyses. The steps for the shock wave propagation analyses are:

1. Obtain the equilibrated single crystals with various orientations and their nano-interfaces,
2. Subject all the single crystalline structures and the nano-interfaces to shock at U_P values ranging from 0.5 km/sec to 4 km/sec for obtaining the U_S-U_P relationships,
3. Use VMD based visualizations with the statistical mechanical characterizations, and with the structural analyses using RDFs to investigate the dynamic structural deformation in all structures. For interfaces, characterize the changes in kinetic energy, potential energy, temperature, pressure, and mass velocity after the passage of shock wave through the interface for obtaining the reactive structural transformation information as a function of applied shock loading.

It is important to analyze the structural order at the interface of Al and Fe_2O_3 before carrying out the shock wave propagation analyses. The next section presents these analyses.

3.7 Equilibrium Structure of an Interface between *fcc*-Al and α-Fe_2O_3 lattices

Shock wave propagation analyses through the interfaces of *fcc*-Al and α-Fe_2O_3 are useful for analyzing the reactive structural transformation as a function of shock loading.

Because of complex crystal structure of α-Fe_2O_3, numerous *fcc*-Al and α-Fe_2O_3 interfacial constructions are possible. Without loss of generality, we focus on analyzing an interface between{100} surface of Al and Fe terminated {0001} surface of Fe_2O_3 for reaction initiation. In order to obtain the interface, the rhombohedral primitive unit cell of α-Fe_2O_3 is converted into a hexagonal unit cell using the procedure specified by Rollman et al. (2004). In this procedure three rhombohedral primitive unit cells of Fe_2O_3 combine to form a hexagonal unit cell. A hexagonal supercell is formed by translating the hexagonal unit cell along all Cartesian axes. The hexagonal supercell is then cut to obtain a neutral rectangular α-Fe_2O_3 supercell with {0001} surface along the longitudinal axis. The supercell is then geometrically placed next to the {100} surface of *fcc*-Al supercell in order to obtain the interfacial supercell. From now onwards, the interfacial supercell is denoted as *InterfaceS.* In order to obtain the natural position of atoms, *InterfaceS* is subjected to room temperature (300K) MD equilibration for 10 ps. PBCs are imposed in the transverse direction during equilibration. This configuration resembles thin films of Al and Fe_2O_3 in contact with each other. During MD equilibration structural reconfiguration at the interface takes place. As a result of reconfiguration, the potential energy of the interfacial region is converted into the kinetic energy. Since temperature is constant, a part of the kinetic energy is dissipated in the temperature scaling process during MD equilibration. It is observed that the change in potential energy occurs for the initial 2 ps of equilibration. The MD equilibration, however, is carried out for a period of 10 ps to allow for proper annealing and relaxation of the interface. Figure 3.22 shows adjacent atomic planes of Al and Fe_2O_3 at the interface before and after the MD equilibration. From the viewgraphs, it is clear that there is a significant shift in the atomic

positions of Fe and O atoms. The shift in the position of Al atoms is comparatively insignificant. An accurate characterization of the interfacial structure requires more information. Therefore, *InterfaceS* is further subjected to structural analyses using partial Al-Al RDF, total Fe_2O_3 RDF, BDF, and average coordination number. The structural analyses are carried out for a range of interfacial widths in order to recognize the extent of the region at the interface that has structural order different from both the bulk Al as well as the bulk Fe_2O_3. Figure 3.23 (a) and (b) show the partial Al-Al RDF and the total Fe_2O_3 RDF, respectively, for *InterfaceS* at a range of interfacial widths. In Figure 3.23 (a), the first neigbor Al-Al peak is unchanged for interfacial widths of 30 Å and 20 Å. However, a shift in the Al-Al first neighbor peak is observed beginning with the interfacial width of 10 Å. For 8 Å and 6 Å interfacial widths, no shift in the first RDF peak is observed. In addition, for all interfacial widths the bond distance predicted by the second peak of the partial Al-Al RDF is the same. Similar features are observed by examining the total Fe_2O_3 RDF in Figure 3.23 (b). There is a shift in the bond length predicted by the first peak at 10 Å interfacial width. Further reducion in the interfacial width doesn't cause any change in the bond length predicted by the first peak. The long range order predicted by the secondary peaks of the RDF is the same in the case of the interfacial widths of 6 Å, 8 Å, and 10 Å. However, it differes from that in case of the interfacial widths of 20 Å, and 30 Å. From these observations it is clear that within the interfacial region with width of 10 Å on both sides of the inteface, the structural order differs from that in bulk. In addition, the change in the Al region is restricted to the nearest neighbor distance. This is possibly because of very small movement of Al atoms

at the interface compared to the movement of Fe and O atoms in Fe_2O_3. This is in agreement with the observations in Figure 3.22.

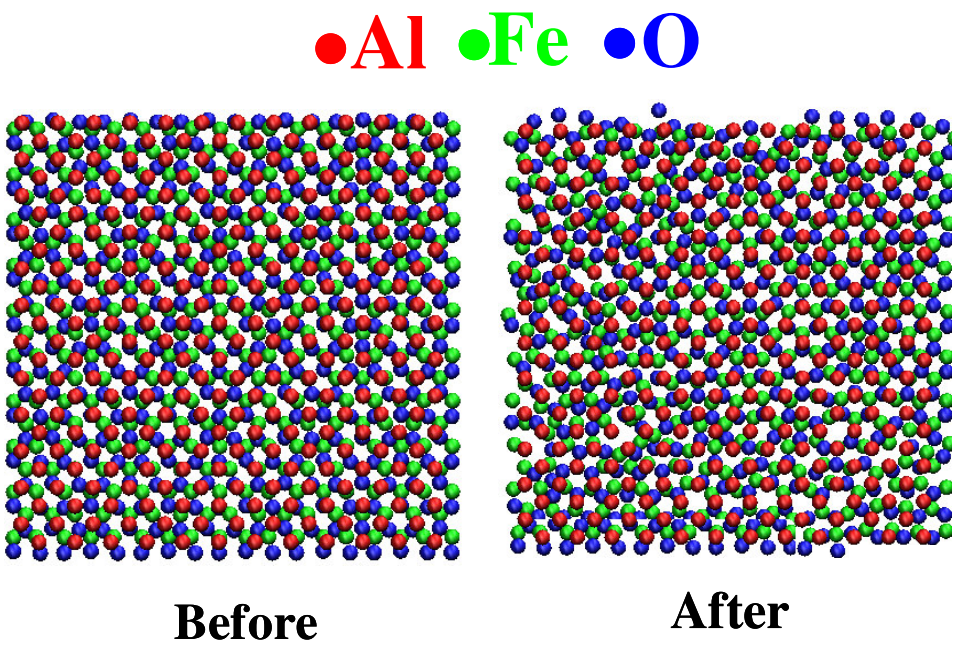

Figure 3.22 A comparison of the change in the structure of adjacent Al, Fe, and O planes in *InterfaceS* before and after the MD equilibration

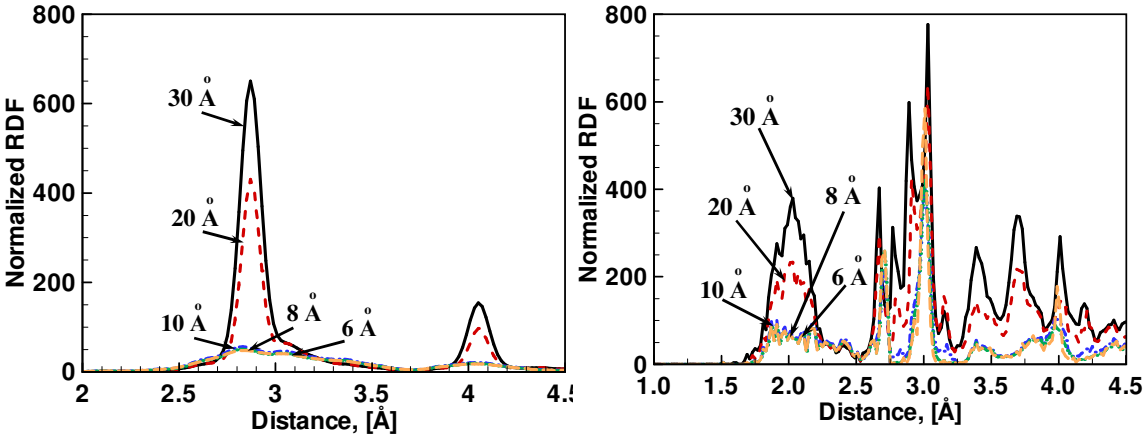

Figure 3.23 An illustration of the change in structural order of the interface as a function of interfacial width using (a) the partial Al-Al RDF and (b) the total Fe_2O_3 RDF

No experimental evidence of the interfacial width and the structural arrangement at the interface of Al and Fe_2O_3 is available. However, recently some metal-metal oxide interfaces have been studied using the density functional theory. In a study of {111} Cu-{0001} Al_2O_3 interfaces, Dehm et al. (1998) found that the change in the interfacial structure from the bulk is limited to an interfacial width of approximately 10 Å. Schweinfest et al. (1999) in their study of Al-$MgAl_2O_4$ interfaces also report an interface width of nearly 10 Å. In order to gain further insight into the structural order at the interface within the interfacial width of 10 Å, the short range structural information of the interface is compared with the reference first neighbor Fe-Al, Fe-O, Al-O, Fe-Fe, Al-Al, and O-O bond lengths and nearest neighbor bond angle values for *fcc*-Al, *bcc*-Fe, α-Fe_2O_3, and α-Al_2O_3, see Figure 3.24 (a) and (b).

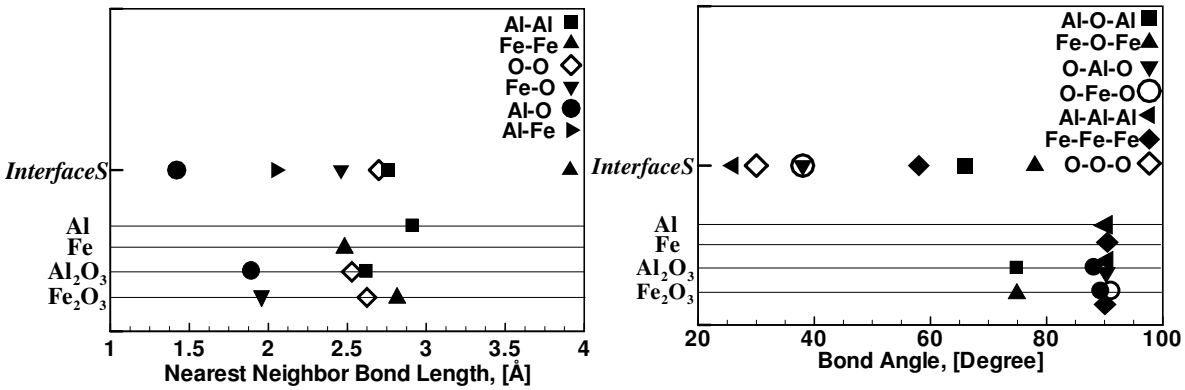

Figure 3.24 A comparison of (a) bond lengths and (b) bond angles for Al_xFe_y, Al_pO_q, and Fe_lO_m interfacial structures with the reference single crystalline values

An examination of Figure 3.24 (a) reveals that the interface has the Al-Al bond length close to the metallic *fcc*-Al value. The Al-Fe bond length is close to the first neighbor distance value in the case of B2 Fe-Al. In addition, the interface structure has the Al-O

bond length closer to the theoretical Al-O reference value. The O-O bond length, however, is close to the reference Fe_2O_3 value. The Fe-Fe bond length shows a big deviation from the reference α-Fe_2O_3 value of 2.81 Å. The Fe-O bond length shows similar shift as in the case of the Fe-Fe bond length indicating that the Fe-Fe bond arrangement is changing/shifting from its original position in α-Fe_2O_3. A combination of these observations suggests that the interface has strong presence of Fe_xAl_y and Al_pO_q phase constructions.

To consolidate the observations made using the RDFs, the BDFs at the interface were calculated. As pointed out earlier, the peak of a BDF denotes the primary bond angle. Figure 3.24 (b) plots the angle corresponding to the peak value of the BDF plots for Al-Al-Al, Fe-Fe-Fe, Al-O-Al, O-Al-O, Fe-O-Fe, O-Fe-O, and O-O-O bond-angles. For the purpose of comparison, Figure 3.24 (b) also shows the reference values of the same angles in *fcc*-Al, *bcc*-Fe, α-Fe_2O_3, and α-Al_2O_3 structures. Investigations on bond angles for a possible Fe_xAl_y phase in the interface cannot be carried out since the reference angle values for the same are not available. Al-O-Al and Fe-O-Fe angles are found to have a value near to the reference value of 74^o. However, Al-Al-Al, O-Al-O, O-Fe-O, O-O-O and Fe-Fe-Fe bond angles show a big shift from the reference values for the <0001> oriented α-Fe_2O_3 and α-Al_2O_3. Based on a large shift in the Al-Al-Al angle, the possibility of metallic Al at the interface is ruled out. No definitive conclusion regarding the exact molecular construction at the interface can be drawn from the values of the angles. Since the structure of α-Fe_2O_3 and α-Al_2O_3 is based on a rhombohedral primitive cell, it is possible that the angle values correspond to some other orientation.

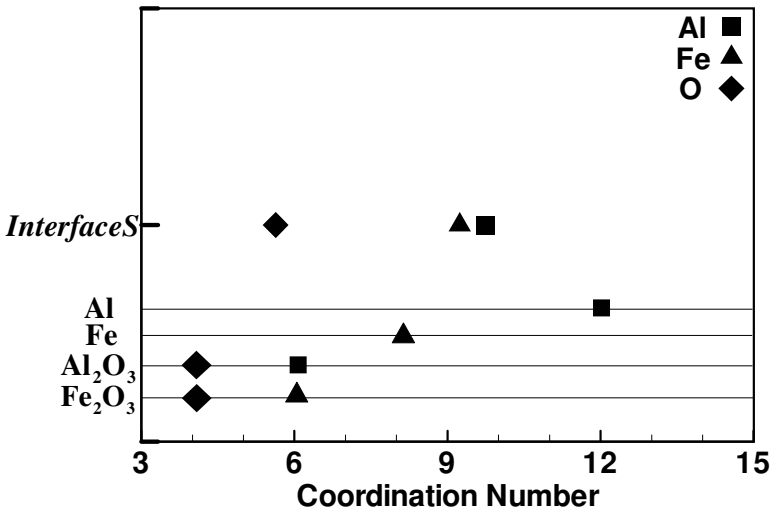

Figure 3.25 A comparison of coordination numbers at the interface with those for the single-crystalline components

In order to support the observations made using RDFs, first neighbor coordination numbers for Al, Fe, and O are plotted in Figure 3.25. The figure also shows a comparison of these values with the reference coordination values in *fcc*-Al, *bcc*-Fe, α-Fe_2O_3, and α-Al_2O_3. The coordination numbers for all three species show a shift from their respective original values before equilibration. The Al coordination number decreases from the metallic *fcc*-Al value of 12 to 10. However, the coordination numbers for Fe and O increase from their reference values of 6 and 4, respectively. The value of the coordination number for Fe after equilibration is found to be close to the bcc-Fe value of 8. The shift in the coordination number for O is comparatively lower. A combination of the observations from Figure 3.24 and Figure 3.25 suggests that the interface has stronger presence of a combination of Fe_xAl_y and Al_pO_q phases compared to the other phases.

Intuitively, the above conclusion is obvious, given that the potential is fitted to a combination of the properties of four different crystal systems. An experimental verification of this observation is therefore necessary. No standard experimental or quantum mechanical account of *fcc*-Al+α-Fe_2O_3 interfacial structures is available. An experimental comparison of the observed interfacial structure can be made with the XRD data values from literature on mechanically alloyed Al+Fe_2O_3 composites, see Goya and Rechenberg (2000) and Lee et al. (2004), in terms of the nearest neighbor bond length values at the interface. Goya and Rechenberg (2000) obtained a $Fe_{100-x}Al_x$ alloy through mechanical alloying of Al+Fe_2O_3 in Ar atmosphere. They also reported that with Al_2O_3 as the diluent, the reduction of α-Fe_2O_3 by Al in an Ar atmosphere yields a mixture of α-Fe, Fe-Al alloy, and $FeAl_2O_4$ phases. Lee et al. (2004) analyzed nanocomposite formation of Fe_2O_3-Al metal-metal oxide systems by mechanical alloying. It was found that nanocomposite powders with Al_2O_3 dispersed in Fe matrix with nano-sized grains are obtained by mechanical alloying Fe_2O_3 with Al.

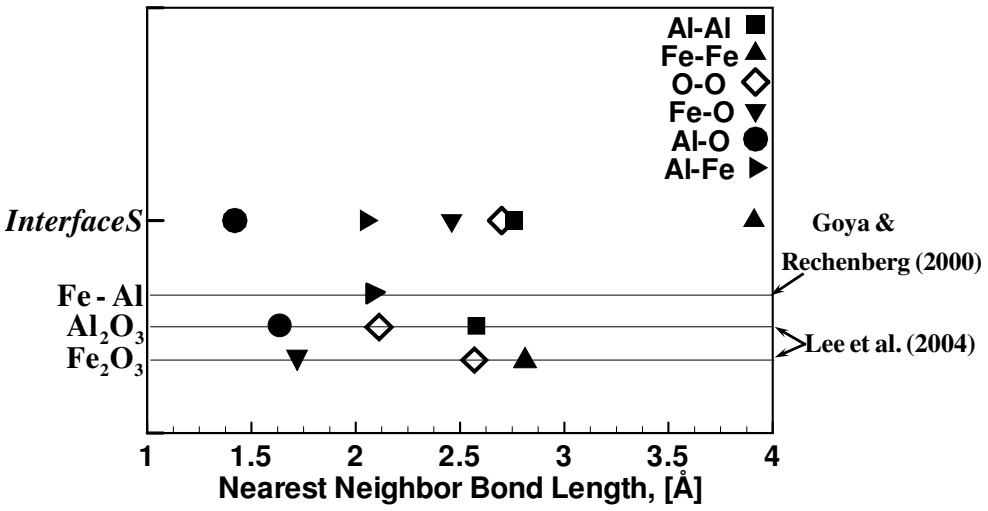

Figure 3.26 A comparison of nearest neighbor bond-length values with that reported in literature using XRD data

Figure 3.26 compares the Al-Al, Fe-Fe, Al-Fe, Al-O, Fe-O, and O-O bond length data from the analyses of Goya and Rechenberg (2000) and Lee et al. (2004) with the first neighbor bond length data from MD simulations. The bond lengths from the reported data by Goya and Rechenberg (2000) and Lee et al. (2004) are obtained by analyzing the orientation of the hexagonal crystals corresponding to the peaks in the XRD data. As shown, the Fe-Al bond length for the interface lies close to experimental Fe_xAl_y value. In addition, the Al-O and Al-Al bond length values lie close to experimental Al_2O_3 values. However, a big deviation in the Fe-Fe and Fe-O values from the corresponding experimental values is observed. These observations further suggest that the structure of the interface has strong presence of Fe_xAl_y and Al_pO_q phases. It should be remembered that the interface still has significant crystallinity. The focus of the shock wave propagation investigation in the chapter 5 is on measuring the change in the structural order at the interface as a function of the U_P values as one of the measures of the reactive structural transformation.

3.8 Chapter Summary and Insights

This chapter focused on the development of a MD framework for carrying out the nanomechanical deformation analyses under quasistatic and shock loadings. The description focused on important components of the framework such as a scalable parallel MD code, a visualization scheme, an algorithm for generation of the nanocrystalline composites, and algorithms for carrying out the quasistatic and shock simulations. The high level programming involved more than 30000 lines. A substantial

modification to two high level programming language codes GULP 1.3 and DLPOLY 2.14 was carried out. In addition, a separate program for generating nanocrystalline composites was developed. DLPOLY 2.14 was standardized to carry out MD simulations of atomic ensembles with upto 100000 atoms. The accessible lengthscales and timescales for the mechanical behavior analyses are of the order of 10 nm and 10 ps, respectively. The visualization scheme consists of using a combination of the slip-vector approach with the partial Al-Al RDF and the total Fe_2O_3 RDF. The Al+Fe_2O_3 nanocrystalline composites were generated along with nanocrystalline Al and Fe_2O_3 structures to conform to the log-normal grain size distribution with 10% standard deviation. After MD equilibration, the crystalline order of the Fe_2O_3 phase changes to an amorphous one in all the nanocrystalline structures. In contrast, there is an insignificant change in the crystallinity of the Al phase in all nanocrystalline structures after MD equilibration. Consequently, the Al+Fe_2O_3 nanocomposites have the quasi-crystalline structural order.

The algorithm for quasistatic strength calculations is based on a combination of the algorithms for the NVT and modified NPT ensembles. The shock simulations were standardized using the momentum mirror method based on constant energy non-equilibrium MD. For the purpose of the shock simulations three different orientations of single crystalline Al, one orientation of single crystalline Fe_2O_3, and an interface between the {100} surface of Al with the {0001} surface of Fe_2O_3 were chosen. Structural analyses of the interface after MD equilibration reveal a shift of the interface structure from pure *fcc*-Al+α-Fe_2O_3 construction to a construction in which Fe_xAl_y+Al_pO_q phases dominate. The width of the corresponding region is found to be approximately 10 Å.

These observations are in accordance with the experimental results. The following chapters report the results of the calculations carried out using the MD framework.

CHAPTER 4

MECHANICAL BEHAVIOR OF THE NANOCRYSTALLINE MATERIALS

This chapter presents analyses of the quasistatic deformation in nanocrystalline Al, nanocrystalline Fe_2O_3, and their composites. Simulations are carried out under tension as well as under compression for nanocrystalline Al and Fe_2O_3 and under compression for nanocrystalline Al+Fe_2O_3 composites at room temperature (300 K). Nanocrystalline structures with 3 different average grain sizes, viz., 3.9 nm, 4.7 nm, and 7.2 nm, are analyzed. The structures are generated using Voronoi tessellation with grain sizes following the log-normal grain size distribution. The analyses focus on the following tasks:

1. Investigation of relationships between the material constant values (Young's modulus and flow strength) and square root of the average grain sizes as the average grain size of a nanocrystalline material is varied;
2. Comparison of the strength values of the nanocrystalline structures with corresponding single crystalline values;
3. Analyses of the effect of nanoscopic lengthscale on the strengths of nanocrystalline structures;
4. Analyses of the effect of loading directionality (tension or compression) on the strength and deformation levels in nanocrystalline Al and Fe_2O_3;
5. Investigation of the atomistic mechanisms responsible for tension-compression strength and deformation asymmetry in nanocrystalline Al and Fe_2O_3;

6. Analyses of the effect of variations in the volume fractions of individual phases in a nanocrystalline composite on its compressive strength;
7. Comparison of the compressive deformation mechanisms in a nanocomposite and the deformation mechanisms in a single phase nanocrystalline material under compression; and
8. Investigation of a mathematical relationship to calculate the strength of a nanocomposite based on the summation of the strengths of the nanocrystalline structures of individual phases with similar morphology multiplied with their volume fraction values.

The next section provides an overview of the synthesis and the mechanical response characterization of nanocrystalline materials using analytical and experimental means. This is followed by a description of the current state of the research in the area of mechanical strength characterization of nanocrystalline materials using MD. The analyses of the quasistatic mechanical deformation in the current research are reported thereafter.

4.1 Nanocrystalline Material Systems

Nanocrystalline materials are defined as polycrystalline bulk materials with grain sizes in the nm range (less than 100 nm). A further classification into four different groups according to their dimensionality can be made: zero-dimensional atom clusters, one-dimensional modulated multilayers, two-dimensional ultrafine-grained overlayers, and three-dimensional nanocrystalline structures, cf. Siegel (1994a), see Figure 4.1 (a). Each

of the groups may contain crystalline, quasi-crystalline, and amorphous (nano-glasses) phases. They can be metals, inter-metallics, ceramics, and composites. Gleiter (2000) classifies nanocrystalline materials into twelve different groups according to the shape (dimensionality) of the constituting crystallites as well as according to the chemical composition of the constituent structural elements, see Figure 4.1 (b).

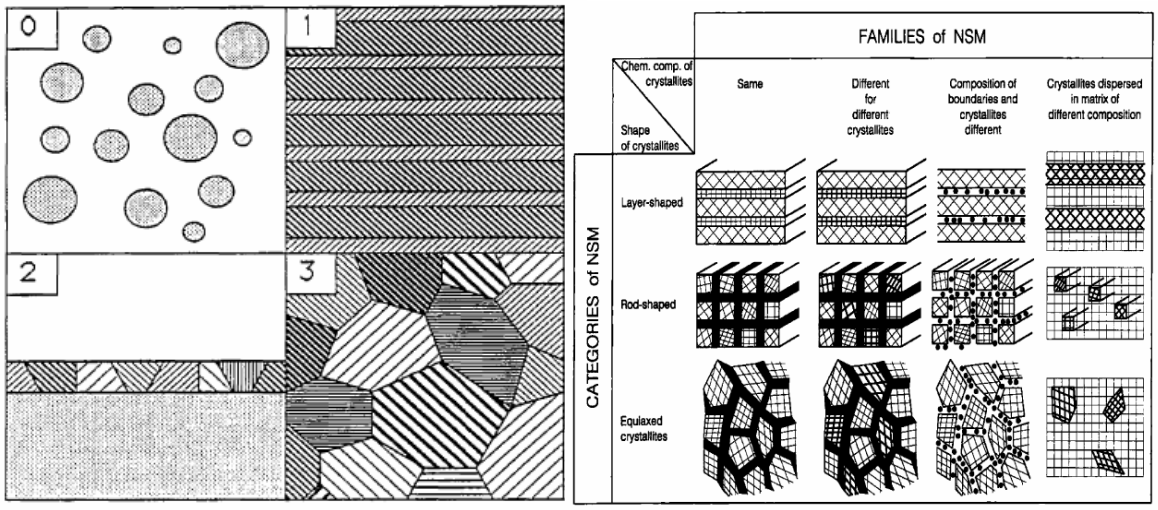

(a) (b)

Figure 4.1 (a) Schematic of the four types of nanocrystalline materials according to Siegel, cf. Siegel (1994a), and (b) classification scheme for nanocrystalline materials according to the chemical composition and the dimensionality of crystallites forming the materials, cf. Gleiter (2000)

According to the shape of constituting crystallites, three categories of nanocrystalline materials may be distinguished: layer-shaped crystallites, rod-shaped crystallites (with layer thickness or rod diameters of the order of a few nm) and equiaxed nm-sized crystallites. Depending on the chemical composition of the constituent structural elements, the above three categories of nanocrystalline materials can be further grouped into four families. In the first family, all crystallites and interfacial regions have the same

chemical composition. The second family consists of the crystallites with different chemical compositions. If the composition variation occurs primarily between the crystallites and the interfacial regions, the third family is obtained. In this case, one type of atoms tends to segregate preferentially to the interfacial regions. The fourth family is formed by nm-sized crystallites (layers, rods, equiaxed crystallites) dispersed in a matrix of different chemical composition. Precipitation alloy, e.g. dispersion of Ni_3Al in Ni matrix is a typical example of this family. While the single phase nanocrystalline Al and Fe_2O_3 belong to the first family, their composites belong to the second family. Until now, the majority of the computational mechanical research on nanocrystalline materials has focused on the first family. Current research is the first MD investigation of mechanical deformation in a nanocomposite material.

Table 4.1 Classification of the available techniques to synthesize nanocrystalline materials

Route	**Processing**
Vapor	Physical Vapor Deposition, Chemical Vapor Deposition, Aerosol Processing
Liquid	Sol-gel process, Wet Chemical Synthesis
Solid	Mechanical Alloying/milling, Mechanochemical Synthesis
Combined	Vapor-Liquid-Solid Approach

The state of the art in the fabrication technology for nanocrystalline materials includes a wide range of vapor, liquid, and solid state processing routes. Available techniques for synthesis via vapor routes range from physical vapor deposition and chemical vapor deposition to aerosol spraying. The liquid route involves sol–gel and wet chemical methods. The solid state route preparation takes place via mechanical milling and

mechanochemical synthesis. Table 4.1 summarizes the most common routes for synthesis of nanocrystalline materials, cf. Tjong and Chen (2004). Among all techniques, sol-gel synthesis and mechanochemical synthesis are currently the most appropriate techniques for manufacturing nanocomposite materials. Various metal oxide nanocrystalline powders have been synthesized using the sol–gel synthesis, e.g. SnO_2, $Ba_2Ti_2O_5$, $PbTiO_3$, $(Pb,La)(Zr,Sn,Ti)O_3$ powders, cf. Tang et al. (1998), Shek et al. (1999), Manorama et al. (1999), Xu et al. (2003), and Zhai and Chen (2003); nanocomposite powders containing elemental particulates, e.g. nano-Ni/SiO_2, $Fe–Al_2O_3$, cf. Piccaluga et al. (2000) and Huang et al. (2003); and oxide nanocomposites, e.g. $Fe_2O_3–SiO_2$, $NiO–SiO_2$, $3Al_2O_3–2SiO_2$, cf. Vendange and Colomban (1993), Bruni et al. (1999), and Tillotson et al. (2001) (~ 3-10 nm Fe_2O_3 grains with ~ 25 nm ultrafine-grained Al with ~ 5nm thick oxide layer). Mechanochemical synthesis has been used successfully to prepare nanoparticles of a number of materials, including transition metals, cf. Ding et al. (1996) and Baburaj et al. (1997); oxide ceramics (e.g. Al_2O_3, ZrO, ZnO, PBT (mixture of PbO, ZrO_2 and TiO_2)), cf. for example Tsuzuki and McCormick (2001) and Brankovic et al. (2003), and oxide semiconductors (e.g. SnO_2), cf. Cukrov et al. (2001).

A vast amount of effort has been directed towards experimental, analytical, and computational research on nanocrystalline materials, see for example Gleiter (1998) and Kumar et al. (2003a). Nanocrystalline materials exhibit strain rate sensitivity, superplastic characteristics, flow strength, and ductility different from their microcrystalline counterparts. In addition, their properties depend on the composition in a manner different from microcrystalline materials. Conventional polycrystalline metals and alloys

show an increase in yield strength (σ_y) with decreasing grain size (d) according to the well-known H–P relation. The σ_y and hardness (H_v) tend to increase with decreasing grain size following the equations,

$$\sigma_y = \sigma_0 + kd^{-1/2}; \text{and} \quad H_v = H_0 + k_H d^{-1/2} \cdot \tag{4.1}$$

Here, σ_0 is the friction stress resisting the motion of gliding dislocations, H_0 is a constant similar to σ_0 and k and k_H are called H-P slopes. The H-P slopes are a measure of the resistance of a grain boundary to slip transfer. The H–P relation is attributed to the grain boundaries acting as efficient obstacles to dislocations nucleated mostly from the Frank–Read sources. Consequently, a dislocation pileup can be formed against a grain boundary inside a grain. By decreasing the grain sizes of metals down to the order of a few tens of nm, the H–P slope remains positive but with a smaller value, cf. Hoffer and Averbach (1990), Nieman et al. (1991), and El-Sherik et al. (1992). At ultra-fine grain sizes below a critical value, a reverse softening effect or the reverse H–P relation has been observed for some metals, cf. Siegel and Fougere (1995), Konstantinidis and Aifantis (1998), Takeuchi (2001), and Chokshi et al. (1989). Apparently, the H–P slope varies gradually from positive to zero to negative, see Schiøtz and Jacobsen (2003). In certain instances, only a plateau regime in the H-P curve is observed with reduction in grain size, cf. Sun et al. (1994). For pore free and dense electroplated Ni samples, El-Sherik et al. (1992) observed a deviation from the H–P relation. A plateau is found in the hardness versus grain size curve when the grain sizes are less than 20 nm. It is conjectured that at the nanoscopic length scale, dislocation sources inside grains don't exist. This is because the

size of a Frank–Read source cannot exceed the grain size. Therefore, pile-up of dislocations against grain boundaries cannot occur. This implies that dislocation pile-ups cannot form and the H–P relationship for conventional coarser-grained materials can no longer be valid. Instead the reverse H–P relation, i.e. softening, is obtained with reduction in grain size. Several factors such as the grain boundary sliding, creep diffusion, triple junctions, pores, and impurities could also contribute to the reverse H–P relation in metals and alloys, cf. Suryanarayana et al. (1992) and Sanders et al. (1997). The atomistic mechanism responsible for the H-P relation varies from one system to another. Research work in this area is too new to provide a clear account.

Nanocrystalline metals have been found to exhibit *superplasticity* at lower homologous temperatures (ratio of the test temperature to the melting point) and at higher strain rates than their microcrystalline counterparts. Superplasticity is defined as the ability of a material to exhibit extremely large extensibility, often without the formation of a neck prior to fracture. Superplasticity in microcrystalline materials is attained at low strain rates from 10^{-5} s^{-1} to 10^{-3} s^{-1}. Tensile superplasticity has been observed in nanocrystalline Pb–62Sn alloy at room temperature, cf. Mishra et al. (1997). Low temperature and high strain rate tensile superplasticity have been found to occur in nanocrystalline Ni, Ni_3Al, and Al alloys with grain sizes of 20, 50 and 100 nm, respectively, (1420Al; Al–Mg–Li) at 623, 573 and 998 K, respectively. Among them, 1420Al alloy is of particular interest because of its higher superplastic strain rate (10^{-2} s^{-1}) and lower superplastic temperature (573 K). Microscopic examination of superplastically deformed alloys showed that extensive grain boundary sliding, accompanied by considerable grain rotation, occurs

during superplasticity, cf. Courtney (1990). However, a clear understanding of the mechanism of superplasticity in nanocrystalline materials is not yet available.

Lu et al. (2001) report that the flow strength of nanocrystalline Cu increases slowly from 84 MPa to 122 MPa with increasing strain rates. The strains to failure and the fracture stress are found to increase dramatically with increasing strain rates for nanocrystalline Cu. Dalla Torre and Van Swygenhoven (2002) report that the average tensile strength of nanocrystalline Ni samples (average grain size 20 nm) remains approximately 1388 MPa for strain rates from 5.5×10^{-5} to 5.5×10^{-2}. However, the tensile ductility decreases dramatically with increase in strain rates from 5.5×10^{-5} to 5.5×10^{-2}. The average tensile strength increases dramatically to approximately 2500 MPa at a strain rate of 10^{3} s^{-1}. Schwaiger et al. (2003) also found that the flow stress of nanocrystalline Ni increases with increasing strain rate. The positive strain rate sensitivity in the flow stress of nanocrystalline Ni can be attributed to the localized plastic deformation in grain boundaries and nearby regions. Due to the lack of dislocation sources in nanocrystalline Ni, the grain interior deforms at stress levels close to the theoretical strength and contributes little to the overall plastic deformation.

The submicron and nanocrystalline Ni samples exhibit higher tensile strength than coarser polycrystalline Ni, thereby possessing a higher endurance limit. Hanlon et al. (2003) studied the high cycle fatigue behavior of submicron and nanocrystalline Ni under stress-controlled conditions. They reported that both submicron and nanocrystalline Ni samples have higher endurance limit than conventional coarse-grained Ni. A remarkably

large enhancement in fatigue life is observed in submicron Al-alloy compared to coarser-grained counterparts subjected to stress-controlled cycling, cf. Chung et al. (2002) and Patlan et al. (2001). In contrast, it is expected that nanocrystalline metals and their alloys exhibit lower low cycle fatigue life than their microcrystalline and macrocrystalline counterparts due to their poorer strain controlled properties. Patlan et al. (2001) have observed deterioration in the low cycle response with grain refinement.

From the above review, it is clear that nanocrystalline materials exhibit a range of properties that are different from their microcrystalline and macrocrystalline counterparts. The deformation mechanisms operating at the nanoscopic lengthscales to cause this deviation in the properties are poorly understood. The experimental tools are extremely limited in their means. In addition, the theoretical characterizations to account for the nanoscopic mechanical properties are highly idealized. In the following, the current state of the art in the experimental and analytical characterizations of mechanical deformation in nanocrystalline materials is presented.

4.1.1 Experimental Characterization

Experimental characterization of the mechanical deformation in nanocrystalline materials has primarily been carried out using nano-indentation experiments. In general, nanocrystalline material samples are too small to be used in the conventional large scale tests. In this regard, the nano-indentation method appears to be an effective route to study the mechanical deformation of nanocrystalline materials. Yang and Li (1995) demonstrated the use of indentation and impression creep for investigating the creep

deformation mechanism in nanocrystalline materials at high homologous temperatures. The technique of in-situ straining of TEM foil specimens is also an effective method to explore the deformation and the grain-boundary structures of nanocrystalline materials, cf. Ke et al. (1995) and Kumar et al. (2003a). Using TEM, Liao et al. (2004) found that some stacking faults in nanocrystalline Al are 1.4–6.8 nm wide, which is 1.5–11 times higher than the reported experimental value for single crystalline Al. Their analytical model shows that such wide stacking faults are formed due to small grain sizes and due to the interaction of stacking fault ribbons with high density of dislocations in grain boundaries.

Molecular dynamic simulations have predicted deformation twinning in 2-dimensional nanocrystalline Al with grain sizes from 30 nm to 90 nm, cf. Yamakov et al. (2002a), which is interesting because no deformation twin has ever been observed in coarse-grained Al due to its high stacking fault energy. The MD simulations by Yamakov et al. (2002a) also predict two other twinning mechanisms;

1. Heterogeneous twins nucleated from grain boundaries and;
2. Twin lamellae via the dissociation and migration of grain boundaries.

The deformation twins have been confirmed in nanocrystalline Al films produced by physical vapor deposition, cf. Chen et al. (2003). Using TEM observations on a nanocrystalline Al sample produced by cryogenic ball milling, Liao et al. (2003b) show that the deformation twins could form via dynamic overlapping of stacking fault ribbons formed by the Shockley partial dislocations emitted from grain boundaries. This observation is found to be consistent with the homogeneous twinning mechanism

predicted by MD simulations of Yamakov et al. (2002a). Liao et al. (2003a) report TEM observations of the other two types of twins in nanocrystalline Al processed using the cryogenic ball milling. The twins were observed to be formed via the mechanisms suggested by MD simulations of Yamakov et al. (2002a).

4.1.2 Analytical Characterization

Most of the current models for describing polycrystalline plasticity are independent of the sizescale and therefore don't predict the H-P relation, cf. Lubarda (2002). Analytical modeling of the constitutive behavior in nanocrystalline materials has primarily focused on analyzing the H-P relation as a function of the average grain size accounting for the underlying role of grain boundaries, triple junctions, and bulk dislocations, cf. Kim and Bush (1999), Kim et al. (2000), Fu et al. (2001), Sharma and Ganti (2003), and Kim et al. (2001). In analytical modeling approaches, a nanocrystalline material is essentially considered as a composite comprising the grains interior and grain boundaries. Additional factors related to the structure and to the elastic-plastic deformation are incorporated into the formulations by individual researchers according to the simulation needs.

Kim and Bush (1999) modeled the grain-size-dependence of the elastic moduli of nanocrystalline materials. Porosity was included in their numerical modeling. Their simulations predict that the elastic moduli of nanocrystalline materials decrease with decrease in the grain size. In addition, the decrement is relatively large at grain sizes below 10 nm. The effect of porosity, however, is substantially greater than the effect of grain size. Later, Kim et al. (2000) used the phase mixture model to describe the plastic

deformation in nanocrystalline materials. The mechanical properties of the crystallites were represented by a unified viscoplastic constitutive model based on the evolution of dislocation density. The total strain rates of the crystallites were calculated by summing up the contributions of dislocations, boundary diffusion mechanisms, and lattice diffusion mechanisms. The deformation mechanisms at the grain boundaries were modeled as diffusional flow of matter through grain boundaries. In another approach, Sharma and Ganti (2003) evaluated the elastic properties of nanocrystalline materials as a function of grain size by taking the grain boundary sliding into consideration. They treated nanocrystalline materials as two-phase systems consisting of a crystalline matrix phase and an ellipsoidal grain boundary phase. Fu et al. (2001) treated nanocrystalline materials as composites, comprising the grain interior, with flow stress σ_{fG}, and the work-hardened grain boundary layer, with flow stress σ_{fGB}. Gradient terms for a double-slip crystal system for modeling plastic deformation were proposed by Estrin et al. (1998). Benson et al. (2004) focused on modeling individual grains as having boundaries of finite thickness with hardening properties that are different from the grain interior. Thickness of the boundary region was a function of the grain size. Ovid'ko and Sheinerman (2004) suggested a theoretical model to describe the generation and the evolution of nanoscale cracks (nano-cracks) at triple junctions in deformed nanocrystalline materials. In the framework of the model, nano-cracks in nanocrystalline materials are nucleated at triple junctions due to accumulation of the dislocation charge that accompanies the grain boundary sliding through triple junctions. A number of models have been proposed to explore the grain boundary associated deformation mechanisms in nanocrystalline metals,

e.g. grain boundary sliding, grain boundary rotation, grain boundary diffusion, and triple junction effect, see for example Hahn et al. (1997) and Hahn and Padmanabhan (1997).

In nanocrystalline materials with grain sizes less than 10 nm, the reverse H–P effect has been primarily considered to be associated with the sliding of grain boundaries. Ashby and Verrall (1973) suggested a deformation mechanism carried out by four grain clusters, the inter-grain distance in the elongation direction increases, and that perpendicular to the elongation decreases. Yang and Wang (2003) exploited this idea by suggesting a model based on clusters consisting of nine grains and incorporating both the insertion mechanism of Ashby and Verrall (1973) and a 30^{o} rotation of closely linked grain pairs. Wang and Yang (2004) considered the insertion and the rotation processes together as a cooperative deformation mechanism. The lattice dislocation slip and the grain boundary sliding have also been identified as dominant deformation modes in nanocrystalline materials exhibiting a substantial ductility, cf. Kumar et al. (2003a), and super-plasticity, cf. Mukherjee (2002). The lattice dislocation slip is suppressed in very small nano-grains, cf. Gryaznov et al. (1991) and Weertman and Sanders (1994), in which case it can not support intense grain boundary sliding. In addition, the grain boundary dislocation pile-ups can not be sustained in nanocrystalline materials with very fine grain sizes.

Efforts are also in progress to analyze atomistic deformation mechanisms in nanocrystalline materials using MD and to incorporate the insights into the continuum mechanical models. Warner et al. (2004) investigated the deformation of nanocrystalline Cu with grain size less than 10 nm using a 2D continuum model incorporating

atomistically based constitutive relations. The local constitutive response of a series of symmetric and asymmetric tilt grain boundaries under tension as well as under shear was obtained using an atomistic quasi-continuum method. The grain boundary strength was always weaker in shear than in tension. The constitutive information obtained was incorporated into a continuum model using the finite element method (FEM). Under uniaxial compression, the model revealed that the grain boundary sliding in a microstructure having no intra-granular plastic deformation can produce macroscopic quasi-plasticity. Higher stress heterogeneities across the boundaries promote the grain boundary sliding. In addition, these stresses also play an important role in triggering the cooperative grain deformation mechanisms. The model provided a useful insight that even in the absence of the intra-granular plasticity the onset of the macroscopic quasi-plasticity can result from the grain boundary sliding and from collective grain rotation mechanisms.

These observations and results suggest that a combination of the analytical and experimental characterizations is not sufficient to model the mechanical behavior of nanocrystalline materials. Experimental characterizations are in the development and standardization stage. Analytical characterizations are based on certain assumptions that are material system specific and may not hold true at all levels of the mechanical deformation. In addition, analytical characterizations incorporate limited sets of grain boundary structures and defect evolution mechanisms. In order to make further advances, approaches similar to the methods of Warner et al. (2004) and of Spearot (2005), where fundamental atomistic deformation information obtained from MD is incorporated into an

analytical continuum model, warrant attention. It is important that for a material system, first, the deformation features associated with the applied loading are delineated using MD before developing analytical continuum models. This is the philosophy adopted in the current research. The focus is on analyzing atomistic deformation mechanisms using MD in nanocrystalline material samples described in chapter 3. The following section provides an overview of the research work carried out to delineate deformation mechanisms in nanocrystalline materials using MD.

4.2 Characterization of the Mechanical Behavior of Nanocrystalline Materials Using Classical Molecular Dynamics

MD simulations of nanocrystalline materials are strongly dependent on an appropriate selection of the interatomic potentials for describing interatomic interactions and the material samples with realistic grain structures. Most MD simulations have been performed on fully dense *fcc* metals (primarily Ni, Cu, and Pd). The samples are free from impurities with adjacent grains separated by primarily the high-angle grain boundaries. Using MD simulations of nanocrystalline metals, it has been established that the deformation mechanisms at room temperature fall into main three categories, cf. Hahn et al. (1997), Hahn and Padmanabhan (1997), Konstantinidis and Aifantis (1998), Van Swygenhoven et al. (2001), Derlet et al. (2003), Fedorov et al. (2003), Gutkin et al. (2003), and Kumar et al. (2003b);

(1) Inter-granular mechanisms consisting of uncorrelated atom shuffling events at the high-angle grain boundaries resulting in the grain boundary sliding, cf. Schiøtz et al. (1998) and Schiøtz et al. (1999);

(2) Intra-granular mechanisms such as partial dislocation emission and twinning in nanocrystalline metals with grain size larger than 10 nm, cf. Liao et al. (2003b); and

(3) Cooperative grain behaviors, i.e. micro-shear banding or rotation of clusters of grains, cf. Hasnaoui et al. (2003).

Plastic deformation in ultrafine (< 5 nm) nanocrystalline materials has been attributed primarily to the grain rotation and the grain boundary sliding. With increase in grain size (5nm-20 nm) the mechanism of deformation shifts to dislocation emission from grain boundaries and the corresponding combination of stacking fault formation and twinning. Beyond the grain size of 20 nm, the deformation is governed by dislocation generation and locking in grains, cf. Yamakov et al. (2002b). In addition to the grain boundary sliding, diffusion along grain boundaries, cf. Masumura et al. (1998), Kim et al. (2000), Cai et al. (2000), and Yamakov et al. (2002b), and along triple junctions, cf. Gottstein et al. (2000), Fedorov et al. (2002), and Fedorov et al. (2003), has been proposed to account for the plastic deformation without dislocation motion below the critical grain size of approximately 10 nm and temperatures above room temperature. Rotational deformation occurring through the motion of grain boundary disclination dipoles has also been suggested as one of the deformation mechanisms contributing to the plastic flow, cf. Ovid'ko (2002), Murayama et al. (2002), and Gutkin et al. (2003). With decrease in the grain size to 10 nm or lower, the effect of triple junctions on the deformation mechanism

becomes significant owing to the increase in the volume fraction of triple junctions. The volume fraction of triple junctions approaches that of grain boundaries when the grain size is reduced to approximately 3 nm. In this context, Palumbo et al. (1990) suggest that the softening in the H–P relation occurs when the volume fraction of triple junctions in a nanocrystalline material reaches a critical value. It has been found that the triple junctions of grain boundaries play the role of enhanced diffusivity pipes, nuclei of second phase segregation, sources of lattice dislocations during plastic deformation, drag centers of grain boundary migration upon grain growth, and nucleation site for voids, etc., cf. Gottstein et al. (2000), Konstantinidis and Aifantis (1998), Fedorov et al. (2003), and Kumar et al. (2003a).

Van Swygenhoven and Caro (1997), Van Swygenhoven and Caro (1998), and Van Swygenhoven and Caro (1999) conducted MD simulations of creep in nanocrystalline Ni samples at temperatures below 120 K. They concluded that the low-temperature and high-stress creep deformation occurs at constant volume by the motion of very mobile atoms within the interface, inducing viscous slide of grains with respect to each other, keeping constant the amount of interface, without pore or crack formation. The mechanisms responsible are the grain boundary sliding, grain rotation, and grain boundary motion. The local atomic shuffling in grain boundaries often involves stress-assisted diffusion of free volume from a nearby triple junction to the region of misfit surrounding a grain boundary dislocation. This allows the formation of the Burgers vector of a partial lattice dislocation, resulting in dissociation of the grain boundary dislocation. Upon subsequent propagation of the partial lattice dislocation further

structural relaxation within the grain boundary region takes place, especially in regions where partial dislocations impinge on grain boundaries. The resulting slip across a grain can be accommodated in grain boundaries leading to changes in the misorientation of the neighboring grains and thus further structural changes at the atomic level. The grain boundaries can be considered to be acting as the sources as well as the sinks for the dislocation activity, cf. Van Swygenhoven et al. (1999b) and Van Swygenhoven and Derlet (2001). Van Swygenhoven et al. (2002) and Derlet et al. (2003) showed that in samples of nanocrystalline Ni with 12 nm and 20 nm grain sizes, the degree of delocalization surrounding the grain boundary determines whether the atomic shuffling can associate the corresponding displacements into the Burgers vector necessary to emit a partial dislocation. Keblinski et al. (1998) and Yamakov et al. (2002b) used MD simulations to study the grain boundary diffusion creep in Si and Pd at high temperatures. The creep behavior was found to be controlled by the grain boundary diffusion that can be described quantitatively by Coble creep, i.e. the strain rate increases with decreasing grain size, d, as $1/d^3$. When d is of the order of the width of a grain boundary, the grain size dependence of the strain rate changes from d^{-3} to d^{-2}. The grain boundary diffusion and the grain boundary sliding form an integral part of the creep deformation. The grain boundary sliding is needed to accommodate the homogeneous grain elongation induced by the Coble creep, with the entire deformation process being controlled by the grain-boundary diffusion, cf. Yamakov et al. (2002b). These observations are in accordance with the experiments by Chokshi et al. (1989) and Wang et al. (1997). However, these results disagree with the MD predictions of Van Swygenhoven and Caro (1999) in which the grain boundary sliding, without diffusion accommodation, is proposed as the

principal room temperature deformation mechanism in nanocrystalline Ni. In summary, MD performed at room temperature suggests that the deformation mechanisms can be identified with the grain boundary sliding triggered by atomic shuffling and to some extent the stress assisted diffusion. On the other hand, MD performed at temperatures above 0.7 times the melting temperature by Yamakov et al. (2001) and Yamakov et al. (2002b) suggests a Coble creep mechanism. In other words, the grain boundary sliding is primarily governed by the grain boundary diffusion at these temperatures. There is, however, no real justification for extrapolation of Coble creep mechanism to room temperature since one can in no way assume that the rate limiting process close to the melting temperature remains dominant at room temperature.

By analyzing the mechanical deformation in 2D columnar nanocrystalline structures of Al, Yamakov et al. (2001) pointed out that the length of stacking faults connecting two Shockley partials that form an extended dislocation depends not only on the stacking-fault energy but also on the resolved dislocation nucleation stress. The mechanical properties of nanocrystalline materials, such as the yield stress, therefore depend critically on the grain size. However, Derlet and Van Swygenhoven (2002) revealed that the reported features of dislocation dominated deformation in 2D columnar structures of Yamakov et al. (2001) is a result of a geometrical consequence that in the nanocrystalline regime, strains arising from the nucleation and the propagation of dislocations have a limiting lengthscale equal to that of grain size. By simulating the mechanical deformation in similar 2D columnar structures, Yamakov et al. (2002a) and Yamakov et al. (2003) revealed that under relatively high stresses (of 2.5 GPa) and large plastic strains (of

~12%), extensive deformation twinning takes place, in addition to the deformation caused by the conventional dislocation-slip mechanism in nanocrystalline materials with grain sizes of the order of 30-100 nm. Hasnaoui et al. (2004) used large-scale molecular dynamics simulations of nanocrystalline Au to investigate the interactions between dislocations emitted under an indenter and the nearby grain boundary network. It was shown that for the cases where the indenter size is smaller than the grain size, grain boundaries act as a sink for dislocations and that they can also reflect or emit dislocations depending on their local structure and stress distribution. The emission and the absorption process are accompanied by local atomic activity involving the atomic shuffling and the free volume migration within grain boundaries.

From the above review, it is clear that MD is quite capable of delineating the details of mechanical deformation in nanocrystalline materials. It is also clear that so far MD has focused on primarily *fcc* or *bcc* nanocrystalline materials, for example Pd, Ni, Al, Au, and Cu. The *fcc*-Al calculations have been carried out only in 2-D columnar settings of Yamakov et al. (2002b). They have focused on a limited set of orientations with well defined grain boundary mismatch. The interpolation of these effects in a real 3-D polycrystalline setting with a random mismatch of grain orientations is not yet clear. Past research on nanocrystalline materials using MD has focused on either highly structured material samples or material samples consisting of primarily the high-angle grain boundaries. The difference between the effect of low-angle grain boundary and the effect of high-angle grain boundary on the deformation mechanisms has not yet been clearly characterized. Van Swygenhoven et al. (1999b) in their study of the mechanism of plastic

deformation in nanocrystalline Ni with average grain sizes ranging from 3 to 12 nm under uniaxial load at finite temperatures found that the transition from the inter-grain sliding at lower limit of the grain size range to a combination of the inter-grain sliding and the dislocation emission from grain boundaries at the upper limit of grain size range occurs at smaller average grain size when samples had a larger fraction of the low-angle grain boundaries. However, a distinction between the role of high-angle grain boundaries and the role of low-angle grain boundaries in deformation mechanisms at the nanoscale has not been made clear.

As pointed out earlier in chapter 3, the orientations of individual grains in the nanocrystalline structures used in the current research are chosen randomly. Accordingly, there is a random distribution of the low-angle and high-angle mismatches at the grain boundaries. In addition, the fraction of grain boundary atoms varies from 24.5% in 7.2 nm grain sized nanocrystalline Al to 51.65% in 3.9 nm grain sized nanocrystalline Al. There is a big gap in the average grain sizes 3.9 nm and 7.2 nm for the size effect to be clearly observed. Since up to 50% of the atoms are grain boundary atoms in 3.9 nm grain sized nanocrystalline Al, inter-crystalline deformation mechanisms are expected to become relevant, as opposed to intra-crystalline mechanisms based on the dislocation activity. In the case of nanocrystalline Al samples with grain sizes 3.9 nm and 4.7 nm there is a big difference in the fraction of grain boundary atoms and the degree of mismatch at the grain boundaries, see Figure 3.6. Since size-scales are nearly the same in these structures, the role of grain boundary mismatch in the deformation mechanisms can be more clearly delineated. Overall, the range of average grain sizes chosen enables the

analyses of the effect of grain size on strength as well as the analyses of the role of grain boundary mismatch in the deformation mechanisms. The calculations also focus on analyzing the effect of loading direction (tension vs. compression) on the deformation mechanisms. Besides analyzing nanocrystalline Al for the first time in a 3-D setting, the current research is the first to analyze mechanical behavior of nanocrystalline Fe_2O_3 and Al+Fe_2O_3 composite systems using MD. The focus here is on analyzing the deformation mechanisms operative in a nanocrystalline composite and on understanding the effect of mixing two separate phases (Al and Fe_2O_3) at the nanoscale on the mechanical strength. A combination of all the above issues gives this research a unique perspective.

In the following, Young's modulus (E) is the slope of stress-strain curve in the initial linear region. When calculating Young's modulus from the simulation data, a compromise must be made between getting enough data points for a reliable fit, and staying within clearly linear region. We have found that a reasonable compromise is to use first 4 data points within 1% strain for tension as well as compression for all four material systems. This ensures that we have enough data for a reliable fit, but results in a slight underestimate of the Young's modulus, as some plastic deformation is beginning in this interval. The onset of plastic deformation is usually described by σ_y traditionally defined as the stress where strain is 0.002 larger than what would be expected from extrapolation from the elastic region. In these simulations the stress continues to increase after the yield point, until it reaches a plateau (the flow stress) and becomes constant or begins to decrease slightly. The difficulties leading to an underestimate of the Young's modulus thus lead to a slight overestimate of the yield stress, and also lead to large

uncertainties in the calculated yield stress values. Schiøtz et al. (1999) calculated the yield stress at strain levels with a deviation of approximately 0.2% from the initial linear portion of the stress-strain curve. However, we feel that this is quite arbitrary and the use of the flow stress to represent the strength of nanocrystalline structures would be more appropriate since the flow stress is a far more well-defined quantity. The flow stress in this research is calculated based on an average of the stress values at three different strains in the region between the point on the stress-strain curve where stress starts to become constant as a function of strain and the point where it starts to decrease. Schiøtz et al. (1999) calculated the flow stress value by averaging the stress values at 3 arbitrary points in the strain interval from 7% to 10%. In the next section, the mechanical deformation and its mechanism in polycrystalline Al under tension as well as under compression is discussed.

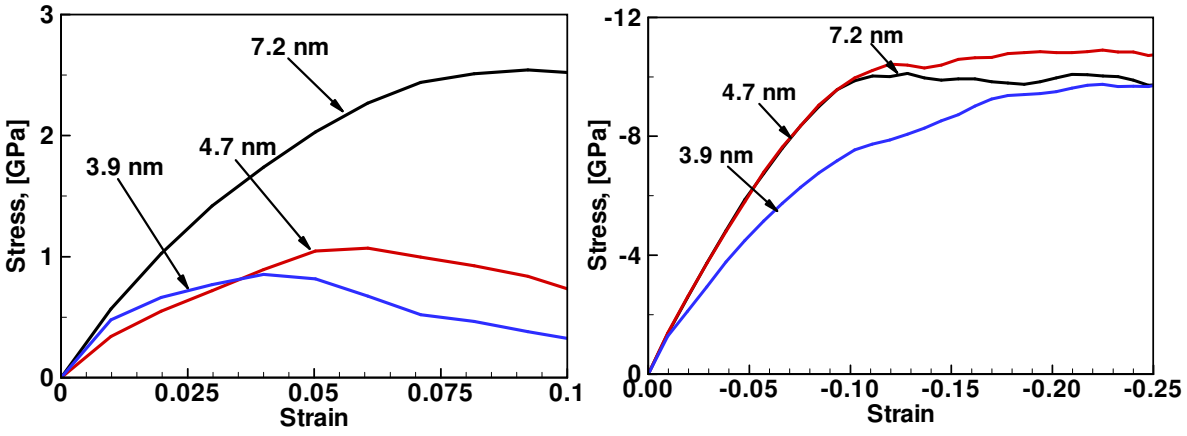

(a) (b)

Figure 4.2 Stress-strain curves for polycrystalline Al with different grain sizes (a) in tension and (b) in compression

4.3 Tensile and Compressive Mechanical Behavior of Nanocrystalline Al

Figure 4.2 (a) shows stress-strain plots for PAl1, PAl2, and PAl3 in tension. The values of Young's modulus are 57.7 GPa for PAl1, 33.9 GPa for PAl2, and 48.4 GPa for PAl3. The flow stress calculations are carried out by averaging the stress values at 4%, 6%, and 8% strains. These strain values and the similar values for further calculations are chosen since the stress in at least one of the structures either becomes constant or reaches the maximum at these strain values. The similar strain levels have been used by many computational and experimental researchers in the past because of the finite strain deformation in nanocrystalline materials, see for example Schiøtz et al. (1999) and Lu et al. (2001). The flow strength values are found to be 2.5 GPa for PAl1, 0.98 GPa for PAl2, and 0.74 GPa for PAl3. Overall, it is clear that there is a softening in the mechanical strength of structures with reduction in the average grain size, with one exception in terms of the Young's modulus value of PAl3 which is higher than that of PAl2.

Based on the results available in literature, distinctive softening in the flow strength with reduction in grain size can be explained based on the role of grain boundaries in the deformation mechanism. At the lengthscale of analyses, sliding of grains along grain boundaries is the primary mechanism of deformation. Dislocation activity is minimal during the deformation. The grain boundary surface area increases with reduction in the grain size resulting in softening of structures. In PAl3, the fraction of grain boundaries with the high-angle mismatch is higher than that in PAl2, see Figure 3.6. Since the size scales are similar for both structures, two significant factors that separate deformation

mechanisms in the two structures are the difference in the fraction of grain boundaries with high-angle mismatch and the difference in the fraction of atoms in defects and grain boundaries. Higher fraction of defect atoms and higher fraction of the high-angle mismatch grain boundaries in PAl3 as compared to that in PAl2 result in restricted movement of atoms in PAl3 during initial stretching. Atoms locked in the high-angle grain boundaries resist initial tensile deformation making PAl3 initially stronger than PAl2. However, after significant stretching, the plastic deformation is mainly governed by the grain boundary sliding which is dominant in PAl3. Because of increased elongation, grain boundary atoms have stronger mobility in PAl3 than in PAl2 during later stages of deformation. Accordingly, PAl3 has lower flow strength value than PAl2.

In all structures, we see a linear elastic region with the Young's modulus values ranging from 33.9 GPa to 57.7 GPa (increasing with increasing grain size). These values are smaller than the Young's modulus value of 70 GPa in single crystalline Al. Similar elastic region with the Young's modulus values ranging from 90–105 GPa is seen in nanocrystalline Cu, compared with the Young's modulus value of 124 GPa for macrocrystalline Cu, cf. Gschneidner (1964). As explained earlier, the primary reason behind this trend is a large fraction of atoms in grain boundaries having lower Young's modulus than the bulk value. A similar reduction in the modulus and in the flow strength values is seen in simulations where the nanocrystalline metal is grown from a molten phase, see melt growth method, cf. Phillpot et al. (1995). In current research, the plastic yielding occurs at the stress values of approximately 0.5 GPa to 1.5 GPa in all structures. Finally, the plastic deformation saturates at the flow stress values ranging from 0.74 GPa

to 2.5 GPa. It is important to note that, the theoretical shear stress of the perfect single crystalline Al ($Gb/2\pi d$) is approximately 3 GPa for the interatomic potential used.

Figure 4.2 (b) shows stress-strain plots for nanocrystalline Al in compression. Values of the Young's modulus for PAl1, PAl2, and PAl3 are 127.9 GPa, 127.3 GPa, and 97.83 GPa, respectively. The flow strength calculations are carried out by averaging the stress values at 15%, 17.5%, and 20% compressive strains. These values are 9.9 GPa, 10.66 GPa, and 9.01 GPa for PAl1, PAl2, and PAl3, respectively. Overall, as the average grain size increases from 3.9 nm to 7.2 nm, the structures become stiffer. However, there is one exception. At large compressive strains, PAl2 is the strongest of all the structures. This is attributed to stronger dependence of the deformation in PAl2 on the grain boundary sliding than in PAl1. In PAl1, the grain size is significantly larger than that in PAl2. Therefore, during later stages of deformation, dislocations emanate from grain boundaries in the bulk of grains with higher density in PAl1 than in PAl2. The mechanism of deformation at large compressive strains is, therefore, a combination of the dislocation emission and the grain boundary sliding in PAl1 and primarily the grain boundary sliding in PAl2. Correspondingly, PAl2 is stronger than PAl1 at large compressive strains. A combination of observations from Figure 4.2 (a) and (b) suggests that all structures are stronger in compression than in tension. In addition, ductility in compression is higher than that in tension. Besides the difference in the grain sizes of the structures, the difference in the fraction of atoms in defects and grain boundaries and the difference in the fraction of the high-angle and low-angle mismatch grain boundaries affect the

observed constitutive behavior. Overall, a reverse H-P relation in the Young's modulus and flow strength values as a function of the average grain size is observed.

Figure 4.3 shows three dimensional slip-vector based viewgraphs for all three grain sizes of nanocrystalline Al at 7.5 % tensile and 15% compressive strains. When viewed along the cross-section, it is possible to make a clear distinction in the motion of atoms along defects and grain boundaries in all structures. In addition, it is observed that in a structure the qualitative features related with dislocation emission and with the motion of atoms along grain boundaries remain unchanged regardless of the examined cross-section. Accordingly, the same cross-sections as those shown in Figure 3.6 are chosen for analyzing the deformation mechanisms in all structures in this research. By doing so, it is possible to clearly understand the role of the grain boundary atoms and the role of the high-angle as well as the low-angle grain boundaries in the deformation mechanism. During MD simulations, grain-coarsening was observed at very high strains (~25%). The focus of the current research is limited to analyzing deformation mechanisms at smaller strains (≤15%). Correspondingly, grain-coarsening is not analyzed. Figure 4.4 and Figure 4.5 show slip-vector viewgraphs for all three grain sizes of nanocrystalline Al at 2.5%, 5%, and 7.5 % tensile strains and 5%, 10%, and 15% compressive strains The strain levels are chosen to correspond to the following three different stages of deformation:

1. Material is strain hardening (2.5% tensile and 5% compressive strains);
2. Material has acquired the maximum stress levels during strain hardening (5% tensile and 10% compressive strains); and

3. Material has undergone severe plastic deformation (7.5% tensile and 15% compressive strains).

Clearly, the above strain levels do not conform to the infinitesimal strain elasticity. Similar strain levels for the mechanical deformation in nanocrystalline materials have been reported in MD simulations of Schiøtz et al. (1999), Lund et al. (2004), and Zheng et al. (2005) and in the experimental work on polycrystalline Ni, see Wei and Anand (2004).

In Figure 4.4, increase in the thickness of high-angle grain boundaries in all structures as a function of applied strain is higher than that seen in the case of low-angle grain boundaries. This indicates that atoms have higher mobility in the high-angle grain boundaries. As deformation proceeds, these atoms move into the grain interiors resulting in increased thickness of the grain boundaries. On the other hand, atoms in the low-angle grain boundaries have limited mobility. This is primarily because of a little difference in the orientation of grains sharing the boundary. Because of the limited mobility, the low-angle grain boundary atoms cannot move into the grain interiors. This results in a minimal change of the grain boundary thickness as the deformation proceeds.

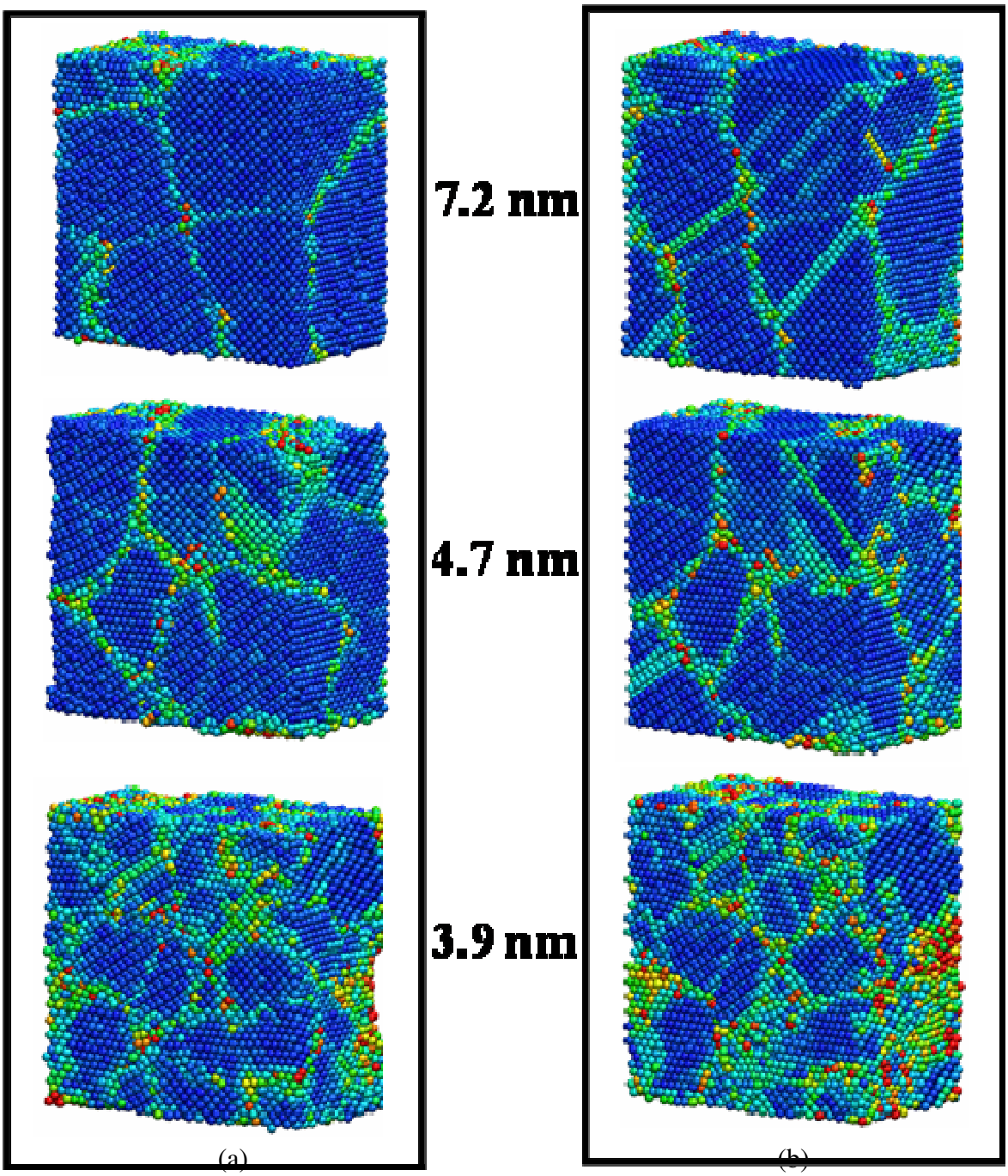

Figure 4.3 Viewgraphs of all three nanocrystalline Al structures at (a) 7.5% tensile strain and (b) 15% compressive strain

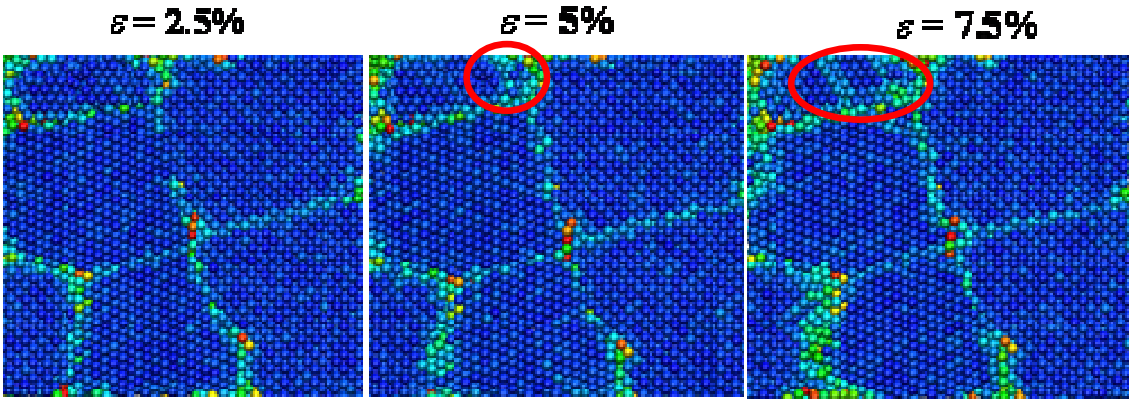

(a)

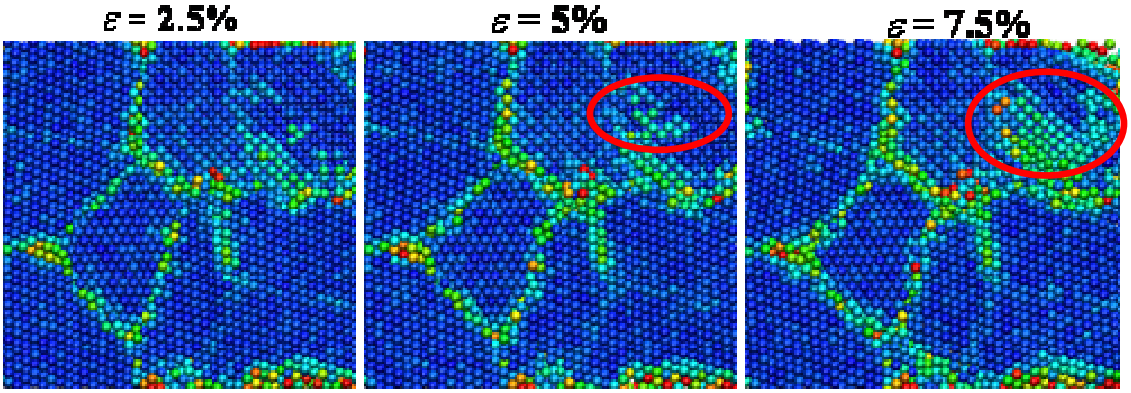

(b)

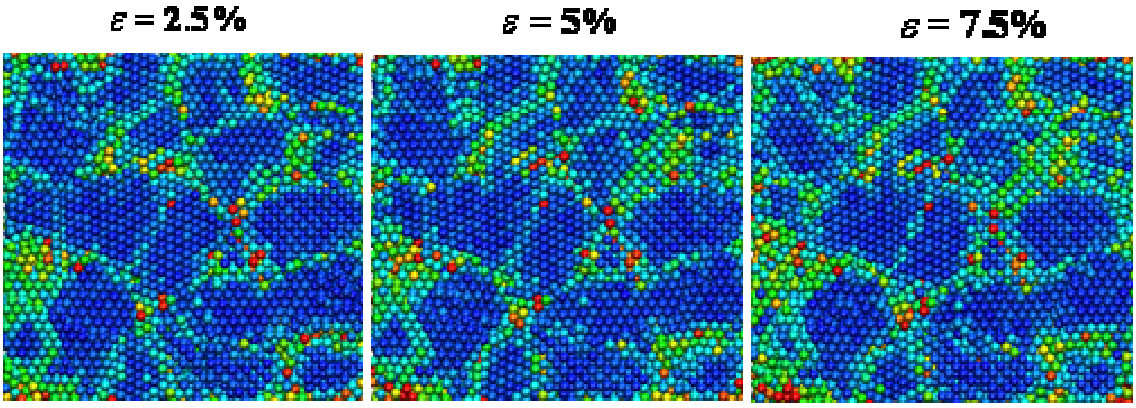

(c)

Figure 4.4 Viewgraphs of nanocrystalline Al with grain size (a) 7.2 nm, (b) 4.7 nm, (c) 3.9 nm, at 2.5%, 5%, and 7.5% tensile strains

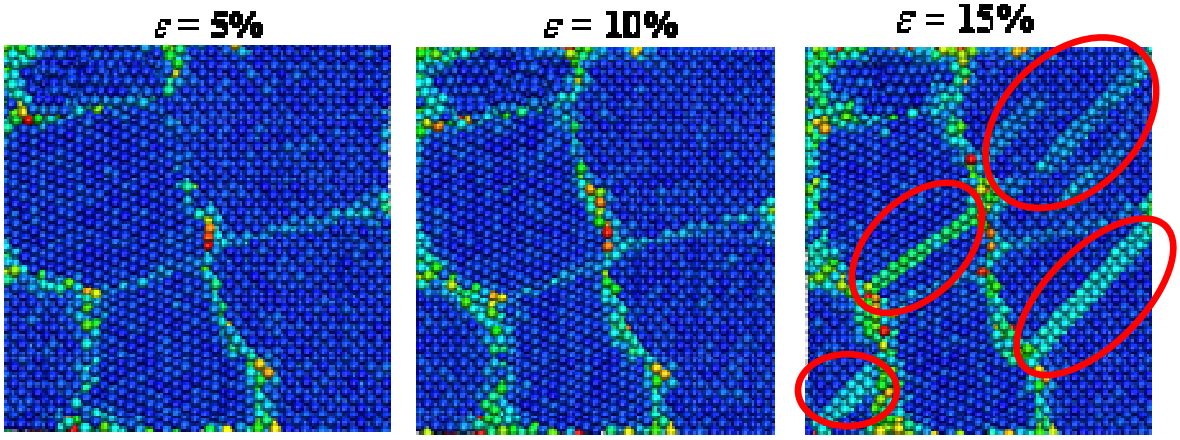

(a)

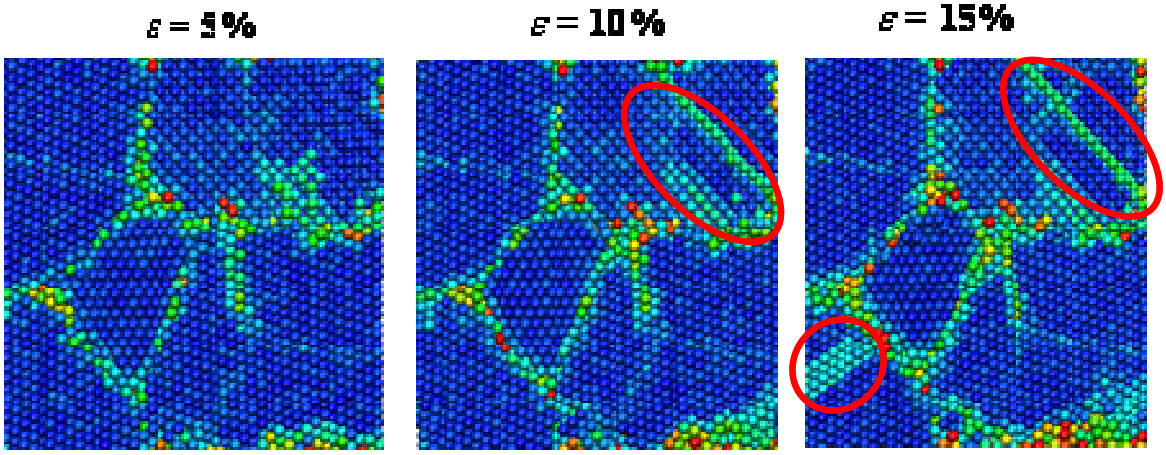

(b)

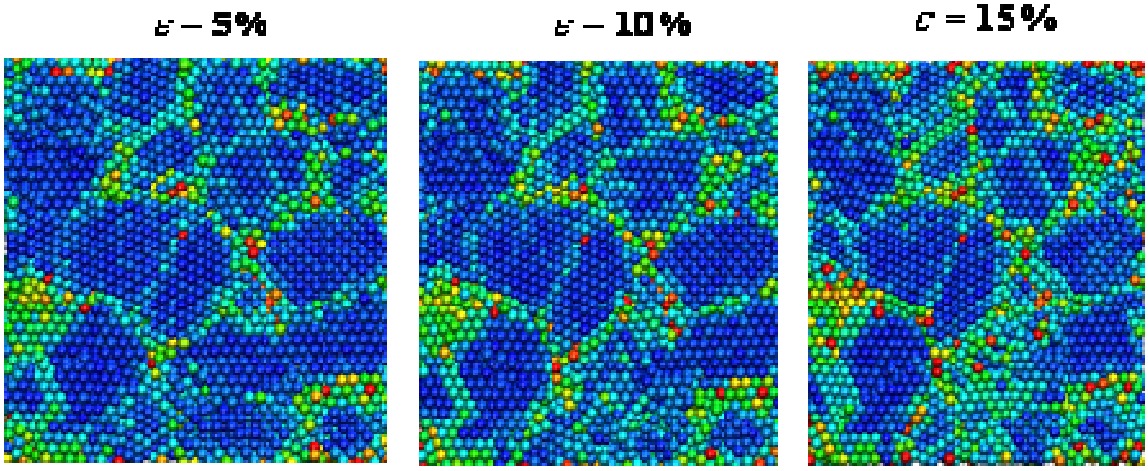

(c)

Figure 4.5 Viewgraphs of nanocrystalline Al with grain size (a) 7.2 nm, (b) 4.7 nm, (c) 3.9 nm, at 5%, 10%, and 15% compressive strains

In PAl1 and PAl2, the dislocation emission occurs during later stages of the tensile deformation. Stacking faults begin to appear at 5% strain, (see circled grains). At 7.5% tensile strain, the width of stacking faults is of the order of the corresponding grain size. In PAl1, the dislocation emission occurs from the {110}-{111} high-angle grain boundary at 5% strain level and from the {110}-{111} and {111}-{100} high-angle grain boundaries at 7.5% strain level (see circled grains). No emission of dislocations is observed from the low-angle grain boundaries. In PAl2, the dislocation emission starts from the {111}-{100} high-angle grain boundary at 5% tensile strain. At 7.5% tensile strain, the stacking fault as a result of dislocation emission has reached the low-angle {100}-{100} grain boundary, (see circled grains). In PAl3, significant thickening of the grain boundaries as a function of tensile strain is observed. However, no dislocation emission is observed at any stage of the deformation. In addition, in PAl3, the thickness of grain boundaries is higher than that in PAl1 and PAl2. The thickness of some of the grain boundaries in PAl3 is the same as the size of corresponding grain. When such grain boundaries share a junction or when they are close to each other, the initial movement of atoms in these grain boundaries is interlocked with each other. Consequently, the majority of initial loading is shared by these grain boundaries resulting in a Young's modulus value of PAl3 that is higher than that in PAl2.

In Figure 4.5, thickening of the high-angle and the low-angle grain boundaries as a function of deformation in all structures is the same as that in Figure 4.4. However, the corresponding deformation levels differ from each other. Dislocation emission from the high-angle grain boundaries during compressive deformation occurs during later stages of

the deformation. In the case of PAl1 dislocation emission occurs from the {111}-{100} high-angle grain boundaries, (see circled grains). In PAl2 and PAl3 the emission occurs from the {110}-{111} and {111}-{100} high-angle grain boundaries, (see circled grains). No dislocation emission occurs from the low-angle grain boundaries. Increase in the number of stacking faults in PAl1 is much higher than that in PAl2 as the deformation level changes from 10% compressive strain to 15%. This indicates that in PAl1, the dislocation motion after 10% compressive strain is more dominant in comparison to that in PAl2. This is in accordance with the softening of PAl1 seen in Figure 4.2 (b) after 10% compressive strain. A combination of these observations suggests that the deformation mechanism in compression is strongly governed by the sliding of grains along grain boundaries. A comparison of Figure 4.4 with Figure 4.5 reveals that at the same level of deformation (see at 5% tensile and compressive strains), dislocation emission occurs earlier during tension. In addition, the grain boundaries that emit dislocations are different in tension and compression. However, the dominant deformation mechanism during tension as well as in compression is the sliding of grains along grain boundaries. With the same underlying mechanism of deformation, the dissimilarity in dislocation emission points towards asymmetric mobility of grain boundary atoms during tensile and compressive deformations. This asymmetric mobility ultimately results in an asymmetry in the strength and deformation levels during tensile and compressive deformations seen in Figure 4.2 (a) and (b).

An important finding from the figures is that most of the dislocation emission occurs from the high-angle grain boundaries. Fang et al. (2004) in their 2D simulations on highly

structured Ni samples with the high-angle and the low-angle grain boundaries found that the dislocation emission in samples with low-angle grain boundaries occurred earlier than that it did in samples with high-angle grain boundaries. However, their samples had only one type of grain boundary stacked in an array along the longitudinal axis. In the current research, the low-angle and high-angle grain boundaries are present in nearly the same proportion. Clearly, under this condition maximum load is transferred to the high-angle grain boundaries. Consequently, with increase in the deformation levels, higher mobility coupled with higher energy of atoms in the high-angle grain boundaries result in earlier dislocation emission. In all the structures, dislocations are emitted from high-angle grain boundaries that are aligned both parallel as well as perpendicular to the loading axis. It is clear that the direction of loading with respect to the orientation of the high-angle or the low-angle grain boundaries does not affect the dislocation emission. Earlier, Yamakov et al. (2002a) observed twinning in 2D-columnar nanocrystalline Al grains in the size range of 30 nm to 90 nm. In the present simulations no twinning is observed because the deformation occurs predominantly due to the movement of atoms along grain boundaries.

Overall the picture that emerges is that most of the plastic deformation is due to a large number of small 'sliding' events of atomic planes in grain boundaries, with only a minor part being caused by dislocation motion inside the grains. Most of the deformation occurs in grain boundaries in the form of a large number of sliding events, where only a few atoms (or sometimes a few tens of atoms) move with respect to each other. Occasionally a partial dislocation is nucleated at a grain boundary and moves through the corresponding grain. Such events are responsible for a minor part of the total

deformation, but in the absence of diffusion they are primarily responsible for the deformations of grains, as they slide past each other. The softening at small grain sizes is, therefore, due to a larger fraction of atoms at grain boundaries. As the grain size is reduced a larger fraction of the atoms belongs to grain boundaries and the grain boundary sliding becomes easier. This leads to a softening of the material as the grain size is reduced. The observed deformation mode is in some ways similar to the manner in which grain boundaries carry most of the deformation in superplasticity. However, in superplasticity the grain boundary sliding occurs at temperatures above room temperature, whereas here it occurs at room temperature driven by high stresses.

In Figure 4.6 the partial Al-Al RDFs after 7.5% tensile strain and 15% compressive strain in all three structures are compared with the partial Al-Al RDFs of the corresponding structures before loading. The strain levels are chosen such that a comparison of the structural order can be made after the stress in all the structures has reached the maximum value during tension as well as compression. In all the RDFs, reduction in the valley depth signifies increase in the fraction of atoms in defects such as grain boundaries. Height of the peaks in RDFs signifies the fraction of atoms in bulk crystalline setting. The steeper the peak is, the higher fraction of atoms in the bulk setting will be. A shift in the peak towards or away from the origin signifies a change in bond length. Following these guidelines, it is clear from Figure 4.6 that the fractions of atoms in the bulk crystalline setting decrease after tensile as well as compressive deformations. In PAl1, change in the fraction of defect atoms as well as in the fraction of bulk atoms is higher than that in PAl2 and PAl3. In PAl3, there is insignificant change in the fraction of

atoms in bulk and defects after stretching. This indicates that in PAl3 the stretching strictly involves the sliding along grain boundaries. The defect formation in this process is minimal. The same trend is observed for PAl3 during compression. The majority of atoms remains in grain boundaries. However, during compressive deformation of PAl1 there is a significant change in the fraction of grain boundary atoms. Overall, after tensile as well as compressive deformations, there is an increase in the fraction of defect atoms including the grain boundary atoms. However, the increase is higher for all structures after tensile plastic deformation. It is clear that even with the same starting configurations, the change in fraction of atoms in defects is different during tensile and compressive deformations.

In order to further understand the deformation mechanisms, the fractions of atoms in defects for all structures were obtained as a function of applied strain during tension as well as compression, see Figure 4.7. The fraction is calculated as a ratio of the atoms in a structure having the magnitude of slip-vector greater than 0.3 relative to the total number of atoms in the structure, see Figure 3.1.

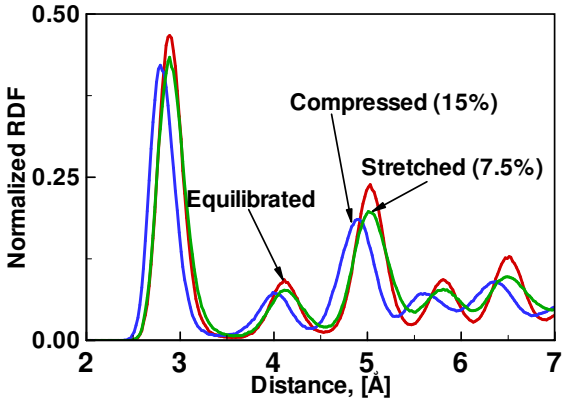

(a)

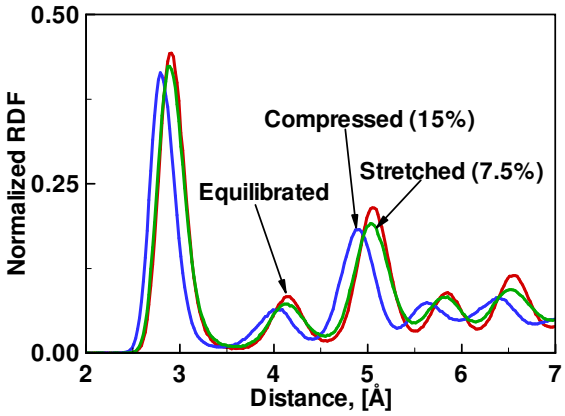

(b)

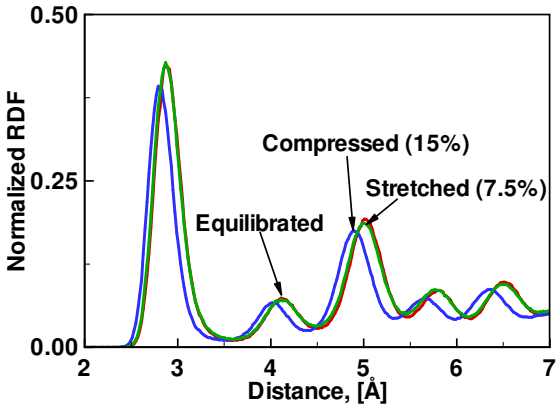

(c)

Figure 4.6 A comparison of the partial Al-Al RDFs of undeformed nanocrystalline Al with that after 7.5% tensile strain and 15% compressive strain for the grain size (a) 7.2 nm, (b) 4.7 nm, and (c) 3.9 nm

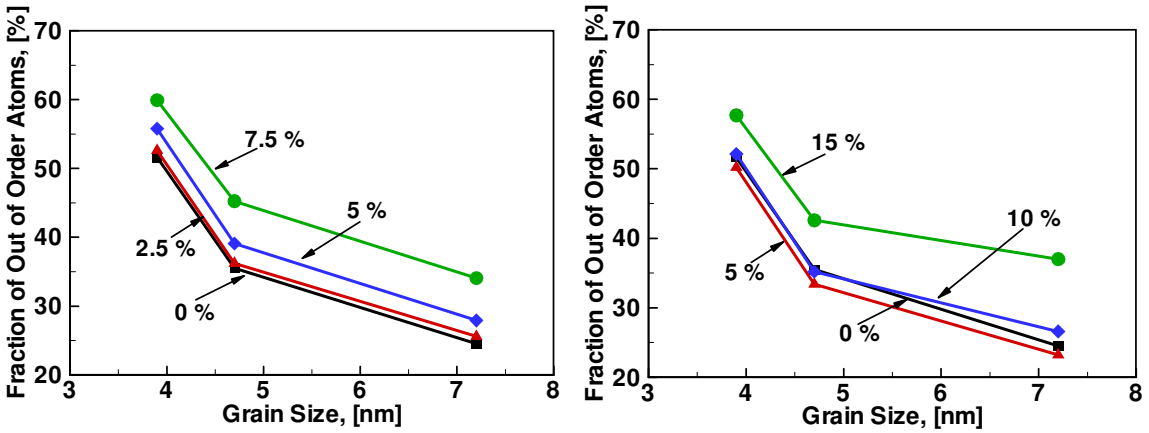

(a) (b)

Figure 4.7 A comparison of the fraction of defect atoms as a function of grain size at different levels of (a) tensile and (b) compressive strains in nanocrystalline Al

It is clear from Figure 4.7 that changes in the fraction of defect atoms in all structures are non-linearly related with increase in the levels of deformation. An initial increase in the fraction of defect atoms as a function of the deformation level is very small. At large strains the increase is up to 3 times than that at smaller strains. This is in accordance with the earlier explanations of the deformation mechanism. Initially sliding along grain boundaries dominates the deformation mechanism. During later stages, the dislocation emission adds to the increase in the fraction of defect atoms. In compression as well as in tension, the increase in the fraction of defect atoms is the highest in PAl1. In addition, for PAl1 at the same level of tensile and compressive straining, the fraction of defect atoms during compression is lower than that during tension. Another important observation is that in all structures during compression there is a decrease in the fraction of defect atoms from 0% to 5% compressive strains followed by a uniform increase with further increase in compressive strains. During tension, however, there is a uniform increase in the fraction of defect atoms from the beginning of the deformation. It is important to note that at 5% compressive strains no dislocations are observed. This is in accordance with

the earlier finding that the grain boundary atoms move differently during tension and compression. There is a deviation from the regular lattice structural order at the grain boundaries resulting in different movement of atoms during tensile deformation.

The plots in Figure 4.7 underline the mechanism of tension-compression asymmetry in nanocrystalline Al. The force between any two particles is inversely proportional to the square of the distance between them. Consequently, the force required to move two particles towards each other has higher spatial gradient along the line joining the two particles during compression. Correspondingly, single crystalline systems with no defects also show asymmetry in measured tensile and compressive strengths as well as deformation levels, for example Ni based superalloy single crystals show compressive strengths that are 1.1 to 1.3 times higher than tensile strengths, see Jiao et al. (1996) and Osterle et al. (2000). However, in nanocrystalline materials this asymmetry is accentuated. In the current investigation, the Young's moduli of PAl1, PAl2, and PAl3 in compression are found to be almost twice the corresponding values in tension. The flow strengths in compression for PAl1, PAl2, and PAl3 are found to be 3 to 4 times the corresponding values in tension. Clearly, the strength asymmetry increases with increase in the deformation levels. The deviation of the structural setting in nanocrystalline Al from a single crystalline one *accentuates* the asymmetry.

Earlier, Liao et al. (2004) found the same behavior in their analyses of the plastic deformation in idealized nanocrystalline Ni. They suggested that the plastic flow resulting from shear shuffling of atoms located at the grain boundaries is reminiscent of

the plastic behavior seen in metallic glasses, where local shear transformation zones, composed of a small number of neighboring atoms, undergo shear distortion and self-assemble into large planar shear bands. In a recent work on metallic glass plasticity, Schuh and Lund (2003) found that the shear transformation zones behave asymmetrically for specimens loaded in net tension versus net compression. Specifically, glasses in states of compression were found to be clearly stronger than those in tension, indicating that some amount of internal friction impacts plastic flow. It can be concluded that the disordered structure in the grain boundaries is the primary contributor for the tension-compression asymmetry. The mobility of grain boundary atoms in tension is different from that in compression since the atomic arrangement in grain boundaries does not follow a regular lattice structure. Consequently, after first few time steps of integration the force experienced by an atom in tension is different from that in compression. This also brings about the difference in the defect structures observed during tensile and compressive deformations.

In disordered structural setting of a grain boundary, collective difference in the movement of atoms accentuates the tension-compression strength asymmetry observed for a single crystalline structure. Since the initial position of an atom is the same at the beginning of deformation in tension as well as in compression, the tension-compression asymmetry is smaller at the beginning (difference of Young's modulus in tension and compression). With increase in the strain levels, the environment of grain boundary atoms during tension and compression begins to differ, resulting in significantly higher difference in further mobility of atoms. As a result, the asymmetry increases with

increase in the levels of deformation. An order of two times asymmetry in the Young's modulus values accentuates to an order of three times asymmetry in the flow strength values. The difference in the mobility also results in the dislocation emission occurring earlier from the grain boundaries during tensile deformation than from those during compressive deformation, see Figure 4.4 and Figure 4.5. In addition, dislocation emission during tensile and compressive deformations occurs from different grain boundaries. The deformation level corresponding to severe plastic deformation during compression is found to be approximately two times that during tension. This is in accordance with the observations made for other *fcc* nanocrystalline materials. The tensile elongation of consolidated inter gas condensed (IGC) Cu with grain sizes below 50 nm is found to be approximately 1.6–4%, cf. Legros et al. (2000), which is much less than the compressive elongation in nanocrystalline Cu samples with strains of 12% to 18%, cf. Fougere et al. (1995).

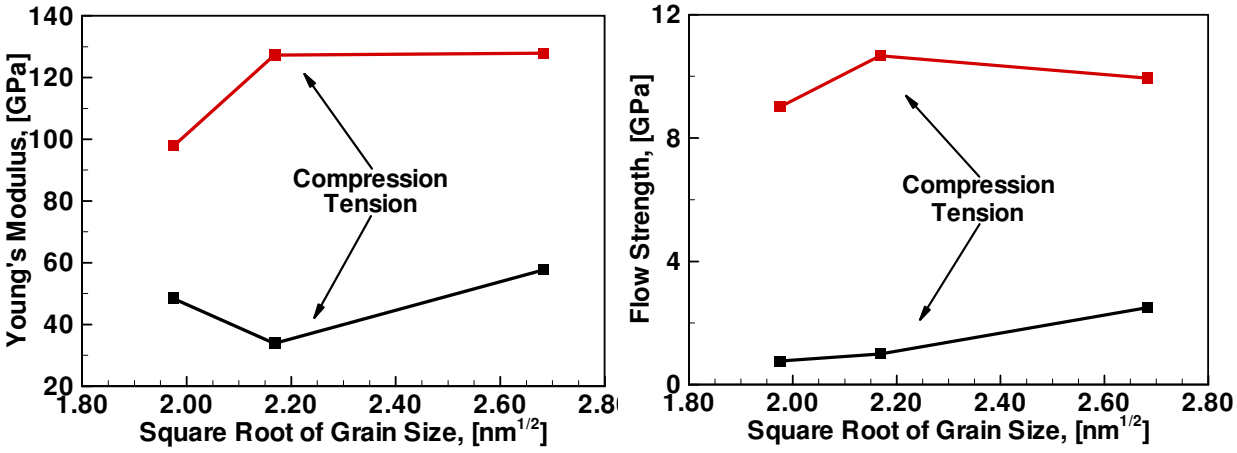

(a) (b)

Figure 4.8 An examination of the dependence of (a) Young's modulus and (b) flow strength on the variation in square root of average grain size in nanocrystalline Al

Figure 4.8 shows variations in the compressive and tensile strengths of nanocrystalline Al with square root of the average grain size. Overall, a reverse H-P relation (softening with reduction in grain size) is observed. A similar effect is observed by Schiøtz et al. (1998) and Schiøtz et al. (1999) on defect free nanocrystalline Cu and Latapie and Farkas (2003) on nanocrystalline α-iron, in agreement with the experimental data by Bonetti et al. (1995). In both plots a clear linear relationship of the strength with square root of the grain size is not observed. This effect is observed because of the difference in the role of the high-angle grain boundaries of PAl2 and PAl3 in the mechanical deformation. At smaller grain sizes, arrangement of grain boundaries (high-angle vs. low-angle) plays an important role in the deformation mechanism. Consequently, a linear variation in the strength values with change in the square root of average grain sizes does not occur. A similar kink in the H-P relationship is reported by Schiøtz et al. (1998) in MD simulations of nanocrystalline Cu, by Liao et al. (2004) in MD simulations of nanocrystalline Ni and by El-Sherik et al. (1992) during experiments on electroplated Ni samples.

From the results of MD simulations presented so far, it is obvious that plastic deformation takes place in the majority of cases by means of the grain boundary sliding. The sliding is associated with reduction in the elastic moduli of disordered grain boundary atoms. Grain boundaries are elastically softer than the grain interiors. The capability of the potential is an important factor in the strength and defect predictions. As pointed out earlier in chapter 2 the potential does a god job in this respect. The stacking fault and surface energy predictions indicate that the insights obtained into the material

behavior using the simulations are experimentally correct. The same is true for the strength values calculated using the stress-strain calculations.

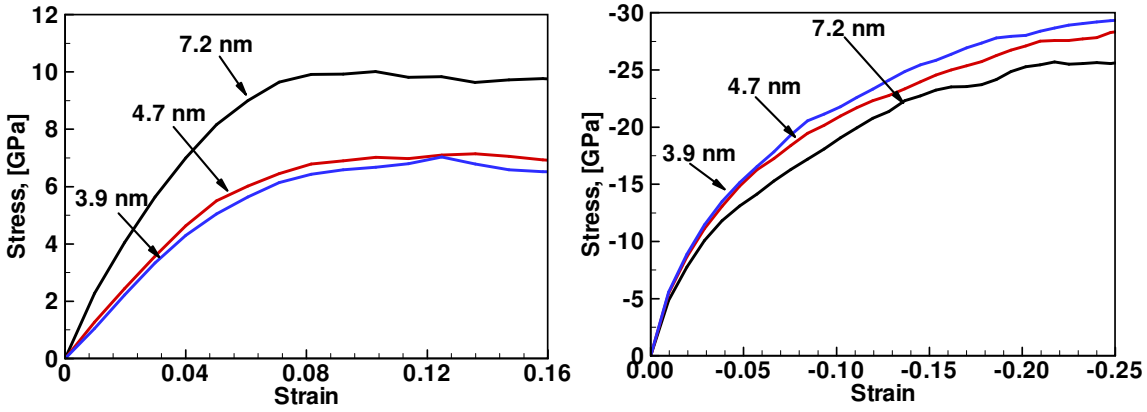

(a) (b)

Figure 4.9 Stress-strain curves for polycrystalline Fe_2O_3 with different grain sizes (a) in tension and (b) in compression

4.4 Tensile and Compressive Mechanical Behavior of Nanocrystalline Fe_2O_3

Figure 4.9 (a) shows tensile stress-strain plots for all three grain sizes of nanocrystalline Fe_2O_3. The Young's modulus values for PHt1, PHt2, and PHt3 are 174.25 GPa, 115.25 GPa, and 107 GPa, respectively. Ductility at all grain sizes is found to be higher than that in the case of nanocrystalline Al. Accordingly, the flow strength calculations are carried out by averaging the stress values at 10%, 12%, and 14% strains. The values of flow strength are 9.88 GPa, 6.98 GPa, and 6.7 GPa for PHt1, PHt2, and PHt3, respectively. Overall, the Young's modulus and flow strength values show softening as the grain size is reduced. Figure 4.9 (b) shows the compressive stress-strain curves for Fe_2O_3 at all three grain sizes. The values for Young's modulus in the case of PHt1, PHt2, and PHt3 are found to be 347.9 GPa, 382.76 GPa, and 396.5 GPa, respectively. The flow strength

calculations for all three grain sizes are carried out by averaging the stress values at 15%, 17.5%, and 20% compressive strains. The strength of Fe_2O_3 in nanocrystalline setting is found to increase with reduction in the average grain size. The flow strength values are 25.03 GPa, 26.97 GPa, and 28.2 GPa in case of PHt1, PHt2, and PHt3, respectively. Overall, with reduction in the average grain size from 7.2 nm to 3.9 nm, the structures become stiffer. The tensile strength values observed here for nanocrystalline Fe_2O_3 are much higher than what is observed during experiments on larger grain sized samples, cf. Thadhani (2005). During tensile testing, specimens with large grain sizes (of the order of millimeters) show high degree of fragmentation resulting in low tensile strength values. Microstructural examinations show that the samples exist in powder form because of low cohesive strength among Fe_2O_3 grains. At the nanoscale, however, experiments have shown that there is a possibility of a high degree of mixing in nanocrystalline Fe_2O_3, cf. Long et al. (2004) and Cannas et al. (2004), resulting in a morphology where Fe_2O_3 grains are mixed closely together. In such a setting, the cohesive strength of the Fe_2O_3 grains is expected to increase. The nanocrystalline Fe_2O_3 in the present simulations represents similar morphology with a high degree of mixing and high inter-grain cohesive strength justifying high tensile strength values during MD simulations.

A combination of the observations from Figure 4.9 (a) and (b) indicates that at the length scale under study, Fe_2O_3 in nanocrystalline setting shows a direct H-P relation in compression and a reverse H-P relation during tension. As expected, values of the Young's modulus and the flow strength are consistently higher than that of polycrystalline Al. In addition, strengths of all samples are higher in compression than in

tension. The macrocrystalline Young's modulus value of Fe_2O_3 is 235 GPa that is higher than the Young's modulus values in tension and lower than the Young's modulus values in compression. The same trend is observed in the case of nanocrystalline Al. Similar to nanocrystalline Al, after few initial time steps of motion, forces on grain boundary atoms in Fe_2O_3 during in tensile and compressive deformations are different. Because of high density of atoms in grain boundaries, difference in the force experienced by atoms results in accentuation of the tension-compression strength asymmetry. The order of magnitude for the Young's modulus values of Fe_2O_3 and Al is the same in the nanocrystalline and macrocrystalline settings. The same, however, is not true in the case of flow strength values. Nanocrystalline values of the flow strengths are one order of magnitude higher than the corresponding macrocrystalline values for both Al and Fe_2O_3. The primary factor responsible is the difference between the deformation mechanisms operative at the two lengthscales. At the macroscale, dislocation motion dominates the deformation mechanism. At the nanoscale, the deformation mechanism is the sliding of atoms along grain boundaries. The softening in the strength because of the motion of dislocations at the macroscale does not occur at the nanoscale resulting in higher flow strength values at the nanoscale.

An examination of the tension-compression strength asymmetry in Fe_2O_3 reveals that the level of asymmetry in the Young's modulus values and the flow strength values are the same as those in the case of nanocrystalline Al. The Young's modulus values in compression are approximately two times the corresponding values in tension. The difference in strength increases as a function of deformation. The flow strength values in

compression are approximately three times the corresponding values in tension. However, unlike Al, in Fe_2O_3 a significant fraction of atoms belongs to defects because of amorphous structural order. Apparently, the absence of crystalline order does not affect the asymmetry. The predominant factor affecting the asymmetry is the difference in the mobility of atoms in defects and grain boundaries. However, amorphous structural order contributes to significantly higher deformation levels in Fe_2O_3 in comparison to that in Al. In nanocrystalline Fe_2O_3, electrostatic forces dominate the interatomic interactions. As shown in Figure 3.13, the increase in electrostatic forces as a function of interatomic distance is higher in compression than in tension. Accordingly, compressive straining of nanocrystalline Fe_2O_3 requires a higher load than is required tensile straining. During compression, the sliding of grains along grain boundaries, which is the primary factor responsible for the reverse H-P relation in nanocrystalline Al, is offset by increased resistance to the straining caused by strong compressive electrostatic forces. The result of this is an increase in the strength of Fe_2O_3 as grain size is reduced, which is the direct H-P relation. The total Fe_2O_3 RDFs of unstrained PHt1, PHt2, and PHt3 are compared with the total Fe_2O_3 RDFs for the same structures at 7.5% tensile and 15% compressive strains in Figure 4.10. The strain levels are the same as in case of nanocrystalline Al and they correspond to the strain levels for the flow strength measurement. As shown, shape of the total RDF plots after tension as well as compression remains the same as those before straining. Clearly, this is observed because Fe_2O_3 is amorphous in the current nanocrystalline setting. A leftward shift in the RDFs after compression is because of the change in the nearest neighbor distance. However, because of amorphous structure, the tensile strains do not change the nearest neighbor distance. This results in a very small

change in the total RDFs after stretching. The higher shift of the RDFs in compression than in tension for all structures indicates a smaller nearest neighbor distance, the result of which is higher differential in the flow strength values in tension and compression as well as an increase in the compressive strength with reduction in the average grain size. The structural order in all structures remains unaffected after tensile and compressive deformations. Figure 4.11 shows the variation of compressive and tensile strengths of Fe_2O_3 in nanocrystalline setting as a function of the square root of the average grain size. As shown, a reverse H-P relation (softening with reduction in grain size) is observed in tension and a direct H-P relation is observed in compression. In addition, the H-P relationships in both cases are linear as against the non-linear relationship observed in the case of nanocrystalline Al. This behavior is attributed to amorphous structural order in Fe_2O_3 which results in decreasing dependence of strength on the extent of the high-angle or the low-angle mismatch at the grain boundaries. The amorphous structural order also results in closer packing of atoms. These two factors combine to cause the linear H-P relationships during tensile and compressive deformations. Experiments have shown, see Siegel (1994a), that closer packing of atoms at in pore-free and dense nanocrystalline structures is one of the primary factors responsible for observing a linear H-P relation. Seeing two different mechanisms of deformation operative for nanocrystalline Al and Fe_2O_3, it is important and interesting to understand what happens if the two crystal structures are present simultaneously in a nanocomposite setting with different volume fractions. The next section presents the analyses carried out to understand the mechanism of deformation in 60%Fe_2O_3+40%Al and 40%Fe_2O_3+60%Al nanocomposites with grain sizes 7.2 nm, 4.7 nm, and 3.9 nm.

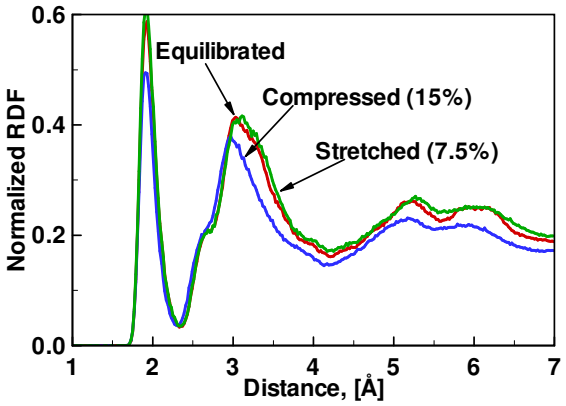

(a)

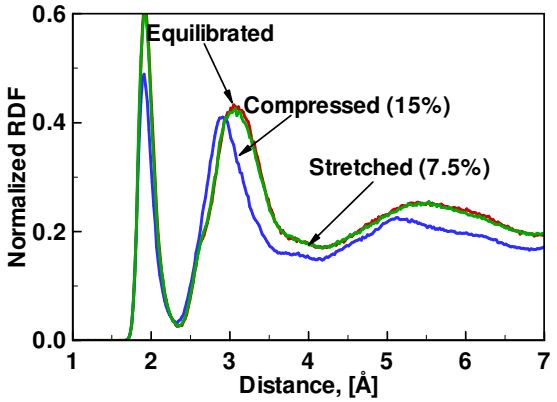

(b)

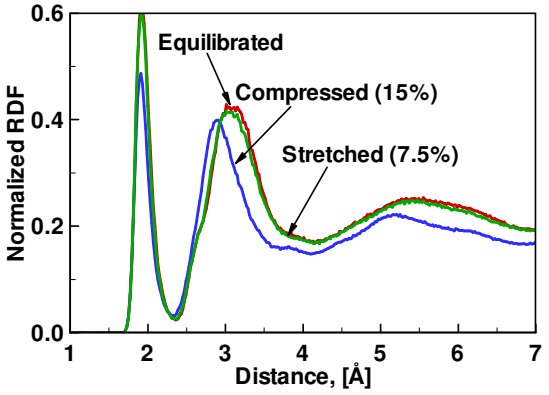

(c)

Figure 4.10 A comparison of the total Fe_2O_3 RDFs of undeformed nanocrystalline Fe_2O_3 with that after 7.5% tensile strain and 15% compressive strain for the grain size (a) 7.2 nm, (b) 4.7 nm, and (c) 3.9 nm

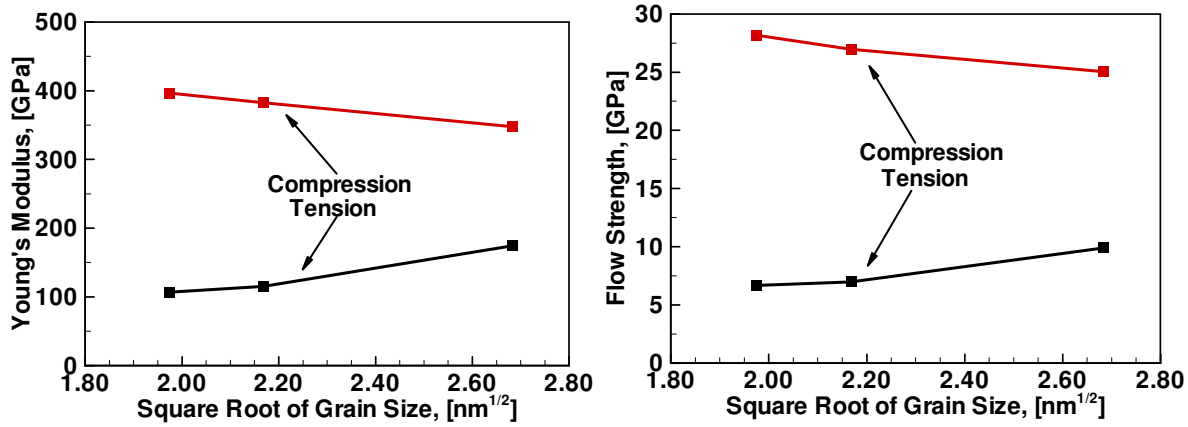

(a) (b)

Figure 4.11 An examination of the dependence of (a) Young's modulus and (b) flow strength on variation in the square root of the average grain size in nanocrystalline Fe_2O_3

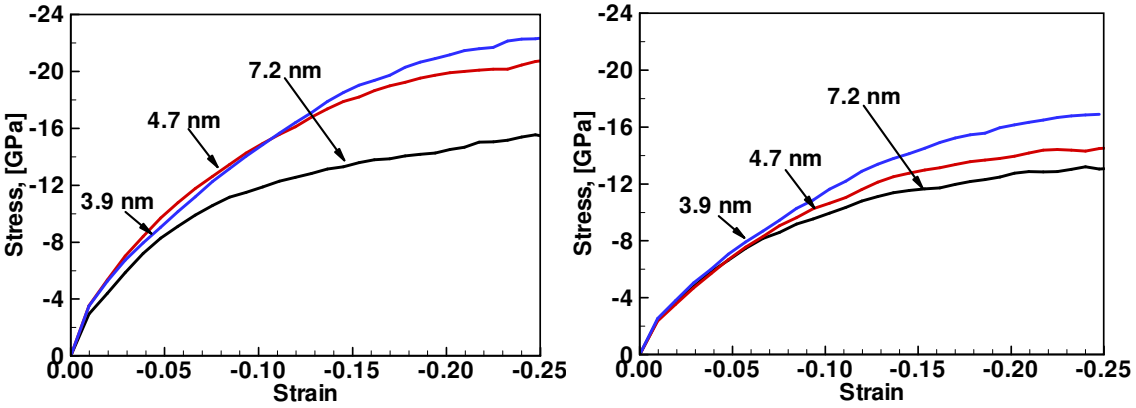

(a) (b)

Figure 4.12 Stress-strain curves at different grain sizes of nanocrystalline (a) 40%Al+60%Fe_2O_3 and (b) 60%Al+40%Fe_2O_3 in compression

4.5 Compressive Mechanical Behavior of Nanocrystalline 40%Al+60%Fe_2O_3 and 60%Al+40%Fe_2O_3 Composites

Al+Fe_2O_3 mixture system is primarily intended for use under compressive loading. Therefore, in the current research the focus is only on analyzing the compressive

strengths of the Al+Fe_2O_3 nanocrystalline composites. Figure 4.12 (a) and (b) show the compressive stress-strain curves for all grain sizes of NCP46 and NCP64, respectively. The Young's modulus values for NCP461, NCP462, and NCP463 are 186.8 GPa, 227.8 GPa, and 209.74 GPa, respectively. In the case of NCP641, NCP642, and NCP643, values of the Young's modulus are 164.5 GPa, 161.3 GPa, and 173.8 GPa, respectively. The flow strength calculations are carried out by averaging the stress values at 15%, 17.5%, and 20% compressive strains. Values of the flow strength are 14.62GPa, 19.8 GPa, and 21.2 GPa for NCP461, NCP462, and NCP463, respectively. In the case of NCP641, NCP642, and NCP643 the flow strength values are 12.5 GPa, 13.9 GPa, and 15.99 GPa, respectively. The overall trend indicates softening of the mechanical strength with the increase in average grain size from 3.9 nm to 7.2 nm.

NCP462 has a higher value of the Young's modulus than does NCP463. Similarly, NCP641 has a higher Young's modulus than NCP642. A similar anamoly was observed earlier in the case of nanocrystalline Al. In nanocrystalline Fe_2O_3 the trend is not visible because of amorphous structural order. Since average grain sizes in NCP462 and NCP463 are nearly the same, the deformation mechanism is primarily affected by differences in the compressive electrostatic forces at Al and Fe_2O_3 interfaces and the grain boundary sliding at Al-Al grain boundaries. The fraction of Al-Al grain boundary atoms is higher in NCP463 and therefore the grain boundary sliding dominates. In NCP462, the sliding is overshadowed by strong compressive electrostatic forces. This results in NCP463 having lower compressive Young's modulus value than NCP462.

During later stages of compressive deformation, dislocations start to play significant role making structures with bigger grain size weaker.

In NCP64 material system, higher volume fraction of Al results in increase in the effect of the grain boundary sliding as a deformation mechanism. This initially offsets the effect of strong compressive electrostatic forces in NCP641 and NCP642 where initial softening in the Young's modulus values with reduction in grain size is observed. In NCP641 and NCP642 the fraction of Al-Al grain boundaries is higher than that of Al-Fe_2O_3 interfaces. NCP643, however, shows compressive hardening when compared to NCP641. In NCP643, the fraction of Al-Al grain boundaries is nearly equal to the fraction of Al-Fe_2O_3 interfaces. Overall, in all composite structures the deformation mechanism is governed by a mix of the grain boundary sliding and the compressive electrostatic forces which, depending upon the volume fraction of Al and Fe_2O_3, determine compressive strength. An anamoly, in the strength variation with grain size is observed for 4.7 nm grain sized structures in both NCP46 and NCP64. Similar anamoly in the strength variation is observed for nanocrystalline Al. It can be presumed that this is a consequence of the presence of a specific mix of the high-angle and low-angle grain boundaries. This conclusion is supported by the similar anamoly observed in MD simulations on other material systems, see for example Schiøtz et al. (1998) for nanocrystalline Cu and Liao et al. (2004) for nanocrystalline Ni. During later stages of deformation in both NCP46 and NCP64, the effect of compressive electrostatic forces at Al-Fe_2O_3 interfaces causes the direct H-P relation to reappear.

The deformation curves for both composite systems differ in shape from each other unlike that in the case of nanocrystalline Al or nanocrystalline Fe_2O_3. The deformation curves show consistent strain hardening. During compressive deformation, compressive electrostatic forces act at Al- Fe_2O_3 interfaces against the grain boundary sliding to cause strain hardening. It is also clear from the above calculations that the compressive strengths for all composites lie in between that of nanocrystalline Al and nanocrystalline Fe_2O_3. For all grain sizes, NCP46 has higher compressive strengths than NCP64. It can therefore be concluded that the contribution of Al and Fe_2O_3 phases to the mechanical strength of the composites is proportional to their respective volume fractions. Regardless of the grain size, the structure with lower volume fraction of Al is stronger than the structure with higher volume fraction of Al. Strength of composites increases with increase in the volume fraction of Fe_2O_3. Clearly, electrostatic forces in the Fe_2O_3 phase strongly affect the mechanical strength of composites. This observation emphasizes the different roles played by the Al-Fe_2O_3 interface atoms and the Al and Fe_2O_3 grain boundary atoms in the deformation mechanisms.

Figure 4.13 shows the viewgraphs for NCP64 material system 15% compressive strain. From the view graphs it is clear that the maximum atomic movement in the Al phase takes place along Al-Fe_2O_3 interfaces. As pointed out earlier in chapter 3, the identification of structural defects in Fe_2O_3 phase is not possible. Therefore, it seems appropriate that only the Al phase of the composites be analyzed for structure defect formation. Accordingly, in Figure 4.14 plots based on the slip-vector information for both composite systems in compression show only the Al grains.

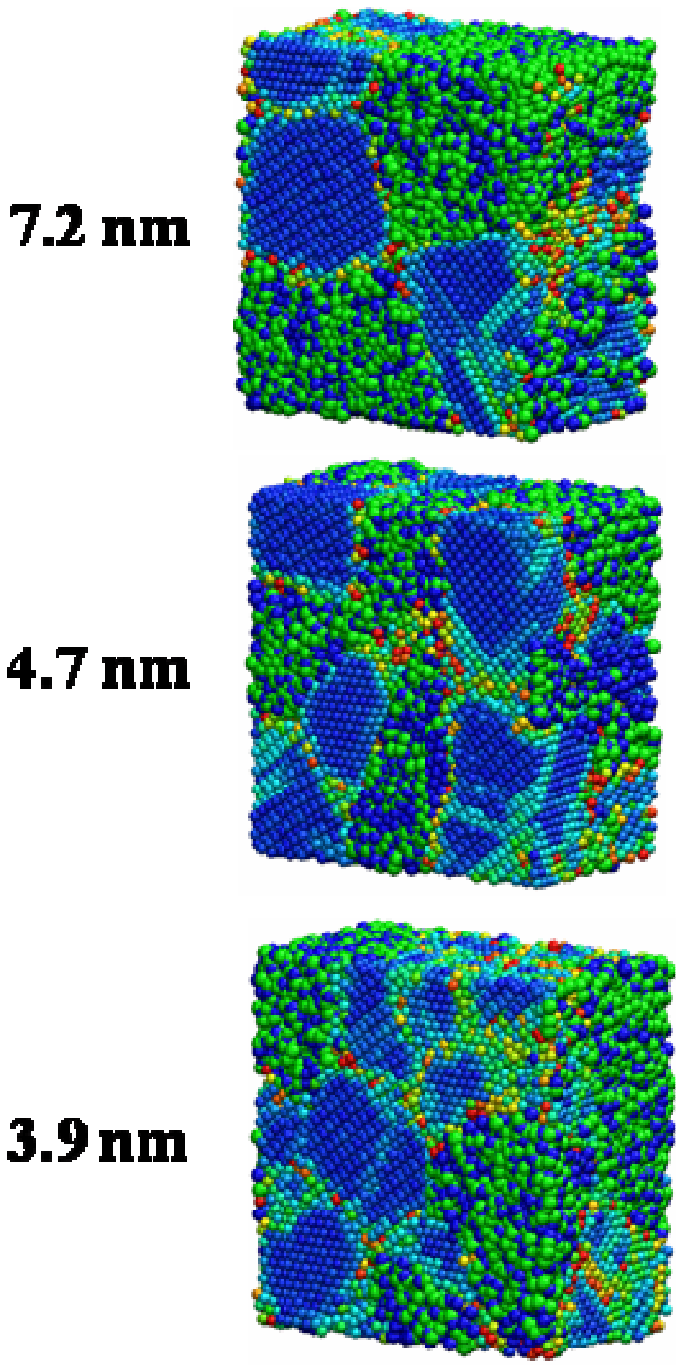

Figure 4.13 Viewgraphs of all three grain sizes of 60%Al+40%Fe_2O_3 nanocomposites at 15% compressive strain (Al atoms are shown using the slip-vector approach, Fe and O atoms are represented by blue and green spheres, respectively)

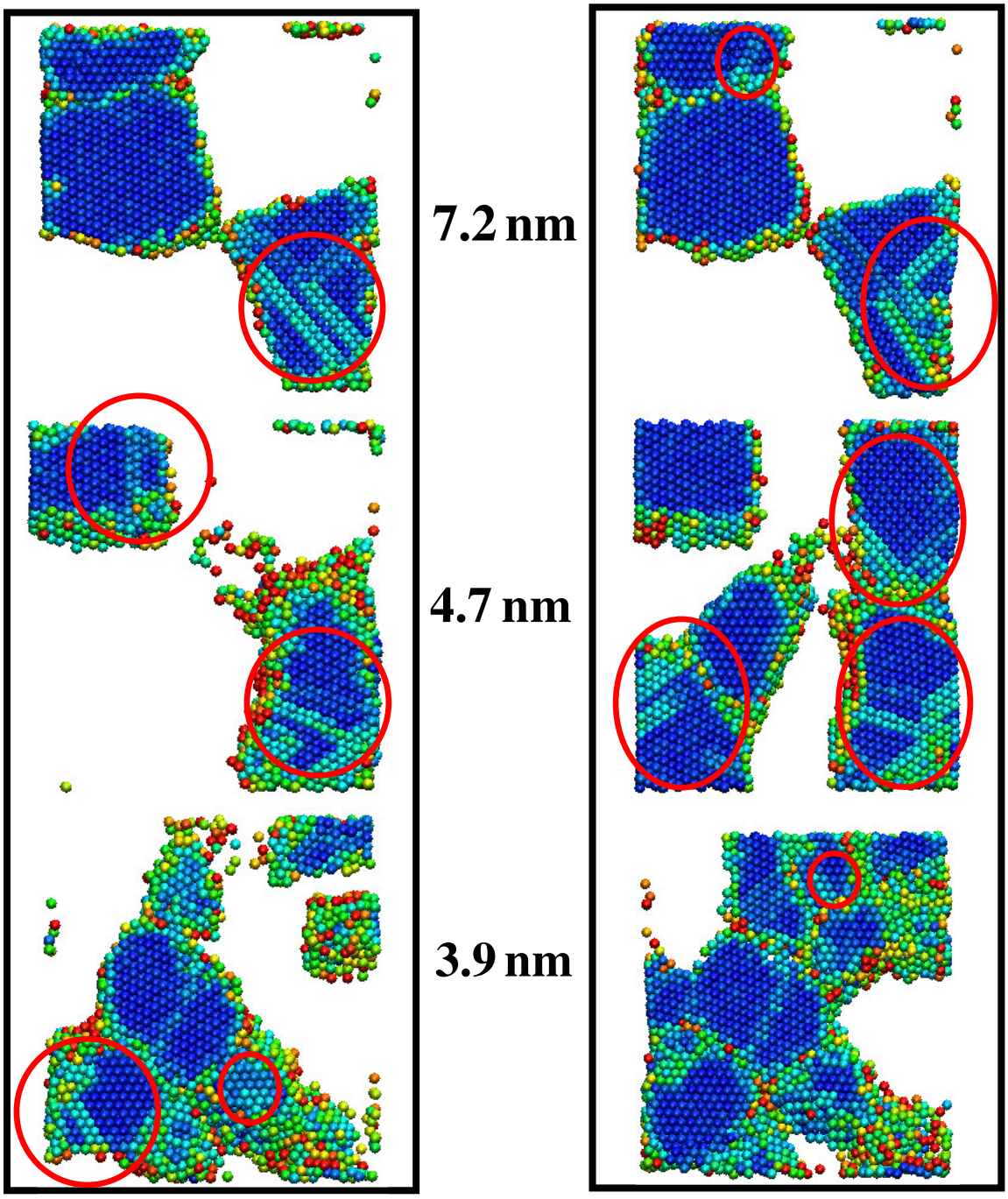

Figure 4.14 Viewgraphs of Al grains for all grain sizes in (a) 40%Al+60%Fe_2O_3 and (b) 60%Al+40%Fe_2O_3 at 15% compressive strain

The compressive strain of 15% for the viewgraphs is chosen since at this strain level sufficient ductility is observed in all structures facilitating easier comparison of the deformation mechanisms. In order to compare the deformation mechanisms in composite systems with that in nanocrystalline Al, the same cross sections as that in Figure 4.5 are shown in the viewgraphs. In addition, the comparison of structural deformation features in NCP46 and NCP64 is carried out for the Al grains common to both systems.

In Figure 4.14, a comparison of the same Al grains in NCP64 and NCP46 reveals that the compressive deformation in NCP46 is accompanied by higher dislocation density than that in NCP64. NCP46 has higher dislocation emission than NCP64. This is due to an increase in the interfacial stresses which, in turn, is caused by an increase in the volume fraction of Fe_2O_3 phase in NCP46. A comparison of the viewgraphs in Figure 4.14 with those for nanocrystalline Al (PAl1, PAl2, and PAl3) in Figure 4.5 reveals that during compression the dislocation emission in both composites is higher than that in nanocrystalline Al. This indicates that the presence of a second phase in the form of Fe_2O_3 induces interfacial stresses at the Al-Fe_2O_3 interfaces that have strong short as well as long range effects to cause escalation in the movement of grain boundary atoms and in the emission of dislocations. Increased interfacial activity at the grain boundaries of the Al grains in composites compared to that at the grain boundaries of the Al grains in nanocrystalline Al causes an increase in strength with changes in the movement of atoms supporting dislocation emission. This is supported by another important observation that the thickness of the Al layer at the Al and Fe_2O_3 interfaces in all composites is higher than the thickness of corresponding grain boundary in nanocrystalline Al. Overall, higher

interfacial stresses due to strong compressive electrostatic forces result in earlier dislocation emission as a function of compressive deformation in Figure 4.14 in comparison to that in Figure 4.5. Clearly, the interfacial stresses at the Al-Fe_2O_3 interfaces strongly affect the deformation mechanism. The electrostatic Al-Fe_2O_3 interfacial forces act against the grain boundary sliding during compressive deformation resulting in higher interfacial stresses. These stresses, in turn, result in an increase in the compressive strength while simultaneously causing earlier emission of dislocations.

The above observations indicate that the mechanisms of deformation in composites during compression are affected primarily by grain boundary sliding and strong compressive electrostatic forces. Offsets provided by stronger electrostatic forces in compression cause the composites to have a direct H-P relation during compressive deformation. In addition, it is also apparent from Figure 4.14 that the stresses induced at the Al-Fe_2O_3 interfaces cause the dislocation emission through the high-angle as well as the low-angle grain boundaries. In order to compare changes in the fraction of atoms along the grain boundaries and in the bulk, the partial Al-Al and total Fe_2O_3 RDFs for both composite systems at all grain sizes are calculated at 15 % compressive strains. In Figure 4.15 and Figure 4.16, the partial Al-Al RDFs for undeformed NCP46 and NCP64 are compared with those at 15 % compressive strains, respectively. In Figure 4.17 and Figure 4.18, the total Fe_2O_3 RDFs for undeformed NCP46 and NCP64 are compared with those at 15 % compressive strains, respectively.

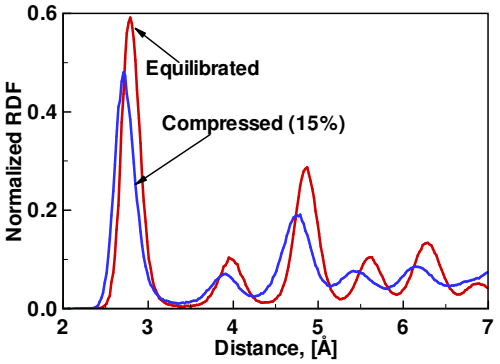

(a)

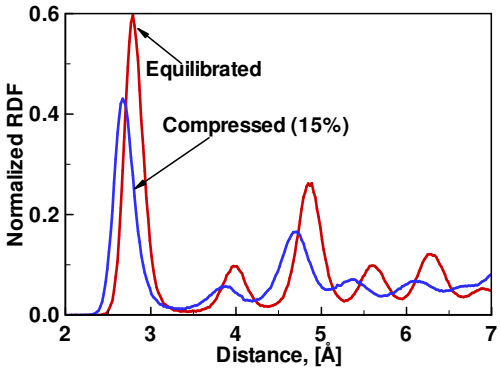

(b)

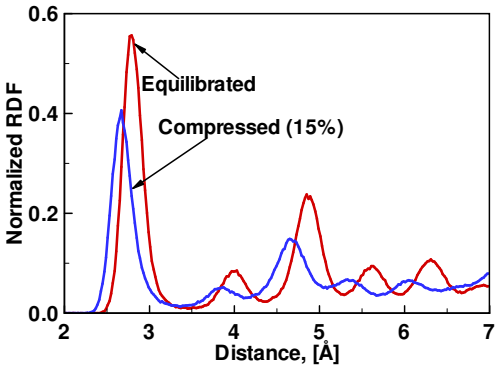

(c)

Figure 4.15 A comparison of the partial Al-Al RDFs of undeformed nanocrystalline 40%Al+60%Fe_2O_3 with that after 15% compressive strains for the grain size (a) 7.2 nm, (b) 4.7 nm, and (c) 3.9 nm

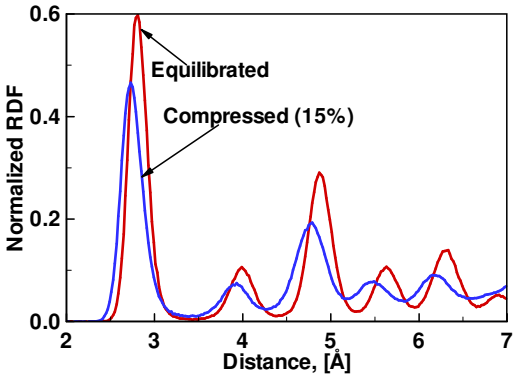

(a)

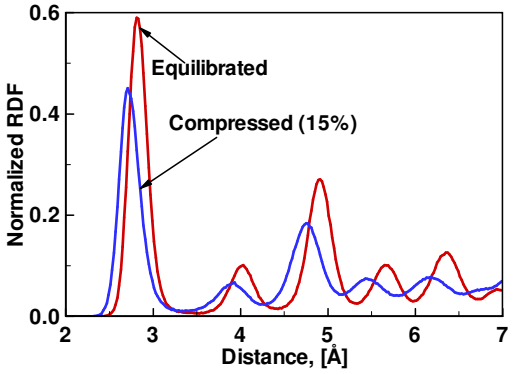

(b)

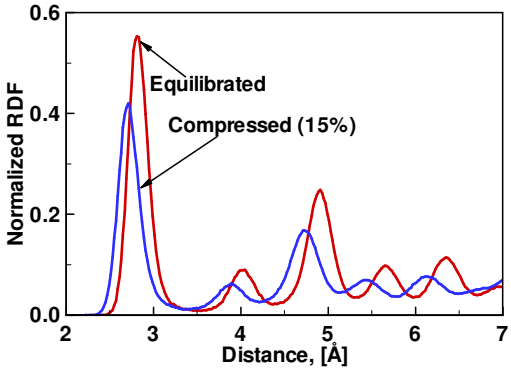

(c)

Figure 4.16 A comparison of the partial Al-Al RDFs of undeformed nanocrystalline 60%Al+40%Fe_2O_3 with that after 15% compressive strains for the grain size (a) 7.2 nm, (b) 4.7 nm, and (c) 3.9 nm

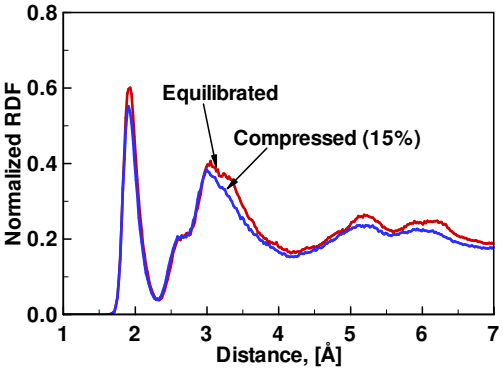

(a)

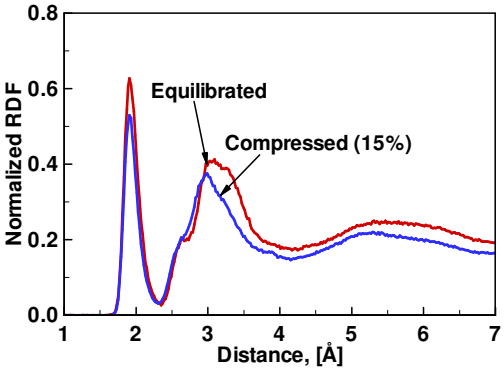

(b)

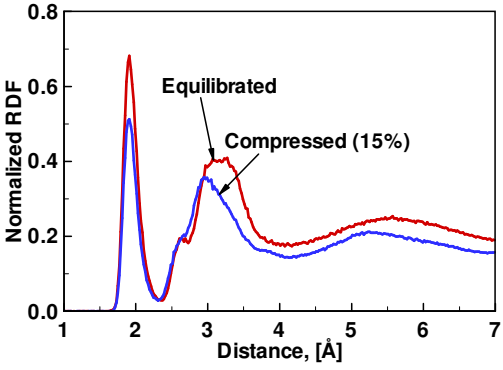

(c)

Figure 4.17 A comparison of the total Fe_2O_3 RDFs of undeformed nanocrystalline 40%Al+60%Fe_2O_3 with that after 15% compressive strains for the grain size (a) 7.2 nm, (b) 4.7 nm, and (c) 3.9 nm

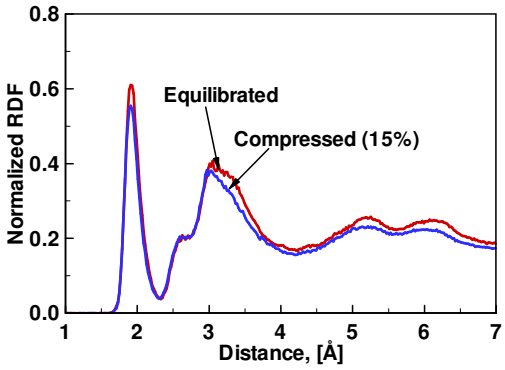

(a)

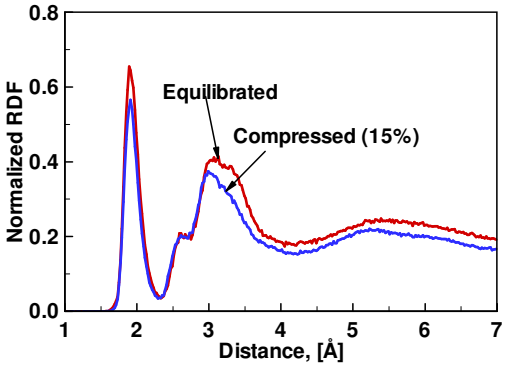

(b)

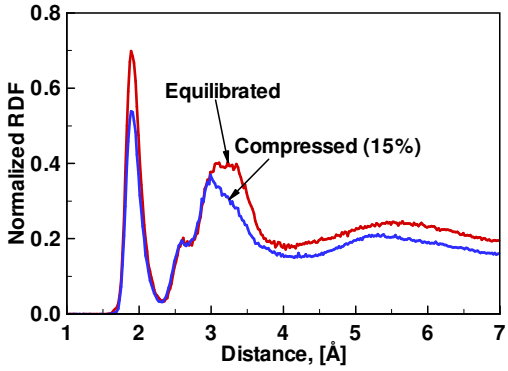

(c)

Figure 4.18 A comparison of the total Fe_2O_3 RDFs of undeformed nanocrystalline 60%Al+40%Fe_2O_3 with that after 15% compressive strains for the grain size (a) 7.2 nm, (b) 4.7 nm, and (c) 3.9 nm

A comparison of the partial Al-Al RDFs in both composite systems in Figure 4.15 and Figure 4.16 with the partial Al-Al RDFs for nanocrystalline Al in Figure 4.6 reveals that at all grain sizes, there is a significant increase in the fraction of Al atoms in defects and grain boundaries with increase in deformation level. In nanocrystalline Al, increase in the fraction of atoms in defects and grain boundaries is greatest in PAl1 and the least in PAl3. In PAl3, there is a significant downward shift in the RDF peaks while the depths of RDF valleys are the same as that in the undeformed configuration. In PAl1 downward shift in the RDF peaks is accompanied by reduction in the depths of RDF valleys indicating a significant increase in the fraction of defect atoms. In the case of NCP46 as well as of NCP64, a significant reduction in the depths of RDF valleys accompanied with the corresponding downward shift in the heights of RDF peaks is observed. In addition, change in the depth of RDF valleys is higher for the larger grain sizes. Increases in the fractions of Al atoms in defects and grain boundaries as a function of compressive strains are higher in composites than in nanocrystalline Al. This indicates that the Al-Fe_2O_3 interfacial stresses strongly affect the deformation mechanism in the Al phase of the composites. Also, increase in the fraction of defect atoms as a function of deformation is higher in NCP46 than in NCP64. The higher the volume fraction of Al in the composite, the lower is the fraction of Al atoms in defects and grain boundaries.

A comparison of Figure 4.17 and Figure 4.18 with Figure 4.10 reveals that in composite systems the structural order of Fe_2O_3 at all grain sizes is not affected significantly by the level of deformation. As explained in chapter 3, Fe_2O_3 in nanocrystalline setting has amorphous structural order. It is therefore natural that the total RDF of the Fe_2O_3 phase

remains unaffected by compression except that the compression will cause a shift in RDF peaks corresponding to the nearest neighbor distance. There is an insignificant difference between the total Fe_2O_3 RDFs in Figure 4.17 and Figure 4.18 and the total Fe_2O_3 RDFs in Figure 4.10.

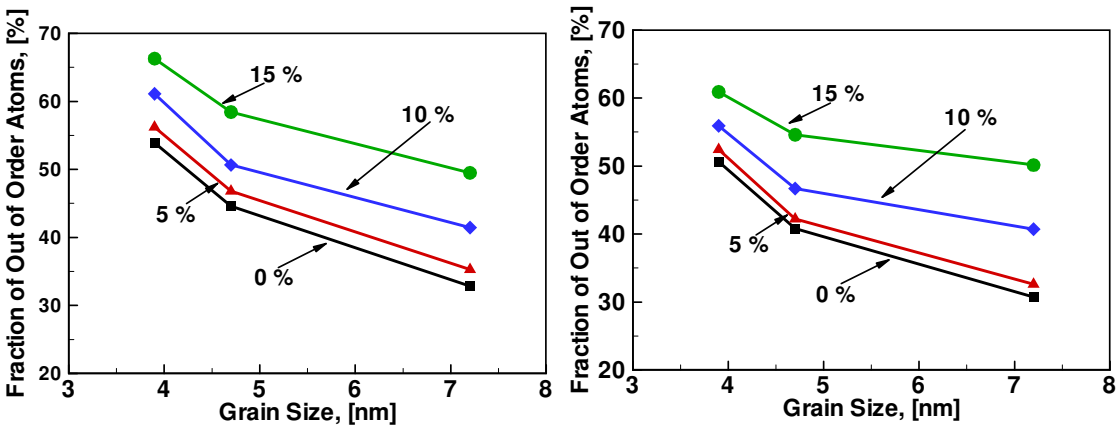

Figure 4.19 A comparison of the fraction of the Al atoms in defect and grain boundaries as a function of grain size at different values of compressive strain in (a) 40%Al+60%Fe_2O_3 and (b) 60%Al+40%Fe_2O_3

In order to further understand the compressive deformation mechanism, the fractions of Al atoms in defects and grain boundaries as a function of the grain size and strain levels are plotted in Figure 4.19. The fractions are calculated using the methodology established earlier in chapter 3 and used earlier in this chapter. For comparison, these plots are compared to the plots in Figure 4.7 (b). A comparison reveals that in composites, an increase in the fraction of Al atoms in defects and grain boundaries as a function of applied strain is higher for structures with larger grain sizes which is similar to the case nanocrystalline Al in Figure 4.7 (b). In both composites, increase in the fraction of Al atoms in defects and grain boundaries as a function of applied strain is higher than that in case of PAl at all grain sizes due to the effect of interfacial stresses caused by the Fe_2O_3

phase. The fraction of Al atoms in defects and grain boundaries in NCP46 is higher than that in NCP64. As pointed out earlier, interfaces of Fe_2O_3 with Al have higher fraction of Al atoms in defects and grain boundaries. Consequently, a smaller grain size and a higher interfacial area cause an increase in the fraction of Al atoms in defects and grain boundaries as a function of applied strains. This is in accordance with the earlier explanations of the effect of Al-Fe_2O_3 interfacial stresses on the increase in the fraction of Al atoms in defects and grain boundaries. Overall, due to the presence of the Fe_2O_3 phase defect formation is increased in the Al phase. Consequently, the Al phase in the composite systems is stiffer than that in nanocrystalline Al.

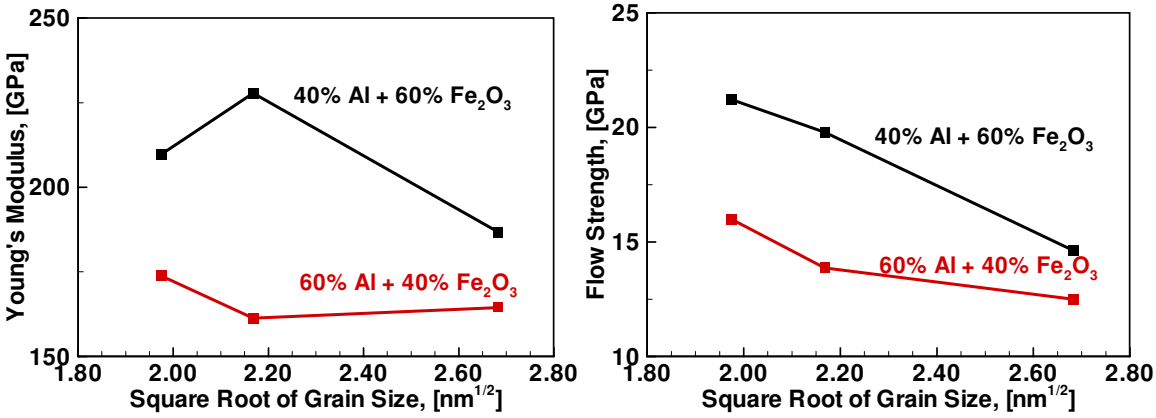

(a) (b)

Figure 4.20 An examination of the dependence of (a) the Young's moduli and (b) the flow strengths on the variation in square root of the average grain size in nanocrystalline 40%Al+60%Fe_2O_3 and 60%Al+40%Fe_2O_3

In order to examine the H-P relations in the composites, the Young's moduli and the flow strengths for NCP46 and NCP64 are plotted as a function of the square root of the average grain size in Figure 4.20. Except for the anamoly in the value of Young's modulus for NCP462, the Young's moduli and the flow strengths for both composite systems show a direct H-P relation. As pointed out earlier, the direct H-P relation in both

composites in compression is a consequence of strong compressive electrostatic forces. In Figure 4.20, slope of the line showing the direct H-P relationship for NCP64 is less than that of the same line for NCP46. This is expected since NCP64 has a higher fraction of the Al phase. In compression, the grain boundary sliding and the electrostatic forces work to cancel out each other resulting in a direct H-P relation with increasingly lower slope with increasing volume fraction of the Al phase. Grain boundary sliding in the Al phase counteracts the effect of compressive electrostatic forces at the Al-Fe_2O_3 interfaces in a more significant manner. Evidence of the strength of electrostatic forces in compression is the tension-compression strength asymmetry visible in both figures. With reduction in the volume fraction of the Fe_2O_3 phase, the effect of compressive electrostatic forces diminishes. From the analyses so far, it is clear that the strengths of composites can be related to the strengths of pure nanocrystalline structures of the individual phases based on the values of volume fractions. Similar to the continuum mixture theories based on the volume fractions, it should be possible to predict the strength of a composite using the strengths of the constituent phases. The next section presents an analysis on this issue.

4.6 Hall-Petch Relation as a Function of Volume Fraction

Figure 4.21 shows plots of the Young's moduli and the flow strengths under compression for all material samples as a function of average grain size. As expected, in both figures the H-P relationships are dependent upon the volume fraction. For composite structures, the H-P relationships lie in between those of PAl and PHt. However, the H-P relationships for the composite structures cannot simply be obtained by combining the H-

P relationships for PAl and PHt based on the values of volume fractions of the Al and Fe_2O_3 phases. This is expected since the tensile and compressive deformation mechanisms in composites are strongly affected by the type of Al-Fe_2O_3 interfaces. Depending upon the orientation of the two phases at an interface, the contribution of the interface to the strength of a composite varies.

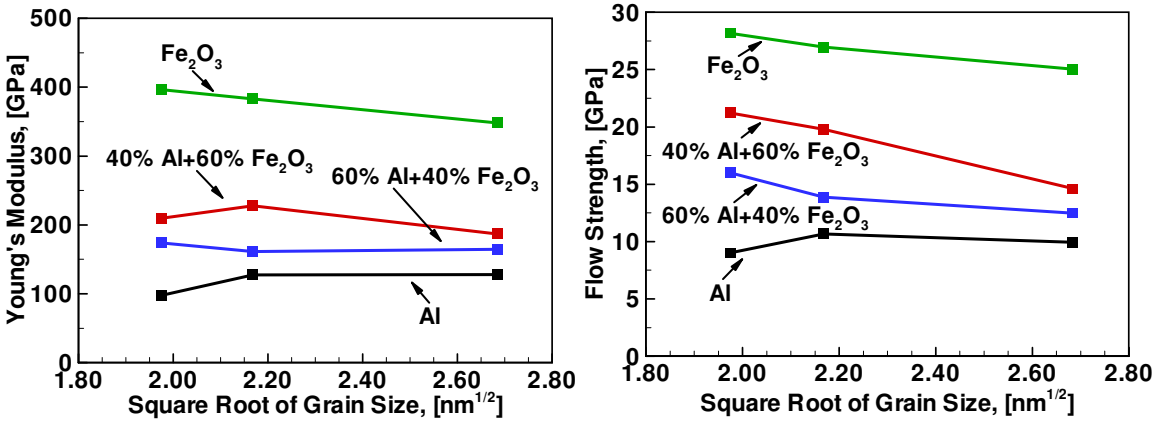

(a) (b)

Figure 4.21 An examination of the dependence of (a) the Young's moduli and (b) the flow strengths on the variation in square root of the grain size in all the nanocrystalline structures during compressive deformation

As shown earlier, the interface has a stronger effect on structures with smaller average grain sizes than on structures with larger average grain sizes because of larger available interfacial area at smaller grain sizes. Consequently, for larger average grain sizes the relationship for the strength of composites based on the volume fraction of the individual phases should be more feasible. This is clear form the strong dependence of the strengths of all the 7.2 nm grain sized structures on volume fractions of the Al and Fe_2O_3 phases. The compressive strengths of composites with the average grain size of 7.2 nm is close to the summation of the strengths of pure phases multiplied by their volume fraction values. This, however, can not be carried out for the structures with average grain sizes of 4.7 nm

and 3.9 nm. At these grain sizes there is a non-proportional increase in the defect and interfacial atoms in all the structures. Consequently, the interfacial and grain boundary atoms have stronger contributions to the calculated strength values.

An important observation from these figures is the direct H-P relations are strongly dependent on the volume fraction of the Fe_2O_3 phase. For structures with higher volume fraction of the Fe_2O_3 phase, stronger direct H-P relation is observed. Electrostatic forces act against the grain boundary sliding during compressive mechanical deformation setting up the direct H-P relation. Accordingly, the slope of the direct H-P relationship is found to reduce as the volume fraction of the Fe_2O_3 phase is reduced. In all structures, the dependence of strengths on the square root of average grain size becomes non-linear as the volume fraction of the Fe_2O_3 phase is reduced. Infact, a linear H-P relation has never been observed in *fcc* metallic nanocrystalline structures at the lengthscale of study in the current analyses. Such strong dependence of the H-P relationships, the strengths, and the deformation mechanisms operating in all nanocrystalline structures on the volume fractions of individual phases, and on the atomic level activity in grain boundaries, defects and interfaces is an important insight for forming continuum relations for multi-component materials with nanoscopic morphology.

4.7 Chapter Insights and Conclusions

In this chapter, analyses of the quasistatic mechanical deformation in nanocrystalline Al, nanocrystalline Fe_2O_3, and their composites with three different average grain sizes (3.9

nm, 4.7 nm, and 7.2nm) are presented. Important findings are summarized in the following:

1. In nanocrystalline Al and Fe_2O_3 structures the Young's modulus values during tension are lower than those found for the corresponding macrocrystalline values. However, during compression the values are higher than the corresponding macrocrystalline values. The flow strength values in nanocrystalline Al and Fe_2O_3 structures approach ideal shear strengths of the corresponding single crystalline systems. In other words, at the lengthscale of analyses the strength of materials approaches the ideal shear strength.
2. In nanocrystalline Al, the deformation mechanism at the lengthscale of analyses is affected by sliding along grain boundaries. The extent of grain boundary sliding is dictated by the fraction of high-angle grain boundaries since the motion of grain boundary atoms occurs primarily along high-angle grain boundaries. It can be concluded that the most of the applied load is shared by the high-angle grain boundaries. Consequently, the dislocation emission during tensile as well as during compressive loading occurs primarily from the high-angle grain boundaries. The effect of the grain boundary mismatch on observed strength values is the most at smaller grain sizes where the fraction of grain boundary atoms is almost 50%. With increase in the average grain size, the effect of grain boundary mismatch on observed strength values diminishes.
3. The deformation mechanisms at the lengthscale of analyses are inherently linked with the high fraction of grain boundary atoms. The underlying mechanism of mechanical

deformation in the Al phase in nanocrystalline Al as well as in composites is the grain boundary sliding. Dislocation emission in Al phase of the composites is higher than that in nanocrystalline Al due to interfacial stresses associated with presence of the Fe_2O_3 phase in the composites. In nanocrystalline Al dislocation emission occurs primarily along the high-angle grain boundaries. In composites, however, the dislocations emission occurs from the high-angle as well as the low-angle grain boundaries. In the case of composites the compressive deformation is also affected by electrostatic forces that results in a reverse H-P relation. In composites, Al phase has higher fraction of defect atoms in comparison to the Al phase in nanocrystalline Al. The fraction increases with increase in the volume fraction of the Fe_2O_3 phase. In nanocrystalline Al, there is minimal increase in the fraction of defect atoms as a function of applied strains for smaller grain sizes. However, the same is not true in the case of composites where the increase is highest for smaller grain sizes under the effect of interfacial stresses. Coupled with increase in the fraction of defect atoms, the Al phase in the composites also has higher strength than the Al phase in nanocrystalline Al.

4. An order of two times tension-compression asymmetry in the Young's modulus values for nanocrystalline Al and Fe_2O_3 structures is observed. The order is three in the case of flow strength values. There is also an asymmetry in the strain levels for plastic deformation during tensile and compressive deformations in nanocrystalline Al and Fe_2O_3 structures. Stress reaches the maximum value earlier during tensile deformation. In the case of nanocrystalline Al, dislocation emission occurs at smaller strains during tensile deformation. However, the mechanism of deformation is the

same during tension and compression. The difference in the movement and the mobility of atoms along grain boundaries causes the deformation as well as the strength tension-compression asymmetry in all structures. The asymmetry is smaller in the beginning of the deformation, since initial positions of grain boundary atoms are the same for tensile as well as for compressive deformations. However, with increase in applied strains, difference in the movement and the mobility of grain boundary atoms results in an escalation in the magnitude of asymmetry. An order of two times asymmetry in the Young's moduli is accentuated to an order of three times asymmetry in the flow strengths. This asymmetry is independent of the structural order. Nanocrystalline Fe_2O_3 with amorphous structural order has the same level of asymmetry as that in the case of nanocrystalline Al. Clearly, it is the difference in the movement of atoms in disordered state along grain boundaries and defects that causes the asymmetry.

5. A direct H-P relation during compression and a reverse H-P relation during tension are observed for nanocrystalline Fe_2O_3. The reverse H-P relation is associated with the sliding of grains along grain boundaries. The direct H-P relation occurs because of strong electrostatic forces in compression. For nanocrystalline Fe_2O_3, the H-P relation is linear during tensile as well as compressive deformations. This can be attributed to denser packing of atoms in nanocrystalline Fe_2O_3 because of its amorphous structural order. As the volume fraction of Fe_2O_3 phase reduces, the linearity in the H-P relation diminishes. For nanocrystalline Al, a linear H-P relation is not observed because of the strong coupling of the high-angle and low-angle grain boundaries with the deformation mechanism.

6. It is not appropriate to obtain the strength of a nanocomposite based on the values of the volume fractions and the strength of the individual phases. The grain boundary mismatch and the interfacial stresses also need to be considered to form an appropriate relation, especially at small nanoscale grain sizes. The effects of grain boundaries and the interfaces diminish with increase in the average grain size. For nanocrystalline structures with grain sizes in the domain where dislocations contribute significantly to the mechanical deformation mechanism, it should be possible to neglect the effects associated with the grain boundary mismatches and the interfacial stresses.

CHAPTER 5

ANALYSES OF THE SHOCK WAVE PROPAGATION

This chapter presents MD simulations of shock wave propagation in <100>, <110>, and <111> oriented single crystalline Al, in <0001> oriented single crystalline Fe_2O_3, and through an interface between {100} surface of Al and {0001} surface of Fe_2O_3. Shock wave propagation analyses in the Al and Fe_2O_3 single crystals focus on analyzing the U_S-U_P relationship as a function of crystalline orientation. The analyses also focus on analyzing the formation and the propagation of defects as shock waves propagates in the single crystalline systems. The shock wave propagation analyses through the interface aim at obtaining an account of the change in structural order in a region surrounding the interface as a function of U_P. The change is structural order is correlated with the changes in pressure, temperature, and energy in the interfacial region to investigate a possibility that the structural transformation may be reactive. Overall, the following research problems are focused upon:

1. U_S-U_P relationships for <100>, <110>, and <111> oriented single crystalline Al and <0001> oriented single crystalline Fe_2O_3;
2. Relationship of the elastic and plastic wave-front velocities with the crystallographic orientations of single crystalline Al;
3. Quantification of the transition of a shock wave from an elastic wave to a plastic wave in terms of the normal and shear stresses in single crystalline Al;

4. Change in structural order of the single crystalline systems as a function of their crystallographic orientations and U_P values;
5. Investigation of the change in structural order at an interface between {100} surface of Al and {0001} surface of Fe_2O_3 during shock wave propagation at a range of U_P values ;
6. Identification of the change in structural order in a region surrounding the interface as a function of U_P; and
7. Quantification of changes in the interfacial structural order in terms of the energy, pressure, and temperature values for investigating a possibility that the structural transformation under shock loading may be reactive.

The next two sections present a review of past work in the area of shock wave propagation analyses using MD. The framework used in the current research is coherently deduced from this information. Thereafter, results of analyses carried out in the current research are presented. The chapter ends with an investigation of the structural transformation between an interface of {100} surface of Al and {0001} surface of Fe_2O_3 as a function of applied shock-loading.

5.1 Why Study Single Crystal Shock Using MD?

The propagation of shock wave in a solid medium involves displacement of an interface between uncompressed material and highly compressed final state at a timescale of the order of ns. The interface is commonly referred to as the shock-front. Currently, the

standard method to analyze the effect of shock wave propagation on a material is microstructural characterization of the samples preserved for post-shock analyses after a shock-wave experiment. Real time measurements of the pressure and the temperature using differential thermal analysis, X-ray diffraction (XRD) line-broadening analysis, and PVDF gauges provide only the qualitative features of the shock-induced deformation, cf. Boslough (1990), Thadhani et al. (1997), and Vandersall and Thadhani (2003). There is an overall limitation on the experiments in terms of simultaneous resolution of the length- and time-scales for analyzing the effect of shock-loading on a material microstructure. In order to accurately characterize the effect of shock wave propagation on a material microstructure, a detailed description of the underlying atomistic processes within the shock-front is necessary. Currently MD calculations are the most potent tool for this purpose.

A wide disparity exists in terms of the length- and time-scales between continuum mechanical systems and MD systems. A macroscopic chunk of metal with dimensions of an inch on a side would have a size of 30 μm a side if divided into one billion cells, which is 100 times bigger than the biggest MD calculational cell. If the continuum calculations were conducted at the maximum Courant-condition timestep (mesh size divided by sound speed), the timestep would be approximately 5 ns, which is approximately 50 times the longest MD calculation time. There is a gap of 100 in lengthscale and 50 in timescale between MD and behemoth engineering calculations, cf. Holian et al. (1999). In continuum simulations, sub-grid physics and chemistry is introduced by means of constitutive models—plastic flow in solids, viscous flow in

fluids, heat conductivity, and failure mechanisms for fracture and fragmentation etc. At the atomic level all of these behaviors are not introduced as input models. Rather, these are the outcome of a cooperative motion of large numbers of atoms moving under the influence of forces from neighboring atoms. Therefore, MD is useful for elucidating unit processes such as mechanisms of the initiation of plastic flow and phase transformation in the heterogeneous nucleation regime for weak shock waves. It fits into overall picture of micro-, meso-, and macro-scopic physics by providing a physically reliable source of input into mesomechanical models, which average over the behavior of large ensembles of atoms, see for example Makarov (1998) and Yano and Horie (1999). One cannot put fundamental physics modeling into continuum level simulations without mesoscale modeling; and mesoscale modeling cannot be done reliably without atomistic input. The length- and time-scales of shock-wave processes, caused by high-velocity impacts, are ideal for investigations of mechanical deformation at the atomic level. Because shock-front velocities are supersonic in the uncompressed medium, the risetime of shock in a solid can be as short as the vibrational period of atoms (or mean collision time in the fluid), which is of the order of 0.3 ps. This time period can be easily resolved in an atomistic MD simulation. Shock-induced chemistry has been analyzed using MD at the semiempirical level by Brenner et al. (1993) and at the level of tight-binding MD by Kress et al. (1999). Atomistic modeling of the shock wave propagation and other high strain rate phenomenon in solids must include a large number of atoms. For this reason, only MD simulations using empirical potentials rather than first-principles or tight binding methods can be used at present. In the near future, it is expected that ultra-fast dynamic x-ray diffraction performed in the shock-wave experiments (either gas-gun, cf.

Rigg and Gupta (2001), or laser-driven, cf. Loveridge-Smith et al. (2001)) will be able to verify the kinds of defect structures that have been seen in MD shock simulations.

MD simulations have been used to study shock waves for over fifty years, cf. Alder and Wainwright (1957), Alder and Wainwright (1970), and Hoover and Ashurst (1975), and Holian et al. (1999). Results of the MD shock simulations in solids have been primarily restricted to perfect crystals, whose yield strength (the threshold for plastic flow, or hugoniot elastic limit (HEL)) is very high (at shock pressures approaching the shear modulus of the material) compared to real polycrystalline or single crystalline samples containing pre-existing defects. The HEL in this case corresponds to strains that are much larger than the strains observed in experiments, cf. Rigg and Gupta (2001), by as much as one order of magnitude. In early 1980s, shock wave structure in solids was demonstrated at Los Alamos national labs in the USA using MD simulations, cf. Holian and Straub (1979) and Holian (1988). These calculations showed that shock waves in single crystals became steady waves by virtue of the transverse displacements of atoms – not by viscous flow, as in fluids, cf. Hoover (1979) and Holian et al. (1980), but rather by plastic flow, or concerted slippage of atoms over each other. Holian et al. (1980) and Zhakhovskii et al. (1999) observed that the velocity distribution in the shock-front, for solids, liquids, and gases, is significantly anisotropic and distinctly in nonequilibrium, being well approximated by a bimodal distribution. Moreover, for solids, the final state can be distinctly nonequilibrium, in that the stress tensor need not be isotropic, and the structures can be highly defective and metastable on very long time-scales. Thus, the approximation of local thermodynamic equilibrium is never obeyed during shock wave

propagation, particularly in the shock-front. However, far behind the shock-front in solids equilibrium is necessarily achieved.

Atomistic simulations of shock wave propagation in LJ solids and metals have revealed that the mechanism of shock-induced plasticity in crystals shows a strong dependence not only on the direction of shock wave propagation, cf. Germann et al. (2000) and Zhakhovskii et al. (2000), but also on the fundamental properties of the crystal lattice. Specifically, under certain conditions of shock-loading, the plastic deformation can occur not as a consequence of the emission of stacking fault arrays at the shock-front but through alternative relaxation mechanisms, such as martensitic transformation, cf. Hirth et al. (1999), or twinning, cf. Christian and Mahajan (1995). In a very early work on the static uniaxial compression of the ⟨100⟩ *fcc* lattice, Mogilevsky observed similar behavior, cf. Mogilevsky (1981), but at noticeably higher strains than the HEL in MD shock simulations. Recently, the appearance of twinning like chevron band patterns has been observed in a uniaxial Hugoniostat simulation, cf. Maillet et al. (2001) and Reed et al. (2003), of a <100> shock wave in a LJ crystal (at 26% compression) preceding a structural change from *fcc* to *hcp* crystal structure. This work is based on the uniaxial strain formulation of Mogilevsky (1981). In 1991, the splitting of shock wave into an elastic and a plastic wave was observed for the first time using MD simulations of polymorphic phase transitions in a two-dimensional material undergoing a dissociative transition. Later, large-scale MD simulations have been used to study shock-induced plasticity, cf. Holian and Lomdahl (1998), Holian et al. (1998), Robertson et al. (1998), Holian et al. (1999), Zhakhovskii et al. (1999), Germann et al. (2000), Selezenev et al.

(2001), Tanguy et al. (2003), and Kum (2003); orientation dependence of shock-induced chemistry, cf. Zybin et al. (2001) and Zybin et al. (2002); detonations, cf. Brenner et al. (1993); melting, cf. Zhakhovskii et al. (2000); amorphization, cf. Chaplot and Sikka (2000); shock wave splitting caused by phase transitions, cf. Robertson et al. (1991) and Kadau et al. (2002); spallation cf. Wagner et al. (1992) and Strachan et al. (2001); and shock-induced structural transformation in Iron, cf. Kadau et al. (2002), Kadau et al. (2004), and Kadau et al. (2001).

In all investigations, shock wave propagation analyses have been carried out primarily in single crystals. An important reason behind this trend is the limitation imposed by the computational speed and memory requirements of computers used for carrying out the analyses. In order to analyze shock wave propagation in a composite polycrystalline structure, we require the average grain-size to be large enough to form a steady shock-front. The typical sizescale requirement for this purpose is of the order of 100 nm which is approximately 10 times higher than the sizescale required for forming a steady shock-front in single crystals, cf. Sapozhnikov et al. (2003). The increase in minimum size for forming a steady shock-front is due to reflections in the shock-front introduced by grain boundaries of polycrystalline materials. Since the maximum sizescale accessible in the simulations carried out in the current research is of the order of 10 nm, the focus is on analyzing shock wave propagation in single crystalline Al, single crystalline Fe_2O_3, and their interfaces. The next section presents the contributions of various researchers in the area of MD shock simulations. The framework for shock wave propagation analyses in the current research is coherently deduced from the contributions.

5.2 Some Important Results from Shock Wave Propagation Analyses in Single Crystalline Systems

Computational time in a MD simulation of shock wave propagation is restricted by the velocity of sound in the shock wave propagation direction. The limitation is of the order of 5 ps for a system with approximately 100 lattice planes in the direction of shock wave propagation. Shock-front thicknesses are, therefore, restricted to be less than 10 nm, with rise times of the order of ps. Accordingly, weak shock waves, whose thicknesses are measured in the fractions of micrometers, with similar sizes of cross-sectional structures, are well beyond the reach of atomistic simulations. MD simulations done a decade ago, cf. Holian (1988), Holian et al. (1991), and Holian and Ravelo (1995), were severely limited in the length of run in the direction of shock wave propagation, in the time required to achieve a steady shock wave, and in the extent of transverse cross-sectional area. Larger samples for shock wave propagation were analyzed for the first time by Holian and Lomdahl in 1998, cf. Holian and Lomdahl (1998). Various <100> oriented *fcc* material samples with 4×4, 6×6, 10×10, 15×15, and 100×100 cross-sectional dimensions were analyzed in their work. With 15×15 *fcc* unit cells in the cross-sectional area, it was demonstrated that instead of a single slip system being triggered by the shock wave, slippage occurred along two different {111}-type planes. This behavior is similar to the idealized model of Smith, cf. Smith (1958), where the shock-front in a perfect lattice creates pairs of dislocations that accommodate increased density of the shocked material. This leaves the crystal orientation virtually unchanged while simultaneously relieving the shear stress.

The snapshots of the propagating shock wave in the work of Holian and Lomdahl (1998) showed that the slippage on the two <111> systems 'compete' with each other, causing the shock-front to become somewhat unstable, with the leading slip system making the front bulge out ahead by two or three lattice spacings (as in the 2D case). The slipped regions are stacking faults and they can be seen by looking at the oncoming shock-front along the shock wave propagation direction. Above a certain shock-strength, the uniaxially compressed material becomes unstable and relaxes to a hydrostatically compressed state by a plasticity mechanism governed primarily by stacking faults. Plastic deformation is accomplished by further emission and motion of dislocations, which are inherently long-range in the volume of their structure and influence. This occurs under a stress one or two orders of magnitude higher than the engineering yield stress (the deformation is of the order of 10%) and under extreme strain rates corresponding to the shock-front velocities of the order of km/sec i.e. nm/ps.

Holian (1988) has shown that transverse plastic flow in perfect crystals relieves the shear stress (one-half the normal-stress difference) that builds up to a maximum at the center of the shock-front. With testing on a cross-sectional area of 100 × 100 *fcc* unit cells in a 10 million atoms simulation cell, the size effect of the cross-sectional area on shock-induced plasticity has been analyzed by Holian and Lomdahl (1998). With 4×4, 6×6, 10×10, or 15×15 cross-sections, at most two stacking faults in the region of transition (U_P/C_0~ 0.2) were observed (C_0 is speed of longitudinal sound wave). With 100×100 cross-section, it was observed that shock wave propagates about 60 lattice planes, at which time a large number of stacking faults are generated relatively quickly. The stacking faults are

distributed randomly on all four <111> slip systems. As the shock wave propagates further, the front becomes pronouncedly non-planar, with slippage appearing to make the front bulge in by as much as 10 lattice planes. When viewed at an arbitrary <100> plane, the intersections emerge as a randomly spaced plaid pattern.

With reduction in the shock-strength from U_P/C_0=0.20 to U_P/C_0=0.18, the shock-induced plasticity dropped sharply to zero. Above the threshold of U_P/C_0=0.18, shock-induced plasticity follows closely the total volumetric strain, U_P/U_S, across the shock-front. The existence of threshold for the 100×100 system is similar to that for the smaller cross-sectional systems, and is clearly due to ideal crystal yielding, rather than due to the periodic boundaries, i.e., system size. This is confirmed by noting that at the critical strength where shock-induced plasticity commences, the maximum non-hydrostatic (shear) pressure times half the volume change across the shock-front is almost *exactly* equal to the potential barrier to the partial dislocation emission (the unstable stacking fault energy). When shock wave reached the free surface and a rarefaction (relief) wave is produced, the stacking faults that were produced by the shock compression were almost annihilated. This is consistent with the observation of much smaller dislocation densities in recovered shocked materials, cf. Zaretsky (1995). This confirmed conclusively that the periodic boundaries used during shock wave simulations don't affect the shock-induced plasticity, particularly in the intermediate regime of shock-strength in which MD shock-simulations are carried out, cf. Holian and Lomdahl (1998).
The effect of pre-existing point defects on the shock-induced plastic deformation has been analyzed by first placing a vacancy, and then a bi-vacancy, in the path of a shock

wave, whose strength had been insufficient to initiate plastic flow in a perfect crystal with the same cross-section, cf. Holian et al. (1998). No plastic deformation was triggered by either of the defects, though there was some structural decoherency in the shock-front as shock wave passed over defects. This is in contrast to the shock wave propagation in 2D lattices, where vacancies are more effective in triggering plastic flow. It was also found that the critical transition in the shock-strength between the elastic and plastic behaviors is essentially independent of the initial temperature T_0 of the single crystal (provided that T_0 is not strictly zero, where purely elastic behavior is 'frozen in', regardless of the shock-strength, cf. Holian and Straub (1979)). The initial temperature was varied all the way from half the melting temperature T_M down to $0.001T_M$, with no visible effect on the threshold in plasticity versus the shock-strength, cf. Holian and Lomdahl (1998).

The effect of pre-existing *extended* defects on the plastic deformation has been tested by replacing the perfectly flat piston face with a 'warped' one having rough surface. With the warped surface, the production of stacking faults was observed after shock wave had traveled nearly 50 lattice planes. This suggests that extended line or surface defects, such as roughness (even on an atomistic scale) at the impact interface, or interior large-scale inhomogeneities in the crystal, such as stacking faults, dislocations, or grain boundaries, will probably trigger plastic flow when a planar shock wave passes over them. The mode of plasticity was the same, i.e. the production of stacking faults by emission of partial dislocations near the shock-front. However, the mechanism of nucleation changed from being heterogeneous at low shock-strengths, requiring the help of pre-existing extended defects, to the homogeneous nucleation, or intrinsic plasticity due to perfect-crystal

yielding at higher shock strengths, cf. Holian and Lomdahl (1998). It can be safely concluded that the shock-induced plasticity is not affected by the PBCs, the initial temperature, and the point defects in the path of a shock wave.

Recently, with an enormous increase in the capability of computers, bigger and longer material samples are being tested under shock wave propagation, see for example Kadau et al. (2001) and Kadau et al. (2004). Shock-simulations by Kadau et al. (2001) and Kadau et al. (2004) on *bcc*-Fe single crystals reveal that above a critical shock strength many small close-packed grains nucleate in shock-compressed crystals. In addition, solitary waves are produced ahead of the shock-front in *fcc* single crystals shocked in the <111> crystallographic orientation. Zybin et al. (2004) carried out MD simulations of shock wave propagation in the <110> crystallographic orientation of diamond. A split two-wave (elastic-plastic) shock structure due to lattice transformation was observed above a piston velocity threshold of U_P~1.8 km/sec corresponding to the Hugoniot elastic limit of 125±15 GPa.

Most of the results cited so far have been obtained using frameworks based on LJ potentials for ideal lattice structures. Therefore, the issue that these results will apply to materials with realistic potential is of contention. Kum (2003) has tested an EAM type potential and a pair potential for shock wave propagation analyses in Nickel single crystals and observed that the structural features during shock wave propagation using the two potentials differ from each other. The prediction of defect properties was better with EAM than with the pair potentials. Similar results were obtained by Bringa et al. (2004)

for single crystalline Cu. These observations point out that it is possible that the features of structural deformation obtained under ideal settings may not be observed if material properties are described using realistic potential. Accordingly, in the current research interest is not only in obtaining the dynamic strength of structures under shock wave propagation but also in examining that whether the physical observations reported earlier using ideal potentials hold true when a realistic potential is used.

The primary focus of the current research is on analyzing shock wave propagation through an interface of {100} surface of Al with {0001} surface of Fe_2O_3. In addition, shock wave propagation in <100>, <110>, and <111> oriented single crystalline Al and in <0001> oriented single crystalline Fe_2O_3 is analyzed. This research is the first such study on this material system using realistic MD potentials. Results obtained from shock wave propagation analyses in single crystalline systems are used as a building block in the reaction initiation study through the Al-Fe_2O_3 interface. The framework of analyses, however, is based on the results obtained by other researchers so far. Three important steps of the framework are:

1. Calculations of the shock wave profile;
2. Calculations of the interatomic forces; and
3. Calculation of the shock wave hugoniot.

The next subsections describe these steps.

5.2.1 Shock Wave Profile Calculations

Shock wave profile calculations yield P_{xx}, shear stress (τ), temperature (T), mass velocity in the shock wave propagation direction (V_x), and the potential energy per atom (E_a) as a function of position along the shock wave propagation direction in a single crystalline block at a particular time instance of the shock wave propagation. The profiles are obtained by lumping particles and their individual kinetic and potential contributions into rectangular bins along the direction of shock wave propagation, cf. Hardy (1981). The center point of a bin denotes the spatial location of a property calculated for particles in the bin. The particles are lumped into bins in order of their initial longitudinal coordinates. In other words, before the start of a simulation a bin number related to a particle is identified based on its position along the direction of shock wave propagation. The particle belongs to that bin number for the rest of the simulation. Hence, bin size is not constant but the number of particles in each bin is. These planar Lagrangian mass elements developed by Holian, cf. Holian (1988), lead to smoother shock wave profiles than fixed Eulerian boxes, particularly in the case of solids. The shock wave profiles are further smoothed by a running average across three adjacent bins. The formulas for determining the local properties during shock wave propagation are based on Hardy's modification of the microscopic formulas of Irving and Kirkwood, cf. Hardy (1981) and Root et al. (2003). For calculating the temperature and the mass velocity, the center of mass velocity of each bin is subtracted from the individual particle velocities in the bin, cf. Hardy (1981). The localization function for T, V_x, and E_a is simply 1/AL; A is the cross-sectional area of a bin and L is the length of the bin. As pointed out earlier in

chapter 3, stress calculations based on Hardy's method, cf. Hardy (1981), have been shown to be more general cases of virial stress formulation of Zhou, cf. Zhou (2003). We use Hardy's method, cf. Hardy (1981), to calculates stress profiles. For stress calculations, the contribution of a particular particle to the spatial point defined by a bin is based on its position in the bin. If the particle is at the center then its contribution to the stress at the spatial point is considered to be 100%. However, if the particle is located at the edge of the bin, its contribution to the stress at the spatial point is neglected. The shock wave propagation analyses are carried out at eight different impact velocity values ranging from 0.5 km/sec to 4.0 km/sec at an interval of 0.5 km/sec. As explained earlier in chapter 1, at impact velocities lower than 0.5 km/sec the shock-front widths are of the order of micrometers. These shock-front widths are inaccessible for MD simulations which can only be carried out at the lengthscales of the order of nm.

5.2.2 Interatomic Potential for Calculations of Forces

Kum (2003) examined shock wave propagation in the <100>, <111>, and <110> crystallographic orientations of Ni single crystals using two different potentials: 1. Morse type pair potentials, 2. EAM potential. At a particular U_P value above the critical speed for initiating plastic waves, the analyses revealed that the EAM and Morse potentials show differences in the features of shock wave propagation. In terms of crystal deformation, the EAM potential shows a greater degree of plasticity than the pair potential. The wave speed for the EAM potential is also found to be smaller than that calculated using the Morse potential. Further structural analyses revealed that the

difference in the results between the EAM and Morse-type potentials is primarily due to different unstable stacking fault energy predicted by the two potentials. The interaction potential does not affect shock-induced slippage as much as the geometry of crystal lattice. Shock-induced slippage is observed in materials with both the LJ pair-potential and the EAM many-body potential (e.g., copper, Holian et al. (1991)).

Consistent with the easier generation of dislocations, however, the EAM systems have a lower threshold shock strength for plastic flow, cf. Holian et al. (1991). Shock Hugoniot simulations for Cu by Bringa et al. (2004) revealed that the EAM potentials more closely reproduce the experimental relationships in comparison with the LJ or similar pair potentials. Simulations with different potentials by Kadau et al. (2002) and Kadau et al. (2001) have shown that the qualitative results do not depend on the specific potential, but the quantitative data such as the pressure threshold for the transformation does. This universal trend indicates that realistic potentials are required in order to have the right quantifications of the qualitative features observed during shock wave propagation analyses. EAM potentials with parameters calibrated to cohesive energy, lattice EOS, elastic constants, bulk modulus, and stacking fault and surface energies show features of shock wave propagation that are in close agreement with the experimental results. Consequently, it can be concluded that the features of shock wave propagation observed in the current research represent realistic material behavior.

5.2.3 Hugoniot Calculations

The density ρ of a shocked material increases with increase in the shock-strength. Because the sound velocity is linearly proportional to ρ, the vibrational frequency of a compressed solid increases with ρ in a rapid nonlinear fashion (approximately the power 4/3). The volumetric strain ε caused by a shock wave is given as,

$$\varepsilon = 1 - \frac{V}{V_0} = 1 - \frac{\rho_0}{\rho} = \frac{U_p}{U_s}. \tag{5.1}$$

(V is the volume). In general, the shock-front thickness is inversely proportional to the shock-strength, or strain ε, cf. Swegle and Grady (1985). In the shock-front, P_{xx} is larger than the transverse components, due to uniaxial compression. This leads to a buildup of the shear stress τ:

$$2\tau = P_{xx} - \tfrac{1}{2}(P_{yy} + P_{zz}) \cdot \tag{5.2}$$

As plastic deformation occurs, the shear stress is relieved, though not necessarily all the way back to zero, as it would be in a fluid-like state. For proper understanding of the failure of a material to shock loading, it is important to understand the profiles of P_{xx} and 2τ along the length of shock wave propagation. A comparison of these quantities with each other and with material constants provides insights into the dynamic strength of a

material to shock failure. However, to characterize the behavior of a material for whole spectrum of shock loading a mathematical description in terms of the equation of state (pressure vs. volume, pressure vs. temperature) is needed. Such a description is usually obtained using experimental characterizations, cf. Vandersall and Thadhani (2003). Another approach to obtain such description is to use MD simulations to calculate U_S-U_P relations, cf. Kadau et al. (2002). Along with the pressure and temperature jump conditions at the shock-front, the U_S-U_P relations can be used to calculate the equation of state of a material. In addition, a combination of information from the U_S-U_P relations and from the profiles of P_{xx} and 2τ tensors gives important information about a material's elastic and plastic strengths under shock loading, cf. Kadau et al. (2002). In the following, shock wave profiles of T, V_x, E_a, P_{xx} and 2τ are used with information from the U_S-U_P relations and from the RDFs of deformed structures to analyze the effects of shock wave propagation on structural deformation. The next section presents the shock wave propagation analyses in <100>, <110>, and <110> oriented single crystalline Al.

5.3 Shock Wave Propagation analyses in <100>, <110>, and <111> Oriented Single Crystalline Al

MD shock simulations are carried out at 8 different U_P values varying from 0.5 km/sec to 4.0 km/sec with an interval of 0.5 km/sec. The shock-front velocity is calculated using the methodology established earlier in chapter 3. In this methodology, by observing the change in position of the shock-front as a function of simulation time, the value of U_S-U_P and, therefore, U_S is calculated. The elastic wave-front in the shock wave propagation direction is located at the position where the uniaxial compression begins. The plastic

wave-front in the shock wave propagation direction is located by visualizing the structural deformation using the slip-vector approach. The slip-vector magnitude of an atom is zero if its neighbors experience uniform translation during structural deformation. However, it becomes non-zero if the relative movement of neighbors results in the atomic slip, cf. for example Zimmerman et al. (2001). Accordingly, for uniaxial elastic compression the slip-vector magnitude is zero. Plastic deformation is easily recognizable by non-zero slip-vector values.

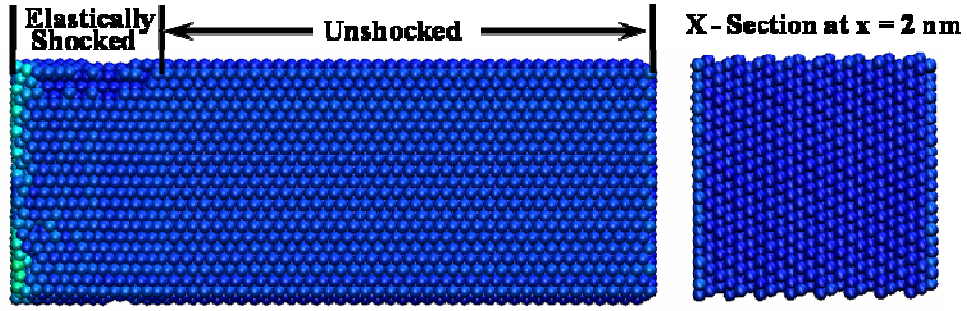

(a)

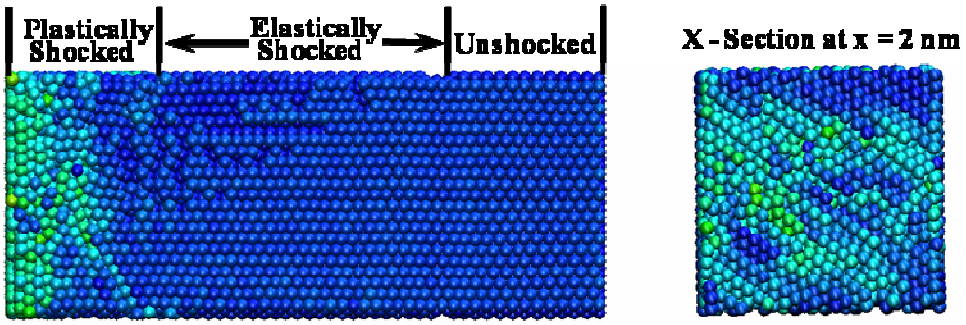

(b)

Figure 5.1 Illustration of (a) the elastic shock-front, (b) the elastic and plastic shock-fronts in <110> oriented single crystalline Al at U_p=2.0 km/sec (Impact plane is located at the far left of the slabs)

Figure 5.1 illustrates this for shock wave propagation in a <110> oriented single crystalline Al structure. In Figure 5.1 (a), magnitude of the slip-vector for every atom is zero for elastically compressed region. However, in Figure 5.1 (b), a plastic wave-front

can easily be located at a position where the slip-vector magnitude becomes non-zero. A distinctive movement of dislocations and the corresponding stacking fault formation to release the stress build up caused by shock wave propagation is clearly visible in the figure. The figure also shows cross-sections of the structures under shock compression. The cross-sections are located at a few lattice planes away from the impact plane. Accordingly, the cross-section in Figure 5.1 (a) is in elastically deformed region and in Figure 5.1 (b) it is in plastically deformed region. It is evident that there is significant transverse movement of atoms in the plastically deformed region. The transverse movement is, however, not at all present in the elastically deformed region because of the uniaxial compression.

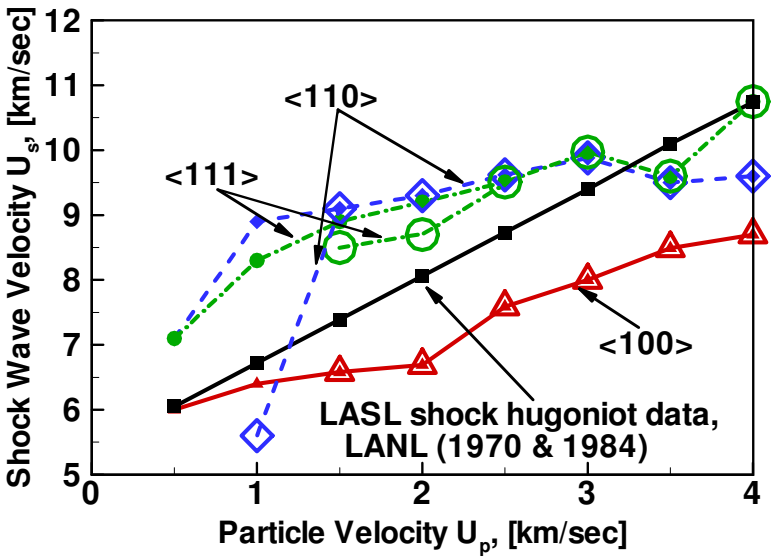

Figure 5.2 A comparison of the U_S-U_P relationships for <100>, <110>, and <111> oriented single crystalline Al with experimental polycrystalline relation

Figure 5.2 shows the U_S-U_P relationships for <100>, <110>, and <111> oriented single crystalline Al and compares them with the experimental polycrystalline Al relationship by Marsh (1980). As shown, the shock-front velocity for various crystallographic

orientations compares favorably with the experimental polycrystalline data. In <100> and <111> oriented single crystalline Al, the plastic deformation begins at U_P=1.5 km/sec that corresponds to the transition threshold for observing a two-wave split structure (elastic wave followed by a plastic wave) in single crystalline Al, cf. Germann et al. (2000). In <110> oriented single crystalline Al the threshold velocity for initiating plastic deformation is 1.0 km/sec. This difference may be caused by different slip-systems getting activated at different times in different orientation of single crystalline Al. Below the threshold U_P value for the plastic deformation only the elastic wave propagation is observed in all single crystalline orientations. Beginning at the threshold U_P value for the plastic deformation, a split shock wave structure is observed in all orientations i.e. the shock wave has an elastic precursor ahead of a lagging plastic transformation wave. For higher shock-strengths, a single overdriven plastic wave is obtained in all orientations. In an overdriven plastic wave, the velocity of the plastic transformation front is very close to the elastic wave-front velocity. The observation of an elastic precursor before the plastic transformation wave is in agreement with continuum mechanical calculations, see for example Zel'dovich and Raizer (1968) and Graham (1993).

The mode of plastic deformation in steady elastic shocks is the onset of transverse distortion caused by high values of the transverse shear stress. Above the HEL, the steady elastic precursor in the elastic-plastic split shock wave structure exhibits a transverse distortion which is the beginning of a shear deformation that accompanies the plastic wave. In the plastic wave, the deformation is irreversible—atoms slip into new positions that are a fraction of the lattice spacing (something of the order of one-half) away from

their initial positions. The coupling in the transverse and longitudinal directions dictates the scale of transverse plastic deformation. As pointed out earlier, if the cross-section is too small, the distortion will be locked *out*, leading to an ever-growing, non-steady shock wave profile, cf. Asay (1993). This behavior is typical for a material that exhibits phase transformations under shock loading. For the single crystalline systems under consideration the active slip systems in transverse orientations are different i.e. {100} type cubic slip systems for the <100> orientation, {112} type secondary slip systems for the <110> orientation, and {110} type secondary slip systems for the <111> orientation. Accordingly, the extent of slippage and defect formation is expected to be higher for the <110> and <111> crystallographic orientations. Shock-front speed for the <110> orientation is the highest because of denser packing of atoms in the {111} planes that are transverse to the <110> orientation. Different elastic properties for various orientations result in the variation of the elastic part of U_S-U_P relationship with crystallographic orientations. Similarly, initiation of the elastic-plastic split shock wave structure formation for different orientations also occurs at different U_P values. The plastic distortion occurs in order to release shear stresses along the directions transverse to the shock wave propagation direction. Accordingly, the orientations with higher Schmidt factor in the transverse directions have lower threshold U_P for forming the elastic-plastic split shock wave. Linear fits to the U_S-U_P relationships of all orientations in Figure 5.2 are;

$$U_S = 5.46 + 0.822\, U_P \tag{5.3}$$

for the <100> orientation,

$$U_S = 7.88 + 0.551\, U_P \tag{5.4}$$

for the <110> orientation, and

$$U_S = 7.26 + 0.847\, U_P \tag{5.5}$$

for the <111> orientation. As explained earlier, the HEL occurs at U_P=1.5 km/sec for the <100> and <111> Al orientations and at U_P=1.5 km/sec for the <110> orientation correspond. The corresponding transition pressure for all three orientations is approximately 1±0.5 GPa which is close to the experimental HEL of approximately 1 GPa in experiments for polycrystalline Al, cf. Lundergan and Herrman (1962) and Razorenov et al. (2002).

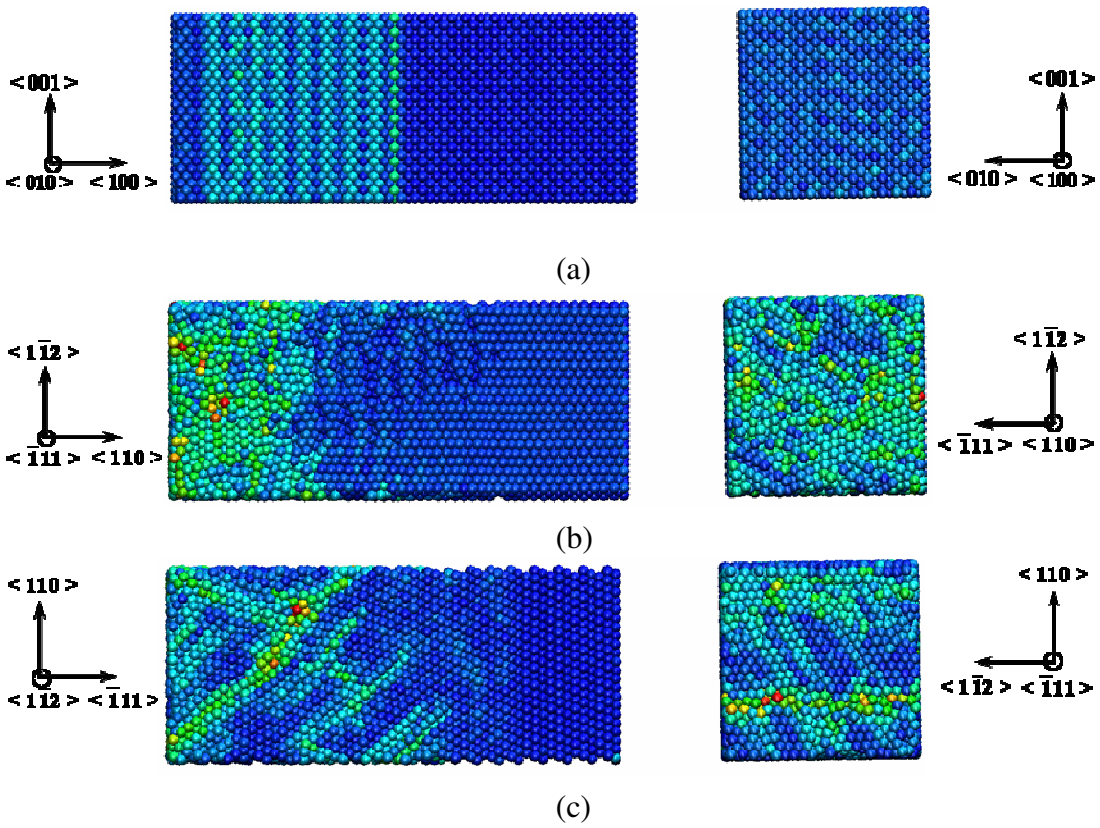

Figure 5.3 A comparison of structural deformation caused by shock wave propagation in (a) <100>, (b) <110>, and (c) <111> oriented single crystalline Al at U_p=2.0 km/sec

In the current research, the primary focus is on quantitatively exploring the relationships among the extent of plastic deformation, the orientation of single crystals, and the values of U_P. In Figure 5.2, beyond U_P=1.5 km/sec the plastic wave front velocity approaches the elastic wave front velocity for all orientations. Accordingly, two different U_P values, viz., 2.0 km/sec and 3.0 km/sec are chosen to explore the plastic deformation caused by shock waves in detail. In Figure 5.3, the structural deformation in all three single crystalline orientations of Al at time t=1.5 ps under U_P=2.0 km/sec is shown. For further elaboration, the cross-sectional views of a plane at a few lattice spacings away from the impact plane are also shown. In all the orientations, the shear stress release is along multiple slip planes. For the <100> orientation, transverse {100} cubic slip systems are active. However, majority of atomic movement occurs along oblique <111> planes. Clearly, the shear strength along oblique planes is smaller than the shear strength along transverse cubic slip planes. In the <110> orientation, the slip occurs on transverse {111} planes along <110> as well as $\langle 1\bar{1}2 \rangle$ crystallographic orientations. In <111> oriented single crystalline Al, the atomic slip is primarily along transverse <110> direction as apparent from the cross-sectional figure. Cross-sectional views for the <110> and <111> orientations also indicate emission of Frank partials (sessile dislocations) from {111} planes in both orientations. Magnitude of the atomic slip as well as of the velocity of plastic shock-front is significantly higher for the <110> and <111> orientations in comparison to that for the <100> orientation. The magnitude of plastic distortion increases with increase in the U_P values for all three orientations, see Figure 5.4. In <100> orientated single crystalline Al, non-equality of the transverse components of stress tensor stimulates formation of stacking faults along 45^o to the shock wave

propagation direction. In <111> and <110> orientated single crystalline Al, the formation of stacking faults is along the primary and secondary slip planes transverse to and along the shock wave propagation direction. Clearly, {111} type slip planes are the most dominant slip planes for all crystalline orientations. However, these slip planes become active at different times and in different magnitudes depending upon the shock-strength and the single crystalline orientation. At U_P=2.0 km/sec, the plastic wave lags behind the elastic wave, see Figure 5.3. At U_P=3.0 km/sec the plastic wave turns into an overdriven wave catching up the elastic wave front, see Figure 5.4.

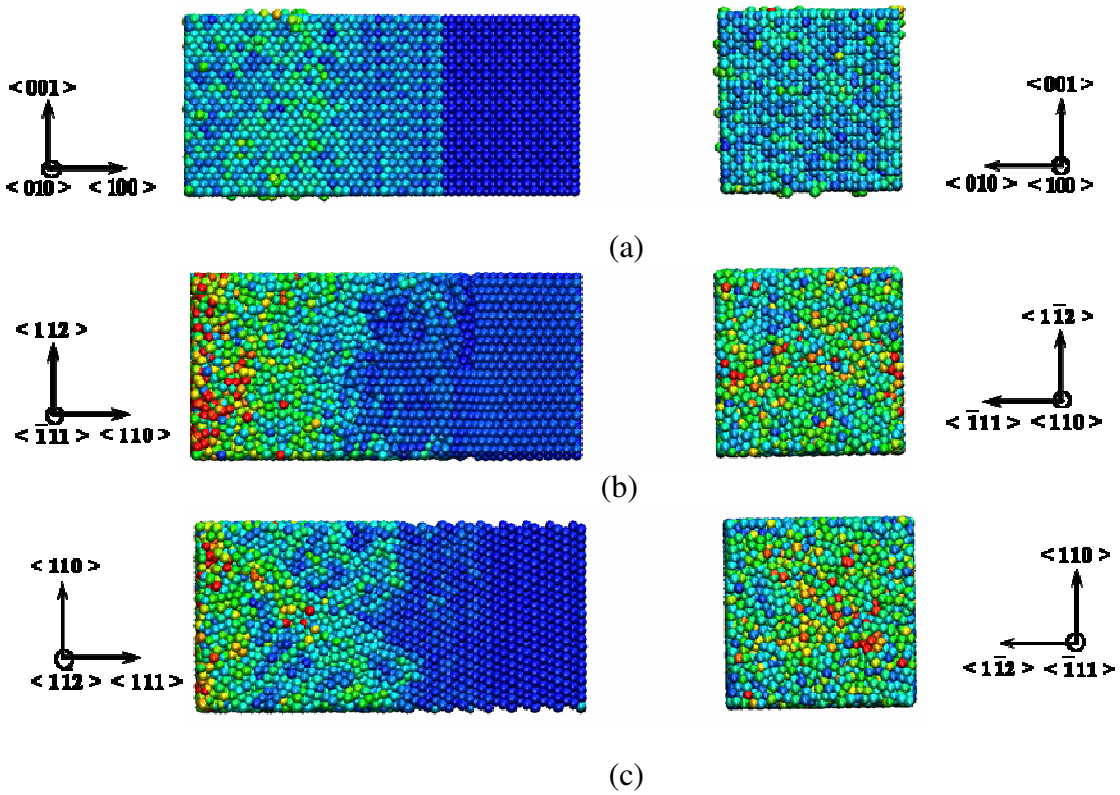

Figure 5.4 A Comparison of structural deformation caused by shock wave propagation in (a) <100>, (b) <110>, and (c) <111> oriented single crystalline Al at U_p=3.0 km/sec

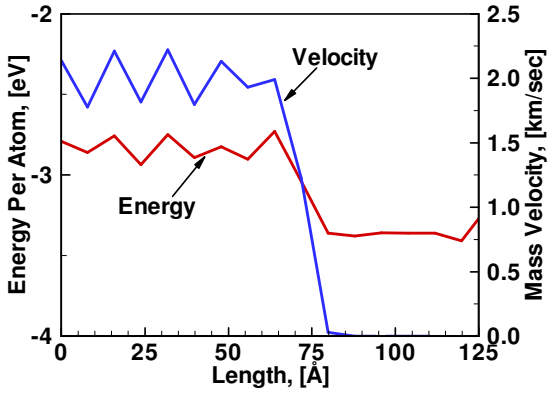

(a)

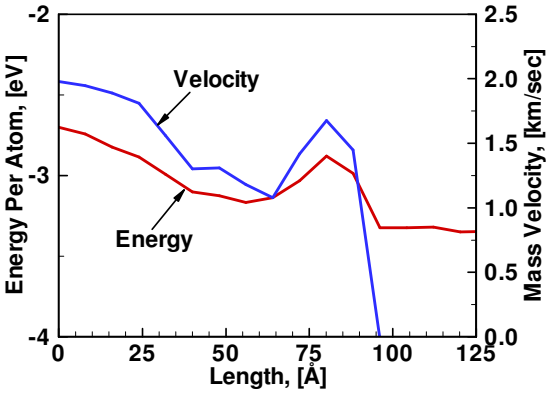

(b)

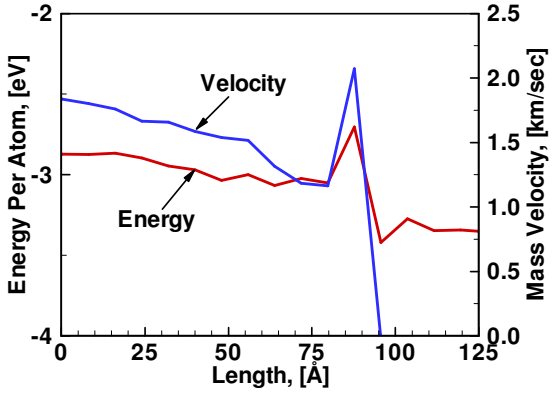

(c)

Figure 5.5 The potential energy per atom and mass velocity profiles in (a) <100>, (b) <110>, and (c) <111> oriented single crystalline Al at U_p=2.0 km/sec and at time t=1.5 ps

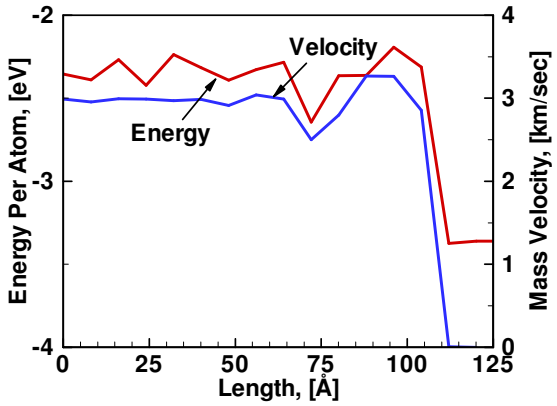

(a)

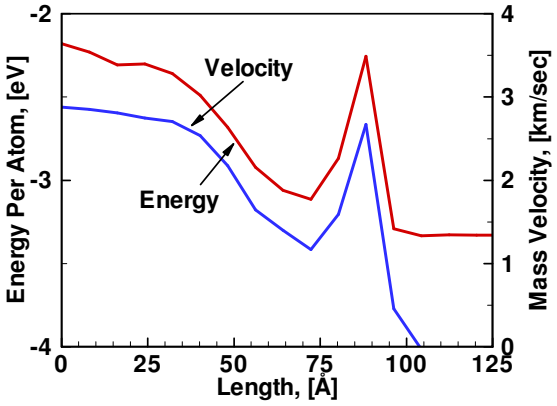

(b)

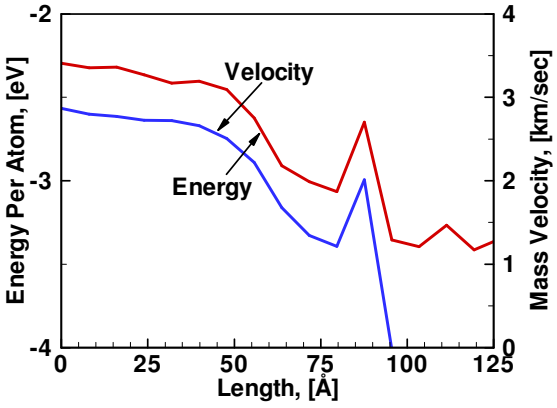

(c)

Figure 5.6 The potential energy per atom and mass velocity profiles in (a) <100>, (b) <110>, and (c) <111> oriented single crystalline Al at U_p=3.0 km/sec and at time t=1.5 ps

The qualitative observations of plastic deformation in single crystalline Al agree well with the findings of Germann et al. (2000) for a *fcc*-crystalline material described by LJ potential. However, quantitative calculations and visual observations in this research provide a clearer picture of the effect of shock wave propagation in single crystalline Al. The dynamics of defects during shock wave propagation depends strongly on the shock-strength and on the crystallographic orientation for shock wave propagation. The elastic and plastic shock-front speeds as well as the extent of plastic deformation are strongly dependent upon the crystallographic orientation. The material response is entirely elastic below HEL, above which plastic deformation begins. Different slip systems become active in different crystalline orientations in different manners. Some slip systems are harder to activate than others, and their numbers depend on the geometrical considerations related to the crystallographic orientations. In polycrystalline materials, and even in single crystals that contain dislocations and other sources of heterogeneous nucleation sites, the HEL occurs at very low strains (~ 2%), cf. Kadau et al. (2004). In perfect single crystals here, the HEL occurs at extreme levels of deformation (~ 10–15%).

Figure 5.5 and Figure 5.6 show the potential energy per atom and the mass-velocity profiles for shock wave propagation at U_p=2.0 km/sec and 3.0 km/sec, respectively, in all three orientations. From the profiles, split elastic-plastic shock wave structures are apparent for the <110> and <111> orientations. However, for <100> orientation such division is observed only in Figure 5.6. In Figure 5.5 (a) the potential energy per atom rises from approximately -3.3 eV/atom before the shock-front to -2.9 eV/atom after the

shock-front and the mass velocity rises from zero before the shock-front to 2.0 km/sec after the shock-front. Following a steep rise in both profiles at the shock-front there is a small dip in the energy and the mass velocity profile for all orientations. This dip determines the shock-front width. The shock-front width therefore represents a region in which the change form undeformed structural state to completely deformed structural state takes place. In Figure 5.5 (b) and (c), a similar rise in the velocity and energy/atom profiles at the shock-front is observed. However, the dip in the velocity and energy/atom profiles is steeper than that in Figure 5.5 (a). This indicates that the elastic-plastic split in the shock wave structure is more pronounced for the <110> and <111> orientations owing to the greater possibility of shear release (Schmidt factors in transverse directions are higher for these orientations). The shock-front width at U_P=2.0 km/sec is found to be approximately 20 Å for the <100> orientation, 15 Å for the <110> orientation, and 10 Å for the <111> orientation. Observations of the profiles in Figure 5.6 at U_P=3.0 km/sec point to the similar features of structural deformation. Dual elastic-plastic shock-front is more pronounced in the <100> orientated single crystalline Al in Figure 5.6 (a) than that in Figure 5.5 (a). The shock-front width is reduced in all the single crystalline orientations because of the formation of a plastically overdriven wave. The shock-front width is approximately 15 Å for <100>, 10 Å for <110>, and 10 Å for <111> orientations. The wave profiles for the <110> and <111> orientations in Figure 5.5 and Figure 5.6 show a rise in the energy and the mass velocity at a few lattice spacings from the shock front. These regions of the profiles correspond to severe plastic deformation and mixing. The rise becomes pronounced with increasing U_P values. Similar rise is not observed for the <100> orientation. Higher amenability of the <110> and <111>

orientations towards transverse slippage (higher Schmidt factor) is the primary reason. Larger extent of plastic deformation results ultimately in higher mixing and consequently in higher mass velocity and higher potential energy. This observation also establishes that in the single crystalline systems the mixing zone lies just behind the shock front.

In order to clearly understand the nature of plastic deformation the normal stress, shear stress, and temperature profiles along the shock wave propagation direction are plotted in Figure 5.7 and Figure 5.8 for U_P=2.0 km/sec and 3.0 km/sec, respectively. The shear release and corresponding dual elastic-plastic wave-front is evident from the figures. Figure 5.7 shows the profiles for all three orientations at U_p=2.0 km/sec. In <100> oriented single crystalline Al, the magnitude of shear stress along the length of shock wave propagation is found to be nearly the same as that of the normal stress. There is a small difference between the shear stress and normal stress near the impact plane indicating very little plastic deformation. However, in the <110> and <111> orientations (Figure 5.7 (b) and (c), respectively) there is a significant difference in the shear and normal stress profiles along the shock wave propagation direction. The value of shear stress is the same as that of normal stress at the shock-front. However, there is shear release beyond the shock-front with shear stress reaching to zero value within a distance of few nm from the shock-front indicating plastic transformation. In the case of <111> orientation, see Figure 5.7 (c), the shear release occurs at a smaller distance (~ 3nm) from the shock-front than in the <110> orientation (~4 nm), see Figure 5.7 (b). The ratio of maximum normal stress to the maximum shear stress depends upon the single crystalline orientation.

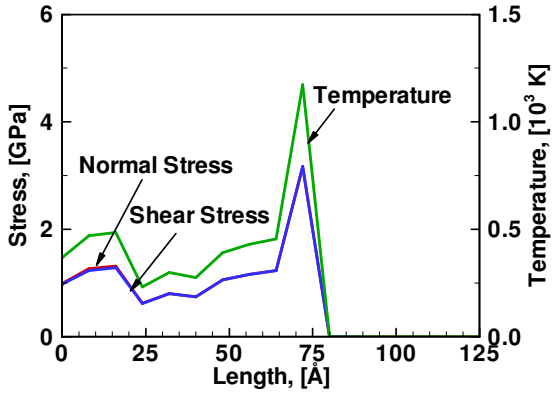

(a)

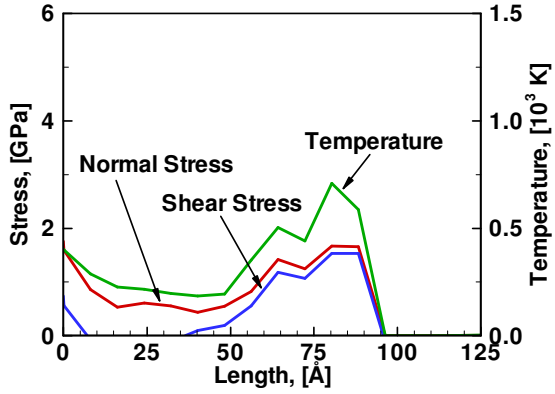

(b)

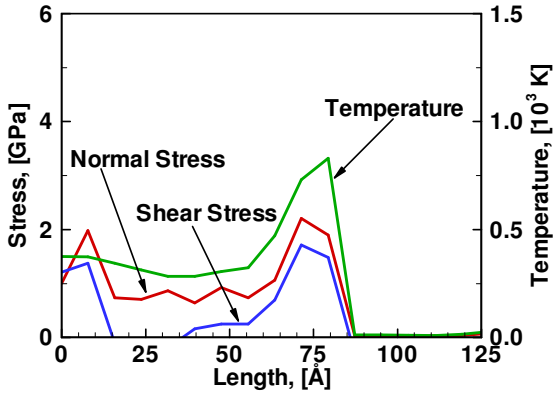

(c)

Figure 5.7 The longitudinal stress, shear stress, and temperature profiles in (a) <100>, (b) <110>, and (c) <111> oriented single crystalline Al at U_p=2.0 km/sec and at time *t*=1.5 ps

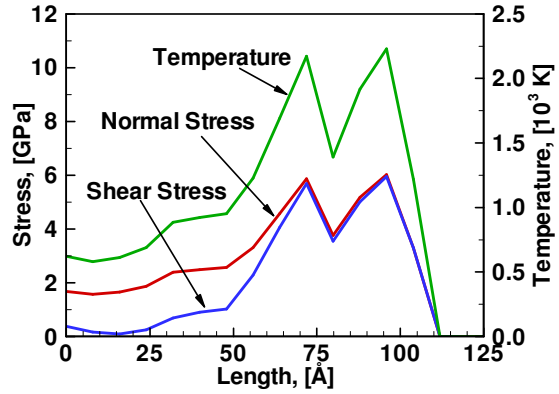

(a)

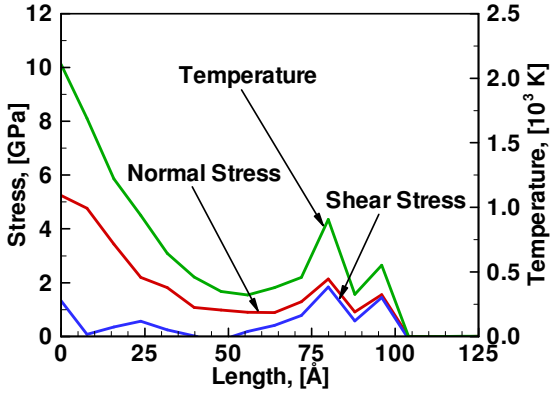

(b)

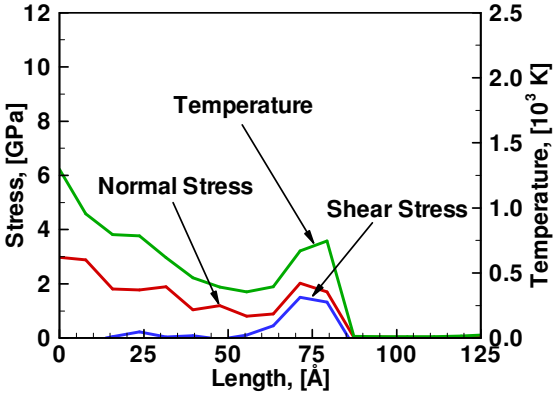

(c)

Figure 5.8 The longitudinal stress, shear stress, and temperature profiles in (a) <100>, (b) <110>, and (c) <111> oriented single crystalline Al at U_p=3.0 km/sec and at time *t*=1.5 ps

It is maximum for <100> orientation at both velocities indicating the least amount of shear release corresponding to this orientation. For all orientations, there is an increase in the ratio with an increase in the extent of plastic deformation. The magnitude of maximum normal stress varies with the crystallographic orientation for shock wave propagation. At both U_P values, the magnitude of normal stress is maximum in the case of <100> orientation. The maximum value of transverse shear stress required to induce plastic deformation in all orientations is approximately 1.5 GPa which is close to the theoretical shear strength predicted by the interatomic potential in the current research (approximately 3.0 GPa). In all the above figures, the temperature profiles are similar to the stress profiles. In specimens with <110> and <111> orientations, a temperature rise is seen near the impact plane. This rise in temperature can be associated with the larger extent of plastic deformation corresponding to these orientations. There is a sharp increase in the temperature at the shock-front in the case of <100> orientation (see Figure 5.7 (a)) indicating a strong elastic compression (the temperature here is T_{xx} i.e. component of temperature in *x* direction calculated using the perturbed velocities in shock wave propagation direction). However, for the <110> and <111> orientations the temperature rise is not as sharp because of the shear release associated with plastic wave-fronts that lie in the vicinity of the elastic wave-front. The temperature in all cases is found to be lower than the melting temperature of Al.

Figure 5.8 supports the observations made in Figure 5.7. A dual elastic-plastic wave front is seen for all the orientations with the maximum stress rise at the shock-front in the case of <100> orientation and the minimum in the case of <111> orientation. The shear stress

release in <100> orientated single crystalline Al is now significant in comparison to that for the same in Figure 5.7. There is a significant rise in temperature towards the impact plane end of the profiles for the <110> and <111> orientations. The temperatures rise approximately to the melting temperature near the impact plane indicating a significant plastic transformation. The same, however, is not true in case of the <100> orientation where the temperature reaches the ambient value. This is in accordance with the observations of the energy and mass-velocity profiles in Figure 5.5 and Figure 5.6. The extent of plastic transformation in the <110> and <111> orientations is higher than that in the <100> orientation. For the <100> orientation, the extent of plastic transformation is insufficient to cause the rise in the wave profiles. In all orientations, the maximum transverse shear stress magnitude is approximately equal to the ideal crystal shear strength. The magnitude is highest for the <100> orientation indicating the least possibility of shear release for this orientation. In other orientations, presence of amenable transverse slip systems results in smaller magnitude of maximum transverse shear stress.

A combination of the observations from all profiles points that there is a mixing and reshuffling zone behind the shock-front in all the single crystals. With an increase in the U_P value, the shock-front width reduces. Correspondingly, the mixing zone shifts nearer to the shock-front. The mixing and the associated phase transformation are inherently dependent on the crystallographic shock direction. Transition to melting is triggered while the temperature increase in the leading shock-front remains negligibly small in comparison to the melting temperature and is limited to moderate shock-strengths. Small

dislocation loops are created from thermal fluctuations just behind the shock-front, in a narrow region of a few lattice parameter widths. Later on depending upon the shock strength they act as the center point for phase transformation. In order to further analyze the deformation in structures under shock wave propagation, the partial Al-Al RDFs for the undisturbed, the elastically compressed, and the plastically deformed structures are plotted in Figure 5.9 and Figure 5.10 for all three orientations at U_p=2.0 km/sec and 3.0 km/sec, respectively. The three regions are identified using the approach established in Figure 5.1.

In Figure 5.9, the shock-induced plastic transformation is apparent from the plastic RDFs for the <110> and <111> orientations. Long range peaks of the plastic RDFs are smeared out indicating amorphization and mixing. The RDF peaks for both elastically compressed as well as for plastically deformed regions in all structures show a shift towards origin indicating uniaxial compression. The elastic region corresponds to pure uniaxial compression. In the plastic region, a change from the pure uniaxial to hydrostatic stress state occurs. Since, the hydrostatic stress state corresponds to pressure release, the shift of the elastic RDF peaks towards origin is higher than that of the plastic RDF peaks. Elastically compressed portions of the structures show insignificant shift from the RDF peaks corresponding to the undeformed structure. Some of the RDF peaks of the undeformed structure disappear during elastic compression indicating an overall shift in the lattice structure which later on triggers the plastic deformation. Smaller number of peaks in the plastic RDF than in the elastic RDF indicates beginning of the plastic deformation.

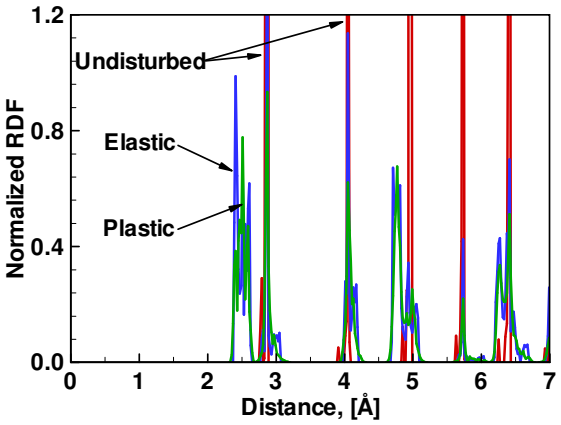

(a)

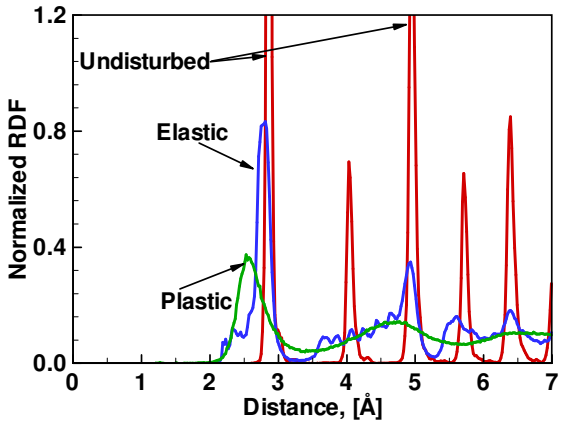

(b)

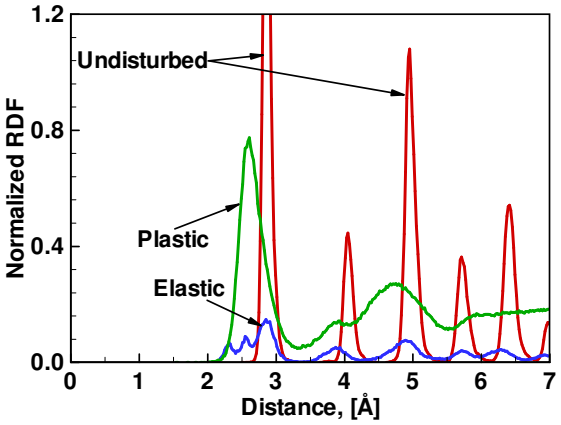

(c)

Figure 5.9 A comparison of the partial Al-Al RDFs for undeformed, elastically deformed, and plastically deformed portions of (a) <100>, (b) <110>, and (c) <111> oriented single crystalline Al at U_p=2.0 km/sec and at time t=1.5 ps

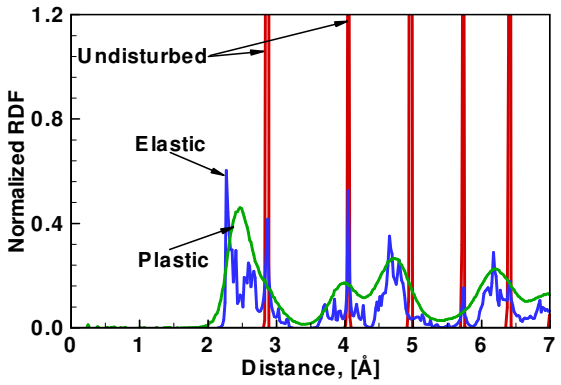

(a)

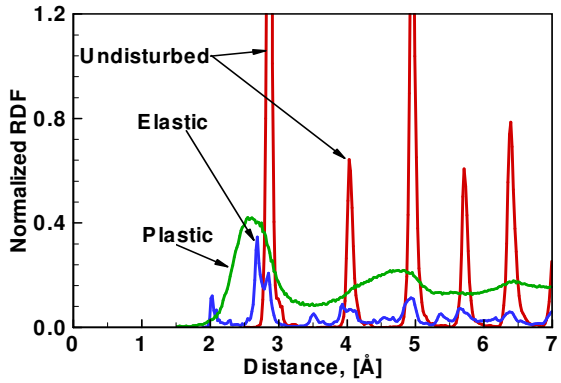

(b)

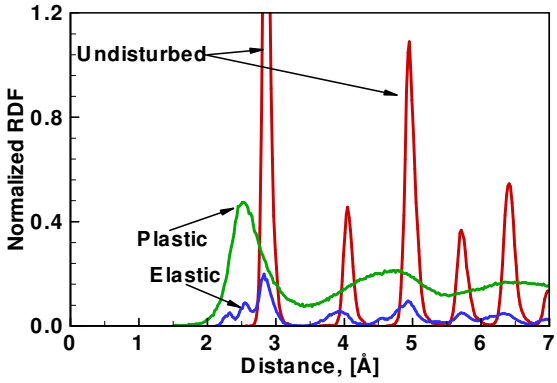

(c)

Figure 5.10 A comparison of the partial Al-Al RDFs for undeformed, elastically deformed, and plastically deformed portions of (a) <100>, (b) <110>, and (c) <111> oriented single crystalline Al at U_p=3.0 km/sec and at time t=1.5 ps

The highest amount of plastic distortion is observed for the <111> orientation. This is primarily because for this orientation, the primary *fcc* <110>{111} slip system is transverse to the shock wave propagation direction. For the <100> orientation, difference between the RDFs for elastically compressed and plastically deformed portions is minimal because of the least possibility of plastic deformation along transverse cubic slip planes. These results confirm the observations of shock-induced plastic deformation in the single crystals in Figure 5.7.

In Figure 5.10, difference among the RDFs for plastically deformed, elastically compressed, and undeformed regions of structures is clear for all the orientations. Due to higher elastic compression, additional elastic RDF peaks as compared to that in Figure 5.9 for all orientations are seen. The most number of peaks are in the <100> orientation indicating this orientation to be the most compressible one with the least possibility of plastic deformation. This is expected since the transverse slip systems for this orientation are cubic <010>{100} systems. From the extent of plastic deformation indicated by the RDFs for plastically deformed regions in the <110> and <111> orientations a high degree of amorphization is clear which is in agreement with the earlier findings from the corresponding temperature profiles in Figure 5.8. Overall, the structural analyses using RDFs confirm earlier conclusions regarding the shock-induced deformation and its dependence on single crystalline orientation.

The primary focus of the current research is on understanding the effect of shock wave propagation through an interface of Al and Fe_2O_3. Therefore, it is important to develop an

understanding of shock-induced structural deformation in single crystalline Fe_2O_3 as a function of shock loading. Accordingly, Next, the shock wave propagation in <0001> oriented single crystalline Fe_2O_3 is discussed.

5.4 Shock Wave Propagation Analyses in <0001> Oriented Single Crystalline α-Fe_2O_3

The U_S-U_P relationship for <0001> orientated single crystalline Fe_2O_3 is shown in Figure 5.11. The relationship lies close to the experimental polycrystalline data provided by Marsh (1980). A linear fit to the U_S-U_P relationship is,

$$U_S = 6.03 + 0.89\, U_P \cdot \tag{5.6}$$

As expected, the shock-front velocities are consistently higher than the ones predicted for all Al orientations.

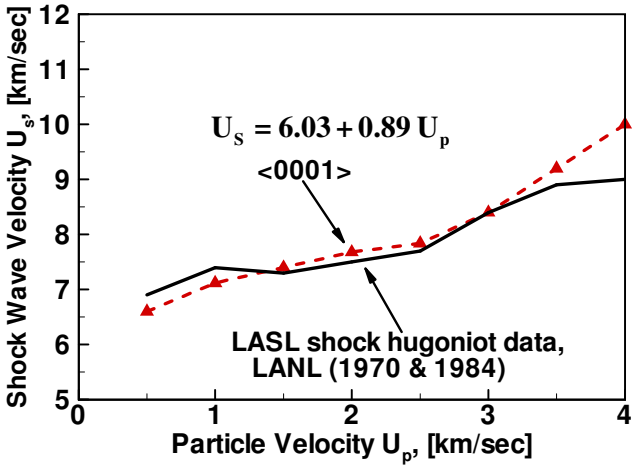

Figure 5.11 A comparison of the U_S-U_P relationship for <0001> oriented single crystalline Fe_2O_3 with the experimental polycrystalline relationship

A visualization scheme similar to the slip-vector approach is required to analyze the structural features during shock-induced deformation of single crystalline Fe_2O_3. As pointed out earlier in chapter 3, currently there is no such analysis scheme. However, by a combination of the information from visual inspections, from the RDFs, and from the shock-wave profile calculations it is possible to analyze the response of single crystalline Fe_2O_3 to the shock loading.

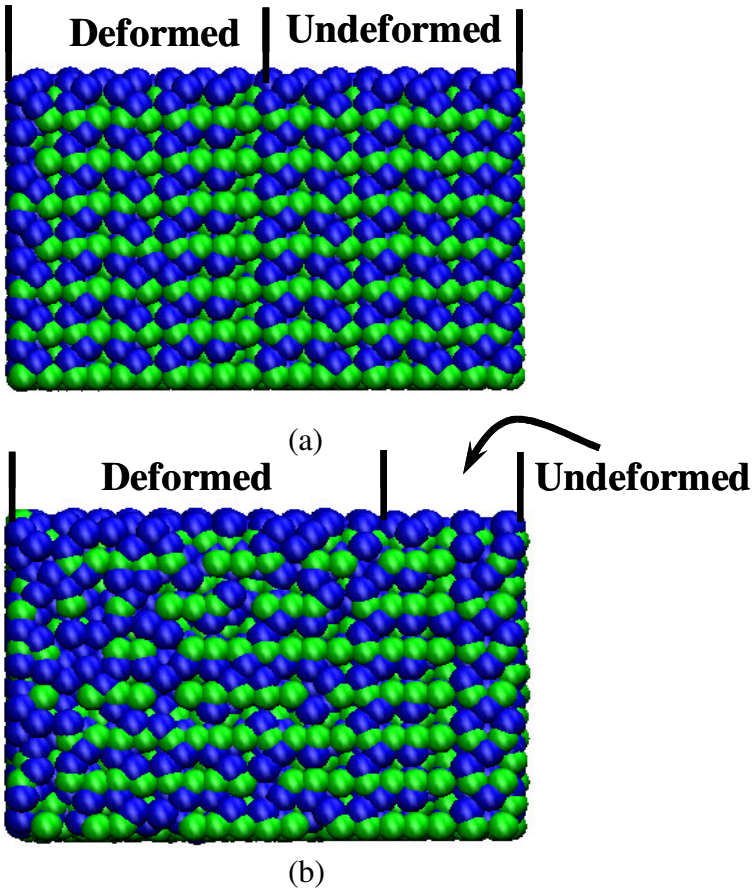

Figure 5.12 Identification of the deformed and undeformed regions in <0001> oriented single crystalline Fe_2O_3 during shock wave propagation at (a) U_p=2.0 km/sec, and (b) U_p=3.0 km/sec

Figure 5.12 (a) and (b) show a snapshot of <0001> Fe_2O_3 when steady shock waves are obtained at U_P=2.0 km/sec and 3.0 km/sec, respectively. A clear difference between the

undeformed and deformed portions of the single crystal can be observed at both velocities. The deformed and undeformed portions are analyzed using the total Fe_2O_3 RDFs to study the structural transformation under shock loading. Figure 5.13 (a) and (b) show the total Fe_2O_3 RDFs for the undeformed and deformed portions of <0001> oriented single crystalline Fe_2O_3 at U_P=2.0 km/sec and 3.0 km/sec, respectively. The RDFs for the undeformed portion are denoted by the legend "before" and for the deformed portion are denoted by the legend "after". As expected the crystalline order of the undeformed portion is subdued in the deformed structure indicating plastic deformation at both values of U_P. At both velocities there is a shift in the RDF peaks indicating uniaxial compression. At U_p=2.0 km/sec, the number of RDF peaks for deformed configuration is significantly less than that in the undeformed one. At U_p=3.0 km/sec the RDF for the deformed configuration is nearly flat after the first peak indicating a loss of the long-range order in the structure. In other words, U_p=2.0 km/sec can be considered as the threshold velocity for the onset of shock-induced plastic transformation. The plastic transformation threshold lies at U_p=2.0 km/sec and the accompanying amorphization is almost complete at U_p=3.0 km/sec. The shock-front velocity of 7.9 km/sec and the corresponding normal stress value of 5 GPa at U_P=2.0 km/sec correspond to the transition threshold for the initiation of plastic deformation in the single crystalline structure. It is important to note that these threshold values are much higher than that for all the orientations of single crystalline Al. In order to further analyze the structural deformation during shock wave propagation, profiles for the potential energy per atom, mass velocity, temperature, and normal and shear stress profiles at U_P=2.0 km/sec and 3.0 km/sec are calculated. Figure 5.14 (a) and (b) show the potential

energy per atom and mass-velocity profiles at U_P=2.0 km/sec and 3.0 km/sec, respectively. As shown, the energy per atom oscillates around the values of -40 eV/atom at U_P=2.0 km/sec and around the values of -35 eV/atom at U_P=3.0 km/sec.

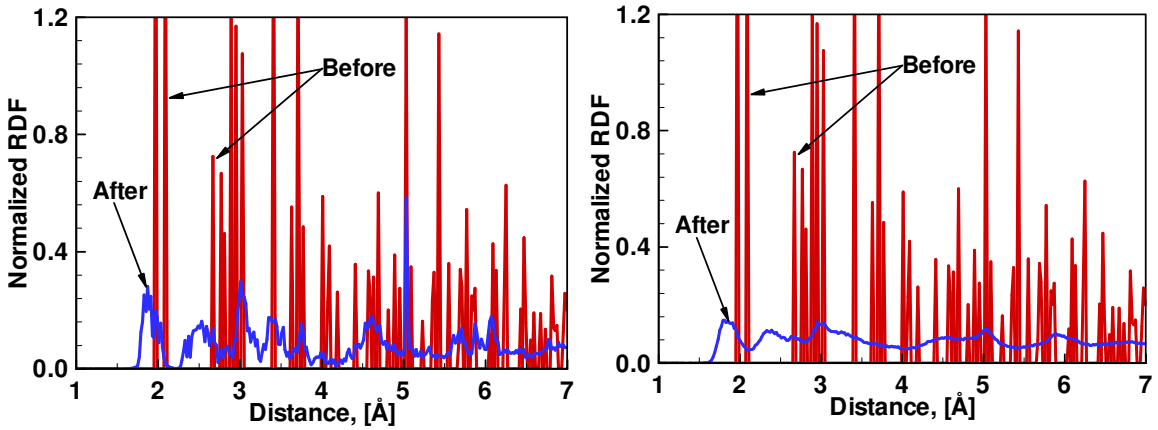

Figure 5.13 A comparison of the total Fe_2O_3 RDFs in <0001> oriented single crystalline Fe_2O_3 before and after shock wave propagation at (a) U_P=2.0 km/sec and (b) U_P=3.0 km/sec

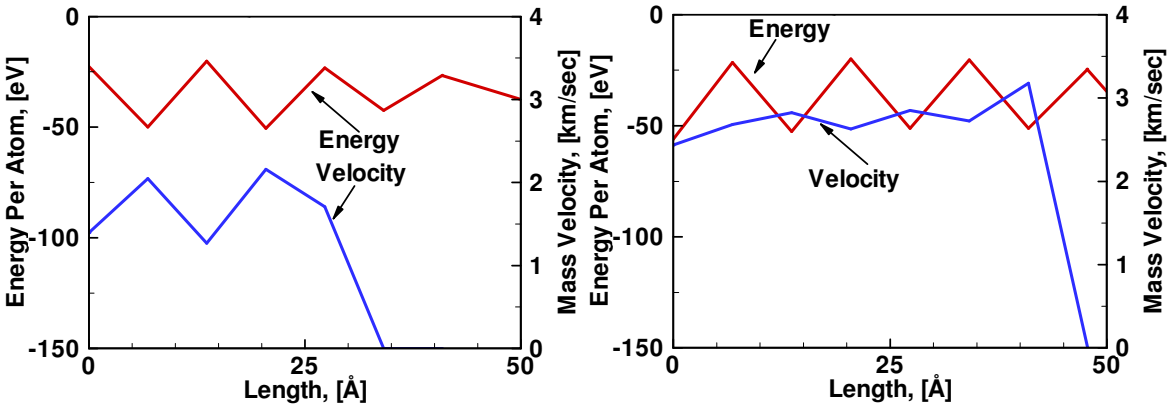

Figure 5.14 The potential energy per atom and mass velocity profiles for <0001> oriented single crystalline Fe_2O_3 at (a) U_P=2.0 km/sec and (b) U_P=3.0 km/sec

The upward shift in this value as a function of U_P is attributed to the difference in the kinetic energy imparted by shock impact. The mass velocity profile indicates a steady shock wave formation at both values of U_P. The steepness in the profiles at the shock-

front is proportional to the impact velocity. The shock-front has a sharper rise as a function of distance at U_P=3.0 km/sec. This is in accordance with the findings from the shock wave propagation in single crystalline Al. With increase in U_P there is an increase in the extent of plastic deformation which further results in steeper rise in the mass-velocity profiles at the shock-front. The stress and temperature profiles at the two U_P values are plotted in Figure 5.15 for analyzing the dynamic strength of the single crystalline structure. The stress levels are higher in the structure at U_P=3.0 km/sec than at U_P=2.0 km/sec. This indicates that in the range of U_P=2.0 km/sec to U_P=3.0 km/sec the elastic compression dominates. The plastic transformation front which is responsible for the stress release lags the elastic shock-front. The shear stress is not fully released to the zero value at U_P=3.0 km/sec. The shock-front width varies from 2.5 nm at U_P=2.0 km/sec to 1.5 nm at U_P=3.0 km/sec. It is interesting that the shock-front widths are nearly the same for Al and Fe_2O_3. However, it is important to note that for the same shock-front width the number of lattice planes in single crystalline Al and in single crystalline Fe_2O_3 vary. A conclusion that irrespective of the crystal structure, it is the impact velocity that determines the shock-front width, can be drawn. The peak temperature is observed to be at the shock-front in a way similar to that in the case of single crystalline Al in Figure 5.7 where extensive shock-induced plastic deformation has not taken place. At U_P=3.0 km/sec the peak temperature approaches the melting temperature of Fe_2O_3 at 1900 K behind the shock-front. This is also similar to the observations made for single crystalline Al at U_P=3.0 km/sec in Figure 5.8. For the <110> and <111> oriented single crystalline Al, peak temperatures at U_P=3.0 km/sec approach Al melting temperature of approximately 1000 K.

Overall, barring the strength, temperature, and energetic aspects, the qualitative observations regarding the passage of shock wave in <0001> oriented single crystalline Fe_2O_3 are similar to the ones in single crystalline Al. Plastic deformation threshold in <0001> oriented single crystalline Fe_2O_3 is approximately 2.0 km/sec and in single crystalline Al is approximately 1.5 km/sec. The shock-front widths for both systems are of the same order. However, features of plastic deformation in both systems differ. Put together, Al and Fe_2O_3 form an energetic system. An interesting problem, therefore, is the shock wave propagation through an interface of Al and Fe_2O_3. In chapter 3, an interface of Al and Fe_2O_3 was analyzed after MD equilibration. The same interfacial structure is analyzed in the next section after shock wave propagation.

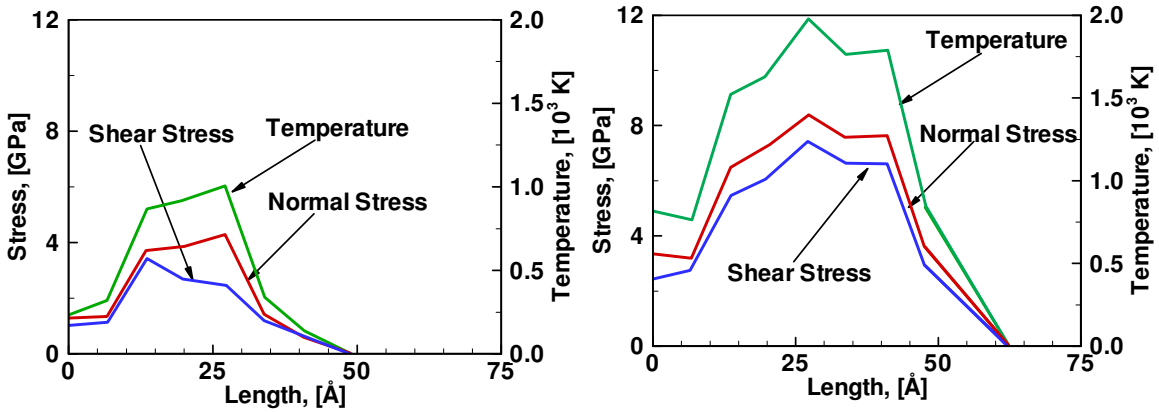

Figure 5.15 The normal stress, shear stress, and temperature profiles for <0001> Fe_2O_3 at (a) U_p=2.0 km/sec, and (b) U_p=3.0 km/sec

5.5 Analyses of Shock Wave Propagation through an Interface of Al and Fe_2O_3

A majority of research in the area of the MD analyses of shock wave propagation has been carried out in single crystalline systems. A few researchers have focused on analyzing shock wave propagation in systems with an interface between two different

crystal systems or in a polycrystalline system. Sapozhnikov et al. (2003) correlated the dynamic strength of a Cu single crystal with that of polycrystalline Cu using MD. The sizescale in the analyses samples is of the order of 100 nm. They observed that the initial stage of fracture in single crystalline samples is the nucleation of vacancies in form of spherical voids. The fusion of spherical voids results in the formation of a crack. The centers of nucleation of the voids are positioned at the intersection of stacking faults created by shock waves. In the polycrystalline samples, the centers of nucleation lie on the grain boundaries. Overall, the effect of shock wave propagation in the single crystalline samples was different from that in the polycrystalline ones due to the presence of grain boundaries.

Similar observations have been reported in a numerical study by Horie and coworkers, cf. Horie and Yano (2001), and by Germann and coworkers, cf. Holian et al. (1999), on nanocrystalline bcc-Fe. It was discovered that the shock wave profiles in polycrystalline samples spreads out to the length of the computational cell, never achieving a steady state. The scattering of initially sharp wave by various crystallites and multiple sources of phase-transition nuclei at grain boundaries, leads to an amorphous distribution of the transformed and untransformed material at a slightly lower shock strength (by about 10%) than the critical shock strength for inducing the amorphous transformation in perfect single crystals (either $\langle 100 \rangle$ or $\langle 110 \rangle$). Due to the presence of grain boundaries, there is a lower limit on the minimum grain size in polycrystalline materials for forming a steady shock wave, cf. Holian et al. (1999). In other words, MD simulations of shock wave propagation in polycrystalline materials have a lower limit on the shock strength,

namely, the shock thickness must be less than the grain size. For moderate shock strengths used during present simulations this limit for polycrystalline materials is of the order of 100 nm. At the grain sizes of polycrystalline materials used in the present simulations, it is not possible to obtain a steady shock wave. Consequently, to analyze the effect of shock wave propagation on structural order of Al-Fe_2O_3 interfaces attention is laid upon simpler configurations such as an interface between single crystalline Al and single crystalline Fe_2O_3. Without loss of generality, an interface of {100} surface of Al with {0001} surface of Fe_2O_3 is chosen for such analyses.

Analyses of shock wave propagation through single crystalline Al and Fe_2O_3 focused on analyzing structural features of deformation as a function of U_P. Insights obtained from such analyses are necessary for developing continuum level relations that are better suited to consider the nucleation and motion of defects at the length- and time-scales of shock wave propagation. Another important aspect of the analyses is an account of the structural features, the temperature, and the pressure at an interface of Al and Fe_2O_3 as a function of U_P. Main interest here is in analyzing the changes in structural order of the interfacial region as a function of shock loading. The pressure, temperature, mass-velocity, and energy changes in the interfacial region are analyzed in order to investigate a possibility that the interfacial structural transformation may be reactive. Insights into the mechanical behavior of single crystalline systems under shock wave propagation are useful for these analyses. Such analyses represent a phenomenological attempt at understanding possibly reactive changes in structural order at the interfaces as a function

of applied shock loading. The analyses are carried out at 8 different U_P values ranging from 0.5 km/sec to 4.0 km/sec at an interval of 0.5 km/sec.

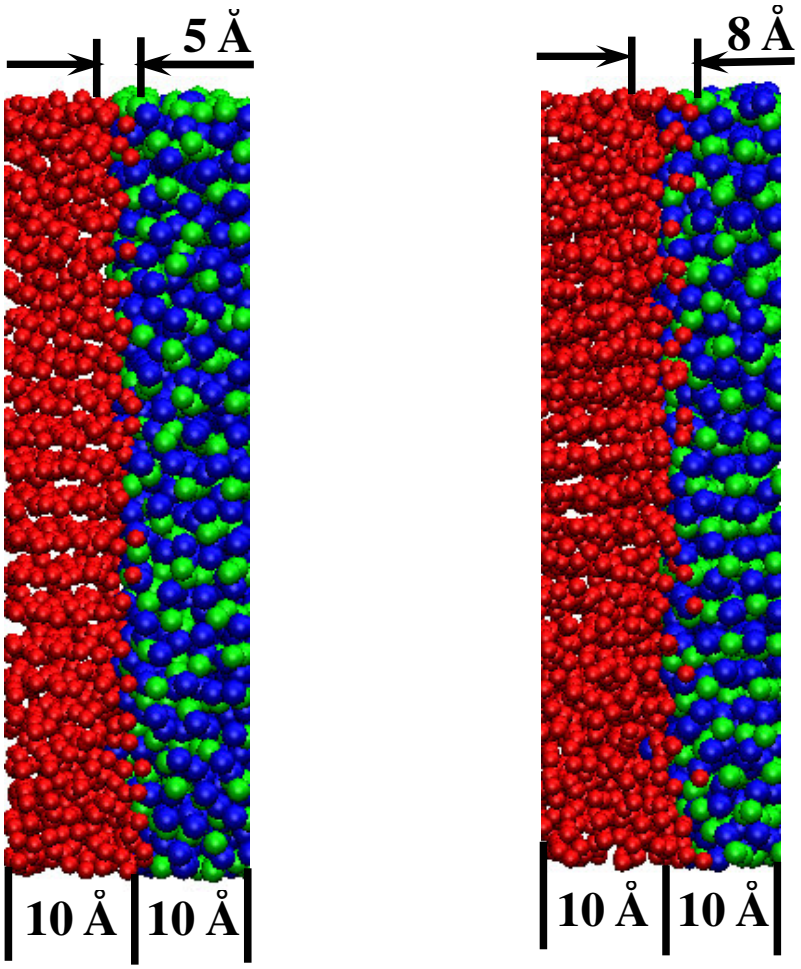

(a) (b)

Figure 5.16 A comparison of structural deformation and mixing at the interface of {100} surface of Al with {0001} surface of Fe_2O_3 after the shock wave passage through the interface at (a) U_p=2.0 km/sec and (b) U_p=3.0 km/sec

Figure 5.16 (a) and (b) show a snapshot of the interfacial structure after the passage of shock wave at U_P=2.0 km/sec and 3.0 km/sec, respectively. It was established earlier in chapter 3 that the structural order within the interfacial region with width of 10 Å differs from that of pure Al and pure Fe_2O_3. Figure 5.16 shows snapshots only for this transformation zone. At the time the snapshots were taken, the shock wave is a few

atomic planes away from the end of sample (the sample length is 15 nm with 7.5 nm Al and 7.5 nm Fe_2O_3 portions). The distance traveled by the shock wave after crossing the interface is approximately 4 nm. It was observed earlier that the shock-front width is of the order of 2 nm in single crystalline Al and Fe_2O_3. Accordingly, the analyses of interface structure after the shock wave has traveled approximately 4 nm from the interface is appropriate since the intent of analyses here is on investigating structural transformation in the interfacial region at an instant corresponding to the maximum in the shock-induced mixing. It is clear that under the effect of shock loading a significant amount of structural deformation and phase mixing at the interface takes place. A high amount of mixing at the interface is apparent at both U_P values. Based on the snapshots, a clear mixing zone with a width of approximately 0.5 nm at U_P=2.0 km/sec and a width of approximately 0.8 nm at U_P=3.0 km/sec can be identified. It is clear that the extent of mixing is dependent upon the impact velocity and it increases with an increase in the impact velocity. The mixing zone has a width of less than 1 nm at all particle velocities and it lies within the interfacial structural transformation zone identified using the MD analyses. Since the phase mixing is limited to the structural transformation zone of 1 nm on the either side of the interface, further analyses of the changes in structural order, pressure, temperature, and energy in the interfacial region are carried out for atoms within this zone.

A comparison of both figures with Figure 3.22 (a) and (b) reveals that the atomic movement here involves bigger shift in positions of all three types of atoms at the interface. Structural order at the interface is completely annihilated resulting in atoms

acquiring positions in an amorphous setting. However, no other information can be obtained form the snapshots. In order to further quantify the changes in the structural order with the change in U_P values, the partial Al-Al, partial Fe-Fe, total Fe_2O_3, and total Al_2O_3 RDFs need to be analyzed before and after the shock wave has passed through the interface. In the following the structural analyses using RDF are carried out within the interfacial transformation zone of 1 nm on either side of the interface at all particle velocities.

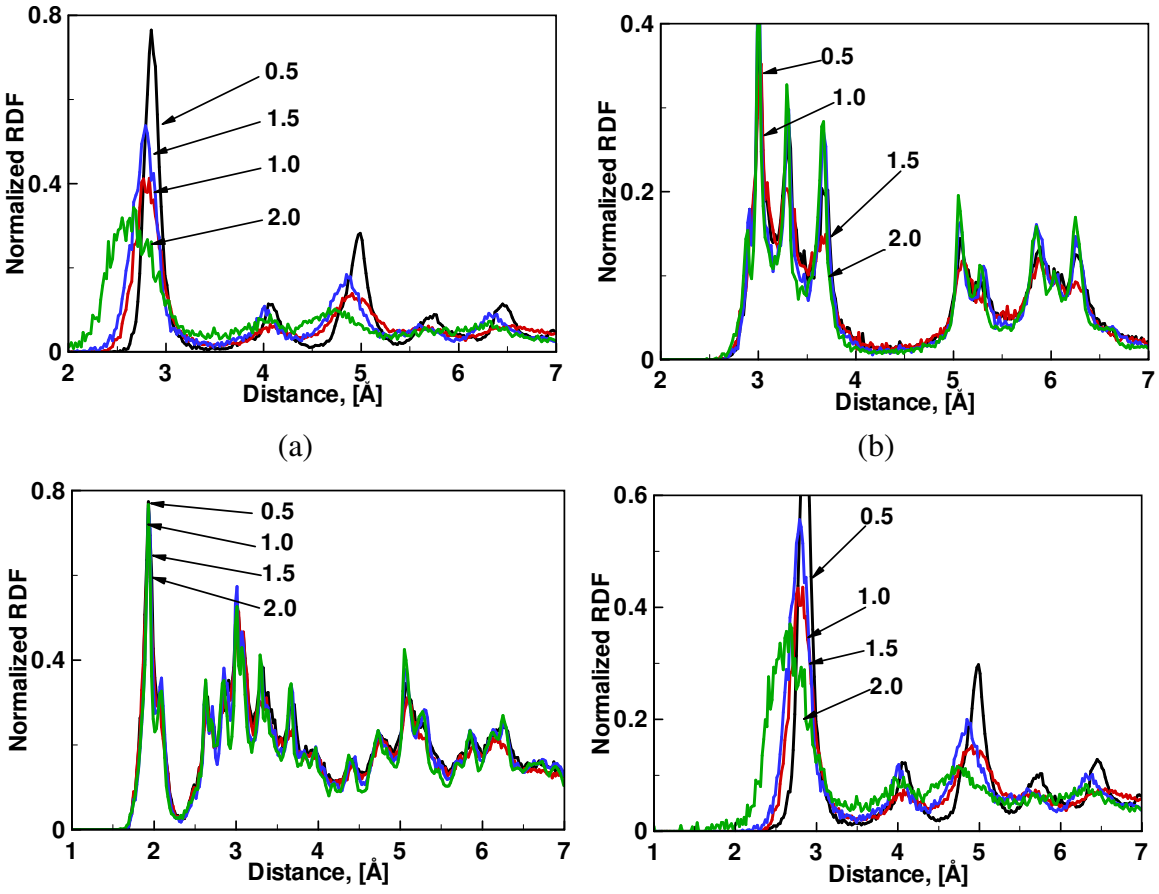

Figure 5.17 (a) The partial Al-Al, (b) partial Fe-Fe, (c) total Fe_2O_3, and (d) total Al_2O_3 RDFs for the interface at four different values of U_P before the passage of shock wave

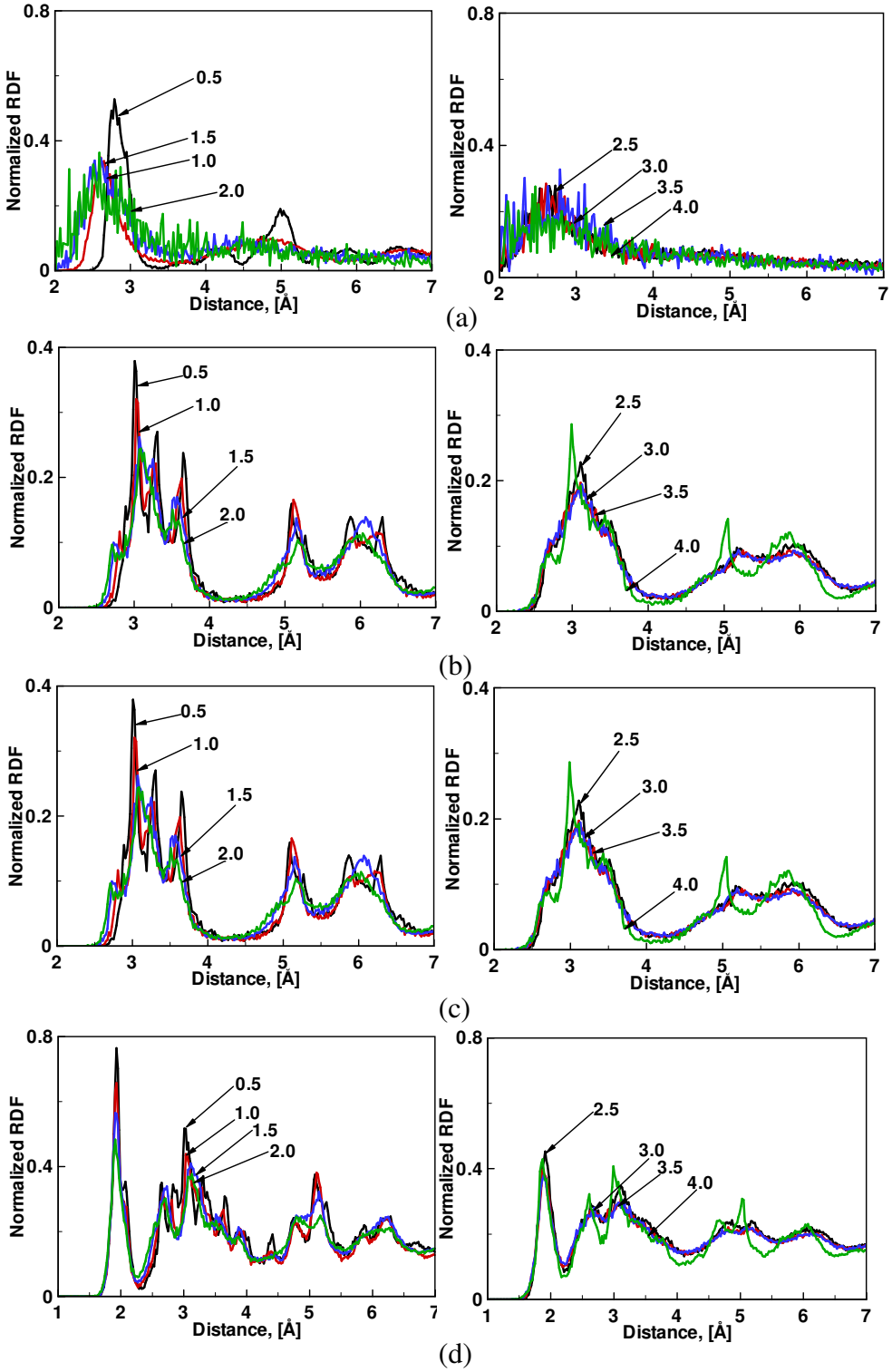

Figure 5.18 (a) The partial Al-Al, (b) partial Fe-Fe, (c) total Fe_2O_3, and (d) total Al_2O_3 RDFs at U_P=0.5 km/sec to 4.0 km/sec for the interface after the passage of shock wave

The partial Al-Al, partial Fe-Fe, total Fe_2O_3, and total Al_2O_3 RDFs obtained at four different U_P values viz., 0.5, 1.0, 1.5, 2.0 km/sec, before the shock wave crosses the interface are shown in Figure 5.17. Respective RDFs at the rest of the U_P values exhibit the same features. The partial Al-Al and total Al_2O_3 RDFs in Figure 5.17 show small changes as a function of U_P. However, the partial Fe-Fe and total Fe_2O_3 RDFs do not change as a function of U_P. This feature is observed because some of the Al lattice planes in the interfacial region have deformed due to shock loading (shock propagates from Al to Fe_2O_3). Consequently, with increase in U_P values the RDF peaks shift away from the positions corresponding to the ideal single crystalline ones.

In Figure 5.18, the partial Al-Al, partial Fe-Fe, total Fe_2O_3, and total Al_2O_3 RDFs after the passage of shock wave through the interface at U_P=0.5 km/sec to U_P=4.0 km/sec are shown. Up to the U_P value of 1.5 km/sec, no significant difference in the RDFs from the respective RDFs in Figure 5.17 is observed. Beginning from U_P=2.0 km/sec significant changes in all RDFs begin to appear. The partial Al-Al RDF at U_P=2.0 km/sec indicates that amorphization is almost complete in the Al region of the interface. However, the same RDF at U_P=1.5 km/sec indicates that significant crystallinity is present in the Al region after shock wave propagation. Earlier, shock wave propagation analyses through <100> oriented single crystalline Al at U_P=2.0 km/sec and 3.0 km/sec showed crystallinity at both velocities. Clearly, the temperature and pressure changes in the interfacial region due to the proximity of the Al and Fe_2O_3 phases have caused the amorphization in <100> Al. It is clear from the RDFs in Figure 5.18 (b), (c), and (d) that the threshold for amorphization in the Fe_2O_3 portion of the interface is the same as that

for the Al portion. Along with Al, the Fe_2O_3 portion of the interface acquires amorphous characteristics beyond U_P=2.0 km/sec. It is important to note that the Fe-Fe partial RDF in Figure 5.18 (b) corresponds to the Fe_2O_3 structure. Consequently, it is a part of the total Fe_2O_3 RDF in Figure 5.18 (c). With melting and amorphization, the nearest neighbor distance shown by the partial Fe-Fe RDF remains close to the value in Fe_2O_3. However, the long-range order is lost which is similar to the characteristics of liquids and amorphous structures. The same applies in case of the total Al_2O_3 and total Fe_2O_3 RDFs.

In a standard setting, the Al and Fe_2O_3 thermite reaction products are in the liquid phase because of accompanying high-temperatures. Accordingly, observed amorphization of the interfacial transformation zone beyond a threshold particle velocity value indicates that this change may be related to reactive nature of the Al and Fe_2O_3 phases in close proximity under applied shock loading. It can be hypothesized that the kinetic energy imparted by shock waves passing through the interface is a function of the structural order in a region surrounding the interface and U_P. At a certain threshold value of U_P (such as U_P=2.0 km/sec here) the kinetic energy imparted to the interfacial region may exceed the energy barrier for initiating a reactive structural transformation. In order to further investigate this issue the total internal energy, pressure, and temperature values at the interface as a function of U_P need to be quantified. Figure 5.19 shows a comparison of the changes in the pressure and temperature values in the interfacial region with the changes in pressure and temperature values in single crystalline Al and Fe_2O_3 having the same orientation as that of the respective phases at the interface after the passage of shock waves. As expected, at all values of U_P, the pressure values as well as the

temperature values in single crystalline Fe_2O_3 are higher than that in single crystalline Al (It is established earlier that the dynamic strength of Fe_2O_3 is higher than that of Al). In Figure 5.19 (a), upto the value of U_P=1.5 km/sec, the pressure in the interfacial region lies in between that of single crystalline Al and Fe_2O_3 indicating a certain amount of mixing in the interfacial region under the applied shock loading. Beginning at the particle velocity value of 2.0 km/sec, the pressure in the interfacial region has a value higher than the corresponding values in pure Al and Fe_2O_3. It is postulated that beyond U_P=2.0 km/sec the change in structural order due to mixing in the interfacial zone is accompanied by an energy release. The energy release causes the sudden rise of pressure because the interfacial zone is in highly compressed state. This postulate is verified by the comparison of temperature rise in the interfacial region with that in single crystalline Al and Fe_2O_3 shown in Figure 5.19 (b). Beginning at the value of U_P=2.0 km/sec, the temperature rise in the interfacial region lies near or above the melting temperature of Al which justifies high energy release accompanying the change in interface structural order.

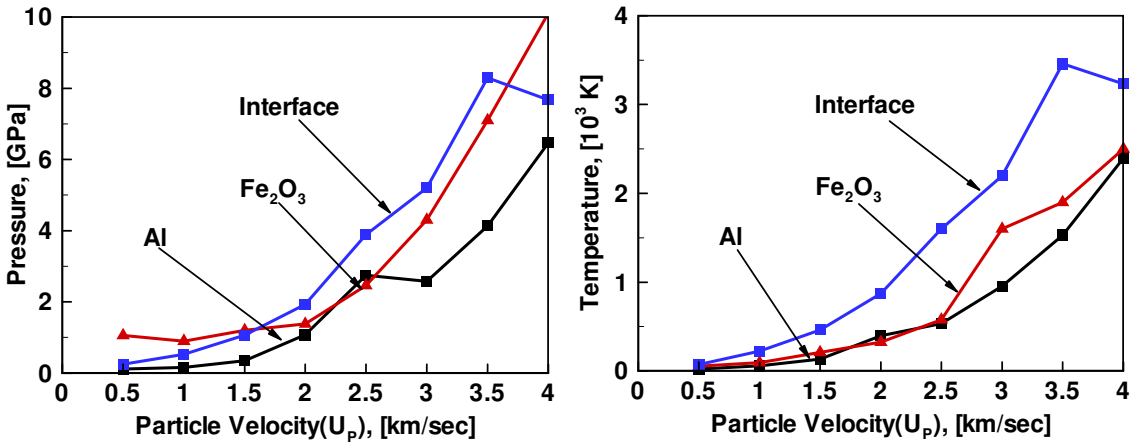

(a) (b)

Figure 5.19 A comparison of the change in (a) pressure and (b) temperature rise at the interface with that in the pure phases after the passage of shock wave

The change in the structural order of the interfacial region further needs to be examined in terms of the energy of atoms in the interfacial region after the shock wave passage through the interface. In this respect, change in the Helmholtz free energy of the interfacial region before and after the passage of shock wave needs to be calculated. However, for the system under consideration it is not possible to obtain the reference entropy values for calculating the change in the interface Helmholtz free energy. Accordingly, only change in the total internal energy in the interfacial region is calculated. It is expected that the energetic trend indicated by the internal energy and the Helmholtz free energy will be the same. However, quantifications may differ. A positive change in the internal energy indicates an exothermic structural transformation and a negative change indicates an endothermic structural transformation.

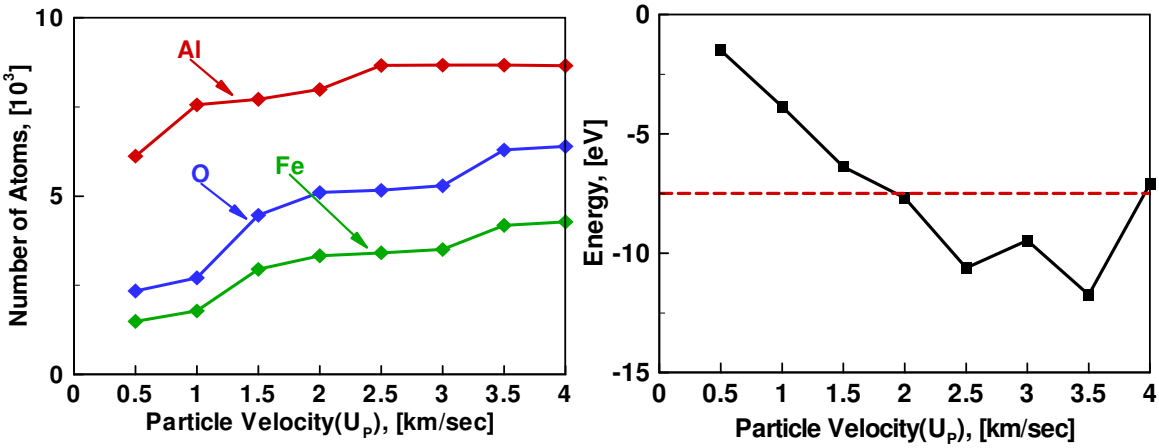

(a) (b)

Figure 5.20 (a) The number of Al, Fe, and O atoms in the interfacial transformation zone analyzed for the change in structural order after the passage of shock wave and (b) the change in the internal energy per atom in the interfacial region after the passage of shock wave (red line indicates threshold energy for standard thermite reaction)

In Figure 5.20 (a), the numbers of Al, Fe, and O atoms in the interfacial zone are plotted as a function of particle velocity. As expected there is a rise in the numbers with increase

in U_P because of accompanying increase in the shock compression and the shock-induced mixing. However, beyond U_P =1.5 km/sec the respective numbers of Al, Fe, and O atoms in the interfacial region examined for energy changes are of the same order representing a saturation in the shock compressed volume. The change in structural order in the interfacial zone is partially attributed to this saturation. To facilitate a comparison of the energy changes in a standard setting the calculated total internal energy in the interfacial region is normalized with the total number of atoms in the interfacial region. The difference in the total internal energy per atom before and after the passage of shock wave through the interface is plotted as a function of U_P in Figure 5.20 (b). The curves clearly indicate that the structural transformation at the interface is exothermic. The amount of energy release clearly increases with increase in the U_P values. The unit thermite reaction energy release in a standard setting is approximately 8.0 eV per atom. The change in internal energy per atom is found to be more than this values beyond U_P=2.0 km/sec. The release of energy is non-linearly related with U_P indicating that the structural transformation and the pressure and temperature conditions at the interface play an important role in deciding the amount of energy release. Change in the extent of mixing at the interface is not directly proportional to the change in U_P values. The extent also depends upon the type of surfaces in contact at the interface. The extent of mixing in turn determines the change in internal energy at the interface. Because of high degree of mixing, the mass velocity of the interfacial region after the passage of shock wave should be less than that before the shock wave arrives at the interface. Figure 5.21 (a) and (b) show the profiles for the mass velocity of the interfacial region before and after the passage of shock waves at U_P=2.0 km/sec and 3.0 km/sec, respectively. As expected,

gradient of the mass velocity as well as the mass velocity along the direction of shock wave propagation are higher before the passage of shock wave. The mixing at the interface is the driving force behind this phenomenon.

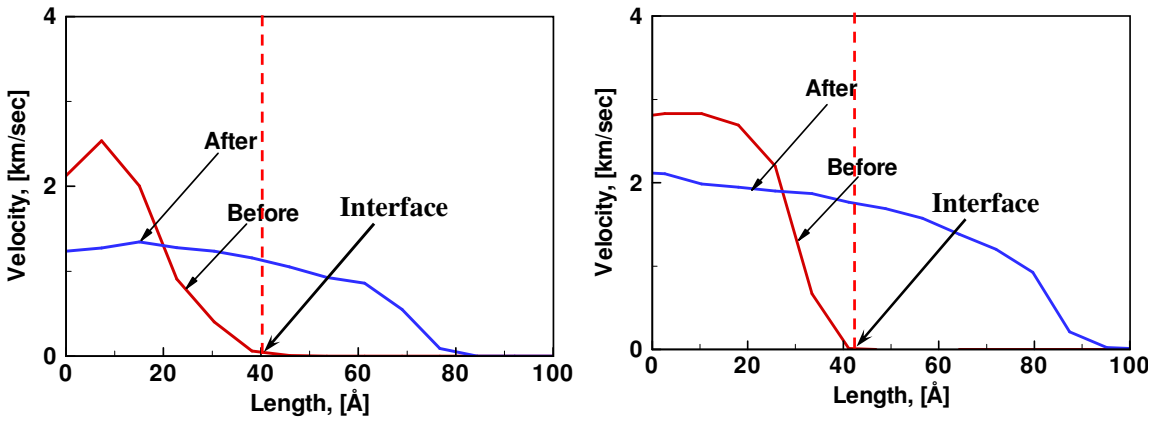

Figure 5.21 The mass-velocity profile before and after the passage of shock wave through the interface at (a) U_p=2.0 km/sec and (b) U_p=3.0 km/sec

Reduction in the mass velocity after the passage of shock wave signifies the reduction in mass transport as a result of shock impact. The structural transformation at the interface is accompanied by mixing and loss of kinetic energy which results in the overall lowering of the mass velocity. Resulting stagnation and mixing of the interfacial atoms works in favor of the exothermic structural transformation at the interface. Since energy release in this transformation is confined to a small shock-compressed volume, pressure in the interfacial region is expected to be higher after the passage of shock wave than before the passage of shock wave. Indeed this is the case. As shown in Figure 5.19 there is a rise in temperature as well as pressure of the interfacial region as a result of mixing. Both, the pressure rise and the temperature rise, have steep gradients beginning at U_P=2.0 km/sec. Corresponding pressure rise is approximately 1.75 GPa and the temperature rise is approximately 900 K. Overall, applied shock-energy input results in an exothermic

change in the structural order that further results in the rises in the temperatures and the pressures at U_P values beyond 2.0 km/sec. One may conjecture that similar transformations accompanied by energy release are possible in even non-reactive material systems such as two metals in contact with each other at sufficiently high impact velocities. Indeed such a possibility cannot be ignored. However, a combination of information from the changes in structural order, pressure, temperature, mass velocity, and energy all point here to a possibility of an existence of an impact velocity threshold beyond which the interfacial structure undergoes reactive changes. For continuum calculations the threshold U_P value of 2.0 km/sec seems high. However, we should remember that the present study is an ideal case. The threshold value of U_P would differ with different orientations of Al and Fe_2O_3 at the interface and with introduction of imperfections in structural order.

5.6 Chapter Insights and Conclusions

This chapter presented MD analyses of shock wave propagation in <100>, <110>, and <111> oriented single crystalline Al, in <0001> oriented single crystalline Fe_2O_3 and through an interface between {100} surface of Al and {0001} surface of Fe_2O_3. Analyses used the U_S-U_P relationships, the shock wave profiles, the structural analyses using the slip-vector approach, and the RDFs for forming conclusions regarding the dynamic mechanical behavior of the systems under study. The conclusions are;

1. The U_S vs. U_P relationship for a single crystal is dependent upon its crystallographic orientation. For different crystallographic orientations of Al, the coupling among the primary, secondary, and cubic slip systems acts in different manners. Consequently,

the slip systems activate in different ways for different orientations in Al. However, in all cases the relationships lay very close to the experimental polycrystalline U_S-U_P relationships. Accordingly, it can be concluded that at nanoscale heterogeneities exist in the dynamic response. However, they get washed out due to averaging of the responses in polycrystalline samples during experiments. For a material with nanoscopic morphology, it is very important to consider the heterogeneities unless an average response is required.

2. In single crystalline Al, with increase in the U_P values, the shock wave changes from initially being purely elastic to a combination of an elastic wave and a plastic wave, and finally into a plastically overdriven wave. Threshold U_P values for this division are dependent upon the crystallographic orientation for the shock wave propagation. Plastic deformation occurs by virtue of the tendency of a uniaxially compressed single crystal to relax in a hydrostatically compressed state. Consequently, the ease of transverse shear stress release plays an important role during shock-induced structural deformation. This, in turn, is dependent upon the type of active slip systems in the transverse direction. The magnitude of shear stress induced in the transverse direction also plays an important role. Higher shear stress is observed for orientations with smaller Schmidt factor values and less favorable slip systems in the transverse directions. Consequently, single crystals with higher value of Schmidt factor in the transverse direction have higher amount of plastic deformation and lower threshold values of U_P for initiation of the plastic deformation.
3. The qualitative results of the shock wave propagation analyses through single crystalline Al agree well with the observations made earlier on model *fcc* materials

using LJ potentials. However, quantifications such as thresholds for initiating plasticity and plastic overdriven wave formation differ. Contrary to the observations made during earlier shock research on *fcc* single crystals using LJ potential, the current result conclusively points out the role of different crystal systems in the shock-induced plastic deformation of Al. Irrespective of the type of transverse slip system, the slip predominantly occurs along {111} planes. However, depending upon the shock-strength, the primary, secondary, and cubic slip systems become active in different extents for various orientations. For the <111> and <110> orientations, sessile dislocations are also observed. This indicates that realistic potentials must be used during MD shock wave propagation analyses for obtaining suitable quantifications for use in the material theories.

4. In the case of Fe_2O_3 it is not possible to make a clear visual distinction between the elastic and plastic wave fronts. However, based on the total Fe_2O_3 RDF calculations it is possible to obtain the threshold for forming a plastically overdriven wave. The threshold is found to be higher than that in all orientations of single crystalline Al. Clearly, the dynamic strength of Fe_2O_3 is higher than that of Al.
5. Depending upon the orientation and the value of U_P the shock-front width varies from 1 nm to 2 nm in both Al and Fe_2O_3. The difference in the shock-front widths of Al and Fe_2O_3 at a particular values of U_P is insignificant. However, for the same shock-front width values, the number of lattice planes in Al and Fe_2O_3 differ. This indicates that at the moderate shock strengths accessible to the MD simulations, the shock-front width is independent of the material construction and depends only on the value of U_P.

6. Qualitative observations of the shock wave propagation in terms of the shock wave profiles are the same for Al and Fe_2O_3. Accordingly, a general conclusion regarding the features of shock wave propagation applies to both systems. However, details of structural deformation for both systems differ from each other. Accordingly, a continuum formulation based solely on the qualitative observations can be calibrated to apply to both material systems. However, incorporation of the structural deformation features would require more careful analyses.
7. Shock wave propagation analyses through an interface of Al and Fe_2O_3 reveal that the crystalline structural order of the interface changes to that of an amorphous phase beyond a threshold impact velocity. The change in structural order occurs partly due to a reduction in mass transport and an increase in atomic mixing in the interfacial region after the passage of the shock wave. The change is accompanied by a net total internal energy release. The internal energy release per atom at and beyond the threshold particle velocity is higher than that in room temperature thermite reaction. Since the energy is released in a shock-compressed volume, the interface temperatures and pressures are higher than those in pure phases beyond the threshold particle velocity. The temperature corresponding to the threshold velocity is approximately 900 K which is close to the melting temperature of Al and the pressure is approximately 2 GPa. The changes in structural order, pressure, temperature, energy, and mass velocity, taken together, suggest the possibility of a shock-induced reactive structural transformation or simple phase mixing. Further analysis is needed to ascertain the exact nature of these changes.

CHAPTER 6

SUMMARY AND CONCLUSIONS

Sound developments in a technology are often based on a strong combination of experimental developments and computational characterizations. However, currently a majority of the advanced materials research is experimental. The computational advances having a predictive capability for advanced materials performance are still in the nascent stage. One of the desired areas of such advancements is the atomistic modeling of the mechanical behavior of materials in which constituents are mixed at the nanoscale. The current research is a significant head-start in this important area. In the current research, fundamental inputs in the form of interatomic interactions and material morphologies are developed from established experimental and computational information. Analyses carried out using the framework provide significant insights into the correlation between the nanostructural morphology and applied loading that affects the constitutive response of a material. Moreover, the material system analyzed is a combination of cubic *fcc*-Al and rhombohedral α-Fe_2O_3. In this respect, the current research is the first to analyze the mechanical behavior of a complex nanoscale material system using an atomistic framework.

Contributions of this research include the development of an interatomic potential, the development of methodologies to calculate the quasistatic and dynamic strengths, the integration of the interatomic potential and the strength calculation methodologies into a scalable parallel MD code, the quasistatic mechanical deformation analyses of

nanocrystalline Al+α-Fe_2O_3 material system, and the shock wave propagation analyses through single crystalline Al, Fe_2O_3, and their interfaces. The interatomic potential includes an EAM cluster functional, a Morse type pair function, and a second order electrostatic interaction function. It is fitted to the lattice constants, elastic constants, and cohesive energies of *fcc*-Al, *bcc*-Fe, α-Fe_2O_3, α-Al_2O_3, and B2 Fe-Al, accounting for the fact that mixtures of Al and Fe_2O_3 are chemically reactive and mechanical deformations may cause the formation of these phases as reaction products or intermediates. In addition, the predictions of the surface and stacking fault energies for the crystalline components using the potential compare well with the predictions of established potentials for the same components in the literature.

The quasistatic deformation analyses are carried out in nanocrystalline Al, nanocrystalline Fe_2O_3, and their composites with three different average grain sizes viz., 3.9 nm, 4.7 nm, and 7.2nm, following the log-normal grain size distribution with 10% standard deviation. The deformation mechanism in the Al phase in nanocrystalline Al as well as in the composites is grain boundary sliding. In structures where the Fe_2O_3 phase is present, the deformation mechanism is also affected by electrostatic forces, particularly during compression where a reverse H-P relation is observed. In nanocrystalline Al majority of applied loading is shared by the high-angle grain boundaries contrary to that in composites where under the effect of Al-Fe_2O_3 interfacial stresses the applied load is shared between the high-angle and low-angle grain boundaries in a manner proportional to their presence. In nanocrystalline Al, dislocation emission primarily occurs from the high-angle grain boundaries. In the composites, however, dislocations are emitted from

the high-angle as well as low-angle grain boundaries under the short and long range effects of interfacial stresses at Al and Fe_2O_3 interfaces. Dislocation emission in Al grains in the composites occurs earlier than in the Al grains in nanocrystalline Al due to the interfacial stresses associated with the Fe_2O_3 phase in the composites. In nanocrystalline Al, dislocation emission occurs earlier during tensile loading than during compressive loading owing to the differences in the movements of grain boundary atoms responsible for dislocation emission. However, the deformation mechanisms during tensile and compressive loadings are the same. The differences in the movements of grain boundary atoms during tensile and compressive loadings are responsible for a high degree of asymmetry in the tensile and compressive strengths and corresponding deformation levels.

Attempts to apply continuum mixture of theory to the composite material system reveal that the strength of a nanocomposite can be calculated using a relation that takes into account the strengths of individual phases, the volume fractions of individual phases, the extent of grain boundary mismatch, and the Al-Fe_2O_3 interfacial stresses. However, with increase in the average grain size, the effects of grain boundary mismatch and interfacial stresses on composite strengths diminish. For nanocrystalline Fe_2O_3, a direct H-P relation in compression and a reverse H-P relation in tension are observed. While the reverse H-P relation during tensile loading is associated with the grain boundary sliding, the direct H-P relation during compressive loading is observed because of strong compressive electrostatic forces. For Fe_2O_3, the H-P relationship is linear in tension as well as in compression due to its amorphous structural order which results in denser packing of

atoms in the structures. As the volume fraction of the Fe_2O_3 phase decreases in the nanocrystalline composites, linearity in the H-P relationship begins to diminish since now the effect of grain boundary mismatch on the observed strength values starts to dominate. For nanocrystalline Al structures, where the effect of grain boundary mismatch on deformation mechanisms is dominant, a linear H-P relationship is not observed.

The shock wave propagation analyses focus on analyzing the dynamic strengths at U_P values ranging from 0.5 km/sec to 4.0 km/sec. For different crystallographic orientations of Al, the coupling among the primary, secondary, and cubic slip systems acts in different manners to cause shock-induced plastic deformation that occurs by virtue of the tendency of a uniaxially compressed single crystal to relax in a hydrostatically compressed state. Consequently, the ease of transverse shear stress release and the type of active slip systems in the direction transverse to the shock wave propagation direction play an important role in the shock-induced plastic deformation. Single crystals with higher value of Schmidt factor in the transverse direction have higher amount of plastic deformation and lower threshold U_P values for the initiation of shock-induced plastic deformation. Irrespective of the type of transverse slip system, the slip predominantly occurs along {111} planes in the primary slip direction. However, depending upon the shock-strength and the single crystalline orientation, the cubic and secondary slip systems also become active. The qualitative results of the shock wave propagation analyses through single crystalline Al agree well with the observations made earlier on model *fcc* materials using LJ potentials. However, quantifications such as thresholds for initiating plasticity and plastic overdriven wave formation differ. Contrary to the observations made during

earlier shock research on *fcc* single crystals using LJ potential, the current result conclusively points out the role of different orientations in the shock-induced plastic deformation of Al. This indicates that realistic potentials must be used during MD shock wave propagation analyses for obtaining suitable quantifications for use in material theories.

In single crystalline Fe_2O_3, it is not possible to make a clear distinction between the elastic and plastic wave fronts. However, based on the total Fe_2O_3 RDF calculations it is possible to obtain the threshold for forming a plastically overdriven wave. The threshold is found to be higher than that in all orientations of single crystalline Al. Clearly, the dynamic strength of Fe_2O_3 is higher than that of Al. Depending upon the single crystalline orientation and the value of U_P the shock-front width varies from 1 nm to 2 nm in both materials. The difference in the shock-front widths of Al and Fe_2O_3 at a particular values of U_P is insignificant. However, for the same shock-front width values, the number of lattice planes in Al and Fe_2O_3 differ. This indicates that at the moderate shock strengths accessible to the MD simulations, the shock-front width is independent of the material construction and depends only on the value of U_P. Qualitative observations of the shock wave propagation in terms of the shock wave profiles are the same in case of Al and Fe_2O_3. Accordingly, a general conclusion regarding the features of shock wave propagation applies to both systems. However, details of structural deformation for both systems differ from each other. Consequently, a continuum formulation based solely on the qualitative observations can be calibrated to apply to both material systems. However, incorporation of the structural deformation features would require a more careful

consideration. Shock wave propagation analyses through an interface of Al and Fe_2O_3 reveal that the crystalline structural order of the interface changes to an anamorphous one beyond a threshold impact velocity. The change in structural order occurs under the effect of the reduction in mass transport and an increase in the atomic mixing in the interfacial region after the passage of shock wave. The change is accompanied by a net total internal energy release. Since the energy is released in a shock-compressed volume, the interface temperatures and pressures are higher than those in pure phases beyond the threshold particle velocity. A combination of the information from the changes in structural order, pressure, temperature, energy, and mass velocity indicates that it may be possible that the interfacial structural order change corresponds to a shock-induced reactive structural transformation.

Overall, the results obtained by applying the framework in different settings not only provide important insights into the atomistic deformation mechanisms but also establish an independent tool for atomistic analyses of the mechanical behavior of materials having more than one crystal system in a complex nanostructural morphology. The analyses including the development of the interatomic potential for a multicomponent material system, the quasistatic strength analyses of composite structures using MD, and the dynamic strength analyses of interface using MD shock wave propagation are new to the materials research community and are carried out for the first time. In this respect, the current research offers a significant contribution towards developing a material design capability for advanced nanomaterials.

CHAPTER 7

RECOMMENDATIONS

The current research establishes an independent tool for atomistic analyses of the mechanical behavior of materials having more than one crystal system in complex nanostructural morphology. However, as with any new research, there are some limitations to the framework. The most important limitation of the framework is that the length- and time-scales of analyses are limited to the order of 10 nm and 10 ps, respectively. In addition, further material characterizations using the framework are required in order to strongly advocate and advance it into the materials research community. In my opinion, the following recommendations should serve as the starting point:

1. The potential should be further improved to minimize the cost of computations. One such possibility is to replace cluster functional for electrostatic components with a dispersion function. Electrostatic calculations are the most expensive part of the MD computations. Replacing cluster functional with the dispersion function would improve the computational speed by 2 to 3 orders of magnitude. Another possibility is to replace the Ewald sum with the Wolf sum for electrostatic calculations. This would require a careful calibration of the Wolf sum parameters. Since, in the current research the primary focus was on the validation, Ewald sum was used exclusively. The replacement would speed up the calculations by 10 orders of magnitude. On combining the above two suggestions, systems with sizes of the order of 20 to 30

times the ones used in the current research can be analyzed for longer simulations times.

2. With the calculation speedup, it should be possible to analyze the steady state shock wave propagation in the nanocrystalline composites with average grain sizes of the order of 100-200 nm. This would enable easier continuum scale up of the calculations. It would be possible to analyze the quasistatic as well as the dynamic strengths of nanocrystalline composites with a range of volume fractions and average grain sizes. Such analyses would enable a closer collaboration of the MD simulations with the mesoscale Eulerian hydrocode simulations.
3. A whole range of impact loading including pure shear impact and combined shear and planar impact should be included in the structural transformation study for conclusions regarding the reactivity. In addition, a whole range of single crystalline orientations need to be analyzed for the structural transformation. Such analyses need to be coupled with the polycrystalline shock simulations in order to obtain a possible reaction initiation criterion for actual morphological constructions.

All the above suggestions point to significant physical and computational advancements. This puts the current research as an exciting beginning of possibly a very fundamental and fruitful materials research avenue in the current scientific world.

APPENDIX A

VISUALIZATION SCRIPT FOR VMD

```
# created by wuwei on 12/12/2002
# modified for MURI by vikas 01/08/2004
# source path-to-script file
# mol delete all
# snap_mols path-to-pdb files

#!/usr/local/bin/vmd

proc one_frame {arg1 args} {
# initialize
if { [file exists $arg1] }  {
mol delete all
set viewplist {}
set fixedlist {}
material change opacity Transparent 0.310000
# Display settings
display projection Orthographic
mol load pdb $arg1
mol delrep 0 top
mol representation VDW 1.600000 8.000000
mol color Occupancy
mol selection {z<5 and z>-5 and occupancy < 3.0 and name H}
mol material Opaque
mol addrep top
mol drawframes top 0 {now}
mol rename top {$arg1:top}
lappend fixedlist [molinfo top]
set viewpoints([molinfo top]) {{{1.000000 0.000000 0.000000 -0.177744}
{0.000000 1.000000 0.000000 0.005797} {0.000000 0.000000 1.000000
0.022167} {0.000000 0.000000 0.000000 1.000000}} {{1.000000 0.000000
0.000000 0.000000} {0.000000 1.000000 0.000000 0.000000} {0.000000
0.000000 1.000000 0.000000} {0.000000 0.000000 0.000000 1.000000}}
{{0.016137 0.000000 0.000000 0.000000} {0.000000 0.016137 0.000000
0.000000} {0.000000 0.000000 0.016137 0.000000} {0.000000 0.000000
0.000000 1.000000}} {{1.000000 0.000000 0.000000 -0.759999} {0.000000
1.000000 0.000000 0.240000} {0.000000 0.000000 1.000000 0.000000}
{0.000000 0.000000 0.000000 1.000000}}}
lappend viewplist [molinfo top]
set topmol [molinfo top]
# done with molecule
# get maximum occupancy value
display projection Orthographic
set sel [atomselect top all]
set centro [lsort -real -decreasing [$sel get occupancy]]
set max_centro [lindex $centro 0]
set centro2 [lsort -real -increasing [$sel get occupancy]]
```

```
set min_centro [lindex $centro2 0]

mol load graphics graphics
mol top [lindex [molinfo list] end]

# draw the color scale bar
color_scale_bar_slip 90 15 $min_centro $max_centro 9

lappend fixedlist [molinfo top]
set viewpoints([molinfo top]) {{{1.000000 0.000000 0.000000 -0.166933}
{0.000000 1.000000 0.000000 0.119583} {0.000000 0.000000 1.000000 -
0.097959} {0.000000 0.000000 0.000000 1.000000}} {{1.000000 0.000000
0.000000 0.000000} {0.000000 1.000000 0.000000 0.000000} {0.000000
0.000000 1.000000 0.000000} {0.000000 0.000000 0.000000 1.000000}}
{{0.014771 0.000000 0.000000 0.000000} {0.000000 0.014771 0.000000
0.000000} {0.000000 0.000000 0.014771 0.000000} {0.000000 0.000000
0.000000 1.000000}} {{1.000000 0.000000 0.000000 -2.450000} {0.000000
1.000000 0.000000 0.230000} {0.000000 0.000000 1.000000 0.000000}
{0.000000 0.000000 0.000000 1.000000}}}
lappend viewplist [molinfo top]
# done with molecule # 2 graphics bar
foreach v $viewplist {
  molinfo $v set {center_matrix rotate_matrix scale_matrix
global_matrix} $viewpoints($v)
}
foreach v $fixedlist {
  molinfo $v set fixed 1
}
unset viewplist
unset fixedlist
mol top $topmol
unset topmol

color Display {Background} white
#color Axes {Labels} black
color Name {H} red
color Name {O} blue
color Name {N} green
color Resname {ALA} blue
color Resname {ARG} red
color Resname {ASN} gray
color Resname {ASP} orange
color Resname {CYS} yellow
color Resname {GLY} tan
color Resname {GLU} green
color Resname {GLN} cyan
color Resname {HIS} purple
color Resname {ILE} silver
color Resname {LEU} silver

axes location off
hsv 0.0 1.0 1024
} else {
puts "The PDB file does not exist!"
}

}
```

```
#===================================
# this proceduer load all the pdb files and render snapshot files
#
proc snap_mols { dir args} {

display update on
# get all the pdb files
set files [glob -directory $dir *.pdb ]

set a 0.0

foreach pdbfile $files {
      set a [expr {$a+1.0}]
      if {[expr (fmod($a,1.0)==0.0)]} {
            set file1 $pdbfile
      }
      if {[expr (fmod($a,1.0)==0.0)]} {
            one_frame $file1
            display update ui
            render  snapshot [file rootname $file1].bmp
      }
}
}

#================================================
```

REFERENCES

[1] Abraham, F. F. (2003). "How fast can cracks move? A research adventure in materials failure using millions of atoms and big computers." *Advances in Physics*, 52(8), 727-790.

[2] Alder, B. J., and Wainwright, T. E. (1957). "Phase transition of a hard sphere system." *J. Chem. Phys.*, 27, 1208-1209.

[3] Alder, B. J., and Wainwright, T. E. (1970). "Decay of the velocity autocorrelation function." *Phys. Rev. A*, 1, 18-21.

[4] Alvarez, L. J., Sanz, J. F., Capitan, M. J., and Odriozola, J. A. (1992). "Molecular dynamics studies of the structure of γ-alumina." *Chem. Phys. Lett.*, 192(5,6), 463-468.

[5] Arnaiz, F. J., Aguado, R., and Arnaiz, S. (1998). "Microscale thermite reactions." *J. Chem. Edu.*, 75(12), 1630-1631.

[6] Asay, J. R. (1993). "High-Pressure Shock Compression of Solids." Springer, New York, 1-90.

[7] Ashby, M. F., and Verrall, R. A. (1973). "Diffusion accomodated flow and superplasticity." *Acta Metallurgica*, 21, 149-163.

[8] Baburaj, E., Hubert, K., and Froes, F. (1997). "Preparation of Ni powder by mechanochemical process." *J. Alloys & Compounds*, 257, 146-149.

[9] Baer, M. R. (2000). "Computational modeling of heterogeneous reactive materials at the mesoscale." *Shock Compression of Condensed Matter-1999*, 27-33.

[10] Baer, M. R. (2002). "Modeling heterogeneous energetic materials at the mesoscale." *Thermochimica Acta*, 384(1-2), 351-367.

[11] Baer, M. R., and Trott, W. M. (2002). "Mesoscale descriptions of shock-loaded heterogeneous porous materials." *Shock Compression of Condensed Matter-2001*, 713-716.

[12] Banerjee, A., Adams, N., Simons, J., and Shepard, R. (1985). "Search for stationary points on surfaces." *J. Phys. Chem.*, 89(1), 52-57.

[13] Barth, E. (2001). *MDT - The molecular dynamics test set*, Springer Verlag Heidelberg.

[14] Baskes, M. I. (1992). "Modified embedded-atom potentials for cubic materials and impurities." *Phys. Rev. B*, 46(5), 2727-2742.

[15] Baskes, M. I., Asta, M., and Srinivasan, S. G. (2001). "Determining the range of forces in empirical many-body potentials using first principles calculations." *Phil. Mag. A*, 81(4), 991-1008.

[16] Baskes, M. I., and Johnson, R. A. (1994). "Modified embedded atom potentials for HCP metals." *Mod. Sim. Mat. Sci. Engg.*, 2, 147-163.

[17] Belashchenko, D. K. (1997). "Computer simulation of the structure and properties of non-crystalline oxides." *Russ. Chem. Rev.*, 66, 733-763.

[18] Belashchenko, D. K., and Ostraovski, O. I. (2001). "Molecular dynamics simulation of oxides with ionic-covalent bonds." *Thermochimica Acta*, 372, 143-152.

[19] Belashchenko, D. K., Ostraovski, O. I., and Saposznikova, S. Y. (1998). "Computer study of structure, thermodynamic, and electrical transport properties of Na_3AlF_6-Al_2O_3 and CaF_2-Al_2O_3 melts." *Metall. Trans.*, 29B, 105-110.

[20] Benson, D. J., Meyers, M. A., and Fu, H.-H. (2004). "Large deformation simulations of nanocrystalline materials." *CP712, Materials Processing and Design: Modeling, Simulation and Applications, NUMIFORM 2004*, 1552-1557.

[21] Besson, R., and Morillo, J. (1997). "Development of a semiempirical n-body noncentral potential for Fe-Al alloys." *Phys. Rev. B*, 55(1), 193-204.

[22] Bonetti, E., Campari, E. G., Del Bianco, L., and Scipione, G. (1995). "Anelasticity and structural stability of nanostructured metals and compounds." *Nanostructured Materials*, 6, 639-642.

[23] Born, M., and Huang, K. (1954). *Dynamical theory of crystal lattices*, Clarendon Press, Oxford.

[24] Boslough, M. B. (1990). "A thermochemical model for shock induced reactions (heat detonations) in solids." *J. Chem. Phys.*, 92(3), 1839-1848.

[25] Brankovic, Z., Brankovic, G., Jovalekic, C., Maniette, Y., Cilense, M., and Varela, J. A. (2003). "Mechanochemical synthesis of PZT powders." *Mater. Sci. Eng. A*, 345, 243-248.

[26] Brenner, D. W. (1990). "Empirical potential for hydrocarbons for use in simulating the chemical vapor deposition of diamond films." *Phys. Rev. B*, 42(15), 9458-9471.

[27] Brenner, D. W., Robertson, D. H., Elert, M. L., and White, C. T. (1993). "Detonation of nanometer resolution using molecular dynamics." *Phys. Rev. Lett.*, 70(4), 2174-2177.

[28] Bringa, E. M., Cazamias, J. U., Erhart, P., Stoelken, J., Tanushev, N., Wirth, B. D., Rudd, R. E., and Caturla, M. J. (2004). "Atomistic shock Hugoniot simulation of single-crystal copper." *J. Appl. Phys.*, 96(7), 3793-3799.

[29] Bruni, S., Cariati, F., Casu, M., Lai, A., Musinu, A., Piccaluga, G., and Solinas, S. (1999). "IR and NMR study of nanoparticle-support interactions in a Fe2O3-SiO2 nanocomposite prepared by a Sol-gel method." *Nanostructured Materials*, 11(5), 573-586.

[30] Buehler, M. J., Hartmaier, A., Gao, H., Duchaineau, M., and Abraham, F. F. (2004). "Atomic plasticity: description and analysis of a one-billion atom simulation of ductile materials failure." *Comput. Meth. Appl. Mech. Engg.*, 193, 5257-5282.

[31] Cai, B., Kong, Q. P., Lu, L., and Lu, K. (2000). "Low temperature creep of nanocrystalline pure copper." *Mater. Sci. Eng. A*, 286(1), 188-192.

[32] Cannas, C., Musinu, A., Navarra, G., and Piccaluga, G. (2004). "Structural investigation of Fe_2O_3–SiO_2 nanocomposites through radial distribution functions analysis." *Phys. Chem. Chem. Phys.*, 6, 3530-3534.

[33] Cappello, F., and Mancuso, A. (2003). "A genetic algorithm for combined topology and shape optimizations." *Computer Aided Design*, 35, 761-769.

[34] Carlsson, A. E. (1990). "Beyond pair potentials in elemental transition metals and semiconductors." *Solid State Physics*, 43, 1-91.

[35] Casula, M. F., Corrias, A., and Paschina, G. (2001). "Iron oxide-slica aerogel and xerogel nanocomposite materials." *J. Non-Crystalline Solids*, 293-295, 25-31.

[36] Catlow, C. R. A., and Mackrodt, W. C. (1982). "Computer Simulation of Solids." Lecture Notes in Physics, H. Araki, J. Ehlers, K. Hepp, R. Kippenhahn, H. A. Weidenmuller, and J. Zittartz, eds., Springer-Verlag, Berlin.

[37] Catti, M., Valerio, G., and Dovesi, R. (1995). "Theoretical study of electronic, magnetic, and structural properties of α-Fe_2O_3." *Phys. Rev. B*, 51(12), 7441-7450.

[38] Chaplot, S. L., and Sikka, S. K. (2000). "Molecular-dynamics simulation of shock-stress-induced amorphization of α -quartz." *Phys. Rev. B*, 61, 11205-11208.

[39] Che, J., Cagin, T., and Goddard III, W. A. (1999). "Generalized extended empirical bond-order dependent force fields including nonbond interactions." *Theor. Chem. Acta*, 102, 346-354.

[40] Chen, D. (1995). "Structural modeling of nanocrystalline materials." *Comput. Mat. Sci.*, 3(3), 327-333.

[41] Chen, M., Ma, E., Hemker, K. J., Wang, Y. M., and Cheng, X. (2003). "Deformation twinning in nanocrystalline Aluminum." *Science*, 300(5623), 1275-1277.

[42] Chokshi, A. H., Rosen, A., Karch, J., and Gleiter, H. (1989). "On the validity of the Hall--Petch relationship in nanocrystalline materials." *Scripta Materialia*, 23(10), 1679-1684.

[43] Christian, J. W., and Mahajan, S. (1995). "Deformation twinning." *Progr. Mater. Sci.*, 39(1), 1-157.

[44] Chung, C. S., Kim, J., Kim, H., and Kim, W. (2002). "Improvement of high-cycle fatigue life in a 6061 Al alloy produced by equal channel angular pressing." *Mater. Sci. Eng. A*, 337(1-2), 39-44.

[45] Courtney, T. H. (1990). *Mechanical Behavior of Materials*, McGraw-Hill, New York.

[46] Cukrov, L. M., Tsuzuki, T., and McCormick, P. G. (2001). "SnO_2 nanoparticles prepared by mechanochemical processing." *Scripta Materialia*, 44(8-9), 1787-1790.

[47] Dalla Torre, F., and Van Swygenhoven, H. (2002). "Nanocrystalline electrodeposited Ni: microstructure and tensile properties." *Acta Materialia*, 50(15), 3957-3970.

[48] Darden, T. A., York, D. M., and Pedersen, L. G. (1993). "Particle mesh Ewald. An N.log(N) method for Ewald sums in large systems." *J. Chem. Phys.*, 98, 10089-10092.

[49] Dehm, G., Scheu, C., Rühle, M., and Raj, R. (1998). "Growth and structure of internal Cu/Al_2O_3 and $Cu/Ti/Al_2O_3$ interfaces." *Acta Materialia*, 46(3), 759-772.

[50] Derlet, P. M., and Van Swygenhoven, H. (2002). "Length scale effects in the simulation of deformation properties of nanocrystalline metals." *Scripta Materialia*, 47, 719-724.

[51] Derlet, P. M., Van Swygenhoven, H., and Hasnaoui, A. (2003). "Atomistic simulation of dislocation emission in nanosized grain boundaries." *Phil. Mag.*, 83(31-34), 3569-3575.

[52] Ding, H.-Q., Karasawa, N., and Goddard III, W. A. (1992). "Atomic level simulations on a million particles: The cell multipole method for Coulomb and London nonbond interactions." *J. Chem. Phys.*, 97(6), 4309-4315.

[53] Ding, J., Tsuzuki, T., McCormick, P. G., and Street, R. (1996). "Ultrafine Co and Ni particles prepared by mechanochemical processing." *J. Phys. D*, 29, 2365-2369.

[54] Do, I. P. H., and Benson, D. J. (2001). "Micromechanical modeling of shock-induced chemical reactions in heterogeneous multi-material powder mixtures." *Int. J. Plasticity*, 17, 641-668.

[55] El-Sherik, A. M., Erb, U., Palumbo, G., and Aust, K. T. (1992). "Deviations from Hall-Petch behavior in as-prepared nanocrystalline nickel." *Scripta Metallurgica et Materialia*, 27(9), 1185-1188.

[56] Ercolessi, F., and Adams, J. B. (1993). "Interatomic potentials from first-principles calculations: the force-matching method." *Europhys. Lett.*, 26, 583-596.

[57] Estrin, Y., Sluys, B., Brechet, Y., and Molinar, I. A. (1998). "A dislocation based gradient plasticity model." *J. de Physique IV*, 8(1), 135-141.

[58] Ewald, P. (1921). "Die Berechnung optischer und elektrostatischer Gitterpotentiale." *Ann. Phys.*, 64, 253-287.

[59] Fang, H., Horstemeyer, M. F., Baskes, M. I., and Solanki, K. (2004). "Atomisitc simulations of Bauschinger effects of metals with high angle and low angle grain boundaries." *Comput. Meth. Appl. Mech. Engg.*, 193, 1789-1802.

[60] Farkas, D., Mehl, M. J., and Papaconstantopoulos, D. A. (2001). "Lattice trapping of cracks in Fe using an interatomic potential derived from experimental data and *ab initio* calculations." *Mat. Res. Soc. Symp. Proc.*, 653, Z6.4.1-6.

[61] Fedorov, A. A., Gutkin, M. Y., and Ovid'ko, I. A. (2003). "Transformations of grain boundary dislocation pile-ups in nano- and polycrystalline materials." *Acta Materialia*, 51(4), 887-898.

[62] Fedorov, A. A., Gutkin, M. Y., and Ovid'ko, I. A. (2002). "Triple junction diffusion and plastic flow in fine-grained materials." *Scripta Materialia*, 47(1), 51-55.

[63] Finnis, M. W., and Sinclair, J. E. (1984). "A simple empirical N-body potential for transition metals." *Phil. Mag. A*, 50, 45-55.

[64] Foiles, S. M., Baskes, M. I., and Daw, M. S. (1986). "Embedded-atom-method functions for the fcc metals Cu, Ag, Au, Pd, Pt, and their alloys." *Phys. Rev. B*, 33(12), 7983-7991.

[65] Fougere, G. E., Weertman, J. R., and Siegel, R. W. (1995). "Processing and mechanical behavior of nanocrystalline Fe." *Nanostructured Materials*, 5(2), 127-134.

[66] Fu, H. H., Benson, D. J., and Meyers, M. A. (2001). "Analytical and computational description of effect of grain size on yield stress of metals." *Acta Materialia*, 49(13), 2567-2582.

[67] Gale, J. D., Catlow, C. R. A., and Mackrodt, W. C. (1992). "Periodic *ab initio* determination of interatomic potentials for Alumina." *Mod. Sim. Mat. Sci. Engg.*, 1, 73-81.

[68] Gale, J. D., and Rohl, A. L. (2003). "The general utility lattice program (GULP)." *Mol. Sim.*, 29(5), 291-341.

[69] Gao, F., Wang, C. M., Maheswaran, S., and Thevuthasan, S. (2003). "Atomic level simulations of misfit dislocation at the interface of Fe_2O_3/Al_2O_3 system." *Nucl. Inst. Meth. in Physics Res. B*, 207, 63-71.

[70] Gavezzotti, A. (2002). "Structure and intermolecular potentials in molecular crystals." *Mod. Sim. Mat. Sci. Engg.*, 10, R1-R29.

[71] Germann, T. C., Holian, B. L., and Lomdahl, P. S. (2000). "Orientation dependence in molecular dynamics simulations of shocked single crystals." *Phys. Rev. Lett.*, 84(23), 5351-5354.

[72] Gleiter, H. (1998). "Nanocrystalline materials." *Prog. Mater. Sci*, 33(4), 223-315.

[73] Gleiter, H. (2000). "Nanostructured materials: Basic concepts and microstructure." *Acta Materialia*, 48, 1-29.

[74] Goddard III, W. A., Zhang, Q., Uludogan, M., Strachan, A., and Cagin, T. (2002). "The reaxFF polarizable reactive force fields for molecular dynamics simulation of ferroelectrics." *Fundamental Physics of Ferroelectrics*, Washington DC, 45-55.

[75] Gottstein, G., King, A. H., and Shvindlerman, L. S. (2000). "The effect of triple-junction drag on grain growth." *Acta Materialia*, 48(2), 397-403.

[76] Goya, G. F., and Rechenberg, H. R. (2000). "Mechanosynthesis of intermetallic $Fe_{100-x}Al_x$ obtained by reduction of Al/Fe_2O_3 composite." *J. Phys.: Condense Matter*, 12, 10579–10590.

[77] Graham, R. A. (1993). *Solids under high pressure shock compression: Mechanics, Physics and Chemistry*, Springer-Verlag, New York NY USA.

[78] Granier, J. J., and Pantoya, M. L. (2004). "The effect of size distribution on burn rate in nanocomposite thermites: a probability density function study." *Combustion Theory Modelling*, 8, 555-565.

[79] Greengard, L., and Rokhlin, V. (1987). "A fast algorithm for particle simulations." *J. Comput. Phys.*, 73, 325-348.

[80] Grimes, R. W. (1994). "Solution of MgO, CaO, and TiO_2 in α-Al_2O_3." *J. Am. Ceram. Soc.*, 77(2), 378-384.

[81] Gross, D., and Li, M. (2002). "Constructing microstructures of poly- and nanocrystalline materials for numerical modeling and simulation." *Appl. Phys. Lett.*, 80(5), 746-748.

[82] Gryaznov, V. G., Polonsky, I. A., Romanov, A. E., and Trusov, L. I. (1991). "Size effects of dislocation stability in nanocrystals." *Phys. Rev. B*, 44, 42-46.

[83] Gschneidner, K. A. (1964). "Physical properties and interrelationships of metallic and semimetallic elements." *Solid State Phys.*, 16, 275-426.

[84] Gutie´rrez, G., and Johansson, B. (2002). "Molecular dynamics study of structural properties of amorphous Al_2O_3." *Phys. Rev. B*, 65(104202), 1-9.

[85] Gutkin, M. Y., Ovid'ko, L. A., and Skiba, N. V. (2003). "Crossover from grain boundary sliding to rotational deformation in nanocrystalline materials." *Acta Materialia*, 51(14), 4059-4071.

[86] Hahn, H., Mondal, P., and Padmanabhan, K. A. (1997). "Plastic deformation of nanocrystalline materials." *Nanostructured Materials*, 9(1-8), 603-606.

[87] Hahn, H., and Padmanabhan, K. A. (1997). "A model for the deformation of nanocrystalline materials." *Phil. Mag. B*, 76, 559-571.

[88] Han, J.-H., and Kim, D.-Y. (1998). "Determination of three-dimensional grain size distribution by linear intercept measurement." *Acta Mater.*, 46(6), 2021-2028.

[89] Hanlon, T., Kwon, Y., and Suresh, S. (2003). "Grain size effects on the fatigue response of nanocrystalline metals." *Scripta Materialia*, 49(7), 675-680.

[90] Hardy, R. J. (1981). "Formulas for determining local properties in molecular dynamics simulations: Shock waves." *J. Chem. Phys.*, 76, 622.

[91] Haslam, A. J., Phillpot, S. R., Wolf, D., Moldovan, D., and Gleiter, H. (2001). "Mechanisms of grain growth in nanocrystalline fcc metals by molecular-dynamics simulation." *Mater. Sci. Engg. A*, 318, 293-312.

[92] Hasnaoui, A., Derlet, P. M., and Van Swygenhoven, H. (2004). "Interaction between dislocations and grain boundaries under an indenter – a molecular dynamics simulation." *Acta Materialia*, 52, 2251-2258.

[93] Hasnaoui, A., Van Swygenhoven, H., and Derlet, P. M. (2003). "Dimples on nanocrystalline fracture surfaces As evidence for shear plane formation." *Science*, 300(5625), 1550-1552.

[94] Herr, U., Jing, J., Gonser, U., and Gleiter, H. (1990). "Alloy effects in consolidated binary mixtures of nanometer-sized crystals investigated by Mössbauer spectroscopy." *Solid State Commun.*, 76(2), 197-202.

[95] Hirth, J. P., Hoagland, R. G., Holian, B. L., and Germann, T. C. (1999). "Shock relaxation by a strain induced martensitic phase transformation." *Acta Materialia*, 47(8), 2409-2415.

[96] Hoffer, H. J., and Averbach, R. S. (1990). "Grain growth in nanocrystalline TiO2 and its relation to Vickers hardness and fracture toughness." *Scripta Metallurgica et Materialia*, 24(12), 2401-2406.

[97] Holian, B. L. (1988). "Modeling shock-wave deformation via molecular dynamics." *Phys. Rev. A*, 37(7), 2562-2568.

[98] Holian, B. L., Germann, T. C., Lomdahl, P. S., Hammerberg, J. E., and Ravelo, R. J. (1999). "Shock waves and their aftermath: A view from the atomic scale." *Shock Compression of Condensed Matter*, 35-40.

[99] Holian, B. L., Hammerberg, J. E., and Lomdahl, P. S. (1998). "The birth of dislocations in shock waves and high-speed friction." *J. Computer-Aided Materials Design*, 5, 207-224.

[100] Holian, B. L., Hoover, W. G., Moran, B., and Straub, G. K. (1980). "Shock-wave structure via nonequilibrium molecular dynamics and Navier-Stokes continuum mechanics." *Phys. Rev. A*, 22(6), 2798-2808.

[101] Holian, B. L., and Lomdahl, P. S. (1998). "Plasticity induced by shock waves in nonequilibrium molecular dynamics simulations." *Science*, 280, 2085-2093.

[102] Holian, B. L., and Ravelo, R. J. (1995). "Fracture simulations using large-scale molecular dynamics." *Phys. Rev. B*, 51(17), 11275-11288.

[103] Holian, B. L., and Straub, G. K. (1979). "Molecular dynamics of shock waves in three-dimensional solids: Transition from non-steady to steady waves in perfect crystals and implications for the Rankine-Hugoniot conditions." *Phys. Rev. Lett.*, 43(21), 1598-1600.

[104] Holian, B. L., Voter, A. F., Wagner, N. J., Ravelo, R. J., Chen, S. P., Hoover, W. G., Hoover, C. G., Hammerberg, J. E., and Dontje, T. D. (1991). "Effects of pairwise versus many-body forces on high stress plastic deformation." *Phys. Rev. A.*, 43(6), 2655-2661.

[105] Honeycutt, J. D., and Anderson, H. C. (1987). "Molecular dynamics study of melting and freezing of small Lennard-Jones clusters." *J. Phys. Chem.*, 91, 4950-4963.

[106] Hoover, W. G. (1979). "Structure of a shock-wave front in a liquid." *Phys. Rev. Letters*, 42(23), 1531-1534.

[107] Hoover, W. G., and Ashurst, W. T. (1975). Theoretical chemistry: Advances and perspectives, H Eyring and D Henderson, eds., 1.

[108] Horie, Y., and Yano, K. (2001). "Nonequilibrium fluctuations in shock compression of polycrystalline α-Iron." *Shock Compression of Condensed Matter-2001*, 553-556.

[109] Huang, Y. L., Xue, D. S., Zhou, P. H., Ma, Y., and Li, F. S. (2003). "α-Fe–Al_2O_3 nanocomposites prepared by sol–gel method." *Mater. Sci. Eng. A*, 359(1-2), 332-337.

[110] Humphrey, W., Dalke, A., and Schulten, K. (1996). "VMD - Visual Molecular Dynamics." *J. Molec. Graphics*, 14.1, 33-38.

[111] Huntington, H. B. (1958). "The elastic constants of crystals." Solid state physics: Advances in research and applications, F. Seitz and D. Turnbull, eds., Academic Press, New York, 213-351.

[112] Iczkowski, R. P., and Margrave, J. L. (1961). "Electronegativity." *J. Am. Chem. Soc.*, 83(17), 3547-3551.

[113] Jiao, F., Bettge, D., Osterle, W., and Ziebs, J. (1996). "Tension-compression asymmetry of the (001) single crystal nickel base superalloy SC16 under cyclic loading at elevated temperatures." *Acta Materialia*, 44(10), 3933-3942.

[114] Kadau, K., Germaim, T. C., Lomdahl, P. S., and Holian, B. L. (2001). "Shock-induced structural phase transformations studied by large scale molecular dynamics simulations." *Shock Compression of Condensed Matter - 2001*.

[115] Kadau, K., Germann, T. C., Lomdahl, P. S., and Holian, B. L. (2002). "Microscopic view of structural phase transitions induced by shock waves." *Science*, 296, 1681.

[116] Kadau, K., Germann, T. C., Lomdahl, P. S., Holian, B. L., and Cherne, F. J. (2004). "Atomistic simulations of shock-induced phase transitions." *Shock compression of condensed matter-2003*, Portland, 229-234.

[117] Kalia, R. K., Campbell, T. J., Chatterjee, A., Nakano, A., Vashishta, P., and Ogata, S. (2000). "Multiresolution algorithms for massively parallel molecular

dynamics simulations of nanostructured materials." *Comput. Phys. Commun.*, 128, 245-259.

[118] Kan Hachiya, Y. I. (2002). "Transition-metal-like interatomic potentials for Aluminum." *J. Alloys Compounds*, 337, 53-57.

[119] Ke, M., Hackney, S. A., Milligan, W. W., and Aifantis, E. C. (1995). "Observation and measurement of grain rotation and plastic strain in nanostructured metal thin films." *Nanostructured Materials*, 5(6), 689-697.

[120] Keblinski, P., Phillpot, S. R., Wolf, D., and Gleiter, H. (1997). "Amorphous structure of grain boundaries and grain junctions in nanocrystalline silicon by molecular-dynamics simulation." *Acta Materialia*, 45(3), 987-998.

[121] Keblinski, P., Wolf, D., and Gleiter, H. (1998). "Molecular-Dynamics Simulation of Grain-Boundary Diffusion Creep." *Interface Sci.*, 6, 205-212.

[122] Keblinski, P., Wolf, D., Phillpot, S. R., and Gleiter, H. (1999). "Structure of grain boundaries in nanocrystalline palladium by molecular dynamics simulation." *Scripta Materialia*, 41(6), 631-636.

[123] Kelchner, C. L., Plimpton, S. J., and Hamilton, J. C. (1998). "Dislocation nucleation and defect structure during surface indentation." *Phys. Rev. B*, 58(17), 11085-11088.

[124] Kenny, S. D., Nguyen-Manh, D., Fujitani, H., and Sutton, A. P. (1998). "*Ab initio* modeling of Alumina." *Phil. Mag. Lett.*, 78(6), 469-476.

[125] Kim, H. S., and Bush, M. B. (1999). "The effects of grain size and porosity on the elastic modulus of nanocrystalline materials." *Nanostructured Materials*, 11(3), 361-367.

[126] Kim, H. S., Estrin, Y., and Bush, M. B. (2000). "Plastic deformation behavior of fine-grained materials." *Acta Materialia*, 48(2), 493-504.

[127] Kim, H. S., Estrin, Y., and Bush, M. B. (2001). "Constitutive modeling of strength and plasticity of nanocrystalline metallic materials." *Mater. Sci. Engg. A*, 316(1-2), 195-199.

[128] Konstantinidis, D. A., and Aifantis, E. C. (1998). "On the "anomalous" hardness of nanocrystalline materials." *Nanostructured Materials*, 10(7), 1111-1118.

[129] Kress, J. D., Bickham, S. R., Collins, L. A., and Holian, B. L. (1999). "Tight-Binding molecular dynamics of shock waves in methane." *Phys. Rev. Lett.*, 83(19), 3897-3899.

[130] Kum, O. (2003). "Orientation effects in shocked nickel single crystals via molecular dynamics." *J. Appl. Phys.*, 93(6), 3239-3247.

[131] Kumar, K. S., Suresh, S., Chisholm, M. F., Horton, J. A., and Wang, P. (2003a). "Deformation of electrodeposited nanocrystalline nickel." *Acta Materialia*, 51(2), 387-405.

[132] Kumar, K. S., Van Swygenhoven, H., and Suresh, S. (2003b). "Mechanical behavior of nanocrystalline metals and alloys." *Acta Materialia*, 51, 5743-5774.

[133] Kumar, S., Kurtz, S. K., Banavar, J. R., and Sharma, M. G. (1992). "Properties of a three-dimensional Poisson-Voronoi tessellation: A Monte Carlo Study." *J. Stat. Phys.*, 67, 523-551.

[134] Latapie, A., and Farkas, D. (2003). "Effect of grain size on the elastic properties of nanocrystalline α-iron." *Scripta Materialia*, 48, 611-615.

[135] Lee, C. H., Lee, S. H., Chun, S. Y., Lee, S. J., and Kwon, Y. S. (2004). "Nanocomposite formation in the Fe_2O_3-M (M=Al, Ti, Zn, Cu) systems by mechanical alloying." *Materials Science Forum*, 449-452(1), 253-256.

[136] Legros, M., Elliot, B. R., Rittner, M. N., Weertman, J. R., and Hemker, K. J. (2000). "Micro-sample tensile testing of nanocrystalline metals." *Phil. Mag. A*, 80(4), 1017-1026.

[137] Levin, I., and Brandson, D. (1998). "Metastable alumina polymorphs: Crystal structures and transition sequences." *J. Am. Ceram. Soc.*, 81(8), 1995-2012.

[138] Lewis, G. V., and Catlow, C. R. A. (1985). "Potential models for ionic oxides." *J. Phys. C: Solid State Physics*, 18, 1149-1161.

[139] Liao, X. Z., Srinivasan, S. G., Zhao, Y. H., Baskes, M. I., Zhua, Y. T., Zhou, F., Lavernia, E. J., and Xu, H. F. (2004). "Formation mechanism of wide stacking faults in nanocrystalline Al." *Appl. Phys. Lett.*, 84(18), 3564-3566.

[140] Liao, X. Z., Zhou, F., Lavernia, E. J., He, D. W., and Zhua, Y. T. (2003a). "Deformation twins in nanocrystalline Al." *Appl. Phys. Lett.*, 83(24), 5062-5064.

[141] Liao, X. Z., Zhou, F., Lavernia, E. J., Srinivasan, S. G., Baskes, M. I., He, D. W., and Zhu, Y. T. (2003b). *Appl. Phys. Lett.*, 83, 632.

[142] Liu, Y.-P., Kim, K., Berne, J., Friesner, R. A., and Rick, S. W. (1997). "Constructing *ab initio* force fields for molecular dynamics simulations." *J. Chem. Phys.*, 108(12), 4739-4755.

[143] Loffler, J., and Weissmuller, J. (1995). "Grain-boundary atomic structure in nanocrystalline palladium from x-ray atomic distribution functions." *Phys. Rev. B*, 52(10), 7076-7093.

[144] Long, J. W., Logan, M. S., Rhodes, C. P., Carpenter, E. E., Stroud, R. M., and Rolison, D. R. (2004). "Nanocrystalline Iron Oxide aerogels as mesoporous magnetic architectures." *J. Am. Chem. Soc.*, 126(51), 16879-16889.

[145] Loveridge-Smith, A., Allen, A., Belak, J., Boehly, T., Hauer, A., Holian, B., Kalantar, D., Kyrala, G., Lee, R. W., Lomdahl, P., Meyers, M. A., Paisley, D., Pollaine, S., Remington, B., Swift, D. C., Weber, S., and Wark, J. S. (2001). "Anomalous elastic response of silicon to uniaxial shock compression on nanosecond time scales." *Phys. Rev. Lett.*, 86(11), 2349-2352.

[146] Lu, K., and Sun, N. X. (1997). "Grain-boundary enthalpy of nanocrystalline selenium." *Phil. Mag. Lett.*, 75(6), 389-392.

[147] Lu, L., Li, S. X., and Lu, K. (2001). "An abnormal strain rate effect on tensile behavior in nanocrystalline copper." *Scripta Materialia*, 45(10), 1163-1169.

[148] Lubarda, V. (2002). *Elastoplasticity Theory*, CRC Press.

[149] Lund, A. C., Nieh, T. G., and Schuh, C. A. (2004). "Tension/compression strength asymmetry in a simulated nanocrystalline material." *Phys. Rev. B*, 69(1), 012101-1.

[150] Lundergan, C. D., and Herrman, W. (1962). "Equation of state of 6061-T6 Aluminum at low pressures." *J. Appl. Phys.*, 34(7), 2046-2052.

[151] Mackrodt, W. C., Davey, R. J., and Black, S. N. (1987). "The morphology of α-Al_2O_3 and α-Fe_2O_3: The importance of surface relaxation." *J. Crystal Growth*, 80, 441-446.

[152] Mackrodt, W. C., and Stewart, R. F. (1979). "Defect properties of ionic solids: II. Point defect energies based on modified electron-gas potentials." *J. Phys. C: Solid State Physics*, 12, 431-449.

[153] Maillet, J.-B., Mareschal, M., Soulard, L., Ravelo, R., Lomdahl, P. S., Germann, T. C., and Holian, B. L. (2001). "Uniaxial hugoniostat: A method for atomistic simulations of shocked materials." *Phys. Rev. E*, 63, 016121-016128.

[154] Makarov, P. V. (1998). "Physical mesomechanics approach in simulation of deformation and fracture processes." *Physical Mesomechanics*, 1, 57-79.

[155] Manassidis, I., and Gillan, M. J. (1994). "Structure and energetics of Alumina Surfaces Calculated from First Principles." *J. Am. Ceram. Soc.*, 77(2), 335-341.

[156] Manorama, S. V., Gopal Reddy, C. V., and Rao, V. J. (1999). "Tin dioxide nanoparticles prepared by sol-gel method for an improved hydrogen sulfide sensor." *Nanostructured Materials*, 11(5), 643-649.

[157] Marsh, S. P. (1980). "LASL shock hugoniot data." University of California Press, Berkely and Los Angeles.

[158] Masumura, R. A., Hazzledine, P. M., and Pande, C. S. (1998). "Yield stress of fine grained materials." *Acta Materialia*, 46(13), 4527-4534.

[159] Meijering, J. L. (1953). "Interface area, edge length, and number of vertices in crystal aggregates with random nucleation." *Philips Research Reports*, 8, 270-290.

[160] Melchionna, S., Ciccotti, G., and Holian, B. L. (1993). "Hoover NPT dynamics for systems varying in shape and size." *Mol. Phys.*, 78(3), 533-544.

[161] Minervini, L., and Grimes, R. W. (1999). "Defect clustering in wustite." *J. Phys. Chem. of Solids*, 60, 235-245.

[162] Minervini, L., Zacate, M. O., and Grimes, R. W. (1999). "Defect cluster formation in M_2O_3-doped CeO_2." *Solid State Ionics*, 116, 339-349.

[163] Mishin, Y., Farkas, D., Mehl, M. J., and Papaconstantopoulos, D. A. (1999). "Interatomic potentials for monoatomic metals from experimental data and *ab initio* calculations." *Phys. Rev. B*, 59(5), 3393-3407.

[164] Mishin, Y., Mehl, M. J., Papaconstantopoulos, D. A., Voter, A. F., and Kress, J. D. (2001). "Structural stability and lattice defects in copper: *Ab initio*, tight-binding, and embedded-atom calculations." *Phys. Rev. B*, 63, 224106-224121.

[165] Mishra, R. S., Valiev, R. Z., and Mukherjee, A. K. (1997). "The observation of tensile superplasticity in nanocrystalline materials." *Nanostructured Materials*, 9(1-8), 473-476.

[166] Mogilevsky, M. A. (1981). *Shock Waves and High Strain Rate Phenomena in Metals*, New York, 531-535.

[167] Moriarty, J. M. (1988). "Density functional formulation of the generalized pseudopotential theory. III. Transition-metal interatomic potentials." *Phys. Rev. B*, 38(3199).

[168] Mortier, W. J., Genechten, K. V., and Gasteiger, J. (1985). "Electronegativity equalization: application and parameterization." *J. Am. Chem. Soc.*, 107, 829-835.

[169] Mukherjee, A. K. (2002). "An examination of the constitutive equation for elevated temperature plasticity." *Mater. Sci. Engg. A*, 322(1-2), 1-22.

[170] Murayama, M., Howe, J. M., Hidaka, H., and Takaki, S. (2002). "Atomic-level observation of disclination dipoles in mechanically milled, nanocrystalline Fe." *Science*, 295(5564), 2433-2435.

[171] Murr, L. E. (1975). *Interfacial phenomenon in Metals and Alloys*, Addison-Wesley Publishing Company, Massachusetts.

[172] Nayak, S., and Dahotre, N. B. (2002). "The laser-induced combustion synthesis of Iron-oxide nanocomposite coatings on Aluminum." *J. Mat.*, 54(9), 39-40.

[173] Nieman, G. W., Weertman, J. R., and Siegel, R. W. (1991). "Mechanical behavior of nanocrystalline Cu and Pd." *J. Mater. Res.*, 6(5), 1012-1027.

[174] Ohira, T., and Inoue, Y. (1998). "Atomistic simulations of the work of adhesion at metal oxide interfaces." *MRS Symposia Proceedings*, 401-406.

[175] Osterle, W., Bettge, D., Bernard, F., and Klingelhoffer, H. (2000). "Modeling the orientation and direction dependence of the critical resolved shear stress of nickel-base superalloy single crystals." *Acta Materialia*, 48, 689-700.

[176] Ovid'ko, L. A. (2002). "Deformation of nanostructures." *Science*, 295(5564), 2386-2388.

[177] Ovid'ko, I. A., and Sheinerman, A. G. (2004). "Triple junction nanocracks in deformed nanocrystalline materials." *Acta Materialia*, 52, 1201-1209.

[178] Palumbo, G., Thorpe, S. J., and Aust, K. T. (1990). "On the contribution of triple junctions to the structure and properties of nanocrystalline materials." *Scripta Metallurgica et Materialia*, 24(7), 1347-1350.

[179] Parr, R. G., and Pearson, R. G. (1983). "Absolute hardness: comParrion parameter to absolute electronegativity." *J. Am. Chem. Soc.*, 105, 7512-7516.

[180] Parry, D. E. (1975). "The electrostatic potential in the surface region of an ionic crystal." *Surface Sci.*, 49, 433-440.

[181] Pasianot, R., Farkas, D., and Savino, E. J. (1991). "Empirical many-body interatomic potential for bcc transition metals." *Phys. Rev. B*, 43(9), 6952-6961.

[182] Patlan, V., Higashi, K., Kitagawa, K., and Kawazoe, M. (2001). "Cyclic response of fine grain 5056 Al–Mg alloy processed by equal-channel angular pressing." *Mater. Sci. Engg. A*, 319, 587-591.

[183] Phillpot, S. R., Wolf, D., and Gleiter, H. (1995). "Molecular-dynamics study of the synthesis and characterization of a fully dense, three-dimensional nanocrystalline material." *J. Appl. Phys.*, 78(2), 847-861.

[184] Piccaluga, G., Corrias, A., Ennas, G., and Musinu, A. (2000). "Sol-Gel preparation and characterization of metal-silica and metal oxide-silica nanocomposites." *Materials Science Foundations*, M. Magini and F. H. Wohlbier, eds., Trans Tech. Publ. Inc. NH, USA, 1-25.

[185] Press, W. H., Teukolsky, S. A., Vetterling, W. T., and Flannery, B. P. (1992). *Numerical recipes*, Cambridge University Press, Cambridge.

[186] Rahman, A. (1964). "Correlations in the motion of atoms in liquid argon." *Phys. Rev. A*, A136, 405-411.

[187] Rappe, A. K., and Goddard III, W. A. (1991). "Charge equilibrium in molecular dynamics simulations." *J. Phys. Chem.*, 95, 3358-3363.

[188] Razorenov, S. V., Kanel, G. I., Baumung, K., and Bluhm, H. J. (2002). "Hugoniot elastic limit and spall strength of Aluminum and Copper single crystals over a wide range of strain rates and temperatures." *AIP Conference Proceedings*, 502-506.

[189] Reed, E. J., Fried, L. E., and Joannopoulos, J. D. (2003). "A method for tractable dynamical studies of single and double shock compression." *Phys. Rev. Lett.*, 90(23), 235503.

[190] Rhee, Y.-J., Halley, J. W., Hautman, J., and Rahman, A. (1989). "Ewald methods in molecular dynamics for systems of finite extent in one of three dimensions." *Phys. Rev. B*, 40(1), 36-42.

[191] Rice, B. M., Mattson, W., Grosh, J., and Trevino, S. F. (1996). "Molecular-dynamics study of detonation. I. A comparison with hydrodynamic predictions." *Phys. Rev. E*, 53(1), 611-623.

[192] Rick, S. W., Stuart, S. J., and Berne, B. J. (1994). "Dynamical fluctuating charge force fields: Application to liquid water." *J. Chem. Phys.*, 101, 6141-6170.

[193] Rigg, P. A., and Gupta, Y. M. (2001). "Multiple x-ray diffraction to determine transverse and longitudinal lattice deformation in shocked lithium fluoride." *Phys. Rev. B*, 63(9), 094112.

[194] Robertson, D. H., Brenner, D. W., and White, C. T. (1991). "Split shock waves from molecular dynamics." *Phys. Rev. Lett.*, 67(22), 3132-3135.

[195] Robertson, D. H., Brenner, D. W., and White, C. T. (1998). "Molecular dynamics analysis of shock phenomena." *High Pressure Shock Compression of Solids III*, 37-57.

[196] Robertson, I. J., Heine, V., and Payne, M. C. (1994). "A database of structural energies of aluminum from *ab initio* calculations." *J. Phys. Cond. Matt.*, 6, 9963-9972.

[197] Rodríguez de la Fuente, O., Zimmerman, J. A., González, M. A., Figuera, J. d. l., Hamilton, J. C., Wu Pai, W., and Rojo, J. M. (2002). "Dislocation emission around nanoindentations on a (001) fcc metal surface studied by scanning tunneling microscopy and atomistic simulations." *Phys. Rev. Lett.*, 88(3), 036101-4.

[198] Rollman, G., Rohrbach, A., Entel, P., and Hafner, J. (2004). "First-principles calculation of the structure and magnetic phases of hematite." *Phys. Rev. B*, 69, 165107-11.

[199] Root, S., Hardy, R. J., and Swanson, D. R. (2003). "Continuum predictions from molecular dynamics simulations: Shock waves." *J. Chem. Phys.*, 118(7), 3161-3165.

[200] Roothan, C. C. J. (1951). "A study of two-center integrals useful in calculations on molecular structure." *J. Chem. Phys.*, 19(12), 1445-1458.

[201] Rustad, J. R., Hay, B. P., and Halley, J. W. (1995). "Molecular dynamics simulation of Iron(III) and its hydrolysis products in aqueous solution." *J. Chem. Phys.*, 102(1), 427-431.

[202] Sanders, P. G., Eastman, J. A., and Weertman, J. R. (1998). "Pore distributions in nanocrystalline metals from small-angle neutron scattering." *Acta Materialia*, 46(12), 4195-4202.

[203] Sanders, P. G., Youngdahl, C. J., and Weertman, J. R. (1997). "The strength of nanocrystalline metals with and without flaws." *Mater. Sci. Engg. A*, 234-236, 77-82.

[204] Sapozhnikov, F. A., Dremov, V. V., and Smirnova, M. S. (2003). "Molecular dynamics investigations of elastic-plastic properties of solids." *J Phys. IV France*, 110, 323-328.

[205] Schiøtz, J., Di Tolla, F. D., and Jacobsen, K. W. (1998). "Softening of nanocrystalline metals at very small grain sizes." *Nature*, 391, 561-563.

[206] Schiøtz, J., and Jacobsen, K. W. (2003). "A maximum in the strength of nanocrystalline Cu." *Science*, 301(5638), 1357-1359.

[207] Schiøtz, J., Vegge, T., Di Tolla, F. D., and Jacobsen, K. W. (1999). "Atomic-scale simulations of the mechanical deformation of nanocrystalline metals." *Phys. Rev. B*, 60, 11971-11983.

[208] Schuh, C. A., and Lund, A. C. (2003). "Atomistic basis for the plastic yield criterion of metallic glass." *Nature Materials*, 2, 449-452.

[209] Schwaiger, R., Moser, B., Dao, M., Chollacoop, N., and Suresh, S. (2003). "Some critical experiments on the strain-rate sensitivity of nanocrystalline nickel." *Acta Materialia*, 51(17), 5159-5172.

[210] Schweinfest, R., Ernst, F., Wagner, T., and Ruehle, M. (1999). "High-precision assessment of interface lattice offset by quantitative HRTEM." *Journal of Microscopy*, 194(1), 142-151.

[211] Selezenev, A. A., Golubev, V. K., Aleinikov, A. Y., Butnev, O. I., Barabanov, R. A., and Voronin, B. L. (2001). "Molecular dynamics simulation of shock wave compression in metals." *Shock Compression of Condensed Matter-2001*, 374-378.

[212] Sharma, P., and Ganti, S. (2003). "On the grain-size-dependent elastic modulus of nanocrystalline materials with and without grain-boundary sliding." *J. Mater. Res.*, 18(8), 1823-1826.

[213] Shek, C. J., Lai, J. K. L., and Lin, G. M. (1999). "On some physical properties of nanostructured Cu-Pb alloy prepared by mechanical alloying." *Nanostructured Materials*, 7(8), 887-903.

[214] Siegel, R. W. (1991). "Cluster-assembled nanophase materials." *Annual Review of Materials Science*, 21, 559-578.

[215] Siegel, R. W. (1994a). "Nanophase materials." Encyclopedia of applied physics, G. L. Trigg, ed., VCH, New York, 173–199.

[216] Siegel, R. W. (1994b). "What do we really know about the atomic-scale structure of nanophase materials?" *J. Phys. Chem. Solids*, 55(10), 1097-1106.

[217] Siegel, R. W., and Fougere, G. E. (1995). "Mechanical properties of nanophase metals." *Nanostructured Materials*, 6(1-4), 205-216.

[218] Siegel, R. W., and Thomas, G. J. (1991). "Grain boundaries in nanophase materials." *Ultramicroscopy*, 40(3), 376-384.

[219] Simonelli, G., Pasianot, R., and Savino, E. J. (1993). "Embedded-atom-method interatomic potentials for BCC-Iron." *MRS Symposia Proceedings*, 567-572.

[220] Smith, C. S. (1958). "Metallographic studies of metals after explosive shock." *Trans. Metall. Soc. AIME*, 212, 574-589.

[221] Smith, W., Yong, C. W., and Rodger, P. M. (2002). "DL_POLY: Application to molecular simulation." *Mol. Sim.*, 28(5), 385-471.

[222] Spearot, D. E. (2005). "Atomistic calculations of nanoscale interface behavior in *fcc* metals," PhD Dissertation, Georgia Institute of Technology, Atlanta.

[223] Spearot, D. E., Jacob, K. I., and McDowell, D. L. (2005). "Nucleation of dislocations from [001] bicrystal Interfaces in aluminum." *In print Acta Materialia*.

[224] Stern, E. A., Siegel, R. W., Newville, M., Sanders, P. G., and Haskel, D. (1995). "Are nanophase grain boundaries anomalous?" *Phys. Rev. Lett.*, 75(21), 3874-3877.

[225] Stillinger, F. H., and Weber, T. A. (1985). "Computer simulation of local order in condensed phases of silicon." *Phys. Rev. B*, 31(8), 5262-5271.

[226] Strachan, A., Cagin, T., and Goddard III, W. A. (2001). "Critical behavior in spallation failure of metals." *Phys. Rev. B*, 63(6), 060103.

[227] Straub, G. K., Holian, B. L., and Petschek, R. G. (1979). "Molecular dynamics of shock waves in one-dimensional chains. II. Thermalization." *Phys. Rev. B*, 19(8), 4049-4055.

[228] Strietz, F. H., and Mintmire, J. W. (1994). "Electrostatic potentials for metal-oxide surfaces and interfaces." *Phys. Rev. B*, 50(16), 11996-12003.

[229] Sun, X. K., Xu, J., Chen, W. X., and Wei, W. D. (1994). "Preparation of Al nanoparticles in a controlled environment." *Nanostructured Materials*, 4, 337-344.

[230] Suryanarayana, C., Mukhopadhyay, D., Patankar, S. N., and Froes, F. H. (1992). "Grain size effects in nanocrystalline materials." *J. Mater. Res.*, 7(8), 2114-2118.

[231] Swegle, J. W., and Grady, D. E. (1985). "Shock viscosity and the prediction of shock wave rise times." *J. Appl. Phys.*, 58(2), 692-701.

[232] Takeuchi, S. (2001). "The mechanism of the inverse Hall-Petch relation of nanocrystals." *Scripta Materialia*, 44(8-9), 1483-1487.

[233] Tang, X. G., Guo, H. K., Zhou, Q. F., and Zhang, J. X. (1998). "Synthesis and structure of nanocrystalline oxides based on $PbTiO_3$ by sol-gel process." *Nanostructured Materials*, 10(2), 161-168.

[234] Tanguy, D., Mareschal, M., Lomdahl, P., Germaim, T. C., Holian, B., and Ravelo, R. J. (2003). "Dislocation nucleation induced by a shock wave in a perfect crystal: Molecular Dynamics simulations and elastic calculations." *Phys. Rev. B*, 68, 144111.

[235] Tersoff, J. (1988). "Empirical interatomic potential for silicon with improved elastic properties." *Phys. Rev. B*, 38, 9902-9905.

[236] Tersoff, J. (1990). "Carbon defects and defect reactions in silicon." *Phys. Rev. Lett.*, 64, 1757-1760.

[237] Thadhani, N. (2005). "*Private Communications*."

[238] Thadhani, N. N., Graham, R. A., Royal, T., Dunbar, E., Anderson, M. U., and Holman, G. T. (1997). "Shock-induced chemical reactions in titanium-silicon powder mixtures of different morphologies: Time-resolved pressure measurements and material analysis." *J. Appl. Phys.*, 82(3), 1113-1128.

[239] Tillotson, T. M., Gash, A. E., Simpson, R. L., Hrubesh, L. W., Satcher Jr., J. H., and Poco, J. F. (2001). "Nanostructures energetic materials using sol-gel methodologies." *J. Non-Crystalline Solids*, 285, 338-345.

[240] Tjong, S. C., and Chen, H. (2004). "Nanocrystalline materials and coatings." *Mater. Sci. Engg. R*, 45, 1-88.

[241] Tsai, D. H., and Trevino, S. F. (1981). "Thermal relaxation on a dense liquid under shock compression." *Phys. Rev. A*, 24(5), 2743-2757.

[242] Tsuzuki, T., and McCormick, P. G. (2001). "ZnO nanoparticles synthesized by mechanochemical processing." *Scripta Materialia*, 44(8-9), 1731-1734.

[243] Vailhe, C., and Farkas, D. (1997). "Shear faults and dislocation core structure simulations in B2 FeAl." *Acta Materialia*, 45(11), 4463-4473.

[244] Van Swygenhoven, H., and Caro, A. (1997). "Plastic behavior of nanophase Ni: A molecular dynamics computer simulation." *Appl. Phys. Lett.*, 71(12), 1652-1654.

[245] Van Swygenhoven, H., and Caro, A. (1998). "Plastic behavior of nanophase metals studied by molecular dynamics." *Phys. Rev. B*, 58(17), 11246-11251.

[246] Van Swygenhoven, H., and Caro, A. (1999). "Molecular dynamics computer simulation of nanophase Ni: structure and mechanical properties." *Nanostructured Materials*, 9, 669.

[247] Van Swygenhoven, H., Caro, A., and Farkas, D. (2001). "A molecular dynamics study of polycrystalline fcc metals at the nanoscale: grain boundary structure and its influence on plastic deformation." *Mater. Sci. Engg. A*, 309-310, 440-444.

[248] Van Swygenhoven, H., and Derlet, P. M. (2001). "Grain-boundary sliding in nanocrystalline fcc metals." *Phys. Rev. B*, 64(22), 224105.

[249] Van Swygenhoven, H., Derlet, P. M., and Froseth, A. G. (2004). "Stacking fault energies and slip in nanocrystalline metals." *Nature Materials*, 3, 399-403.

[250] Van Swygenhoven, H., Derlet, P. M., and Hasnaoui, A. (2002). "Atomic mechanism for dislocation emission from nanosized grain boundaries." *Phys. Rev. B*, 66, 024101.

[251] Van Swygenhoven, H., Farkas, D., and Caro, A. (2000). "Grain-boundary structures in polycrystalline metals at the nanoscale." *Phys. Rev. B*, 62(2), 831-838.

[252] Van Swygenhoven, H., Spaczer, M., and Caro, A. (1999a). "Microscopic description of plasticity in computer generated metallic nanophase samples: A comparison between Cu and Ni." *Acta Materialia*, 47(10), 3117-3126.

[253] Van Swygenhoven, H., Spaczer, M., Caro, A., and Farkas, D. (1999b). "Competing plastic deformation mechanisms in nanophase metals." *Phys. Rev. B*, 60, 22-25.

[254] Vandersall, K. S., and Thadhani, N. N. (2003). "Time-resolved measurements of the shock-compression response of Mo+2Si elemental powder mixtures." *J. Appl. Phys.*, 94(3), 1575-1576.

[255] Vendange, V., and Colomban, P. (1993). "Elaboration and thermal stability of (alumina, aluminosilicate/iron, cobalt, nickel) magnetic nanocomposites prepared through a sol-gel route." *Mater. Sci. Engg. A*, 168(2), 199-203.

[256] Verlet, L. (1967). "Computer "experiments" on classical fluids. I. Thermodynamical properties of Lennard-Jones Molecules." *Phys. Rev.*, 159, 98-103.

[257] Vincent, J., and Merz, K. M. (1995). "A highly portable parallel implementation of AMBER using the Message Passing Interface standard." *J. Comp. Chem.*, 11, 1420-1427.

[258] Voronoi, G. F. (1908). "Nouvelles applications des parameters continus a la theorie des formes quadratiques." *J. Reine Angew. Math., Premiere memoire*, 133, 97-178.

[259] Voter, A. F., and Chen, S. P. (1987). "Interatomic Potentials for Ni, Al and Ni_3Al." *Mat. Res. Soc. Symp. Proc.*, 82, 175-180.

[260] Wagner, N. J., Holian, B. L., and Voter, A. F. (1992). "Molecular-dynamics simulations of two-dimensional materials at high strain rates." *Phys. Rev. A*, 45(12), 8457-8470.

[261] Wang, H.-T., and Yang, W. (2004). "Constitutive modeling for nanocrystalline metals based on cooperative grain boundary mechanisms." *J. Mech. Phys. Solids*, 52, 1151-1173.

[262] Wang, N., Wang, Z., Aust, K. T., and Erb, U. (1997). "Room temperature creep behavior of nanocrystalline nickel produced by an electrodeposition technique." *Mater. Sci. Engg. A*, 237(2), 150-158.

[263] Warner, D. H., Sansoz, F., and Molinari, J. F. (2004). "Modeling of deformation in nanocrystalline Copper using an atomistic-based continuum approach." *Mat. Res. Soc. Symp. Proc.*, Boston, Mass., Q5.31.1-6.

[264] Weertman, J. R., and Sanders, P. G. (1994). "Plastic deformation of nanocrystalline metals." *Solid State Phenomena*, 35-36, 249-262.

[265] Wei, Y. J., and Anand, L. (2004). "Grain-boundary sliding and separation in polycrystalline metals: application to nanocrystalline *fcc* metals." *J. Mech. Phys. Solids*, 52, 2587-2616.

[266] Wilson, M., Exner, M., Huang, Y.-M., and Finnis, M. W. (1996). "Transferable model for the atomistic simulation of Al_2O_3." *Phys. Rev. B*, 54(22), 15683-15689.

[267] Wolf, D. (1992). "Reconstruction of NaCl surfaces from a dipolar solution to the Madelung problem." *Phys. Rev. Lett.*, 68(22), 3315-3318.

[268] Woodley, S. M., Battle, P. D., Gale, J. D., and Catlowa, R. A. (1999). "The prediction of inorganic crystal structures using a genetic algorithm and energy minimization." *Phys. Chem. Chem. Phys.*, 1, 2535-2542.

[269] Wyckoff, R. W. G. (1963). *Crystal Structures*, John Wiley and Sons, New York, London.

[270] Xu, Y., Huang, G., and Long, H. (2003). "Sol–gel synthesis of $BaTi_2O_5$." *Materials Letters*, 57(22023), 3570-3573.

[271] Yamakov, V., Wolf, D., Phillpot, S. R., and Gleiter, H. (2002a). "Deformation twinning in nanocrystalline Al by molecular dynamics simulations." *Acta Materialia*, 50, 5005-5020.

[272] Yamakov, V., Wolf, D., Phillpot, S. R., and Gleiter, H. (2002b). "Grain-boundary diffusion creep in nanocrystalline palladium by molecular dynamics simulations." *Acta Materialia*, 50, 61-73.

[273] Yamakov, V., Wolf, D., Phillpot, S. R., and Gleiter, H. (2003). "Dislocation–dislocation and dislocation–twin reactions in nanocrystalline Al by molecular dynamics simulation." *Acta Materialia*, 51(14), 4135-4147.

[274] Yamakov, V., Wolf, D., Salazar, M., Phillpot, S. R., and Gleiter, H. (2001). "Length-scale effects in the nucleation of extended dislocations in nanocrystalline Al by molecular-dynamics simulation." *Acta Materialia*, 49(14), 2713-2722.

[275] Yang, F., and Li, J. C. (1995). "Comments on a model for nano-indentation creep'." *Scripta Materialia*, 32(1), 139-144.

[276] Yang, W., and Wang, H. T. (2003). "Mechanics modeling for deformation of nano-grained metals." *J. Mech. Phys. Solids*, doi:10.1016/j.jmps.2003.07.003.

[277] Yano, K., and Horie, Y. (1999). "Discrete-element modeling of shock compression of polycrystalline copper." *Phys. Rev. B*, 59(21), 13672-13680.

[278] Zaretsky, E. (1995). "Dislocation multiplication in *fcc* metals at presence of high shear stress." *Acta Metallurgica et Materialia*, 43(1), 193-198.

[279] Zel'dovich, Y. B., and Raizer, Y. P. (1968). *Elements of gas dynamics and the classical theory of shock waves*, Academic Press, New York.

[280] Zhai, J., Tomar, V., and Zhou, M. (2004). "Micromechanical modeling of dynamic fracture using the cohesive finite element method." *J. Engg. Mat. Tech.*, 126, 179-191.

[281] Zhai, Z., and Chen, H. (2003). "Crystallization kinetics and dielectric properties in sol-gel derived (Pb,La)(Zr,Sn,Ti)O_3 ceramics." *J. Appl. Phys.*, 94(1), 589-593.

[282] Zhakhovskii, V. V., Nishihara, K., Anisimov, S. I., and Inogamov, N. A. (2000). "Molecular-dynamics simulation of rarefaction waves in media that can undergo phase transitions." *Pis'ma v Zhurnal Eksperimental'noi i Teoreticheskoi Fiziki*, 71(4), 241-248.

[283] Zhakhovskii, V. V., Zybin, S. V., Nishihara, K., and Anisimov, S. I. (1999). "Shock wave structure in Lennard-Jones crystal via molecular dynamics." *Phys. Rev. Lett.*, 83(6-9), 1175-1178.

[284] Zhao, Y. H., Lu, K., and Zhang, K. (2002). "Microstructure evolution and thermal properties in nanocrystalline Cu during mechanical attrition." *Phys. Rev. B*, 66, 085404.

[285] Zheng, G.-P., Gross, D., and Li, M. (2003). "Atomistic modeling of nanocrystalline ferromagnets." *J. Appl. Physics*, 93(10), 7652-7654.

[286] Zheng, G. P., Wang, Y. M., and Li, M. (2005). "Atomistic simulation studies on deformation mechanism of nanocrystalline Cobalt." *Acta Materialia*, 53, 3893-3901.

[287] Zhou, M. (2003). "A new look at the atomic level virial stress- On continuum-molecular system equivalence." *Proc. Royal Soc. London A*, 459, 2347-2392.

[288] Zhou, M., and McDowell, D. L. (2002). "Equivalent continuum for dynamically deforming atomistic particle systems." *Phil. Mag. A*, 82(13), 2547-2574.

[289] Zimmerman, J. A., Gao, H., and Abraham, F. F. (2000). "Generalized stacking fault energies for embedded atom fcc metals." *Model. Sim. Mater. Sci. Engg.*, 8, 103-115.

[290] Zimmerman, J. A., Kelchner, C. L., Klein, P. A., Hamilton, J. C., and Foiles, S. M. (2001). "Surface step effects on nanoindentation." *Phys. Rev. Lett.*, 87(16), 165507-4.

[291] Zimmerman, J. A., Webb, E. B., Hoyt, J. J., Jones, R. E., Klein, P. A., and Bammann, D. J. (2004). "Calculation of stress in atomistic simulation." *Mod. Sim. Mat. Sci. Engg.*, 12, S319-S332.

[292] Zybin, S. V., Elert, M. L., Harrison, J. A., and White, C. T. (2001). "Atomistic modeling of orientation dependence of shock wave properties in diamond." *Shock Compression of Condensed Matter*, Atlanta, GA, USA, 732.

[293] Zybin, S. V., Elert, M. L., and White, C. T. (2002). "Orientation dependence of shock-induced chemistry in diamond." *Phys. Rev. B*, 66, 220102.

[294] Zybin, S. V., Elert, M. L., and White, C. T. (2004). "Nanoscale view of shock-wave splitting in Diamond." *Metallurgical and Materials Transactions A: Physical Metallurgy and Materials Science*, 35(9), 2647-2650.

VITA

Vikas Tomar was born in Bhind, India on January 6th, 1977. He got his education till high school and junior college in Bilaspur, Mandsor, and Ujjain. He started his technical education in 1994 at Regional Engineering College, Kurukshetra-India (Now, National Institute of Technology, Kurukshetra) in mechanical engineering where he earned bachelor in technology in 1998 with the highest distinction. From 1998 to 1999 he worked for Indian Railways Construction International Ltd. (A Govt. of India Company) as a trainee assistant manager for mechanical operations. After obtaining engineering management work experience for one year in the job, he continued his technical education at Indian Institute of Technology (IIT), Madras from 1999 where he was awarded DAAD scholarship from Germany to continue his master's research work at University of Stuttgart. He graduated from IIT-Madras in 2001 with the highest distinction. He Joined Georgia Institute of Technology for a PhD in mechanical engineering in May, 2001. His research work at Georgia Institute of technology has focused on the analyses of dynamic failure mechanisms in micro- and nanoscale composite material systems. Besides work his interests are in sky diving, running, cricket, badminton, swimming, kayaking, rafting, weight lifting, rock climbing, driving, tourism, cooking, and movie watching.